

AFOSR-TR- 79 - 0937

A012586

2



Department of AERONAUTICS and ASTRONAUTICS
STANFORD UNIVERSITY

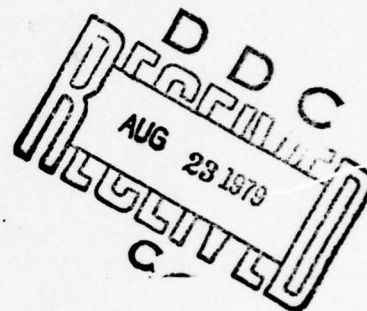
LEVEL

FINAL SCIENTIFIC REPORT

TO

AIR FORCE OFFICE OF SCIENTIFIC RESEARCH
WASHINGTON, D.C.

AD A073074



IMPROVED FLOW VISUALIZATION
BY USE OF RESONANT REFRACTIVITY

AFOSR 74-2670

Submitted by

Professor Daniel Bershader, Principal Investigator
Department of Aeronautics and Astronautics
Stanford University
Stanford, California 94305

DDC FILE COPY

July 10, 1979

Approved for public release;
distribution unlimited.

79 08 22 040

REPORT DOCUMENTATION PAGE		READ INSTRUCTIONS BEFORE COMPLETING FORM	
1. REPORT NUMBER (18) AFOSR-TR-79-0937	2. GOVT ACCESSION NO.	3. RECIPIENT'S CATALOG NUMBER	
4. TITLE (and Subtitle) (6) IMPROVED FLOW VISUALIZATION BY USE OF RESONANT REFRACTIVITY		5. TYPE OF REPORT & PERIOD COVERED (9) FINAL Rept. 1 Mar 74 - 28 Feb 79	
7. AUTHOR(s) (10) DANIEL BERSHADER		8. CONTRACT OR GRANT NUMBER(s) (15) AFOSR-74-2670	
9. PERFORMING ORGANIZATION NAME AND ADDRESS STANFORD UNIVERSITY AERONAUTICS AND ASTRONAUTICS DEPARTMENT STANFORD, CA 94305 332 560		10. PROGRAM ELEMENT, PROJECT, TASK AREA & WORK UNIT NUMBERS (16) 2307A3 (17) A3 61102F	
11. CONTROLLING OFFICE NAME AND ADDRESS AIR FORCE OFFICE OF SCIENTIFIC RESEARCH/NA BLDG 410 BOLLING AIR FORCE BASE, D C 20332		12. REPORT DATE (11) Jul 9 1979	
14. MONITORING AGENCY NAME & ADDRESS (if different from Controlling Office) (12) 292 p.		13. NUMBER OF PAGES 290	
16. DISTRIBUTION STATEMENT (of this Report) Approved for public release; distribution unlimited.		15. SECURITY CLASS. (of this report) UNCLASSIFIED	
17. DISTRIBUTION STATEMENT (of the abstract entered in Block 20, if different from Report)		15a. DECLASSIFICATION/DOWNGRADING SCHEDULE	
18. SUPPLEMENTARY NOTES			
19. KEY WORDS (Continue on reverse side if necessary and identify by block number) RESONANT REFRACTIVITY FLOW VISUALIZATION SPECTRAL LINE BROADENING INTERFEROMETRY SCHLIEREN TUNABLE DYE LASER IMPROVED OPTICAL TECHNIQUES			
20. ABSTRACT (Continue on reverse side if necessary and identify by block number) This report discusses the experimental and theoretical work carried out associated with the use of resonance refractivity to improve flow visualization. The principal accomplishment of the present study was to verify quantitatively the feasibility of using the near-resonance spectral region around the sodium D-lines for obtaining one-to-two order-of-magnitude increase in the sensitivity of refractive methods of flow visualization such as schlieren, interferometric and shadow techniques. It is in this "near" region of the line wings, typically a few angstrom from line center, that the trade-off between refraction and absorption is highly favorable.			

DD FORM 1 JAN 73 1473

332 560

UNCLASSIFIED

SECURITY CLASSIFICATION OF THIS PAGE (When Data Entered)

Unclassified

to permit implementation of the method with an available tunable dye laser light source. Here, the refractivity is high enough to see sound waves, weak vortices, etc. The accomplishments included a combined theoretical and experimental analysis of the near-region refractive and absorptive profile taking into account both doppler and collision broadening. The latter feature included studies to optimize the choice of collision parameters for self-broadening (pure sodium vapor) and for heterogeneous broadening (sodium highly diluted by a carrier gas in a flow facility). Experiments with an interferometer-heat pipe arrangement using a tunable pulsed dye laser gave results which agreed with the analysis. The technique is now at the facility-design stage.

UNCLASSIFIED

TABLE OF CONTENTS

ORIENTATION	1
ABSTRACT-SUMMARY	1
ASSESSMENT	4
PERSONNEL ASSOCIATED WITH THE PROJECT 1974-1979	5
LIST OF APPENDICES	6

Accession For	
NTIS GRA&I	<input checked="checked" type="checkbox"/>
DDC TAB	<input type="checkbox"/>
Unannounced	<input type="checkbox"/>
Justification	<input type="checkbox"/>
By _____	
Distribution/	
Availability Codes	
Dist	Avail and/or special
A	

AIR FORCE OFFICE OF SCIENTIFIC RESEARCH (AFSC)
 NOTICE OF TRANSMITTAL TO DDC
 This technical report has been reviewed and is
 approved for public release IAW AFR 190-12 (7b).
 Distribution is unlimited.
 A. D. BLOSE
 Technical Information Officer

Program on

FINAL SCIENTIFIC REPORT
Grant AFOSR 74-2670

IMPROVED FLOW VISUALIZATION
BY USE OF RESONANT REFRACTIVITY

Professor Daniel Bershader, Principal Investigator
STANFORD UNIVERSITY
Stanford, California 94305

ORIENTATION

This report covers the progress achieved on the subject grant over a five-year period. These introductory sections review the objectives of the program and the underlying technical essentials, together with an assessment of the accomplishments and recommendations for follow-up work. Included also is an abstract-summary which follows below. The detailed technical studies of this program are attached as appendices; they include two graduate dissertations and two published papers. Another paper attached will be published in the Proceedings of the XII International Symposium on Shock Tubes and Waves (AFOSR-sponsored) to be held in Jerusalem, Israel, July 16-19, 1979. Additional archive publications relating to material in the theses are in the planning-preparation stage.

ABSTRACT-SUMMARY

Objective of the present program has been to explore the feasibility of a significant increase in the sensitivity of refractive methods of flow diagnostics, methods which include schlieren, shadow and interferometry. The key idea relates to the enormous increase of the specific refractivity around the resonant frequency corresponding to an electronic transition. The development of the tunable dye laser as a light source enables practical utilization of the idea; and sodium vapor, which has an intense ground-state electronic transition in the visible spectrum, was chosen as a test gas for a calibration study.

Although the idea of refractive resonance dates back to the early part of the century, a quantitative analysis of resonant dispersion needed to be performed, taking into account the effects of doppler and collision broadening. Both effects are very important in modifying the refractive calculations made with a theory based only on natural line broadening. For

applications to flow visualization, both doppler and collisional spectral spreading are significantly present. The combined effects result in the so-called Voigt profile, which has received attention by investigators in connection with absorption line shape studies. By utilizing the integral relations between refractive and absorptive dispersion (Kramers-Kronig relations), we were able to formulate and obtain a computer output for refractive index and absorption coefficient at intervals of $.01 \text{ \AA}$ in the resonant region. These results are plotted in Figures 8 and 9, respectively, of the thesis of G. Blendstrup, (Appendix III, attached).

There are two points of practical importance about the analysis of these profiles. Of special importance is the trade-off required between enhanced absorption and refraction. The refractive maxima occur at the half-power points of the absorption resonance, but the absorption is too great there. In practice, one can work in the "near" region or wings of the line, typically several \AA off resonance. Here, the refractivity is still orders of magnitude higher than the nonresonant value; e.g. at 5880 \AA , the specific refractivity of sodium is 4,500 times larger than the nonresonant value for air. At the same time, the absorption coefficient is small enough so that the vapor is easily penetratable by a dye laser light source of moderate power.

The second point relates to the calculation of the collisional broadening coefficient. The latter is based on a quantum calculation of elastic atomic collision cross section, on whose value there is not full agreement among investigators. However, the profile must be re-calculated when sodium vapor is injected at high dilution into a carrier gas, e.g. nitrogen or argon, because the collision coefficient is much smaller than for self-broadening of pure sodium vapor. That is a favorable feature which increases the refractivity ratio and decreases the unwanted effects of absorption. Values for the collision coefficient for the alkali atoms for self-broadening, and for immersion in any of the inert gases as buffers are given in Table III of Blendstrup's thesis (Appendix III).

The study by Blendstrup also contains a detailed description of the calibration experiment, which will be described only briefly here (see Figures 10-14 of Appendix III). A double heat-pipe oven was designed and built to contain two sodium vapor columns of different lengths in a steady and uniform configuration in the two paths within a Mach-Zehnder interfero-

meter. The latter was illuminated by a tunable dye laser, especially designed and constructed for this experiment. The tunability feature was a blazed diffraction grating with micrometric angular control. The dye laser was, in turn, energized by ultraviolet photons at 3371 Å from a pulsed nitrogen laser (Molelectron Type UV300) focused on the dye cell within the laser cavity.

The essential feature of the experiment was the determination of fringe shift as a function of time resulting from a change of sodium vapor density when more heat was applied to one of the ovens. Data was obtained in the near region from 5863 Å to 5881 Å on the high frequency side of the D₂-line ($\lambda = 5889.96$ Å). As shown in Figure 2 of Appendix II, agreement between theory and experiment is quite satisfactory. The vertical uncertainty bars shown stem from tolerance limits on temperature determination, on the actual length of the sodium column between the two diffusion boundaries, and on the fringe shift count in portions of the data where fringe contrast was poor.

A separate experimental study of absorptive dispersion was made for back-up purposes. The redundancy arising from the Kramers-Kronig relations between refractive and absorptive dispersion was felt to be a desirable feature in establishing further confidence in the results. The work is covered in the thesis of I. J. Benard, attached as Appendix IV. Here again we are especially interested in the trade-off between absorption and dispersion in the near region, so the measurements were made in the wavelength range between 10 and 40 Å off resonance (see Figure 3 of Appendix IV).

Results of the studies are compared with the prediction that the absorption coefficients determined at various pressures and wavelengths should fall on a universal curve C/X^2 plotted against the variable X , where $X = (\omega_r - \omega)/\gamma_L$, C is a constant, $\omega_r - \omega$ is the frequency difference from resonance, and γ_L is the Lorentzian half-width. A systematic deviation is found with pressure which is about twice as large as the estimates of possible errors due to the presence of molecular sodium Na₂, and to the absorption by sodium-argon mixtures at the diffusion boundaries of the vapor column. Less certain are the effects of scattering by condensing sodium droplets.

Fortunately, the deviation just mentioned is more of a basic scientific question and does not affect the objective of the program. The study was important because the experimental results are a data bank for determining

the actual absorption to be encountered in a particular resonant refractive setup. We have learned that absorption values in the near region have only very small effect on the near-region refractivity. The latter is sensitive mainly to the absorption profile much closer to line center. This feature has not been discussed in previous literature, and will be the subject of a publication now in preparation.

The principal accomplishments summarized above, namely, (1) formulation and analysis of resonant dispersion behavior, (2) numerical solutions of refractive and absorptive resonant dispersion for sodium vapor, (3) design and construction of an experimental configuration to measure refractive dispersion and absorption in the near region, (4) measurement of dispersion behavior in the near region, and comparison with predictions of the analysis, (5) verification of the viability of the use of the near region for this work as a consequence of the trade-off between refraction and absorption, represent a principal objective of the program to date. The assessment and recommendations for follow-up work are given in the next section.

ASSESSMENT

The results just discussed confirm the physical foundation for the use of refractive resonant behavior for improved flow visualization, and they include quantitative results obtained for that purpose. It is clearly indicated, in our opinion that follow-up studies are warranted, studies which will establish the method as a working laboratory technique. The major follow-up studies include (1) design of a pilot flow facility using sodium injection in highly diluted amounts, and specially adapted to refractive-type optical studies; (2) construction and testing of such a facility to optimize parameters for the resonant refractive method, and to de-bug the configuration; (3) performance of a series of "case studies" to illustrate the range of applicability - results of which will lead to further recommendations for use of the technique by other engineering research laboratories.

Item (1) above is presently under study as the major program of our laboratory under Grant AFOSR 79-0058, and is to be completed by Feb. 29, 1980. All indications so far are that the scientific and engineering know-how exist to implement a suitably-designed facility.

Items (2) and (3) would follow logically upon the completion of item (1), and their successful completion would accomplish the ultimate purpose of the whole study. It deserves mention that the flow facility construction and test phase need not be expensive, since we envisage a small-scale device capable of moderate speeds and operating around or somewhat below atmospheric static pressures. Several laboratories, including those at Stanford's Department of Aeronautics and Astronautics have the "elements" of such facilities, so that the requirements for items (2) and (3) would constitute design modifications rather than completely new configurations.

The list of applications of resonant refractive methods includes, as examples, visualization of moderate strength sonic noise in the audible region, vortices behind aircraft models in near-incompressible flow, turbulent structure of shear layers and other flows and portions of engine flows, exhausts and plume boundaries, where the refractivity variations are marginal. We feel that we are now one step closer to realization of such applications.

PERSONNEL ASSOCIATED WITH THE PROJECT 1974-1979

FACULTY:	Prof. D. Bershader	- Professor of Aerophysics and Principal Investigator
	Prof. P. Parikh	- Acting Assistant Professor, Dept. of Mechanical Engineering, Stanford University
	Dr. G. Prakash	- Research Associate, Dept. of Aeronautics and Astronautics, Stanford University
	Prof. P. Langhoff	- Professor of Chemistry, University of Indiana, visiting at Stanford University
	Dr. B. Armstrong	- Manager, Applied Physics Department, IBM Scientific Center, Palo Alto, California, Visiting Research Scholar, Stanford
	Prof. F. Hansen	- NASA-Ames Research Center and Consulting Professor at Stanford University
STUDENTS:	G. Blendstrup	- Ph.D., Stanford University 1978
	I. Benard	- Engineer Degree, Stanford 1979
	L. Chan	- Engineer Degree Candidate, Stanford
STAFF SUPPORT:		
	V. Matte	- Technician Specialist, Stanford University
	G. De Werk	- Precision Machinist and Shop Foreman, Stanford
	T. Storm	- Secretary, Stanford

LIST OF APPENDICES

- I D. Bershader, G. Prakash and G. Huhn, "Improved Flow Visualization by Use of Resonant Refractivity", Experimental Diagnostics in Gas Phase Combustion Systems, (B.T. Zinn, Ed.), pp. 595-609.
- II G. Blendstrup, D. Bershader and P. Langhoff, "Resonance Refractivity Studies of Sodium Vapor for Enhanced Flow Visualization", AIAA Jo. 16, October 1978, pp. 1106-1108.
- III G.W. Blendstrup, Resonance Refractivity Studies of Sodium Vapor, for Enhanced Flow Visualization, Doctoral Thesis, Dept. of Aeronautics and Astronautics, Stanford University, December 1978.
- IV I.J. Benard, Experimental Studies of Sodium Resonant Absorption, Engineer Thesis, Dept. of Aeronautics and Astronautics, Stanford University, June 1979.
- V G. Blendstrup, D. Bershader and P. Langhoff, "Recent Results of Resonant Refractivity Studies for Improved Flow Visualization", paper presented at the 12th International Symposium on Shock Tubes & Waves, Jerusalem, July 16-19, 1979. Will appear in the Proceedings of the Symposium at a later date.

Appendix I



Experimental Diagnostics in Gas Phase Combustion Systems

Volume Editor:
Ben T. Zinn

Associate Editors:
Craig T. Bowman
Daniel L. Hartley
Edward W. Price
James G. Skifstad

Series Editor:
Martin Summerfield

1977

**Progress in
Astronautics and Aeronautics**

Volume 53

**American Institute of
Aeronautics and Astronautics
New York, New York**

IMPROVED FLOW VISUALIZATION BY USE OF RESONANT REFRACTIVITY

D. Bershader*, S. G. Prakash[†], and G. Huhn[‡]
Stanford University, Stanford, Calif.

Abstract

Progress is reported on studies to utilize the greatly increased refractivity of gases near their atomic resonant frequencies to obtain correspondingly increased sensitivity of optical refractive methods used in studies of fluid flow. This analysis reviews briefly some highlights of the optical dispersion of gases, and presents results for the modification of resonant dispersion of sodium vapor due both to Doppler and collision broadening. The design of an experiment for measuring and calibrating the dispersion of sodium vapor is discussed, and the importance of the narrow-band tunable dye laser light source in this connection is indicated. Extension of the experimental design to include a flow facility with resonant refractive measurement capability also is discussed. A sample calculation is given of the application of the schlieren system to visualizing audible sound waves in which conventional and resonant-wave length light sources are compared.

I. Introduction

This report covers an early phase of the current study of flow visualization enhancement by use of resonant refractivity. The motivation for the effort stems from a continuing interest in making visible a class of fluid-dynamic phenomena that require refractive sensitivities outside the range of present

Presented as Paper 76-71 at the AIAA 14th Aerospace Sciences Meeting, Jan. 1976, Washington, D.C. This work was supported by the Air Force Office of Scientific Research, Department of Defense, under Contract AFOSR 74-2670A.

*Professor of Aerophysics and Vice-Chairman, Department of Aeronautics and Astronautics.

[†]Postdoctoral Chemical Physicist, Stanford Research Institute, Menlo Park, Calif.

[‡]Research Assistant.

methods. They include vortex phenomena in low-speed flow, aerodynamically generated sound at or near the audible range, and turbulence in low-speed flows, including meteorological flows.

II. Resonant vs Nonresonant Refractivity

Refractive behavior of fluid flowfields underlies several experimental methods used in their analysis, the most widely known of which are schlieren, shadow, and interferometry. The sensitivity of such methods is known¹ to be directly proportional to the refractivity constant, typically denoted by B in the relation

$$n - 1 = B\rho \quad (1)$$

where n is the refractive index and ρ is the fluid mass density.

Now, B depends on the frequency ω of the light source but the dependence over most of the spectrum for gases of common interest is weak, i.e., B is nearly constant (designated by B_0) with the approximate value for air in the visible

$$B_0 \approx 2.3 \times 10^{-4} \text{ met}^3/\text{kg} \quad (1a)$$

However, near a transition frequency ω between electronic states in the gas (often called resonant frequency), B becomes a very strong function of ω . When the latter lies near ω_r , we may write

$$B(\omega) = B_1(\omega, \omega_r, \omega_{r'}, \dots) + \left(\frac{e^2 f_r \mathcal{L}}{4m\epsilon_0 \omega_r \mathcal{M}} \right) \frac{(\omega_r - \omega)}{(\omega_r - \omega)^2 + \gamma_r^2/4} \quad (2)$$

where e, m = the electronic charge and mass, respectively

f = oscillator strength of the spectral line at ω_r

\mathcal{L}, \mathcal{M} = Loschmidt (Avogadro) number and atomic mass

$\omega_r, \omega_{r'}, \dots$ = the transition frequencies of the gas

γ_r = damping constant, controlling the sharpness of the resonant behavior

ϵ_0 = permittivity of free space

and where

$$B_1(\omega, \omega_{r'}, \omega_{r''}, \dots) = \sum_{r' \neq r} \frac{\epsilon^2 f_{r'}^2}{2m\epsilon_0 \omega_{r'} \mathcal{M}(\omega_{r'}^2 - \omega^2)} \quad (3)$$

For air and other diatomic gases, the electronic resonances occur in the ultra-violet so that for visible frequencies of the diagnostic light beams, $\omega_{r'}$ and all $\omega_{r''} \gg \omega$. Then the $\gamma_{r'}$ term can be dropped in Eq. (2), as it is in Eq. (3); and it then becomes evident why the terms in Eqs. (2) and (3) are only weakly dependent on ω . Using the subscript o for this case, we write

$$n_o(\omega) - 1 = B_o(\omega)\rho \quad (4)$$

(far off resonance)

where, in contrast to $B(\omega)$ in Eq. (2), $B_o(\omega)$ is nearly constant. B_o and B_1 differ only in that the summation for B_o includes all r' {see Eq. (3)}. If we switch from frequency to wavelength units, then Eq. (4) reads

$$n_o(\lambda) - 1 = K_o(\lambda)\rho \quad (4a)$$

where the more familiar $K_o(\lambda)$ is the $B_o(\omega)$ function expressed in terms of λ , and often called the Gladstone-Dale constant. Explicitly, we have

$$K_o(\lambda) = \frac{e^2}{m} \sum_{r'} \frac{a_{r'} \lambda^2}{\lambda^2 - \lambda_{r'}^2} \quad (5)$$

where

$$a_{r'} = e^2 f_{r'}^2 \lambda_{r'}^2 / 8\pi^2 \epsilon_0 m c^2 \quad (5a)$$

For $\lambda_{r'} \ll \lambda$, Eq. (4a) can be expanded to give the familiar Cauchy dispersion equation for the nonresonant regime:

$$n_o(\lambda) - 1 = 2.876 \times 10^{-4} + \frac{1.341}{\lambda^2} + \frac{3.78 \times 10^4}{\lambda^4} \quad (6)$$

where the numerical values apply to air at STP, and where the λ values are in millimicrons.

Turning to the resonant region, let us define a reference index n_1 by

$$n_1 - 1 = B_1 \rho \quad (7)$$

Then Eq. (2) may be written

$$n - n_1 = \frac{(\omega_r - \omega)H}{\omega_r \{ (\omega_r - \omega)^2 + \gamma_r^2/4 \}} \rho \quad (2a)$$

with

$$H = e^2 f_r / 4 \epsilon_0 m \eta$$

Figure 1 is a plot of $n - n_1$ vs ω for the sodium D-2 line based on Eq. (2a). That is a so-called Lorentzian function, and the shape around resonance is controlled, of course, by the value of the damping constant γ_r . The value of 1.00×10^8 rad./sec, given in the caption of Fig. 1 includes an allowance for pressure or collision self-broadening correspondence to the presently chosen values of vapor density and temperature. Indeed, $\gamma_r = \gamma_N + \gamma_C$, where γ_N is the natural or classical damping, and γ_C is the collisional damping. What is not treated in constructing Fig. 1 is Doppler broad-

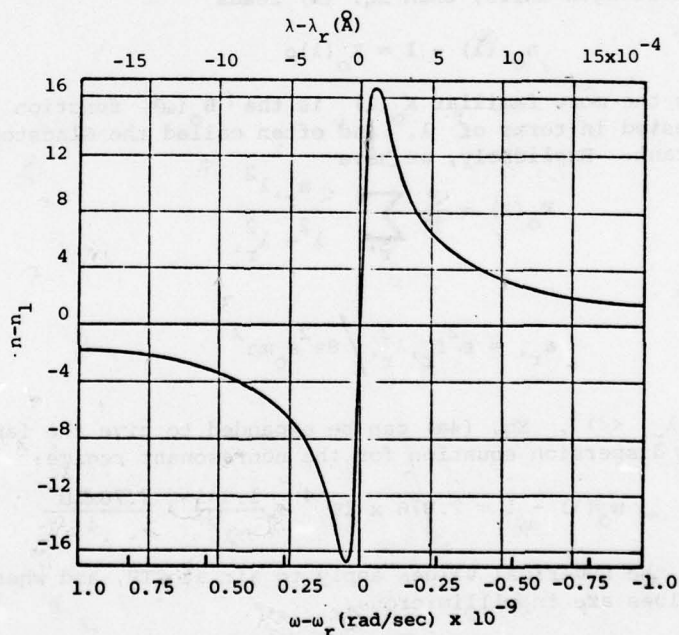


Fig.1 Plot of refractive index variation near resonance with Lorentzian broadening only, for the sodium D-2 line $\lambda_r = 5889.96 \text{ \AA}$. The quantity n_1 is a nonresonant index [see Eq. (7)].

ening, which is actually the controlling factor for the line width in the present work. That feature is discussed later in some detail.

Comparison of Fig. 1 with the resonance absorption or emission curve would show that the positive and negative peaks of n occur at the half-power points. The displacement from resonance of the latter is 7.96 MHz or $0.92 \times 10^{-4} \text{ \AA}$, which, therefore, implies high-resolution optics if one is going to utilize the resonant behavior. Note that the dispersion curves tend asymptotically toward values $>n_1$ at the longer wavelengths, and $<n_1$ at wavelengths smaller than the resonant value. Since n_1 is nearly equal to unity to within a very small fraction of a percent, this means that in the lower-wavelength part of the spectrum, the velocity of light in sodium vapor is greater than the vacuum velocity of light. We deal here with the phase velocity, so that no laws of physics are being violated.

Because Doppler-broadening effects have not been taken into account yet, Fig. 1 is not appropriate for use in resonant refractivity work. For reference, we note that the peak value of 16.7 may be compared with a nonresonant value of 0.000058 at $\lambda = 6200 \text{ \AA}$, based on data given by Wood.² Since it is $n-1$ that determines the specific refractivity, the ultimate gain without Doppler broadening is $15.7/5.8 \times 10^{-6} = 2.71 \times 10^6$. This value in fact, is modified appreciably by Doppler broadening, which we now examine.

III. Doppler Modified Resonant Refractivity

Thermal motion of radiating atoms produces frequency shifts of the well-known Doppler type; i.e., the shifted frequency due to an atom velocity v is $\omega(1 + v/c)$, where ω is the unshifted frequency and v may be positive or negative. If the atomic velocity distribution is Maxwellian, then dN , the number density of particles with velocity components between v and $v + dv$ is

$$\frac{dN}{N} = \frac{M}{2\pi kT}^{1/2} e^{-\frac{Mv^2}{2kT}} dv = 2 \frac{Mv^2}{2kT} \frac{dv}{(\pi/s) v} \quad (8)$$

where \bar{v} is the mean thermal velocity of the particles, and where the other symbols have their usual definitions. Now, the refractive dispersion near resonance for any particle moving with velocity v will be Lorentz-broadened in accord-

ance with Eq. (2a), which now must be integrated over the particle velocity distribution to give the refractivity. Thus

$$n - n_1 = \frac{\pi e N f}{m \omega_r} \int_{-\infty}^{+\infty} \frac{\omega_r - \omega(1+v/c)}{\{\omega_r - \omega(1+v/c)\}^2 + \gamma_r^2/4} \times e^{-Mv^2/2kT} \frac{dv}{\pi^{1/2}/2} \quad (9)$$

Next, it is useful to recast the Eq. (9) by introducing nondimensional variables in terms of ω_r , c , and a characteristic molecular thermal velocity $\sqrt{2kT/M}$. Define

$$x = (\omega_r/c) v / (\omega_r/c) \sqrt{2kT/M} = v \sqrt{M/2kT} \quad (10)$$

$$a = \gamma_r/2 / (\omega_r/c) \sqrt{2kT/M} \quad (11)$$

$$u = \omega_r - \omega / (\omega_r/c) \sqrt{2kT/M} \quad (12)$$

The refractive index now appears in a form more adaptable for evaluation:

$$n - n_1 = \sqrt{\frac{M}{2\pi kT}} \frac{\pi e^2 N f_r c}{m \omega_r} \int_{-\infty}^{+\infty} \frac{u - x}{(u-x)^2 + a^2} e^{-x^2} dx \quad (13)$$

We have evaluated Eq. (13) as a function of the normalized frequency u . The integral was computed by interpolating the tabulated values in the range $0 < u < 3.9$, and a computer program was employed for $u > 3.9$.

The profile is shown in Fig. 2. It should be noted that, apart from a constant, u represents the frequency difference normalized with respect to the Doppler half-width $\Delta\nu_D$

$$u = \frac{\omega_r - \omega}{(\omega_r/c) \sqrt{2kT/M}} = \frac{2 \sqrt{\ln 2} (\nu_r - \nu)}{\Delta\nu_D} \quad (13a)$$

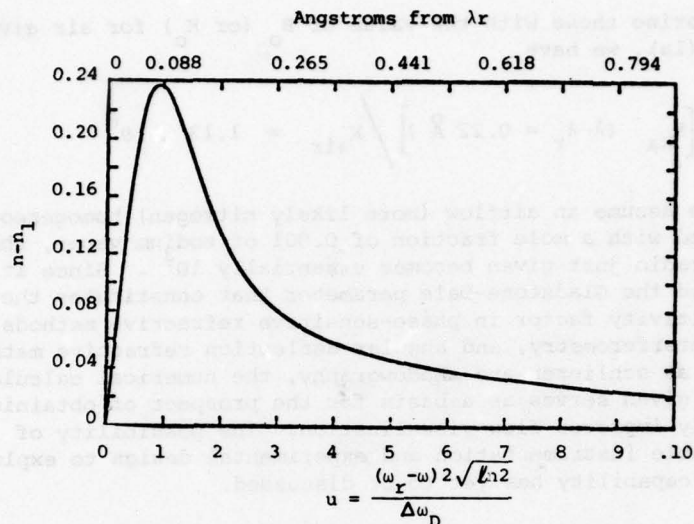


Fig. 2 Dispersion of the D_2 line of sodium vapor including the effects of Doppler broadening: refractive index vs frequency separation from line center. Note that n_1 represents the nonresonant refractivity value, also that $\Delta\omega_D = 2\pi\Delta\nu_D$ as given in Eq. (13b).

where $\Delta\nu_D$ is the Doppler half-width given by

$$\Delta\nu_D = \left(2\nu_r/c\right) \sqrt{2kT/M} \ln 2 \quad (13b)$$

IV. Sensitivity Amplification with Modified Resonant Dispersion

Doppler broadening lowered the peak refractive index value significantly, but it also produced a significant spread of the effective resonant region. Note that there exists a very large refractivity out to nearly 1 Å from line center, and actually well beyond that. Suppose we can probe the gas with a narrow-band beam (we have yet to say how) at about 0.22 Å off resonance, where $n - n_1$ (effectively $n - 1$) equals 0.10, as shown in Fig. 2. An effective "Gladstone-Dale" constant for optical refractive sensitivity calculations would be, for $N = 10^{22}$ particles/m³

$$K_{Na}(\lambda - \lambda_r = 0.22 \text{ Å}) = \frac{n-1}{\rho} = \frac{0.10}{3.82 \times 10^{-4}} = 2.61 \times 10^2 \frac{\text{m}^2}{\text{kg}} \quad (14)$$

Comparing these with the value of B_0 (or K_0) for air given in Eq. (1a), we have

$$\left[K_{Na} (\lambda - \lambda_r = 0.22 \text{ \AA}) \right] / K_{air} = 1.13 \times 10^6 \quad (15)$$

If we assume an airflow (more likely nitrogen) homogeneously seeded with a mole fraction of 0.001 of sodium vapor, then the ratio just given becomes essentially 10^3 . Since it is indeed the Gladstone-Dale parameter that constitutes the basic sensitivity factor in phase-sensitive refractive methods, such as interferometry, and angular deflection refractive methods, such as schlieren and shadowgraphy, the numerical calculation just given serves as a basis for the prospect of obtaining highly improved flow visualization. The possibility of suitable instrumentation and experimental design to exploit this capability has yet to be discussed.

V. Resonant Refractivity Calibration Experiment

To utilize the potential of resonant refraction, one clearly must have a sufficiently narrow-band, preferably tunable light source with sufficient intensity to overcome the non-negligible absorption near resonance. The tunable dye laser can satisfy these requirements; and an interferometer, such as the Mach-Zehnder device, can serve for refractivity measurement or calibration.

Fig. 3 shows a schematic of a system designed for initial experiments to check the predicted resonant dispersion of sodium vapor, and also to test the sensitivity to a primitive disturbance. The dye laser light source, containing principally rhodamine 6G, is activated by an ultraviolet laser beam from a nitrogen pump laser at $\lambda = 3371 \text{ \AA}$ (Molelectron-type) suitable focused on the dye cell with a cylindrical lens. The dye cell is located in its own laser cavity with a blazed grating as one of the terminal elements. Fine rotation of the grating produces correspondingly fine frequency tuning of the output beam. Better operation is obtained by use of a beam expander, which allows use of the total grating area. The beam exits the cavity through a small-angle glass wedge, passes through another beam expander, and enters the Mach-Zehnder interferometer.

The two paths of the interferometer contain two sections of a double heat-pipe oven utilizing clam-shell heaters over a stainless steel tube, and an 80-mesh stainless screen in-

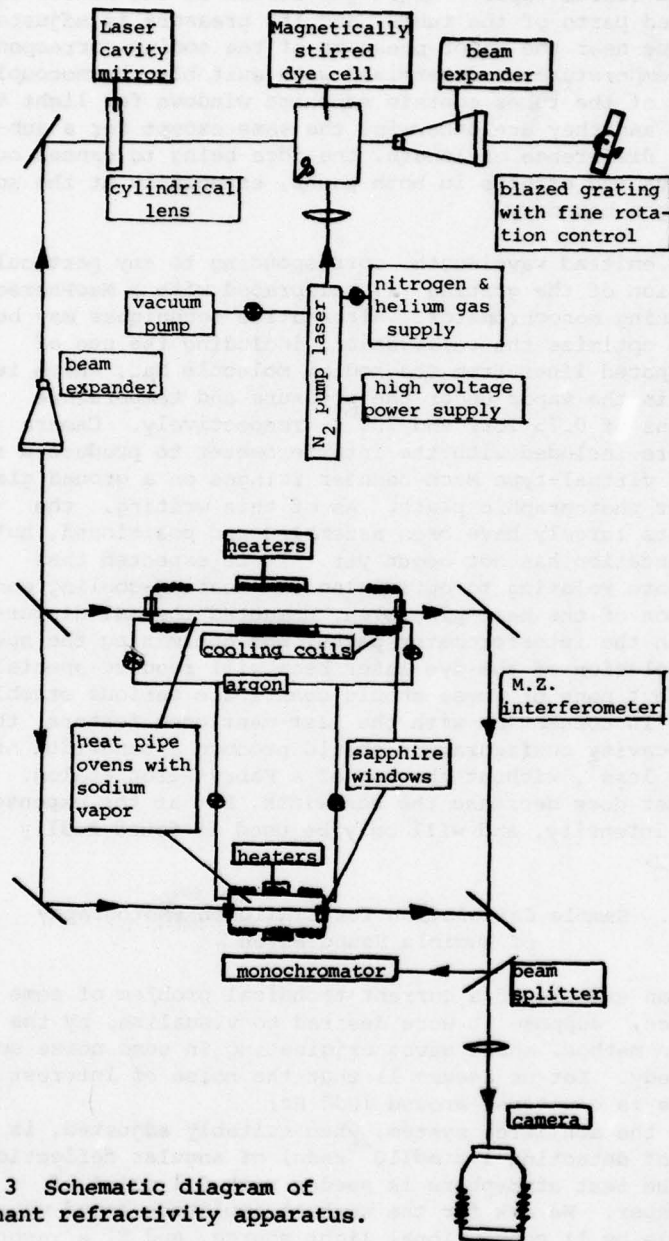


Fig. 3 Schematic diagram of resonant refractivity apparatus.

side the tube for the capillary-motion return path of the condensed sodium vapor. Argon gas serves as the buffer in the cooled parts of the tubes, and its pressure is adjustable to a value near the vapor pressure of the sodium corresponding to the temperature as determined with suitable thermocouples. The ends of the tubes contain sapphire windows for light transmission, and they are otherwise the same except for a substantial difference of length, the idea being to cancel out refractive end effects in both paths, especially at the sodium vapor-argon boundary.

The emitted wavelength corresponding to any particular orientation of the grating is calibrated with a MacPherson 1-m scanning monochromator. Alternative techniques may be tried to optimize the calibration, including the use of finely spaced lines from the sodium molecule Na_2 , which is present in the vapor under the pressure and temperature conditions of 0.75 Torr and 700°K, respectively. Camera optics are included with the interferometer to produce a real image of virtual-type Mach-Zehnder fringes on a ground glass screen or photographic plate. As of this writing, the components largely have been assembled and positioned, but experimentation has not begun yet. It is expected that adjustments relating to optimizing the heating-cooling configuration of the heat-pipe oven, unwanted thermal disturbances in the interferometer paths, and optimizing the spectral resolution of the dye laser beam will require special effort, but none of these should constitute serious stumbling blocks. In connection with the last-mentioned feature, the grating-cavity configuration should produce a bandwidth of 0.1 Å or less, without the use of a Fabry-Perot etalon. The latter does decrease the bandwidth, but at the expense of beam intensity, and will only be used if found really necessary.

VI. Sample Calculation for Schlieren Photography of Audible Sound Waves

As an example of a current technical problem of some importance, suppose it were desired to visualize, by the schlieren method, sound waves originating in some noise source under study. Let us assume 1) that the noise of interest in this case is clustered around 1000 Hz; 2) that the schlieren system, when suitably adjusted, is capable of detecting $1 \mu\text{rad}$ (10^{-6} rads) of angular deflection; and 3) the test atmosphere is seeded with 0.1 mol % of sodium vapor. We ask for the weakest-amplitude sound wave detectable by 1) conventional light source, and 2) a resonant-frequency light source.

The expression for a small angular deflection ϵ by a density gradient component, say dp/dx , is, for a two-dimensional disturbance

$$\epsilon = KL dp/dx \quad (16)$$

where K is the Gladstone-Dale constant [numerically equal to B , see Eqs. (1), (14), and (15)]; and L is the span of the disturbance in the direction of the ignorable coordinate. Let us choose $L = 0.10$ m, and let us interpret dp/dx in terms of the strength of the 1000-Hz sound wave.

We assume that the schlieren light source will be pulsed so as to "stop" the sound wave in snapshot fashion. The sound overpressure p may be assumed to have a sinusoidal distribution in x

$$p = p_o \sin kx \quad (17)$$

where k is the wave number, $2\pi/\lambda$. The density gradient now may be written

$$dp/dx = (dp/dp)_{ad} (dp/dx) = (k/a^2) p_o \cos kx \quad (18)$$

where the subscript ad stands for adiabatic, that derivative thus being equal to the reciprocal of a^2 , the sound speed squared. The gradient's maximum value will be

$$(dp/dx)_{max} = kp_o/a^2 \quad (18a)$$

and it is that value that we should use in Eq. (16). Combining the two relations and solving for p_o , we obtain

$$p_o = (a^2/kLK) \epsilon = a^3 \epsilon / 2\pi \nu KL \quad (19)$$

Choosing $a = 340$ m/sec and using values of K_o (or B_o) given in Eqs. (1a) and (14), the latter adjusted for 10^{-3} mol fraction of sodium vapor, we obtain p_o^{NR} (nonresonant) and p_o^R (resonant).

Substitution of numerical values gives the sound pressure level (SPL) which, when expressed in terms of the usual decibel notation, reads for the nonresonant case

$$(SPL)^{NR} = 20 \log (p_o^{NR} / 2 \times 10^{-5}) = 143 \text{ dB} \quad (20)$$

where 2×10^{-5} Newtons/m² is the conventional threshold value. This is an extremely loud sound, not only painful but damaging to the ear even for short times. It is comparable to the noise quite close to a sizeable jet engine.

Replacing the refractivity constant K with the resonant value adjusted for 0.1 mol % sodium vapor, we obtain a value of maximum pressure, P_O^R , smaller by a factor of 1130 [see Eq. (15)]. The resultant sound pressure level is

$$(\text{SPL})^R = 20 \log (P_O^R / 2 \times 10^{-5}) = 82 \text{ dB} \quad (21)$$

a rather loud sound, but one which is more commonly experienced in many noise-type situations. Note that changing frequency by a factor of 10 modifies the above values by 20 dB, higher threshold values for lower frequencies, and vice versa. Thus, it is evident that the use of resonant refractivity offers a visual capability for sound waves which is more widely applicable than is possible with nonresonant light sources.

VII. Experimental Implementation and Utilization

Calibration of the system will include firstly a wide-band nonresonant, as well as a narrow-band resonant dispersion measurement of sodium vapor. For this purpose, fringe shift counts will be taken at specified wavelengths. Consistency of measured refractivities at (off-resonance) wavelengths where good published data are available will provide a check of experimental precision (e.g., cancellation of end effects at the sodium vapor-argon boundary, etc.) combined with the use of densities based on the sodium vapor pressure-temperature curves.

Accurate wavelength determination in the resonant regime depends on the bandwidth of the dye laser beam. If we assume that, without the use of a Fabry-Perot etalon, the bandwidth will be approximately 0.1 \AA , narrow enough in relation to the resonance curve shown in Fig. 2, then a calibration of the rotational control position of the diffraction grating (see Fig. 3) will be made with the aid of the monochromator, as mentioned earlier. Narrow molecular lines of known wavelength are convenient calibration points. Especially convenient, if feasible, would be the use of the sodium Na_2 lines, also mentioned earlier.

Table 1 is a listing of Na_2 lines on the low-wave length side of the Na-D2 resonance line, $\lambda = 5889.96 \text{ \AA}$, reaching

Table 1 Spectral lines of the Na₂ molecule on the low-wavelength side of the Na D-2 resonance line at $\lambda_r = 5889.96 \text{ \AA}$ ^{a,b}

v''	J''	v'	J'	Wavelength \AA	Relative intensity
3	19	26	20	5889.44	0.848E+04
3	47	27	48	5889.20	0.890E+04
3	15	26	14	5889.14	0.662E+04
0	100	27	99	5889.10	0.788E+01
2	57	26	58	5889.09	0.457E+04
0	37	22	36	5889.04	0.104E+04
1	24	23	25	5889.03	0.244E+04
1	46	24	45	5889.91	0.181E+04
1	62	25	61	5889.89	0.913E+03
2	71	27	72	5888.83	0.224E+04
1	78	26	79	5888.79	0.374E+03
3	18	26	19	5888.79	0.489E+04
0	73	24	74	5888.75	0.217E+03
0	91	26	90	5888.69	0.355E+02
1	20	23	19	5888.66	0.206E+04
0	81	25	80	5888.61	0.931E+02

^aTemperature is 500°C. See discussion in Sec.VII for further information. Note the power-of-ten representation in the column marked "relative intensity", e.g., E + 04 means 10^4 , etc.

^bData kindly supplied by Dr. Mark Kaminsky, Stanford University.

as close as 0.5 \AA of line center. $\bar{\lambda}$ Given along with the wavelengths are the v and j -numbers for the upper (single-prime) and lower (double-prime) states. The transition is one between two singlet states, the A-Band, and the ground electronic state. Relative intensities are also shown in accordance with the relation

$$\text{intensity factor} = \beta F v \star (J' + J'' + 1) e^{-E_a/kT} \quad (22)$$

where β is the nuclear spin population factor ($=5/3$ for J'' odd; $=1$ for J'' even), F the Franck-Condon factor, ν^* is the energy of the transition in wavenumbers (cm^{-1}), and E_a is the energy of the lower state above the potential minimum of the ground state.

These intensities are considerably lower than the D-line intensities, and the proximity to the resonant wavelength at which the molecular lines are still visible has yet to be determined. Also to be checked is the attenuation near resonance by the wings of the absorption line. The exponential absorption coefficient for Doppler broadenings has yet to be calculated, but experience of others studying sodium vapor line structure with dye lasers indicates that the latter have sufficient intensity.

Following determination of the sodium dispersion over an accessible range of temperature corresponding to vapor densities in the range around $10^{22}/\text{m}^3$, a preliminary experiment is planned, involving a small refractive disturbance. The test might take the form of an acoustic disturbance from a transducer mounted in the tube wall, or possibly a thermal disturbance involving free-convective and/or radiative behavior. Comparison of resonant and nonresonant light sources will be made, results recorded, and the differences studied.

If results of the preliminary tests are up to expectations the design of a suitable flow facility will be studied. The flow likely will be nitrogen rather than air, and the chief technical challenge is the admixture of the desired amount of sodium seed material to produce a well-mixed test-section flow without condensation or other undesirable effects. A central goal would be to conduct the experiments with the minimum amount of temperature increase in the test section. It is felt that this should be possible because of the moderate seeding ratio. Whether the sodium itself will be introduced from a side-arm boiler, with the help of an aerosol technique or some other arrangement, has yet to be determined.

A working facility of the type described should be capable of flows of sufficient duration for studies of several types. The nitrogen pump laser pulse repetition can be varied from just a single pulse up to 50/sec; i.e., it can serve as a quasi-continuous light source. On the other hand, the duration of the dye laser pulse is of the order of several nanoseconds, so that there is no problem of photographing nonsteady or very fast-moving flow phenomena.

The remarks in this section are a brief summary of some of the follow-on studies required in this program. It is evident that several problems remain to be solved, and it is anticipated that these will be discussed in future presentations.

References

1. Ladenburg, R. and Bershader, D., "Interferometry," Physical Measurements in Gas Dynamics and Combustion, edited by Ladenburg, R., Princeton University Press, Princeton, 1954, pp. 47-78.
2. Wood, R.W., Physical Optics, Macmillan Co., New York, 1934.
3. Abramowitz, M. and Stegun, I.A., eds., Handbook of Mathematical Functions, National Bureau of Standards, Washington D.C., 1964.
4. Vidal, C.R. and Cooper, J., "Heat Pipe Oven: A New, Well-Defined Metal Vapor Device for Spectroscopic Measurements", Journal of Applied Physics, Vol. 40 No. 8, July 1969 pp. 3370-3374.
5. Hänsch, T.W., "Applications of Dye Lasers," Dye Lasers, edited by F. Schäfer, Springer-Verlag, New York, 1973.

Appendix II

Reprinted from AIAA JOURNAL, Vol. 16, No. 10, October 1978, pp. 1106-1108

Resonance Refractivity Studies of Sodium Vapor for Enhanced Flow Visualization

G. Blendstrup* and D. Bershader†
Stanford University, Stanford, Calif.

and
P.W. Langhoff‡
Indiana University, Bloomington, Ind.

Introduction

REFRACTIVE methods pioneered by the studies of Mach, Zehnder, Toepler, and others have been used for about 100 years to visualize fluid-dynamic flow phenomena. While there have been new developments in sophistication of the optical methodology and instrumentation, the sensitivity of essentially all work to date has been controlled by the specific refractivity of diatomic gases, e.g., air, in the visible portion of the spectrum. That quantity, K_0 , appears in the well-known Dale-Gladstone constitutive relation¹

$$n - 1 = K_0 \rho \quad (1)$$

relating refractive index n and gas density ρ . Its value is relatively constant over the visible portion of the spectrum:

$$K_{0\text{air}} \approx 2.3 \times 10^{-4} \text{ m}^3/\text{kg}$$

The relatively small magnitude of $K_{0\text{air}}$ has largely limited the application of techniques such as interferometry, Schlieren, and shadowgraphy to compressible flows with substantial density gradients; or to free convective flows with sizable thermal gradients. As an example, the density change corresponding to 0.1 fringe shift in a test rig with a transverse light path of 10 cm is $2.2 \times 10^{-3} \text{ kg/m}^3$ or 0.17% of standard atmospheric density. It turns out that a substantially higher sensitivity is desirable for several applications of current interest. These include vortices and turbulence in low-speed flow, propagation of sound or noise in the audible range, rarified gas flow, and meteorological flows.

The idea of using a tunable narrow band dye laser to illuminate a gas near its resonance line in order to increase the effective Dale-Gladstone "constant" was discussed in an earlier paper by two of the present authors.² Since the resonance transitions of air and other diatomic gases lie in the far ultraviolet, the work just referred to as well as the present Note deals with the resonance refractivity of sodium vapor. In a laboratory application of this method, the working fluid would be seeded with small quantities of sodium vapor or other suitable material, probably in the range 10^{-4} to 10^{-3} mole fraction.

The present Note describes recent results, including refinement of both the theoretical calculations and the ex-

Received April 18, 1978; revision received June 12, 1978. Copyright © American Institute of Aeronautics and Astronautics, Inc., 1978. All rights reserved.

Index categories: Experimental Methods of Diagnostics; Lasers.

*Research Assistant, Dept. of Aeronautics and Astronautics.

Student Member AIAA.

†Professor, Dept. of Aeronautics and Astronautics. Fellow AIAA.

‡Professor, Department of Chemistry.

perimental setup to check the resonance dispersion of sodium vapor, as well as the final calibration experiment on sodium vapor refractivity.

Theoretical

Atomic absorption and dispersion line shapes under conditions of Doppler, collision, and natural broadening can be represented by Voigt profiles of the form³

$$n_r(\nu) - 1 = \frac{\sqrt{\ln 2}}{8\pi^2 \sqrt{\pi}} \cdot \frac{e^2 N f_r}{m \epsilon_0 \gamma_D \nu_r} \int_{-\infty}^{\infty} \frac{\epsilon - \nu}{(\epsilon - \nu)^2 + \gamma_L^2/4} \cdot \exp[-4 \ln 2 \cdot (\epsilon - \nu_r)^2 / \gamma_D^2] d\epsilon \quad (2)$$

$$\mu_r(\nu) = \frac{\sqrt{\ln 2}}{4\pi \sqrt{\pi}} \cdot \frac{e^2 N f_r \gamma_L}{m \epsilon_0 \gamma_D} \int_{-\infty}^{\infty} \frac{1}{(\epsilon - \nu)^2 + \gamma_L^2/4} \cdot \exp[-4 \ln 2 \cdot (\epsilon - \nu_r)^2 / \gamma_D^2] d\epsilon \quad (3)$$

where the usual symbols are used for the familiar physical constants. Further, μ is the absorption index, f_r and ν_r are the total integrated oscillator strength of the particular doublet component and the corresponding resonance transition frequency, respectively; and γ_L and γ_D are the Lorentzian and Doppler "full-halfwidths" (full width at half maximum). The Doppler value is

$$\gamma_D = 2 \nu_r \sqrt{\frac{2kT}{M}} \sqrt{\ln 2} \quad (4)$$

while the Lorentzian value is the sum of natural and collision widths

$$\gamma_L = \gamma_n + \gamma_c \quad (5)$$

Recent measurements of sodium self-broadening over the number density range $N \sim 10^{16}$ to 10^{22} (atoms/m³) have given the values for the proportionality constant C_r in the relation

$$\gamma_c = 2C_r N$$

indicated in Table 1. Table 1 also presents values of oscillator strengths, resonant frequencies and wavelengths, and natural widths for the two sodium D-lines.

By use of dimensionless variables

$$u = \frac{2\sqrt{\ln 2}(\nu - \nu_r)}{\gamma_D} \quad (6a)$$

$$a = \frac{\gamma_L}{\gamma_D} \sqrt{\ln 2} \text{ (Voigt parameter)} \quad (6b)$$

$$y = \frac{2\sqrt{\ln 2}(\epsilon - \nu_r)}{\gamma_D} \quad (6c)$$

Table 1 Sodium D-lines parameters*

$\lambda_r, \text{\AA}$	$\nu_r, 10^{14}/\text{s}$ (Ref. 7)	f_r (Ref. 8)	$\gamma_n, 10^6/\text{s}$ (Ref. 8)	$C_r, 10^{-15} \text{ m}^3/\text{s}$ (Ref. 9)
D_1 5895.930	5.083345	0.327	9.99	7.32
D_2 5889.963	5.088500	0.655	10.03	8.59

* D_1 refers to the $^2S_{1/2} - ^2P_{1/2}$ transition, whereas D_2 refers to the $^2S_{1/2} - ^2P_{3/2}$ transition.

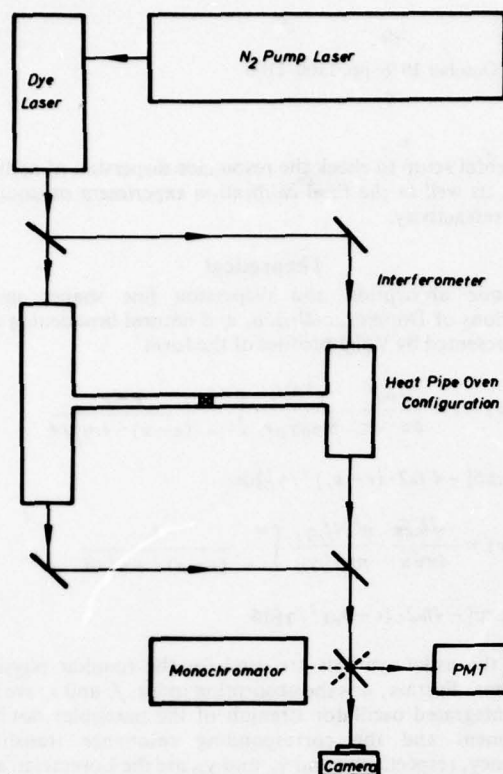


Fig. 1 Schematic diagram of resonant refractivity apparatus.

it is possible to rewrite Eqs. (2) and (3) to read

$$n_r(\nu) - 1 = \frac{\sqrt{\pi}}{8\pi^2} \frac{e^2 N f_r a}{m \epsilon_0 \gamma_L \nu_r} \left[\frac{1}{\pi} \int_{-\infty}^{\infty} \frac{y-u}{a^2 + (u-y)^2} e^{-y^2} dy \right] \quad (2a)$$

$$\mu_r(\nu) = \frac{\sqrt{\pi}}{2\pi} \frac{e^2 N f_r a}{m \epsilon_0 \gamma_L c} \left[\frac{a}{\pi} \int_{-\infty}^{\infty} \frac{1}{a^2 + (u-y)^2} e^{-y^2} dy \right] \quad (3a)$$

where the entities in square brackets can be recognized as the imaginary and real parts, respectively, of the complementary error function of complex argument

$$W(z) = e^{-z^2} \operatorname{erfc}(-i \cdot z), \quad z = u + ia \quad (7)$$

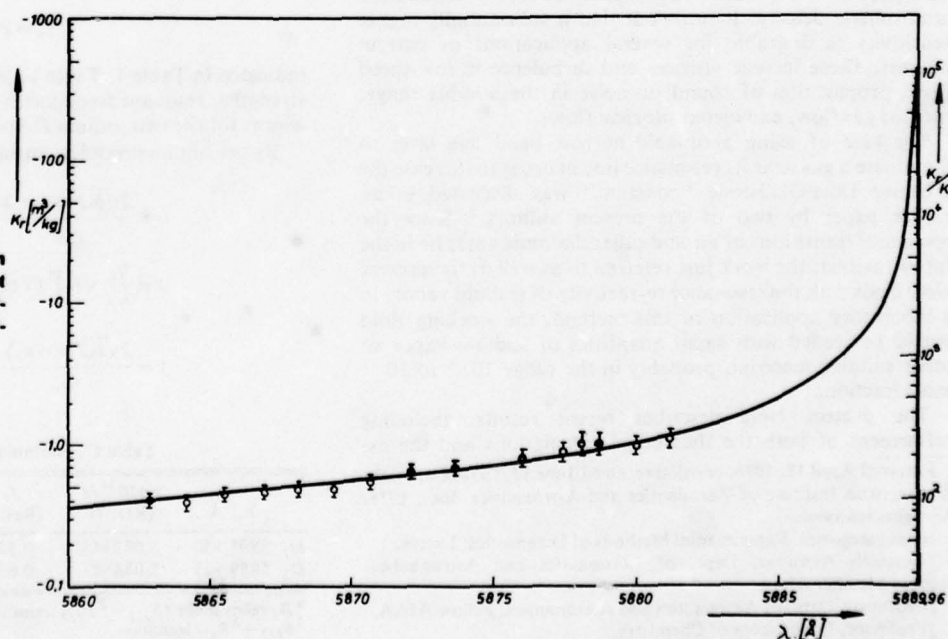
A computer program was used to calculate the $W(z)$ function based, in turn, on a method of Hummer and Rybicki³ to calculate the absorption Voigt profile [real part of $W(z)$]. To obtain the imaginary part, the Kroenig-Heisenberg⁴ expression was employed relating the real and imaginary parts of $W(z)$ to each other. A plot of the theoretical values of specific refractivity vs wavelength is shown in Fig. 2 (solid line).

Experiment

Major features of the experiment are highlighted in the schematic diagram of Fig. 1. Sodium vapor is generated and contained in a defined configuration by use of the heat-pipe oven apparatus. The latter, in turn, occupies a portion of the path in a Mach-Zehnder interferometer, and changes in sodium refractivity are monitored by fringe shifts. The light source is a tunable dye laser which has suitable resolution near the sodium resonance. The description of the transversely pumped dye laser in Hänsch⁵ configuration and the operation of the two heat-pipe ovens was briefly reviewed in Ref. 2. Modifications and refinements required in the more recent work included changing the chromel-alumel thermocouples to more heat-resistant platinum thermocouples, replacing the sapphire windows with fused-silica quartz optical flats of high flatness and parallelism, and enclosing the light beam in the interferometer to eliminate fringe shifts due to ambient air currents.

The dye-laser system itself was mounted together with the nitrogen pump laser (Molelectron UV300) on a heavy 1/2-in.-thick aluminum plate. Its performance was found to be quite comparable with the Molelectron DL22 system, having a repeatability, stability, and accuracy better than 0.1 Å, a bandwidth of 0.2 Å, and a pulse energy of approximately 170 μJ at 5890 Å. The emitted wavelength corresponding to any particular orientation of the grating was calibrated with a MacPherson 1-m-scanning monochromator together with sodium and neon vapor lamps to produce emission lines at 5889.96 and 5852.5 Å, respectively.

Fig. 2 Resonant dispersion in sodium vapor. Points represent measured values. Negative ordinate values relate to high-frequency-line wing where $n > 7$.



Installation of a heater unit with feedback on-off switches made it possible to control the temperatures in the heat-pipe ovens separately to a fraction of a degree Celsius. Holding the temperature in one oven constant and raising or lowering the temperature in the other gave measurable fringe shifts which could then be related to the recorded pressure and density change. Typical fringe-shift studies were carried out in the regime between 440° and 480°C for sodium number density changes of the order of $5 \times 10^{21} \text{ m}^{-3}$ corresponding to temperature changes of approximately 10°C.

The fringes were focused on a plate with a pinhole in front of a high-gain photomultiplier tube (RCA C31000F) which was cooled down to -30°C to lower the dark current and increase the signal-to-noise ratio. The output of the PMT was then recorded with an X-Y plotter, monitoring the intensity changes in a typical periodic fashion as the fringes marched across the pinhole.

Results and Discussion

Investigation of the computed absorption and refractivity profiles showed some noteworthy features which were confirmed by the experimental results. The shape of the refractivity curves are highly insensitive to the Voigt parameter a and temperature T , allowing us to write Eq. (1) in the following form

$$n_r(\lambda, T) - 1 = K_r(\lambda) \rho(T) \quad (1a)$$

where subscript r means near the resonance regime.

Figure 2 shows the graph of the calculated values for $K_r(\lambda)$ which are valid to a high degree of accuracy for a broad temperature range and for λ smaller than 5890 Å. The experimental results in the investigated wavelength range are in good accordance with the theory. As mentioned above, the fringe shifts were measured and then related to the known change of density and effective length of sodium column according to

$$S \cdot \lambda_0 = K_r(\lambda) (\rho_1 \ell_1 - \rho_2 \ell_2) \quad (8)$$

where S denotes the fringe shift, λ_0 the wavelength of the dye laser, and $\rho_{1,2}$ and $\ell_{1,2}$ the mass density and length of the sodium column before and after the temperature change, respectively.

The maximum refractivity enhancement was limited by the resonance absorption of the approximately 0.5-m-long sodium column. At about 7 Å away from resonance and $T = 465^\circ\text{C}$ the absorption coefficient of $\mu \approx 7 \text{ m}^{-1}$ makes it virtually impossible to measure fringe shifts even closer to resonance. Nevertheless, the relatively gentle slope of the

dispersion curve enables us to achieve enhancements in the wings which are of the order of 200 to 300 compared to the zero-frequency Dale-Gladstone constant $K_{0\text{Na}} = 4.051 \times 10^{-3} \text{ m}^3/\text{kg}$ of sodium. If compared with the nonresonant value of air $K_{0\text{air}} \approx 2.3 \times 10^{-4} \text{ m}^3/\text{kg}$ the resonance refractivity enhancement reaches a value of 5.0×10^3 .

Furthermore, the relative magnitude of the absorption line shape in the wings is proportional to the Lorentzian line width, whereas (as mentioned above) the refractivity line shape is quite insensitive to a [see Eq. (6b)] and any change of γ_L . Therefore, any decrease of γ_L would make it possible to go closer to the resonance line and to utilize a larger index of refraction.

In this respect the resonant refractivity technique for seeded flow-field visualization looks quite promising. The collision linewidth for sodium in the presence of an inert buffer gas like argon, which behaves quite similarly to nitrogen and air, is over 25 times smaller than in the present case with sodium-sodium collisions. Assuming the same maximum tolerable absorption and the same length of sodium column it should be possible to make use of an enhanced specific refractivity significantly larger than in the case of sodium self-broadening.

Acknowledgment

This work was supported by the Air Force Office of Scientific Research, Department of Defense, under Contract AFOSR 74-2670A.

References

- ¹Van Vleck, J., *Electric and Magnetic Susceptibilities*, Oxford University Press, 1932.
- ²Bershafer, D., Prakash, S. G., and Huhn, G., "Improved Flow Visualization by Use of Resonant Refractivity," AIAA Paper 76-71, Washington, D.C., Jan. 1976.
- ³Hummer, D. G., *Memoirs of the Royal Astronomical Society*, Vol. 70, 1965, p. 1.
- ⁴Nussenzweig, H. M., *Causality and Dispersion Relations*, Academic Press, New York, 1972.
- ⁵Hänsch, T. W., "Applications of Dye Lasers," *Dye Laser*, edited by F. Schaefer, Springer, New York, 1973.
- ⁶McCartan, D. G. and Farr, J. M., *Journal of Physics*, Vol. B9, June 1976, p. 985.
- ⁷Moore, C. E., "Atomic Energy Levels," National Bureau of Standards Circular 467, Vols. 1, 2, and 3, 1949.
- ⁸Wiese, W. L., Smith, M. W., and Miles, B. M., "Atomic Transition Probabilities," Natl. Standard Reference Data Service, 22, Vol. 22, 1969.
- ⁹Niemax, K. and Pichler, G., *Journal of Physics*, Vol. B8, Feb. 1975, p. 179.

Appendix III

RESONANCE REFRACTIVITY STUDIES OF SODIUM VAPOR
FOR ENHANCED FLOW VISUALIZATION

A DISSERTATION
SUBMITTED TO THE DEPARTMENT OF AERONAUTICS AND ASTRONAUTICS
AND THE COMMITTEE ON GRADUATE STUDIES
OF STANFORD UNIVERSITY
IN PARTIAL FULFILLMENT OF THE REQUIREMENTS
FOR THE DEGREE OF
DOCTOR OF PHILOSOPHY

By
Gerhard Werner Blendstrup
December 1978

TABLE OF CONTENTS

	page
Acknowledgments	iv
List of Tables	ix
List of Illustrations	x
 CHAPTER I. INTRODUCTION	 1
CHAPTER II. THEORY OF DISPERSION AND ABSORPTION IN GASES	8
2.1 Introduction	8
2.2 Historical Overview	9
2.2.1 Early Experimental Investigations	9
2.2.2 First Theoretical Treatments	10
2.3 Classical-Lorentzian Theory of Dispersion	14
2.3.1 The Concept of Oscillator Strength	19
2.3.2 The Kroenig-Heisenberg Dispersion Formula	21
2.4 The Quantum-Mechanical Model	23
2.4.1 Relevant Concepts	23
2.4.2 Modifications of the Classical Model due to the Quantum Theory	26
2.4.3 Boltzmann Distribution and Optical Approximation	27
CHAPTER III. RESONANT LINESHAPES OF ALKALI METAL ATOMS	28
3.1 Introduction	28
3.2 Line-Broadening Mechanisms	28
3.2.1 Collision Broadening	29
3.2.2 Doppler Broadening	32
3.2.3 The Voigt-Profile	33

TABLE OF CONTENTS (continued)

	page
3.3 Resonant Lineshapes for the Doublets of Alkali-Metal Atoms	42
3.3.1 Selfbroadening of Alkali-Metal Atoms	42
3.3.2 Dispersion of Alkali-Metal Atoms in the Presence of an Inert Buffer Gas	44
3.3.3 Voigt-Lineshape Parameters for the Alkali-Metal Atom Vapors	45
3.3.4 Numerical Calculations	50
3.4 Experimental Goal of this Study	54
CHAPTER IV. EXPERIMENTAL APPARATUS	55
4.1 Introduction	55
4.2 The Dye Laser	56
4.2.1 General Description	56
4.2.2 Performance Specifications	63
4.2.3 Wavelength Calibration of Dye Laser.....	69
4.3 The Mach-Zehnder Interferometer	71
4.4 The Heat Pipe Oven	73
4.4.1 General Description	73
4.4.2 Performance Characteristics	77
4.5 The Fringe Shift Recording Device	79
CHAPTER V. THE EXPERIMENTAL TECHNIQUES	81
5.1 Preliminary Experiments	81
5.1.1 Operational Pressure Limits	81
5.1.2 Fringe Contrast with the Dye Laser	82
5.2 The Resonant Refractivity Experiment	84
5.3 Resonant Absorption Measurements	88

TABLE OF CONTENTS (continued)

	page
CHAPTER VI. EXPERIMENTAL RESULTS AND DISCUSSION	89
6.1 Range of Measurements	89
6.2 Data Reduction	89
6.3 Estimation of Experimental Uncertainty	92
6.4 Results and Discussion	96
6.4.1 Experimental Results	96
6.4.2 Comparison of Resonant versus Non- Resonant Sensitivities for Flow Visualization Methods	98
CHAPTER VII. SUMMARY AND OUTLOOK	107
APPENDIX A. COMPUTER PROGRAM AND TABLE OF THE $W(Z)$ -FUNCTION ...	109
APPENDIX B. PROPERTIES OF SODIUM	119
B.1 General Description	119
B.2 Physical Data and Formulas	119
B.2.1 Vapor Pressure	120
B.3 The Spectrum of Atomic Sodium	122
APPENDIX C. ALIGNMENT PROCEDURE OF DYE LASER OPTIMIZING BEAM POWER	126
REFERENCES	131

LIST OF TABLES

	page
I Static Polarizabilities and Dale-Gladstone Constants together with Resonance Wavelengths of the Inert gases and Alkali-Metal Atoms	47
II Alkali-Metal Atom Resonance Doublet Parameters	48
III Collision Broadening Parameter C_r for Alkali- Metal Atom Resonance Doublets under Conditions of Selfbroadening and in the Presence of an Inert Buffer Gas	49
IV Specifications of Dye Laser	65
V Comparison of Experimentally Determined Dale- Gladstone Constants of Sodium Vapor with Theoretical Values Assembling Different Density Profiles along the Axis of the Heat Pipe Oven	93
VI Resonant versus Non-Resonant Refractivity	99
VII Real and Imaginary Parts of the $W(z)$ Function	114
VIII Physical Data and Formulas for Sodium	120

LIST OF ILLUSTRATIONS

Figure	page
1 Normal Dispersion Curve of Air at NTP, Calculated from Two-Term Cauchy Dispersion Formula	11
2 Experimentally Determined Anomalous Dispersion Curve of Sodium Vapor at 644°C	11
3 Lorentzian Lineshapes of the Frequency Dependent Real and Imaginary Parts of the Complex Index of Refraction ...	20
4 Comparison between Doppler and Lorentzian Lineshapes for Equal Area and Equal Linewidths	35
5 Total Linewidth versus Pressure of Sodium Vapor	36
6 Voigt Profile Analysis: Plot of the Imaginary Part of the Complementary Error Function of Complex Argument in Comparison with its Approximation for Large x	40
7 Voigt Profile Analysis: Plot of the Real Part of the Complementary Error Function of Complex Argument in Comparison with its Approximation for Large x	41
8 Computed Refractive Index of Sodium versus Wavelength at D-Lines	52
9 Computed Absorption Coefficient of Sodium versus Wavelength at D-Lines	53
10 Schematic of Experimental Set-Up	57
11 Photograph of Resonant Refractivity Apparatus	58
12 Photograph of N ₂ -Pump Laser together with Dye-Laser Assembly in the Foreground	59
13 Schematic of Dye Laser	60
14 Photograph of Dye Laser Assembly	61

Figure	page
15 Output Power of Dye Laser Using Rhodamine 6G versus Wavelength Compared with Tuning Curve of Molelectron DL200 Dye Laser	66
16 Dye Laser Output at 5890 Å Viewed through 3mm Fabry-Perot Etalon	67
17 Recorded Plot of Wavelength Calibration of Dye Laser to Sodium D-Lines	70
18 Drawing of Small Heat Pipe Oven together with its Principle of Operation	74
19 Typical Output Plot of Recorded Measured Fringe Shifts	87
20 Comparison between Experimental and Theoretical Values	97
21 Voigt Parameter a versus Temperature, Pressure, and Number Density of Sodium Vapor for Homogeneous Broadening	118
22 Total and Monatomic Vapor Pressure of Sodium versus Temperature	123
23 Energy Level Diagram of Atomic Sodium	125

CHAPTER I

INTRODUCTION

Optical studies in gasdynamics such as interferometric investigations or the application of special schlieren techniques are now standard procedure in many laboratories, including those of the Stanford Department of Aeronautics and Astronautics. The aim of this study is to contribute to an improved sensitivity of such methods, to make visible a class of fluid dynamic phenomena whose small density gradients precluded their investigation heretofore.

To make the invisible visible always fascinated researchers and scientists. Since most fluids, gaseous or liquid, are transparent, their motions remain invisible to the naked eye. Unfortunately, due to the complexity of fluid motion and to the difficulties involved in applying and solving the governing equations to even the simplest flow situation, fluid dynamicist have to rely heavily on experimental techniques in order to derive quantitative data about the flow.¹

The advantage of optical techniques lies in the fact that they allow measurements of pressure, temperature and velocity of a complete flow field without introducing any disturbance into the phenomenon being studied. Other flow measuring devices, on the contrary, like a hot-wire anemometer or a pressure or temperature probe perturb the flow and can provide data of the flow for only one point at a time.

Compressible flows do show refractive variations, and the methods of schlieren, shadowgraphy, and interferometry are widely used in their

study.² The refractive behavior stems from the fact that the speed of light varies with the density of the medium through which it is passing. The speed of light c , in turn, is related to the refractive index n by its ratio with the speed of light in vacuo c_0 .³

$$n(\rho) \equiv c_0/c(\rho)$$

In other words, a change in density results in a corresponding change in the refractive index. As a result, a light ray traversing through the flow field will be affected with respect to its direction and phase.

The schlieren, a German word describing blurs or inhomogenities in transparent media, and the shadowgraph methods make use of the angular deflection of light in the presence of transverse refractive gradients.^{1,4} Both techniques were developed over a century ago by co-workers of E. Mach to photograph non-steady shock-wave phenomena and allow the direct measurement of the first (schlieren technique) or second (shadowgraph) spatial derivative of the density. To determine the actual density in the test section the gradient has to be integrated, which makes these methods rather awkward and inaccurate for quantitative measurements.

Fortunately, interference techniques enable the experimentalist to measure density directly. The theory of interference is based essentially on the principle of linear superposition of electro-magnetic waves. In the interferometer, the change of phase of the test beam with

respect to a reference beam is measured by superimposing the two beams, thus forming a pattern of interference fringes. A variation in density in the test section will change this pattern, which then, in turn, can be directly related to the density distribution in the flow field. For wind tunnel work the Mach-Zehnder interferometer^{5,6} is employed almost universally. It represents an improvement of the well-known two-beam interferometer designed by Jamin in 1856.

The ultimate sensitivities of these techniques, however, leave much to be desired and restrict their application to flow fields where relatively large density gradients are present. While there have been new developments in the sophistication of the optical methodology and instrumentation,⁷⁻⁹ the sensitivity of essentially all work to date has been controlled by the specific refractivity of diatomic gases, e.g., air, in the visible portion of the spectrum. That quantity, K_0 , appears in the well-known Dale-Gladstone constitutive relation¹

$$n - 1 = K_0 \rho ,$$

relating refractive index n and gas density ρ . The relatively small value of K_0 for air at normal temperature and pressure in the visible portion of the spectrum

$$K_{0,\text{Air}} \approx 2.3 \times 10^{-4} \text{ m}^3/\text{kg}$$

has largely precluded the application of these flow visualization

methods to various low-pressure compressible-flow phenomena requiring high sensitivity. As an example, the density change corresponding to 0.1 fringe-shifts in a test rig with a transverse light path of 10 cm filled with air at standard stagnation conditions is 0.17 percent of atmospheric density. This density change corresponds to a change in Mach number of approximately 0.02 for isentropically expanding or compressing flows. In flows such as thermal convection the relative density variation is proportional to the relative change in temperature and a 0.17 percent change of air at standard temperature amounts to a temperature difference of about 0.5°K . These resolutions are quite sufficient for the above cases but substantially higher sensitivities are desirable for several applications of current interest. These include vortices and turbulence in low-speed flow, propagation of sound or noise in the audible range, rarified gas flow and meteorological flows, to name only a few.

The use of resonance radiation to increase the sensitivity by many orders of magnitude beyond current techniques was first discussed in the literature by D. A. Leonard and J. C. Keck¹⁰ in 1962. They decided to utilize the enhanced refractivity close to a resonant transition, which is predicted from classical radiation theory, by use of radiation in the vicinity of the strong resonance line of sodium vapor at 5896 \AA by means of interference filters. The results obtained when taking schlieren photographs of projectile wakes at vapor densities less than 1 percent of atmospheric density showed the potential of enhancing the refractivity by using resonant radiation.

D. Bershader^{11,12} proposed in 1970 to illuminate the "near region" of a line with a narrowband tunable light source in order to employ the enhancement of refractivity necessary to observe small flow perturbations. However, the utilization of such enhanced refractivity for flow visualization has been restricted by

- * the limited number of special vapors with convenient resonance characteristic
- ** the non-availability of light sources with suitable spectral resolution.

The technical difficulties associated with working in the vacuum ultraviolet, the region of refractive resonances for air, motivated the work with a gas having strong resonances in the visible portion of the spectrum. Sodium vapor with its strong ground state transitions (D-lines) at 5889.963 \AA and 5895.930 \AA seemed the most convenient choice. The advent of the tunable narrowband dye laser in 1972¹³ provided the necessary reliable light source.

In the meantime, the use of tunable lasers to generate light at the sodium wavelengths has been well developed,¹⁴⁻¹⁶ and by now such sources have been used for several investigations of fluid phenomena. Among these are C. P. Wang's¹⁷ excellent study (1975) of the use of resonance absorption and scattering techniques for measurement of turbulent reactive flows; and the investigations of R. B. Miles, et al.,¹⁸ in 1977 where sodium vapor was seeded into a hypersonic helium flow and a very narrow linewidth dye laser was scanned across the doppler shifted absorption line to observe the resonant fluorescence. Here, a

specific velocity component fluoresces at each laser frequency and can easily be observed by eye.

In accordance with the purpose of this study, detailed theoretical studies are described in Chapter II of the use of the greatly increased refractivity of atoms and molecules near their resonance frequencies to obtain correspondingly increased sensitivities of refractive methods for studies of pure or seeded fluid flows. Descriptions are first given of extinction and dispersion of light in gases and in homogeneous gas mixtures.

Since it was found that the available information on refractive dispersion for alkali metals, more specifically sodium, is remarkably limited -- the only measurements found of refraction and dispersion in sodium vapor date back to 1934¹⁹ -- experimentally determined absorption linewidth parameters for the resonance doublets of alkali-metal atoms are then employed in Chapter III to construct corresponding resonance refractivity lineshapes in the so-called Voigt approximation. A computer program (Appendix A) is used to calculate these refractive and absorptive profiles in the neighborhood of the sodium D-lines.

The experimental part of this study, described in Chapters IV and V, deals with the calibration experiment to verify the theoretically obtained dispersion data of sodium vapor in the resonant regime. For that purpose a tunable narrow band dye laser is used as a light source and a Mach-Zehnder interferometer serves for refractivity measurements. The sodium vapor is generated in so-called heat pipe ovens, a device which allows the vapor to be contained under well defined and stable

conditions in such a way that it is accessible for optical investigations. Finally, in Chapter VI, the results are presented and discussed. The ultimate maximum enhancement obtainable in the case of alkali-seeded flows is found to be determined, for the most part, by absorption considerations, which limit the closest proximity to line center to which the operating wavelength of the dye laser can be tuned. By combining the four governing equations of the fringe shift experiment, the dispersion and absorption formula, Beer's law and the fringe shift equation, an expression is derived which relates in a very concise form various experimental parameters to the maximum number of obtainable fringe shifts for a given disturbance. The latter part of Chapter VI is devoted to detailed comparisons of the sensitivities of schlieren and Mach-Zehnder measurements under non-resonant and resonant conditions.

The results of this study give useful information for the design of a suitable flow facility where sodium vapor is injected to produce a well mixed test section flow. The flow will likely be nitrogen than air, and the major technical challenge is the admixture and injection of the desired amount of sodium seed material without condensation or other undesirable side effects. The measured values of the enhanced refractive index of sodium let the resonant refractivity technique for seeded flow field visualization look quite promising especially in the low pressure regime and will give the follow-up work of designing a flow facility a new impetus.

CHAPTER II

THEORY OF DISPERSION AND ABSORPTION IN GASES2.1 Introduction

The speed of light changes with the density of the medium through which it passes. The refractivity index n is defined as the ratio of the speed of light in vacuo c_0 to its speed in the medium c :

$$n(\rho) = c_0/c(\rho) \quad (2.1)$$

Indices of refraction in the visible spectrum for commonly used gases (at standard temperature and pressure) are in the range of 1.000035 for helium to 1.00030 for nitrogen.

Given a substance, the index of refraction is for any given wavelength only a function of density, $n = n(\rho)$. In gases, the speed of light to a good approximation varies linearly with the density. This is expressed in the well-known Dale-Gladstone equation:

$$n - 1 = K \cdot \rho \quad (2.2)$$

where K and ρ are the Dale-Gladstone constant and the fluid mass density, respectively. K , however, is not a constant for a given gas; rather, for inert gases and atmospheric constituents in the visible

spectrum, it is a weak function of wavelength. Newton was the first who demonstrated the variation of the index of refraction with frequency called dispersion. In this chapter an attempt will be made to explain dispersion and its connected counterpart, absorption, through a historical overview followed by a short treatment of the classical theory developed by Lorentz. To interpret the actual response of real atoms to electro-magnetic waves the necessary quantum-theoretical modifications are included.

2.2 Historical Overview

2.2.1 Early Experimental Investigations*

Marcus in 1648 and Grimaldi in 1665 were the earliest known experimentalists to observe dispersion. They were followed by Newton and his famous glass prism experiment (1666). Until about the 19th century no further discoveries of any importance were made in this field. It was only in 1814 that Fraunhofer discovered the spectrum of sunlight. His findings led the way to numerable investigations such as Le Roux, who in 1862 noticed that the dispersive behaviour of iodine vapor near its absorption lines differed from the dispersion of a glass prism. His observations were disregarded because they were thought to be pure illusions. However, Christiansen²¹ in 1870 and Kundt²² in 1871 confirmed this anomalous phenomenon with several experiments using different substances: Christiansen studied anomalous dispersion of an alcoholic solution of fuchsine, which has a strong absorption band in the green. He found out that the refractive index

* Excellent historical treatments of the theory of light up to the twentieth century are given in references [19, 20].

for the longer wavelengths red, orange and yellow shows the same behavior as for the case with the glass prism where the refractive index increases as the wave-length decreases. The shorter wavelengths, blue and violet, however, are less refracted than the red, and separated from it by a dark interval. The observations of Christiansen were verified by Kundt, who revised the method of crossed prisms, a method first developed by Newton. This experimental technique shows directly the familiar anomalous dispersion curves as in Fig. 2, which displays the anomalous dispersion of sodium vapor at 644°C in the neighborhood of the D-lines, as determined experimentally by Wood²³. Fig. 1 above is a plot of the refractive index of air at NTP versus wavelength, which, in the visible part of the spectrum, has a similar normal dispersive behavior like glass.

2.2.2 First Theoretical Treatments

Cauchy²⁴ in 1836, soon after Fraunhofer's discoveries, deduced an equation which shows the refractive index varying with wavelength. He derived this formula employing the elastic solid theory of light which states that the propagation velocity of transverse waves in an elastic medium is proportional to the square root of the elasticity divided by the density of the medium provided the wavelength is large compared to the distance between particles of the medium. He derived the following equation, which carries his name

$$n = \sum_{m=0}^{\infty} C_m / \lambda^{2m} \quad (2.3)$$

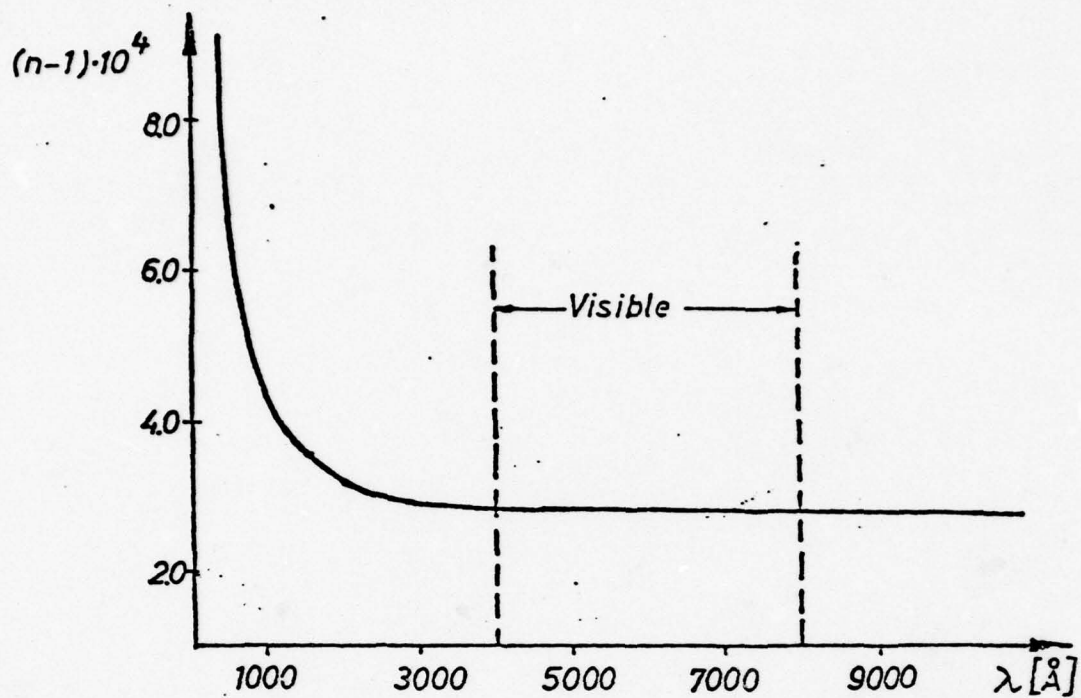


Fig. 1. Normal Dispersion Curve of Air at NTP, Calculated from Two-Term Cauchy Dispersion Formula.

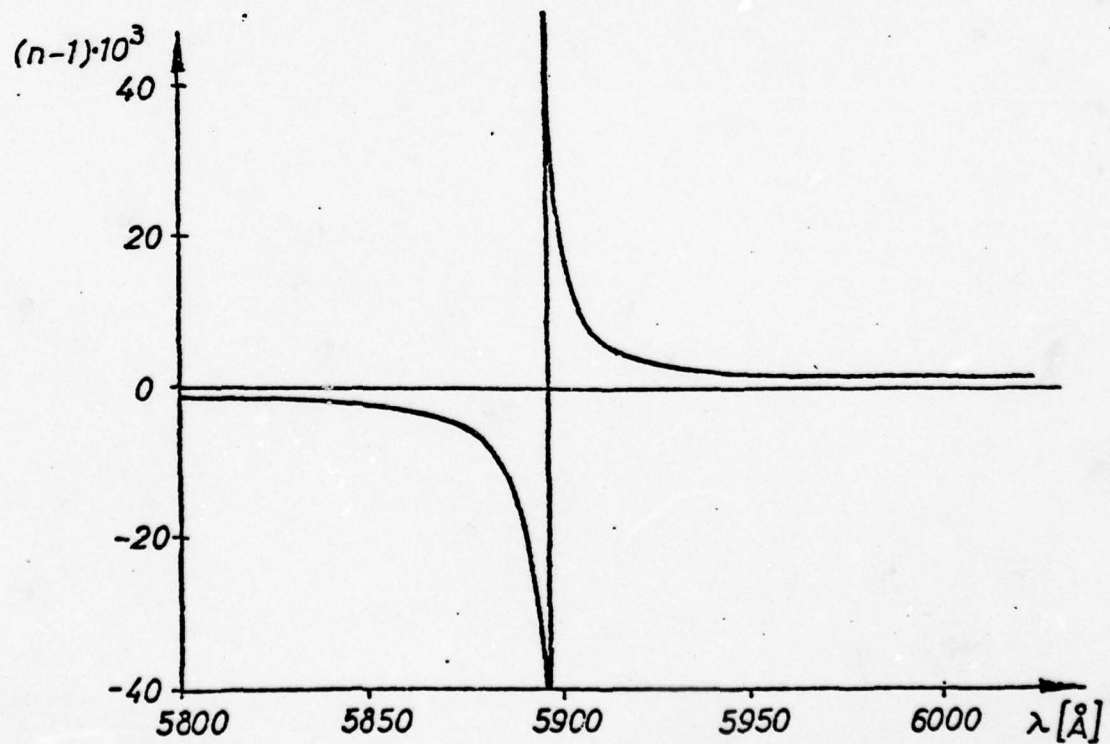


Fig. 2. Experimentally Determined Anomalous Dispersion Curve of Sodium Vapor at 644°C (R. W. Wood, 1902).

and gives the refractive index n in terms of the wavelength λ and the constants c_0, c_1, c_2, \dots , which are positive.

Eq. 2.3 describes to a good approximation that wavelength region where the index of refraction increases regularly as λ decreases, the so-called normal dispersion region. However, the Cauchy formula fails to describe anomalous dispersion. Maxwell²⁵, in the form of a question given in an examination paper, and Sellmeier²⁶ laid the foundation of the modern theory of dispersion. They assumed that the sudden upswing of the refractive index curve in the anomalous dispersion region was due to some sort of resonance and closely connected to the absorption line itself and that the normal dispersion is nothing more than a special case of the anomalous. Maxwell and Sellmeier explained the cause of dispersion as due to the repeated impacts of the light waves on the vibrating atoms. These atoms would have -- very much like a tuning fork -- a resonant frequency or eigenfrequency at which they would be set in motion and vibrate. Maxwell-Sellmeier's formula can be written as

$$n^2 = 1 + \frac{D\lambda^2}{\lambda^2 - \lambda_r^2} \quad (2.4)$$

where the subscript r denotes the resonant value.

Far away from resonance when $\lambda \gg \lambda_r$, this equation reduces to the Cauchy formula (2.3). For more than one resonance Eq.(2.4) takes the form

$$n^2 = 1 + \sum_m \frac{D\lambda^2}{\lambda^2 - \lambda_{r_m}^2} \quad (2.5)$$

where the summation is taken over all different resonances.

These equations give correctly the form of the refractive index curves near resonance. At resonance, however, the formulas yield an infinite refractive index. Von Helmholtz²⁷ was the first to introduce a damping term in the above equations to account for a finite resonant value. His study on the propagation of light results in a complex index of refraction \tilde{n} which can be written as

$$\tilde{n}^2 = 1 + \frac{D\lambda^2}{\lambda^2 - \lambda_r^2 + ib^2\lambda^2} \quad (2.6)$$

where $ib^2\lambda^2$ represents the damping term.

On the experimental side, it was found that this equation was in good accordance with the observations. In particular Wood,^{23,28} in his study of the anomalous dispersion of sodium vapor in the neighborhood of the D-lines, found this expression to give correct results for certain temperatures and pressures. Nevertheless, Helmholtz's formula was soon found not to be sufficiently general, nor was its derivation rigorous enough in the light of the more developed electron theory. Drude and Voigt led the way to a new model, followed by Lorentz²⁹ who finally put the dispersion equations into the form which now bears his name. The presentation of the Lorentz electron model and the derivation of its results is given next.

2.3 Classical-Lorentzian Theory of Dispersion*

Lorentz considered the dispersive medium as consisting of small charged particles which can vibrate like damped harmonic oscillators around an equilibrium position with natural frequency ω_p . He regarded the atom as a small but massive positively charged nucleus, surrounded by one or more lightweight negatively charged electrons orbiting as discrete points around the nucleus. Although the better quantum-mechanical model of an atom views the electrons very much like a "cotton candy" cloud of diffuse negative electronic charge surrounding the nucleus, the classical Lorentzian model gives surprisingly good results for the response of real atoms to an applied electric field (the magnetic field can be neglected since it introduces only a higher order effect). In the classical model this external electric field causes the positive nucleus to move in one direction and the negative electron or electron cloud to move in the opposite direction. When excited and then released the nucleus and electron will behave like a harmonic oscillator and perform some kind of damped oscillatory motion about the equilibrium position. In other words, the atoms in this model show precisely the resonant behavior when excited by an applied external electric field as was first assumed by Maxwell and Sellmeier. This motion of charged particles will then result in an induced dipole moment which in turn is responsible for the dispersive and absorptive behavior of the medium.

* The classical-Lorentzian theory of dispersion is developed in many textbooks. See, for example, references [30, 31].

Maxwell introduced the complex index of refraction n for a non-conducting, non-magnetic medium and showed that it is connected to its relative dielectric constant ϵ_* by

$$\tilde{n}^2 = \epsilon_* \quad (2.7)$$

The physical significance of a complex index of refraction becomes clear by writing the solution for plane waves of Maxwell's equations for a non-conducting, non-magnetic medium

$$\vec{E} = E_0 e^{-i(\tilde{n}\vec{k}_0\vec{r} - \omega t)} \quad (2.8)$$

with

$$\vec{k}_0 = \omega/c \quad (\text{wave vector})$$

and substituting

$$\tilde{n} = n - i\kappa \quad (2.9)$$

where n and κ are real. We obtain

$$\vec{E} = \vec{E}_0 \cdot \underbrace{\exp\{-\kappa\vec{k}_0\cdot\vec{r}\}}_{\text{attenuation}} \cdot \underbrace{\exp\{-i(n\vec{k}_0\cdot\vec{r} - \omega t)\}}_{\text{oscillatory}} \quad (2.10)$$

and it becomes obvious that κ represents an extinction coefficient which results in an exponential attenuation of the electrical field vector \vec{E} in the medium, whereas the index of refraction n produces a phase-shifting effect. The extinction coefficient κ which describes the

attenuation of the amplitude of a traversing electromagnetic wave when passing through a medium is related to the absorption coefficient μ which applies to the absorption of the intensity I of a light beam by

$$\mu = \frac{2\omega}{c} \kappa \quad (2.11)$$

This can be easily proven, since the intensity I in the wave at any given point is proportional to the square of the electric field E^2 and I and E^2 can be written in terms of

$$I = I_0 e^{-\mu x} \quad (2.12)$$

$$E^2 \sim e^{-2\kappa k_0 x} \quad (2.13)$$

Eq. (2.12) is well known under the name Beer's Law, which states that each layer of equal thickness or each single molecule absorbs an equal fraction of the light which traverses it.

Coming back to expression 2.7, it can be shown that according to Maxwell's theory for gases to a good approximation ϵ_* can be written as*

$$\tilde{\epsilon}_* = \tilde{\epsilon}/\epsilon_0 = 1 + \frac{N\tilde{\alpha}}{\epsilon_0} \quad (2.14)$$

in terms of $\tilde{\alpha}$, the complex induced electron polarizability, N , the particle number density, and ϵ_0 , the permittivity of free space. For

* The MKS-system of units will be used throughout this study.

most gases and vapors a linear relationship between the induced electric dipole moment \vec{p} and the applied electric field \vec{E} can be assumed, the factor of proportionality being the polarizability $\tilde{\alpha}$, which can therefore be expressed as

$$\tilde{\alpha} = \frac{\vec{p}}{\vec{E}} \quad (2.15)$$

The induced dipole moment \vec{p} , in turn, is clearly the product of the electron charge e and the displacement vector \vec{r} :

$$\vec{p} = e \cdot \vec{r} \quad (2.16)$$

Substituting for \vec{r} the solution of the differential equation for a damped electron oscillator and combining Eq. (2.15) with Eq. (2.16) yield

$$\tilde{\alpha} = \frac{e^2/m}{\omega^2 - \omega_r^2 + i\omega\gamma_{\text{rad}}} \quad (2.17)$$

where m is the electron mass, ω_r the resonant radiant frequency of the electron oscillator and γ_{rad} the classical radiation damping coefficient, which is given according to the classical radiation theory by

$$\gamma_{\text{rad}} = \frac{e^2 \omega_r^2}{6\pi\epsilon_0 mc^3} \quad (2.18)$$

Now, inserting the expression for the complex polarizability $\tilde{\alpha}$ (Eq. 2.17) into Eqs. 2.14 and 2.7 yields the final explicit expression

for the complex index of refraction of the Lorentz model:

$$\tilde{n}^2 - 1 = \frac{Ne^2}{\epsilon_0 m} \frac{1}{\omega^2 - \omega_r^2 + i\omega\gamma_{rad}} \quad (2.19)$$

Making use of the fact that the refractive index for gases is close to unity, while the extinction coefficient κ is typically two orders of magnitude less and for frequencies near resonance, i.e., for signals for which $\omega \approx \omega_r$ we can make the simplifying approximations

$$\omega^2 - \omega_r^2 \approx 2\omega_r(\omega - \omega_r) \quad (2.20)$$

and

$$\tilde{n}^2 - 1 \approx 2(n - 1 - i\kappa) \quad (2.21)$$

and write Eq. 2.19 by equating real and imaginary part in the final expression for the response of N harmonic oscillators per unit volume having the resonance frequency ω_r and being excited by a signal close to resonance with frequency ω

$$n_r(\omega) - 1 = \frac{Ne^2}{2m\epsilon_0\gamma_{rad}\omega_r} \left\{ \frac{2(\omega_r - \omega)/\gamma_{rad}}{1 + [2(\omega_r - \omega)/\gamma_{rad}]^2} \right\} \quad (2.22)$$

$$\kappa_r(\omega) = \frac{Ne^2}{2m\epsilon_0\gamma_{rad}\omega_r} \left\{ \frac{1}{1 + [2(\omega_r - \omega)/\gamma_{rad}]^2} \right\} \quad (2.23)$$

These forms of response are commonly called the Lorentz or lorentzian lineshapes and are shown in Fig. 3. The full linewidth between the

half-power points of the extinction curve is just equal to the damping coefficient γ_{rad} which describes also the distance between the peaks of the refractivity curve.

2.3.1 The Concept of Oscillator Strength

Ladenburg³², when investigating the absorption of radiation in sodium, found out that there is a difference between the experimental results and the theory. He introduced the f-value or oscillator strength to eliminate this discrepancy.

The oscillator strength takes values between zero and unity and was proposed by Ladenburg as a correction factor. Later in quantum physics it explains why different atomic transitions in real atoms show different strengths of response to an applied electric field, thus linking the f-numbers to the transition probabilities or Einstein coefficients. For a more detailed discussion of this topic see Section 2.4.1.

Supposedly the medium consists of N particles representing n harmonic oscillators with natural frequencies $\omega_{r_1}, \omega_{r_2}, \dots, \omega_{r_n}$ and oscillator strengths f_1, f_2, \dots, f_n then the expression for the complex index of refraction (Eq. 2.19) can be rewritten as

$$\tilde{n}^2 - 1 = \frac{Ne^2}{\epsilon_0 m} \sum_n \frac{f_n}{\omega^2 - \omega_r^2 + i\omega\gamma_{\text{rad}}} \quad (2.24)$$

where the summation goes over all resonances.

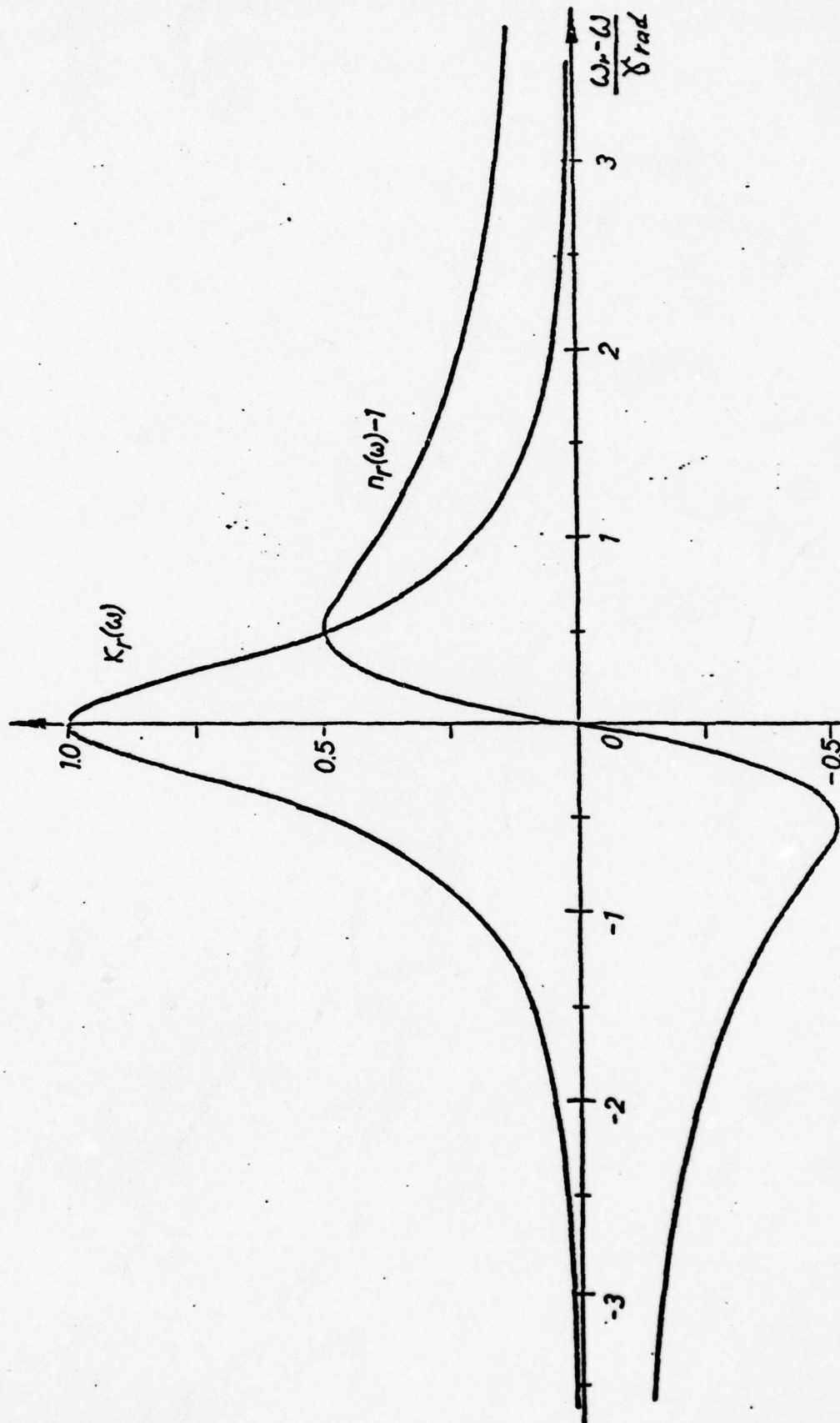


Fig. 3. Lorentzian Lineshapes of the Frequency Dependent Real and Imaginary Parts of the Complex Index of Refraction $n = \tilde{n} - i\kappa$

For frequencies near one particular resonance ω_r , the absorptive influence of all other oscillators at frequencies $\omega_r \neq \omega_r$, is neglectable, whereas the dispersive influence of all the other oscillators having $\omega_r \neq \omega_r$, can be combined as

$$\sum_{r \neq r'} (n-1) \equiv n_0 - 1 \quad (2.25)$$

where n_0 is a weak function of frequency and can be considered as constant for the moment. Thus, the expressions for the dispersive and absorptive behavior of a gas consisting of several different lorentzian oscillators near one of these resonant frequencies can be written as

$$n_r(\omega) - 1 = n_0 - 1 + \frac{Ne^2 f_r}{2m\epsilon_0 \gamma_{rad} \omega_r} \left\{ \frac{2(\omega - \omega_r)/\gamma_{rad}}{1 + [2(\omega - \omega_r)/\gamma_{rad}]^2} \right\} \quad (2.26)$$

$$n_r^r(\omega) = \frac{Ne^2 f_r}{2m\epsilon_0 \gamma_{rad} \omega_r} \left\{ \frac{1}{1 + [2(\omega - \omega_r)/\gamma_{rad}]^2} \right\} \quad (2.27)$$

2.3.2 The Kroenig-Heisenberg Dispersion Formula*

Christiansen and Kundt found out through experimental investigations that the anomalous or resonant dispersion appears in the neighborhood of spectral lines. Furthermore, the theoretical derivation reveals a complex index of refraction consisting of the real index

* An excellent treatment of this topic is given in reference [33].

of refraction and the extinction coefficient whose expressions look rather similar.

Kramers and Kroenig³⁴, followed by Heisenberg³⁵, pointed out that the real and imaginary parts of the complex index of refraction can be related to each other. Following the concept of causality or correspondence ("The effect cannot precede the cause") the absorption of one frequency must be accompanied by a compensating phase shift of all other frequencies and this is exactly what the dispersion does.

The original Kramers-Kroenig relation connects the real and imaginary parts of $\tilde{n}(\omega) - 1$ with

$$\mathcal{P}(\omega) - 1 = \frac{2\omega}{\pi} \mathcal{P} \int_0^{\infty} \frac{\kappa(\omega')}{\omega'^2 - \omega^2} d\omega' \quad (2.27)$$

where

$$\mathcal{P} \int_0^{\infty} = \lim_{\epsilon \rightarrow 0} \left(\int_0^{\omega - \epsilon} + \int_{\omega + \epsilon}^{\infty} \right)$$

denotes Cauchy's principal value and is required when the applied frequency falls within an absorption line. Therefore, the real refractive index at any frequency is completely determined by the values taken by the extinction coefficient for all frequencies as was suspected and the above relation determines the dispersion in such a way that no violation of causality can arise.

The Kramers-Kronig-Heisenberg relationship is very often used to convert experimentally determined absorption profiles into corresponding refractivity lineshapes. As will be shown in Appendix A, the computer program for the calculation of the resonant dispersion curve near the sodium doublet makes use of this relation when first computing the absorption profile from known approximations and then constructing the refractivity lineshape.

2.4 The Quantum-Mechanical Model*

2.4.1 Relevant Concepts

The classical electron-oscillator, developed by Lorentz, gives remarkably good results. Nevertheless, to account for several response phenomena not explainable with the classical model one has to introduce the correct quantum-mechanical model.

In 1901 the idea of quanta was introduced by Planck³⁷ in trying to obtain a theory for the spectrum of the blackbody radiation which did not agree with the classical model. He proposed that the energy of a radiation field is quantized and can assume only certain discrete values, the energy being the product of the frequency and a constant h , known as Planck's constant:

$$E = h \cdot \nu \quad (2.28)$$

Wood³⁸ discovered in 1904 in an experiment the emission of light by a gas when excited at its resonant frequency, a phenomenon he called

* The basic concepts of quantum mechanics together with semi-classical approximations and the elementary quantum theory of dispersion is described in a quite exhaustive manner in reference [36].

resonance radiation. This led to the postulate that atoms can jump from one energy level to another while emitting or absorbing radiation, depending on whether it is a downward or upward transition. This description of the atom having stationary states characterized by a definite energy was proposed by Bohr in 1913. If a transition from a higher state with energy E_u to a lower state with energy E_l is accompanied by emission of radiation, then the frequency of this radiation is given by

$$\nu_{ul} = \frac{E_u - E_l}{h} \quad (2.29)$$

Einstein⁴⁰ in 1917, when describing the transition of an atom from a lower state to an upper state introduced the concept of atomic transition probabilities. He defined the probability per second that an atom will spontaneously undergo the transition from the higher level to the lower level as A_{ul} , a coefficient which now bears his name. It is easily shown that if there is only one possible transition from a given state, then the Einstein A coefficient is just the inverse of the lifetime of the upper state $1/\tau_u$ which is equal to the quantum-mechanical damping constant γ_u :

$$A_{ul} = 1/\tau_u = \gamma_u \quad (2.30a)$$

When the atom is in a state from which it can jump to several sub-levels while emitting radiation, then in order to obtain the total

inverse lifetime of the upper state one has to sum over all possible transitions:

$$\gamma_u = 1/\tau_u = \sum_{l < u} A_{ul} \quad (2.30b)$$

In classical theory it has been shown that the amount of absorption or emission at one particular frequency is proportional to the number of oscillators having that resonant frequency. The quantum-mechanical approach states that absorption and emission are due to transitions between stationary states and that the amount of emission and absorption is proportional to the transition probability or Einstein coefficients. Thus there must be a connection between the f-number and the Einstein coefficients for that particular transition. As a consequence of this relation, Ladenburg⁴¹ showed that the absorption f-value is equivalent to

$$f_{lu} \equiv \frac{1}{3} \cdot \frac{g_u}{g_l} \cdot \frac{\gamma_{ul}}{\gamma_{rad}} = \frac{2\pi c^3 \cdot \epsilon_0 \cdot m}{e^2 \omega_{lu}^2} \cdot g_u/g_l \cdot A_{ul} \quad (2.31)$$

with g_l and g_u describing the degeneracies or statistical weights of the particular levels. Furthermore, he derived the f-number f_{ul} for the downward transition as being related to the absorption oscillator strength f_{lu} (upward transition) as

$$f_{ul} = - g_l/g_u \cdot f_{lu} \quad (2.32)$$

2.4.2 Modifications of the Classical Model due to the Quantum Theory

The expressions 2.25 and 2.26 of the classical Lorentz model can be easily converted to the correct quantum result for real electric-dipole atomic transitions by the following steps:

1. Replace the classical-oscillator resonance frequency ω_r by the actual transition frequency given by the Bohr relation $\omega_{lu} = (E_u - E_l)/\hbar$, where \hbar is the Planck-constant divided by 2π .
2. Replace the damping constant γ_{rad} of the classical oscillator by the real linewidth or inverse lifetime $\gamma_{lu} = 1/\tau_{lu} = A_{lu}$ of the real atomic transition.
3. Replace the total number density N equal to all classical oscillators per unit volume by the number density or population density of the particular state involved.
4. Replace the classical oscillator strengths by the quantum mechanical f -values, the transition probabilities, f_{lu} for an upward (absorptive) and f_{ul} for an downward (emissive) transition.

The modified expressions for the index of refraction and extinction coefficient produced by a collection of real atoms at or near one of their resonance frequencies including both, upward and downward transitions are thus

$$n(\omega) - 1 = n_0 - 1 + \frac{e^2 f_{lu}}{2m\epsilon_0 \gamma_{lu} \omega_{lu}} \left\{ N_l \left[\frac{2(\omega - \omega_{lu})/\gamma_{lu}}{1 + [2(\omega - \omega_{lu})/\gamma_{lu}]^2} \right] - g_l/g_u N_u \left[\frac{2(\omega - \omega_{lu})/\gamma_{ul}}{1 + [2(\omega - \omega_{lu})/\gamma_{ul}]^2} \right] \right\} \quad (2.33)$$

and

$$\kappa(\omega) = \frac{e^2 f_{lu}}{2m\epsilon_0 \gamma_{lu} \omega_{lu}} \left\{ N_l \left[\frac{1}{1 + [2(\omega - \omega_{lu})/\gamma_{lu}]^2} \right] \right. \quad (2.34)$$

$$\left. - g_l/g_u N_u \left[\frac{1}{1 + [2(\omega - \omega_{lu})/\gamma_{ul}]^2} \right] \right\}$$

The second terms in Eqs. 2.33 and 2.34 represent phenomena which cannot be explained with classical theory, namely negative dispersion and negative absorption or induced emission. They are purely quantum-mechanical phenomena and occur when the population of the upper state is higher than the population of the lower state, the so-called population inversion. Negative dispersion was first observed by Ladenburg⁴² (1933) and his co-workers and helped verifying experimentally the quantum mechanical model. Following the Kramers-Kronig relationship, negative absorption was predicted but it took over 20 years until with the development of the first microwave ammonia maser in 1954⁴³ induced emission could actually be utilized.

2.4.3. Boltzmann Distribution and Optical Approximation

If N_l describes the number of atoms in the lower energy level E_l and N_u stands for the number of atoms in the higher energy level E_u , then the Boltzmann ratio for thermal equilibrium at temperature T can be written as⁴⁴

$$N_u/N_l = e^{-(E_u - E_l)/kT} \quad (2.35)$$

27(a)

and applying Bohr's formula yields

$$N_u/N_l = e^{-\omega_{ul} \cdot \hbar / kT}$$

where k is the so-called Boltzmann constant.

Now, for optical frequencies the product $\omega_{ul} \cdot \hbar$ is normally much bigger than the product kT ($\omega_{ul} \cdot \hbar \gg kT$) and the ratio $\omega_{ul} \cdot \hbar / kT$ becomes very large compared to unity (i.e., for frequencies near the sodium D-lines at 5890 Å the value $\omega_{ul} \cdot \hbar / k$ corresponds to approximately 24,400°K). For any two energy levels in thermal equilibrium E_u and E_l , therefore, the upper population N_u becomes negligibly small compared to the population of the lower state N_l and the second terms in Eqs. 2.33 and 2.34 can be omitted.

CHAPTER III

RESONANT LINESHAPES OF ALKALI METAL ATOMS3.1 Introduction

Experimentally determined absorption lineshapes of alkali-metal resonance doublets under conditions of selfbroadening where alkali-metal atoms collide with themselves, and in the presence of an inert buffer gas show good agreement with the so-called Voigt line-shape^{45-47 *}. The purpose of this chapter is to derive the Voigt-function for broadening effects under conditions typical for flow studies. Line-broadening behavior is a principal factor in the resonant refractive behavior. It decreases the peak value while it is accompanied by a wavelength spread of enhanced refractivity. The influence of the different line broadening mechanisms on the line-shape for given experimentally determined absorption linewidth parameters will be explained.

3.2 Line-Broadening Mechanisms

The linewidth of a given transition in a collection of atoms is an important property of that transition, especially in the present study. Already introduced for the classical electron oscillator is γ_{rad} , the radiative damping constant or linewidth. In the absence of any other damping mechanism the classical oscillator will always lose energy due to spontaneous emission of radiation (fluorescence). Thus,

* The absorption measurements of Niemax and Pichler [54] show small asymmetries in the wing beyond $\lambda - \lambda_0 = 0.5\text{\AA}$, the effects of which can be neglected in the present discussion.

the natural or radiative damping constant represents the rate at which the internal motion of the electrons loses energy and constitutes an energy-decay rate. However, it is by no means always the strongest broadening mechanism present and is mostly dominated by non-damping mechanisms like collision or pressure broadening and doppler broadening. Such processes can widen the resonant response of an atomic transition over the natural or radiative linewidth without changing the total energy of the response. They can, therefore, lower the peak value(s) while spreading the resonant enhancement to frequencies further away from the resonance line. Stark broadening effects, due to collisions of electrically excited particles, can be included in an overall collision damping rate but will be omitted as they are not applicable in the present study.

3.2.1 Collision Broadening

The broadening of an atomic response when due to random collisions between atoms, or random dephasing of the resonant response is called collision or pressure broadening, since this process is normally directly proportional to the pressure as will be shown. It may be helpful to picture the collision process in a gas in exactly the same mechanical fashion suggested by the meaning of the word. Atomic dipoles, originally oscillating together in phase, collide and this dephasing event may knock or push atomic internal motion out of phase. Simple expressions for the rates at which such collisions

occur can be predicted from kinetic theory^{*} as functions of the pressure and temperature of the gas.

In order to analyze the broadening effects caused by collisions, a large number of N_0 dipoles all initially at $t = 0$ oscillating in phase is considered. $N(t)$ then describes the number of dipoles still in phase after time t . The number "lost" from the in-phase group per second due to collisions is given by

$$\frac{dN(t)}{dt} = - \frac{N(t)}{T_2} \quad (3.1)$$

where $1/T_2$ describes the collision rate per atom and T_2 is then the meantime between collisions which can be obtained from kinetic theory⁴⁴.

The solution of the above differential equation yields

$$N(t) = N_0 \exp(-t/T_2) \quad (3.2)$$

This result can be compared with the damping term of the polarizability obtained from the electron oscillator model

$$\alpha(t) \sim \exp(-\frac{\gamma_{\text{rad}}}{2} \cdot t) \quad (3.3)$$

where γ_{rad} describes as before the radiative or natural damping.

When combining Eqs. 3.2 and 3.3 the above expression can be rewritten as

* An excellent treatment of kinetic theory is given in Reference 44.

$$\alpha(t) \sim \exp \left[- \underbrace{\left(\frac{\gamma_{\text{rad}}}{2} \right)}_{\substack{\text{Decay} \\ \text{rate due} \\ \text{to radia-} \\ \text{tion damp-} \\ \text{ing}}} + \underbrace{\left(\frac{1}{T_2} \right)}_{\substack{\text{Decay} \\ \text{rate of} \\ \text{coherence} \\ \text{due to} \\ \text{dephasing}}} t \right] \quad (3.4)$$

Lorentz⁴⁸ was the first who found out that the expressions for the atomic response of a gas under collision and natural broadening had the same form as for natural broadening alone and can be combined to an overall damping term or linewidth, which bears his name as the lorentzian linewidth:

$$\gamma_L = \gamma_{\text{rad}} + 2/T_2 \equiv \gamma_{\text{rad}} + \gamma_C \quad (3.5)$$

where γ_C describes the linewidth due to collision broadening.

In gases the collision or pressure broadening is directly proportional to the collision frequency $1/T_2$, which in turn is proportional to the number density N or pressure of the gas and the above expression can be written as

$$\gamma_L = \gamma_{\text{rad}} + C_r \cdot N \quad (3.6)$$

where C_r is a collision parameter and is experimentally and theoretically established for many different gases or gas combinations (see Table III for appropriate values for the alkali-metal atom resonances).

3.2.2 Doppler Broadening

The atoms in a gas undergo rapid but random motions which can be well described as brownian motion for particles in a thermal equilibrium at a finite temperature. Therefore, the frequency of the light received or emitted from an atom moving with velocity \vec{v} will be seen doppler-shifted by an observer as

$$\omega_r' = (1 + \vec{v}/c)\omega_r \quad (3.7)$$

where ω_r is the resonant frequency for a stationary atom.

According to the brownian kinetic theory, the atoms or molecules in a gas have random thermal-velocity components in all directions according to the gaussian or maxwellian distribution. It is found⁴⁴ that the number of atoms whose component of velocity for a given direction lies between v and $(v + dv)$ is given by

$$dN(v) = N \sqrt{\frac{M}{2\pi kT}} e^{-Mv^2/2kt} dv \quad (3.8)$$

for

$$-\infty < v < \infty$$

where M is the mass of the atom or molecule in kg, T the absolute temperature, and k the Boltzmann constant. On the assumption that the doppler and collision broadening mechanisms are two independent processes, we may obtain by convolution of the gaussian and lorentzian functions (Eqs. 2.33, 2.34 and 3.8) the well known Voigt functions for the refractive index and extinction coefficient (please note that in

Eqs. 2.33 and 2.34 γ_{rad} is replaced by the total lorentzian linewidth γ_L to account for collision broadening):

$$n_r(\omega) - 1 = n_0 - 1 + \frac{N e^2 f_{lu}}{m \epsilon_0 \gamma_L \omega_{lu}} \int_{-\infty}^{\infty} \frac{2(\omega'_{lu} - \omega) \gamma_L}{1 + [2(\omega'_{lu} - \omega) / \gamma_L]^2} e^{-4 \ln 2 [(\omega'_{lu} - \omega_{lu}) / \gamma_D]^2} \cdot \frac{\sqrt{\ln 2}}{\sqrt{\pi} \cdot \gamma_D} d\omega'_{lu} \quad (3.9)$$

and

$$\kappa_r(\omega) = \frac{N e^2 f_{lu}}{m \epsilon_0 \gamma_L \omega_{lu}} \int_{-\infty}^{\infty} \frac{1}{1 + [2(\omega'_{lu} - \omega) / \gamma_L]^2} e^{-4 \ln 2 [(\omega'_{lu} - \omega_{lu}) / \gamma_D]^2} \cdot \frac{\sqrt{\ln 2}}{\sqrt{\pi} \cdot \gamma_D} d\omega'_{lu} \quad (3.10)$$

where the expression

$$\gamma_D = \frac{2\omega_{lu}}{c} \sqrt{\frac{2kT}{M}} \cdot \sqrt{\ln 2} \quad (3.11)$$

describes the doppler full width at half maximum.

3.2.3 The Voigt-Profile

Figure 4 shows a comparison between the doppler and lorentzian lineshapes for the absorptive case, the two line broadening processes present under conditions of the present study and joined to the Voigt function of Eq. 3.10. The two curves are plotted in such

a way that the area under the curves and the half-widths are equal. As can be seen, there are some significant differences between the lorentzian and gaussian profiles worth mentioning. The doppler or gaussian curve drops to zero practically after one full linewidth from line center, whereas the lorentzian curve is characterized by a lower peak value and declines much more gradually in the line wings. Therefore, it can be assumed that the Voigt function for the wings of a line can be represented by the lorentzian component alone.

Unfortunately, the Voigt functions (Eqs. 3.9 and 3.10) cannot be solved explicitly and have to be evaluated numerically (see Section 3.3.4 for a listing of numerical Voigt approximations and Appendix A for the actually employed computer program, using the method by Hummer and Rybicki⁷¹). Nevertheless, approximations can be made for the limiting cases of very small and very large doppler broadening and for frequencies many linewidths away from the resonant frequency. At very low pressures (see Fig. 5) when the collision rate is small, the linewidth is dominated by doppler broadening and the lineshape shows the gaussian profile, whereas at higher pressures the collision rate between particles becomes so high that it finally dominates the doppler broadening effect and the profile takes the lorentzian lineshape. Figure 5 shows the change from doppler linewidth at low pressures to collision or pressure linewidth at high pressures for pure sodium computed from absorption data given in Tables II and III.

For a mathematical treatment of the Voigt functions the full expressions (Eqs. 3.9 and 3.10) can be considerably simplified by

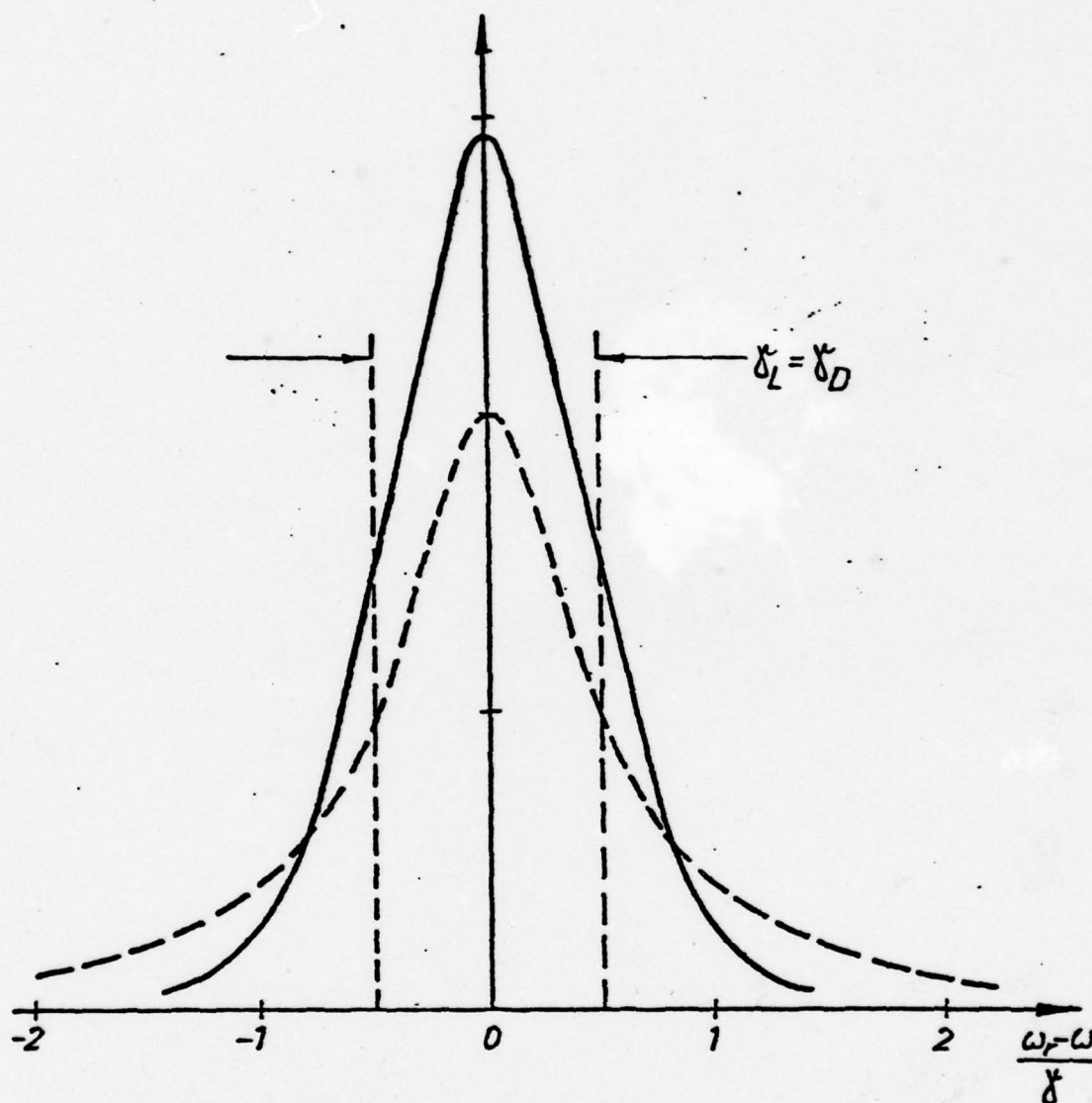


Fig. 4. Comparison between Doppler and Lorentzian Lineshapes for Equal Area and Equal Linewidths.

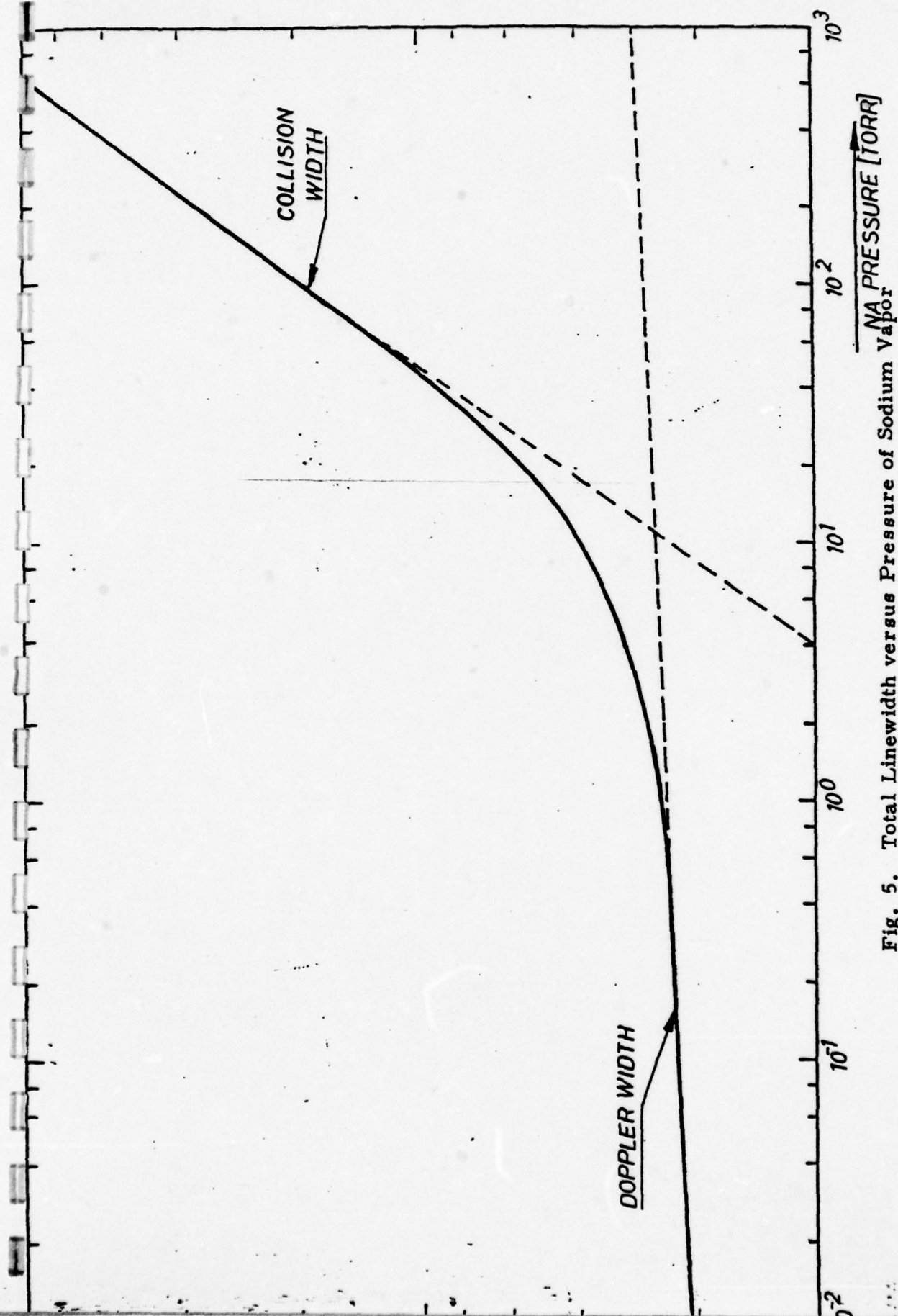


Fig. 5. Total Linewidth versus Pressure of Sodium Vapor

introducing the dimensionless parameters

$$\left. \begin{aligned} a &= \gamma_L / \gamma_D \cdot \sqrt{\ln 2} \\ x &= \frac{2\sqrt{\ln 2} (\omega - \omega_{Lu})}{\gamma_D} \\ \text{and} \\ y &= 2\sqrt{\ln 2} \left(\frac{\omega'_{Lu} - \omega_{Lu}}{\gamma_D} \right) \end{aligned} \right\} \quad (3.12)$$

The parameter "a" describing the ratio of lorentzian broadening to doppler broadening is called Voigt parameter or natural damping ratio.

Eqs. 3.9 and 3.10 now take the form

$$n_r(\omega) - 1 = n_0 - 1 + A \left[\frac{1}{\pi} \int_{-\infty}^{\infty} \frac{x-y}{a^2 + (x-y)^2} e^{-y^2} dy \right] \quad (3.13)$$

and

$$\kappa_r(\omega) = A \left[\frac{a}{\pi} \int_{-\infty}^{\infty} \frac{1}{a^2 + (x-y)^2} e^{-y^2} dy \right] \quad (3.14)$$

with

$$A = \sqrt{\pi} \frac{N \cdot e^2 \cdot f_{Lu} \cdot a}{2m\epsilon_0 \gamma_L \omega_{Lu}}$$

The quantities in square brackets can be recognized as the imaginary and real parts, respectively, of the function⁴⁹

$$W(z) = e^{-z^2} \operatorname{erfc}(-iz); \quad z = x + ia \quad (3.14)$$

where $\operatorname{erfc}(-iz) = 1 + \frac{2i}{\sqrt{\pi}} \int_0^z e^{-t^2} dt$ is the complementary error function of complex argument and Eqs. 3.9 and 3.10 can now be expressed in their final form

$$n_r(\omega) - 1 = n_0 - 1 + A\{\text{Im}[W(z)]\} \quad (3.16)$$

$$\kappa_r(\omega) = A\{\text{Re}[W(z)]\} \quad (3.17)$$

It can be shown that the imaginary and real parts of the $W(z)$ -function, $\text{Im}[W(z)]$ and $\text{Re}[W(z)]$, are Hilbert transforms of each other. This is a consequence of the Kramers-Kronig relationship between the dispersive and absorptive part of the complex index of refraction.

The Voigt linewidth γ_V can be written to a good approximation in terms of the Gaussian and lorentzian halfwidths as (FWHM)⁵⁰

$$\gamma_V = \frac{1}{2}[\gamma_L + (\gamma_L^2 + 4\gamma_D^2)^{1/2}] \quad (3.18)$$

In the limiting cases, for $\gamma_L \gg \gamma_D$ ($a \rightarrow \infty$, $\gamma_V = \gamma_L$), Eqs. 3.13 and 3.14 assume their basic lorentzian forms as in Eqs. 2.33 and 2.34; whereas in the case $\gamma_D \gg \gamma_L$ ($a \rightarrow 0$, $\gamma_V = \gamma_D$), the gaussian lineshapes

$$n_r(\omega) - 1 \rightarrow n_0 - 1 + \frac{\sqrt{2\pi} \omega_L^2 N e^2 f_{lu}}{2\sqrt{\pi} m \epsilon_0 \omega_L \gamma_D} \int_{-\infty}^{\infty} \frac{1}{\epsilon - x} e^{-\epsilon^2} d\epsilon \quad (3.19)$$

(Gaussian Limit)

where ϵ is a dummy integration variable, and

$$\kappa_r(\omega) \rightarrow \frac{\sqrt{\pi} \omega_L^2 N e^2 f_{lu}}{2m \epsilon_0 \omega_L \gamma_D} \cdot e^{-x^2} \quad (\text{Gaussian limit}) \quad (3.20)$$

are obtained, which are special cases of the function $W(z)$.

In order to reveal some noteworthy features of the different behavior of the refractivity and absorption profiles in the line wings it is helpful to approximate the imaginary and real parts of the function $W(z)$ for large x :

$$\text{Im}[W(z)] \rightarrow \frac{1}{\sqrt{\pi}} \cdot \frac{1}{x} \quad (x \gg 0) \quad (3.21)$$

$$\text{Re}[W(z)] \rightarrow \frac{a}{\sqrt{\pi}} \cdot \frac{1}{x^2} \quad (x \gg 0) \quad (3.22)$$

These simple expressions provide excellent agreement with the full equations for $x > 10$, or for conditions of the present study for roughly 0.1 \AA away from line center (Figs. 6 and 7). As can be seen from these graphs and the above expressions when inserted in Eqs. 3.16 and 3.17 the refractivity values in the wings are highly insensitive to the Voigt parameter a and vary relatively slowly with x like a hyperbola, while the absorption coefficient declines much more rapidly as one moves away from line center and is directly proportional to the lorentzian linewidth γ_L . Since the total absorptive linestrength is much more concentrated around the center frequency compared to the dispersive case, significant enhancements of the refractivity can be expected in the far wings of the line. This conforms with the concept of causality which states that the absorption of one frequency must be accompanied by a compensating phase shift of all other frequencies (see Section 2.3.3). This is of utmost importance for the present study, as it makes possible the utilization of enhanced refractivity in a region where the absorption is relatively small.

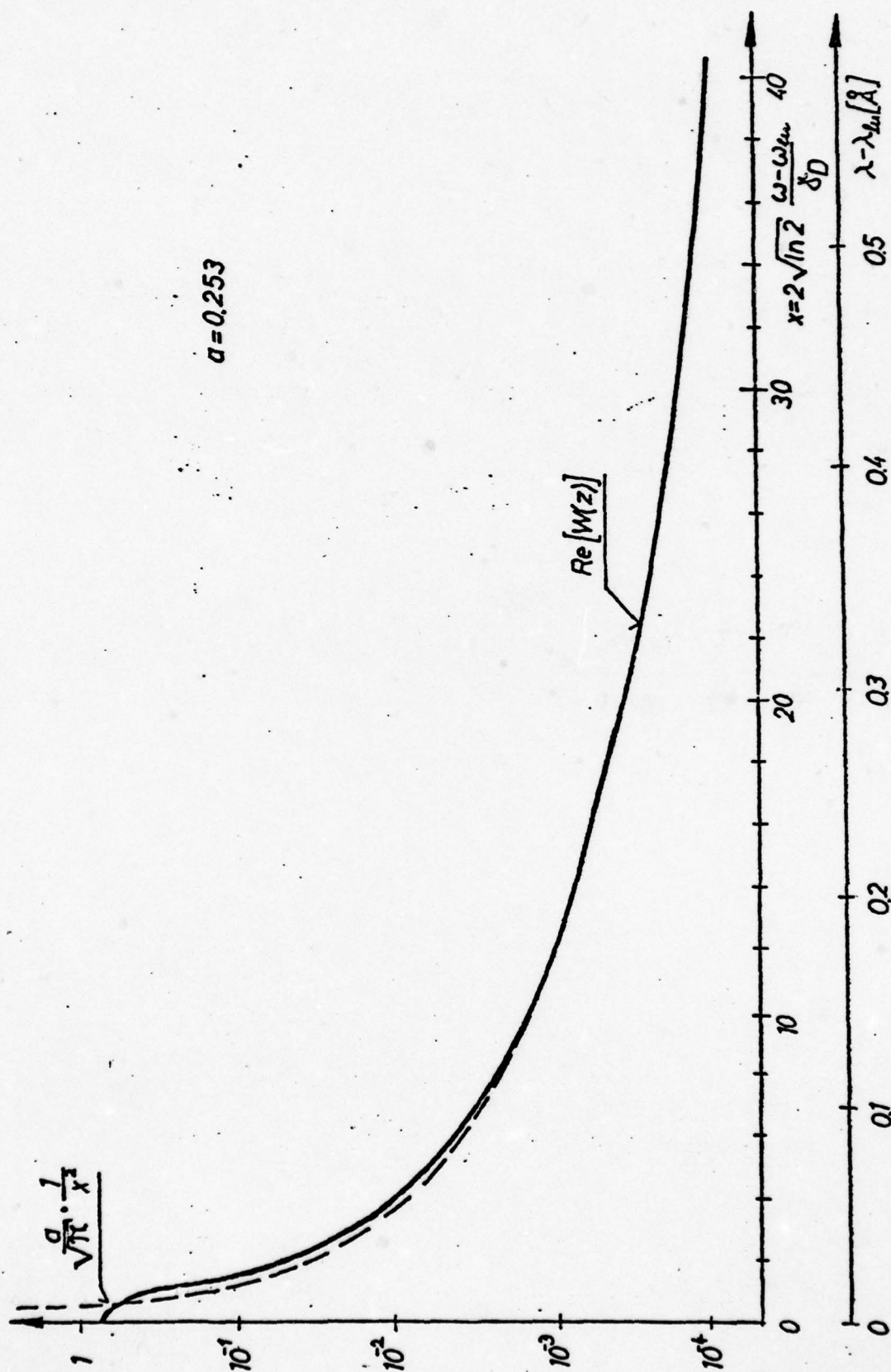


Fig. 6. Voigt Profile Analysis: Plot of the Imaginary Part of the Complementary Error Function of Complex Argument in Comparison with its Approximation for Large x .

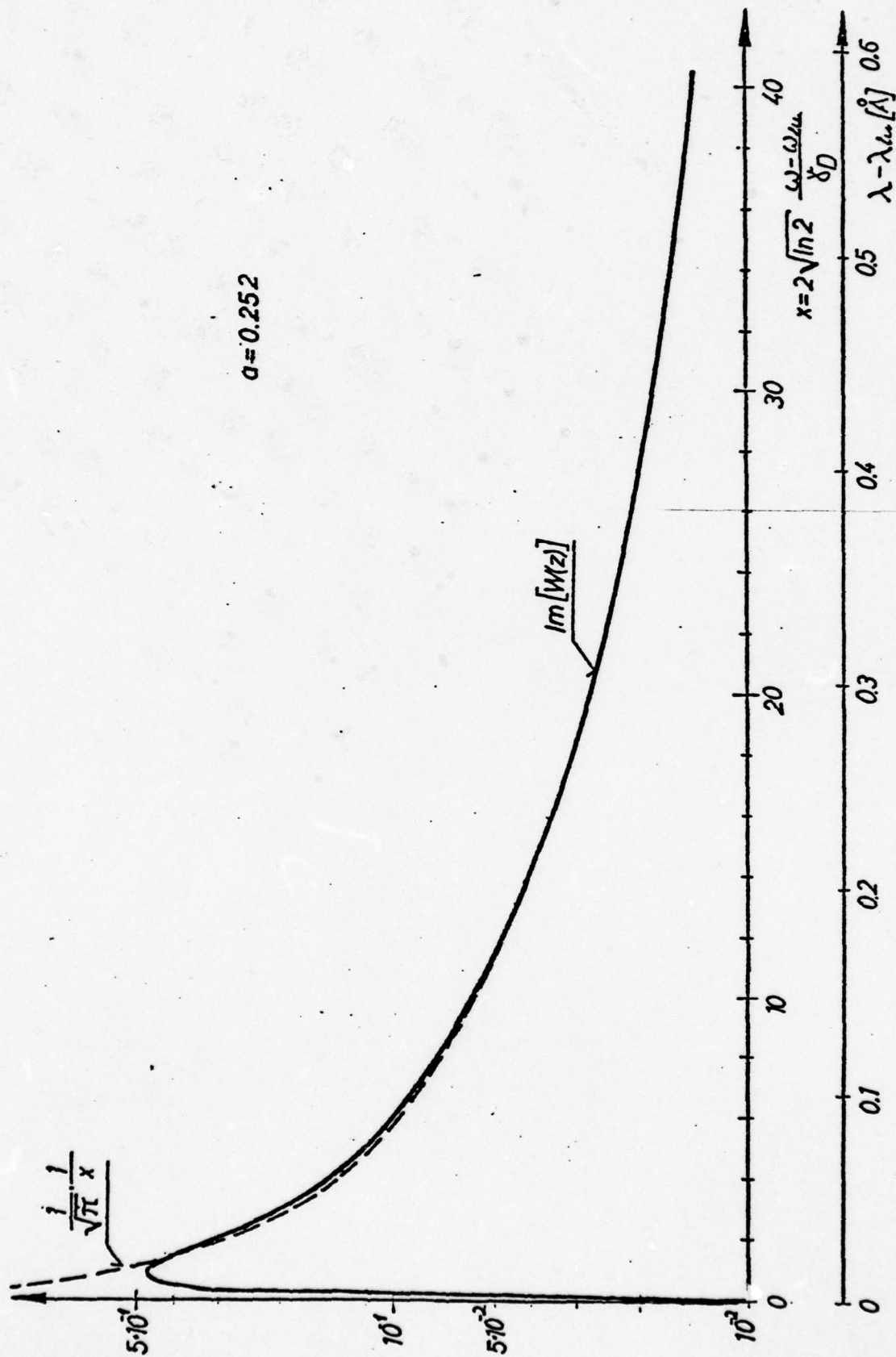


Fig. 7. Voigt Profile Analysis: Plot of the Real Part of the Complementary Error Function of Complex Argument in Comparison with its Approximation for Large x .

3.3 Resonant Lineshapes for the Doublets of Alkali-Metal Atoms

3.3.1 Selfbroadening of Alkali-Metal Atoms

The Cauchy formula (Eq. 2.3) when expressed in terms of polarizability can be written as ⁵¹

$$\alpha(\omega) = \sum_{n=0} \alpha_n \cdot \omega^{2n} \quad (3.23)$$

where α_n are the so-called Cauchy frequency moments.⁵² It was pointed out that for applied frequencies ω less than the first dipole transition, $0 < \omega < \omega_n$ the so-called normal dispersion interval, the above equation gives a good approximation to the actual response of real atoms. Evidently, these normal dispersion regions for the inert gases and atmospheric constituents extend well into the UV spectral regime, whereas those of the alkali-metal atoms terminate in the visible region of the spectrum (see Fig. 1 for the normal dispersion curve of air at NTP and Fig. 2 for the anomalous dispersion of sodium vapor at its D-lines). Since the Cauchy moments of Eq. 3.23 are positive,⁵² the polarizability is an increasing function of frequency in the normal dispersion interval for the atomic and molecular systems of Table I. The polarizabilities of the inert gases and atmospheric constituents show little dispersion in the visible regime, however, since the α_n in these cases are relatively small. Consequently, the static polarizabilities ($\alpha_s = \alpha_0$) shown in Table I in these cases give the major contributions to the total polarizabilities; and the corresponding refractivities shown in Table I control the sensitivities of optical

flow visualization devices in these cases. (The conventional Dale-Gladstone constant is related to the polarizability by the expression $K_0 = \frac{\alpha_0}{2\epsilon_0 M}$, where M is the atomic mass). Therefore, it is not practical to use diatomic gases for resonant refractivity studies. Note also that the small polarizabilities are caused by vibrational and rotational transitions which do not have large resonances.

By contrast the dipole polarizabilities of alkali-metal atoms show significant change with frequency in the visible regime as a consequence of strong dipole-allowed electronic transitions. The increase in polarizability is so rapid near the alkali-metal atom resonance doublets that Eq. 3.23 is no longer adequate and the Maxwell-Sellmeier formula (Eq. 2.4) has to be applied. For the alkali-metals a two-term expression written in terms of the polarizability gives an accurate approximation for frequencies less than the transition frequencies in the following form:⁵³

$$\alpha(\omega) = \frac{C_1}{\omega_D^2 - \omega^2} + \frac{C_2}{\omega_R^2 - \omega^2} \quad (3.24)$$

where the second term in the above expression represents the contribution to the polarizability from all terms of the specific alkali-metal excitation spectrum except the D_1 and D_2 doublet, which are represented by the first term here. Since the separations between the D_1 and D_2 doublet components in Na to Cs correspond to at least 300 Voigt widths in all cases for the temperatures and pressures considered, each component of the doublets can be treated as an individual isolated

resonance. By contrast, the two components in Li overlap strongly at higher temperatures and buffer gas number densities and the resonance in this case must be treated explicitly as a doublet.

Consequently, to calculate total refractivities in the neighborhood of the alkali-metal doublets in Na to Cs it is necessary to replace the first term in Maxwell-Sellmeier's formula by the detailed lineshape of resonant contributions of the doublets in which case Eq. 3.24 becomes,

$$n_r(\omega) - 1 = \frac{1}{2\epsilon_0} \cdot N \left(\frac{C_2}{\omega_R^2 - \omega^2} \right) + n_{D_1}(\omega) - 1 + n_{D_2}(\omega) - 1 \quad (3.25)$$

where the terms $n_{D_1}(\omega) - 1$ and $n_{D_2}(\omega) - 1$ describe the detailed dispersion curve of the D_1 and D_2 doublet, respectively.

For the evaluation of the absorption profiles near the doublets of alkali-metals, however, it is only required to account for the contribution of the doublet itself; and the extinction coefficient in the neighborhood of the D_1 and D_2 lines can be written in the form

$$\kappa(\omega) = \kappa_{D_1}(\omega) + \kappa_{D_2}(\omega) \quad (3.26)$$

3.3.2 Dispersion of Alkali-Metal Atoms in the Presence of an Inert Buffer Gas

In Eq. 2.15 it was assumed that a strong linearity exists between the induced dipole moment p and the applied electric field E . As a consequence the refractive index $n(\omega)$ of a homogeneous binary gas

mixture can be written for a wide range of temperatures and pressures in the additive form

$$n(\omega) - 1 = K_a(\omega)\rho_a + K_b(\omega)\rho_b \quad (3.27)$$

In the present development the subscript a refers to alkali-metal atoms seeded in small amounts ($\rho_a \ll \rho_b$) in inert or atmospheric buffer gas, designated by the subscript b. In order for the alkali-metal contribution to dominate the refractivity it is necessary that $K_a(\omega) \gg K_b(\omega)$. Referring to Table I, it is evident that the static polarizabilities (or static Dale-Gladstone constant) of the alkali-metal atoms are from one to two orders of magnitude larger than those of the inert or atmospheric gases and even larger values of the Dale-Gladstone value can be expected by choosing the operating frequency ω within the alkali-metal atom resonance regions.

3.3.3 Voigt-Lineshape Parameters for the Alkali-Metal Atom Vapors

It was shown that the absorption profile and refractivity profile of alkali-metal atom resonance doublets can be well approximated over wide ranges of temperatures and pressures by employing the Voigt functions (Eqs. 3.13 and 3.14), where the gaussian width γ_G could be represented by the doppler width γ_D . Recent measurements,^{54,55} showed that for the case of selfbroadening as well as in the presence of inert buffer gas, the lorentzian linewidth γ_L of alkali-metal atom resonance doublets can be well approximated in terms of natural and collision widths:

$$\gamma_L(T, N) = \gamma_N + \gamma_C(T, N) \quad (3.28)$$

where

$$\gamma_C(T, N) = \gamma_C(N) = C_r \cdot N \quad \text{in the case of selfbroadening}$$

and

$$\gamma_C(T, N) = C_r(T) \cdot N_b \quad \text{in the presence of a buffer gas.}$$

The natural width $\gamma_N = \gamma_u$ is independent of temperature and equal to the Einstein A coefficient (Eq. 2.30a). The linear variation of the collision width γ_C with buffer gas number density is valid for pressures less than atmospheric pressure. For selfbroadening of alkali-metal atoms C_r can be considered as constant for each of the two doublet components and is listed in Table III. In the presence of buffer gas the collision parameters are temperature dependent and can be expressed by a power law as⁵⁵

$$(C_r)_T = (C_r)_{273} (T/273)^p \quad (3.29)$$

The experimentally determined values for the collision parameter C_r at $T = 273^\circ \text{K}$ as well as the values for p are tabulated in Table III.

Evidently, the pressure widths of Table III for a given atom are relatively insensitive to the colliding inert buffer gas partner considered but are one to two orders of magnitude smaller than in the selfbroadening case. Unfortunately, detailed lineshape studies of the alkali-metal atom resonance doublets in oxygen and nitrogen are apparently not available, but, because of the physical similarity of

Table I. Static Polarizabilities and Dale-Gladstone Constants
together with Resonance Wavelengths of the Inert Gases
and Alkali-Metal Atoms

Atom	Resonance ⁵⁶ Frequency $\omega_r [10^{15} \text{ rad/sec}]$	Resonance [*] Wavelength $\lambda_r [\text{\AA}]$	Static ⁵⁷ Polarizability $\alpha_o [10^{-41} \frac{\text{A}^2 \text{s}^4}{\text{kg}}]$	Dale-Gladstone ^{**} Constant $K_o [10^{-5} \text{ m}^3/\text{kg}]$
He	32.23	584.4	2.282	19.39
Ne	25.33	743.7	4.398	7.411
Ar	17.66	1067	18.28	15.57
Kr	15.24	1236	27.60	11.20
Xe	12.82	1470	45.07	11.67
O ₂	9.29	2028	17.47	18.57
N ₂	18.54	1016	19.36	23.51
Li	28.07	6710	268.7	1317
Na	31.94	5898	275.4	407.4
K	24.46	7701	474.9	413.1
Rb	23.69	7950	520.9	207.3
Cs	21.05	8946	588.6	150.3

* Vacuum wavelengths in Angstrom units ($1 \text{ \AA} = 10^{-10} \text{ m}$), obtained from the resonance frequencies of the preceding column and the speed of light in vacuo.

** Zero frequency Dale-Gladstone constant calculated from the preceding column and the expression $K_o = K_s = \frac{\alpha_o}{2\epsilon_o M}$, where M is the atomic mass of the species.

Table II. Alkali-Metal Atom Resonance Doublet Parameters*

Atom		Frequency ⁵⁶ $\omega_{\lambda u}$ [10^{15} rad/sec]	Wavelength ⁵⁶ $\lambda_{\lambda u}$ [\AA]	f-number ⁵⁸ $f_{\lambda u}$	Natural Width ⁵⁹ (FWHM) γ_N [10^7 rad/sec]	Atomic Mass ⁶⁰ M [10^{-26} kg]
Li	D ₁	2.807335	6709.76	0.251	3.72	1.152
	D ₂	2.807399	6709.61	0.502	3.72	
Na	D ₁	3.193960	5895.93	0.327	6.28	3.817
	D ₂	3.197199	5889.96	0.655	6.30	
K	D ₁	2.445956	7701.10	0.339	3.82	6.492
	D ₂	2.456032	7667.70	0.682	3.86	
Rb	D ₁	2.369439	7949.79	0.350	3.70	14.189
	D ₂	2.414194	7802.42	0.700	3.84	
Cs	D ₁	2.105596	8945.95	0.353	2.95	22.065
	D ₂	2.209972	8523.43	0.714	3.25	

* D₁ refers to the $^2S_{1/2} \rightarrow ^2P_{3/2}$ transition whereas D₂ refers to the $^2S_{1/2} \rightarrow ^2P_{1/2}$ transition.

Table III.

Collision Broadening Parameter C_r for Alkali-Metal Atom Resonance

Doublets Under Conditions of Selfbroadening and in the Presence of

Inert Buffer Gas*

Alkali Atom	Self-Broadening ⁵⁴	Buffer Gas									
		He		Ne		Ar		Kr		Xe	
		C_r	p	C_r	p	C_r	p	C_r	p	C_r	p
Li	D_1^{61}	-	3.64 .36	2.52 .34	4.00 .32	4.97 .32	5.57 .32				
	D_2	-	-	-	-	-	-	-	-	-	-
Na	D_1^{62}	88 ± 8	3.00 .34	2.18 .10	4.54 .36	-	-	4.32 .32			
	D_2	104 ± 10	-	-	-	-	-	-	-	-	-
K	D_1^{63}	100 ± 4	7.33 .43	-	-	11.8 .33	10.4 .32	-	-	-	-
	D_2	134 ± 12	-	-	-	-	-	-	-	-	-
Rb	D_1^{64}	126 ± 10	3.59 .42	1.88 .27	3.58 .32	3.58 .32	4.12 .32				
	D_2	170 ± 16	-	-	-	-	-	-	-	-	-
Cs	D_1^{65}	124 ± 8	-	5.93 .29	11.3 .33	-	-	10.5 .32			
	D_2	162 ± 16	-	-	-	-	-	-	-	-	-

* Values in units of 10^{-15} rad/secm⁻³ for the D_1/D_2 alkali-atom doublet components in the indicated inert buffer gas at $T = 273$ K. Values in the range $250 \text{ K} < T < 1000 \text{ K}$ are obtained by multiplying the appropriate entry by the factor $(T(^{\circ}\text{K})/273)^p$. p-values taken from reference [55].

Argon to these two gases, the values of Table III shown for Ar are presumably appropriate and can be used for the computation of the lineshapes.

3.3.4 Numerical Calculations

Sodium was chosen to serve as the test medium. This was mainly due to the fact that sodium is the best documented of the alkali-metals and despite its high reactivity is still relatively easy to handle compared to the heavier alkali-metals.

Numerical calculations were employed to obtain the refractivity and absorption curve in the neighborhood of the D-lines at 5889.96 \AA and 5895.93 \AA for various temperatures and pressures. For saturated sodium vapor in equilibrium the temperature T can be related to the pressure P in terms of the vapor pressure curve which can be written for atomic sodium to a high degree of accuracy over the temperature range 400 K to 800 K in the form⁶⁶ (see also Appendix B for details)

$$\log P[\text{Torr}] = 10.86423 - 5619.406/T + (3.45 \times 10^{-6})T - 1.04111 \log T \quad (3.30)$$

The ideal gas law, in turn, was then used to obtain the sodium vapor number densities N . The temperatures and number densities together with the line broadening parameters taken from Table II and III were then employed to calculate the linewidths γ_D and γ_L as well as the Voigt width γ_V according to the Eqs. 3.11, 3.28 and 3.18, respectively.

There are numerous empirical fits to calculate the real (absorptive) part of the $W(z)$ -function (Eq. 3.15). Among these to be stressed are the approximations by Posener,⁶⁷ Penner,⁶⁸ Whiting,⁶⁹ Armstrong,⁷⁰ and Kielkopf.⁵⁰ The method developed by Hummer⁷¹ was chosen for its efficiency. Unfortunately, the most recent publication on this topic by Hui, et al.⁷², was not available at the time the computer program was written. This procedure is simpler and faster than previous methods, requiring only two arithmetic statements in FORTRAN.

Since apparently no computer program is described in the literature to evaluate the imaginary or dispersive part of the $W(z)$ function, the Kramers-Kronig-Heisenberg relation (Eq. 2.27) was used to transform the real into the imaginary part. For values of the dimensionless frequency $x > 30$ the approximations of Eqs. 3.21 and 3.22 were applied. A listing of the program and a tabulation of the numerical values obtained are given in Appendix A.

The two-term Maxwell-Sellmeier formula (Eq. 3.24) for sodium reads⁵³

$$\alpha(\omega) = \frac{2.7796 \times 10^{-6}}{(3.194 \cdot 10^{16})^2 - \omega^2} + \frac{4.8214 \cdot 10^{-8}}{(5.8264 \cdot 10^{15})^2 - \omega^2} \quad (3.31)$$

where the second term was used in the calculation of the index of refraction near the resonance doublet according to Eq. 3.25. Figures 8 and 9 show the computed refractive index and absorption curves versus wavelength in the neighborhood of the sodium D-lines for different temperatures. Note again the difference in resonance behavior, the large peak value of the absorption coefficient $\mu_r(\lambda)$

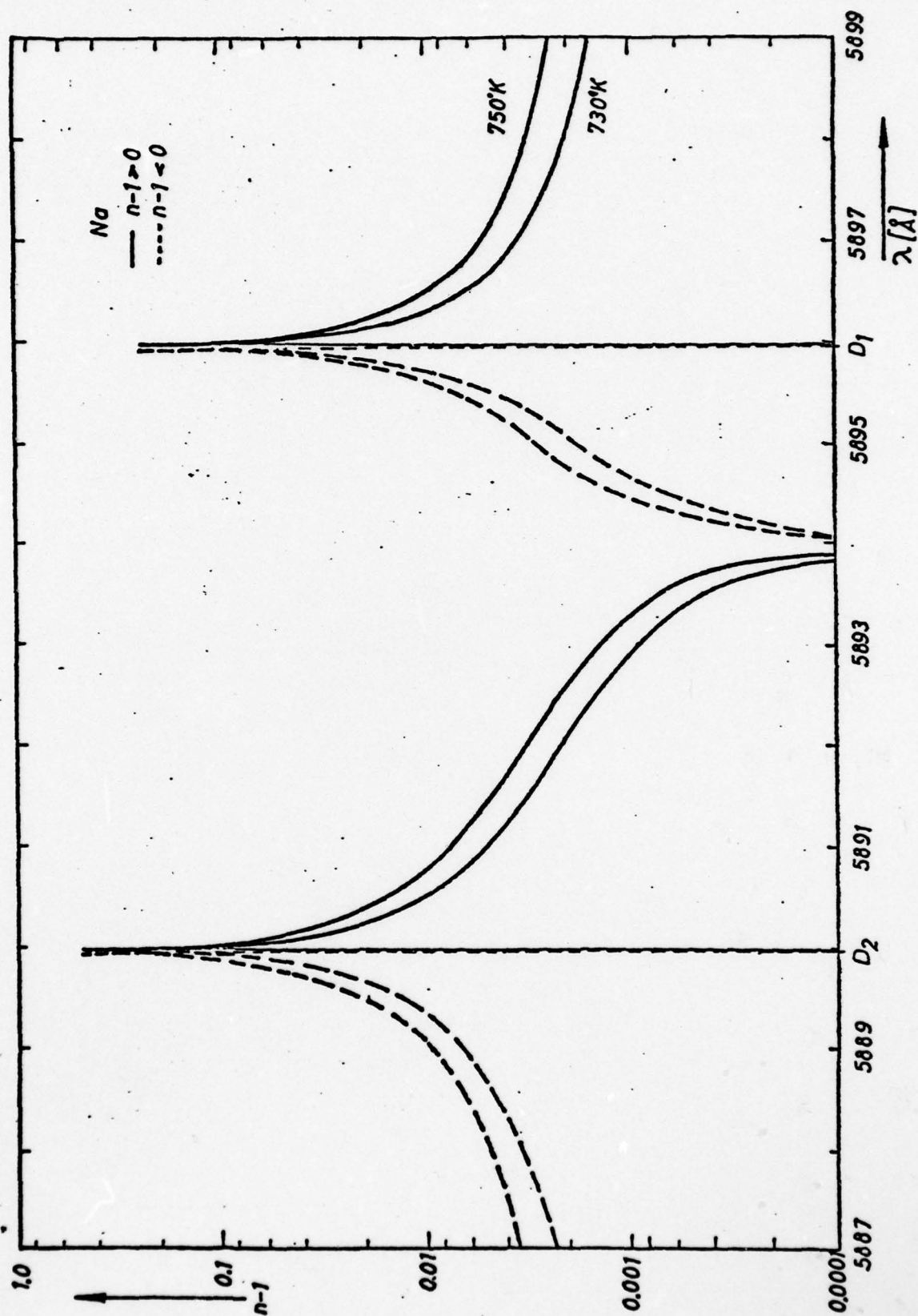


Fig. 8: Computed Refractive Index of Sodium at D-Lines
(Note that dashed lines represent negative values.)

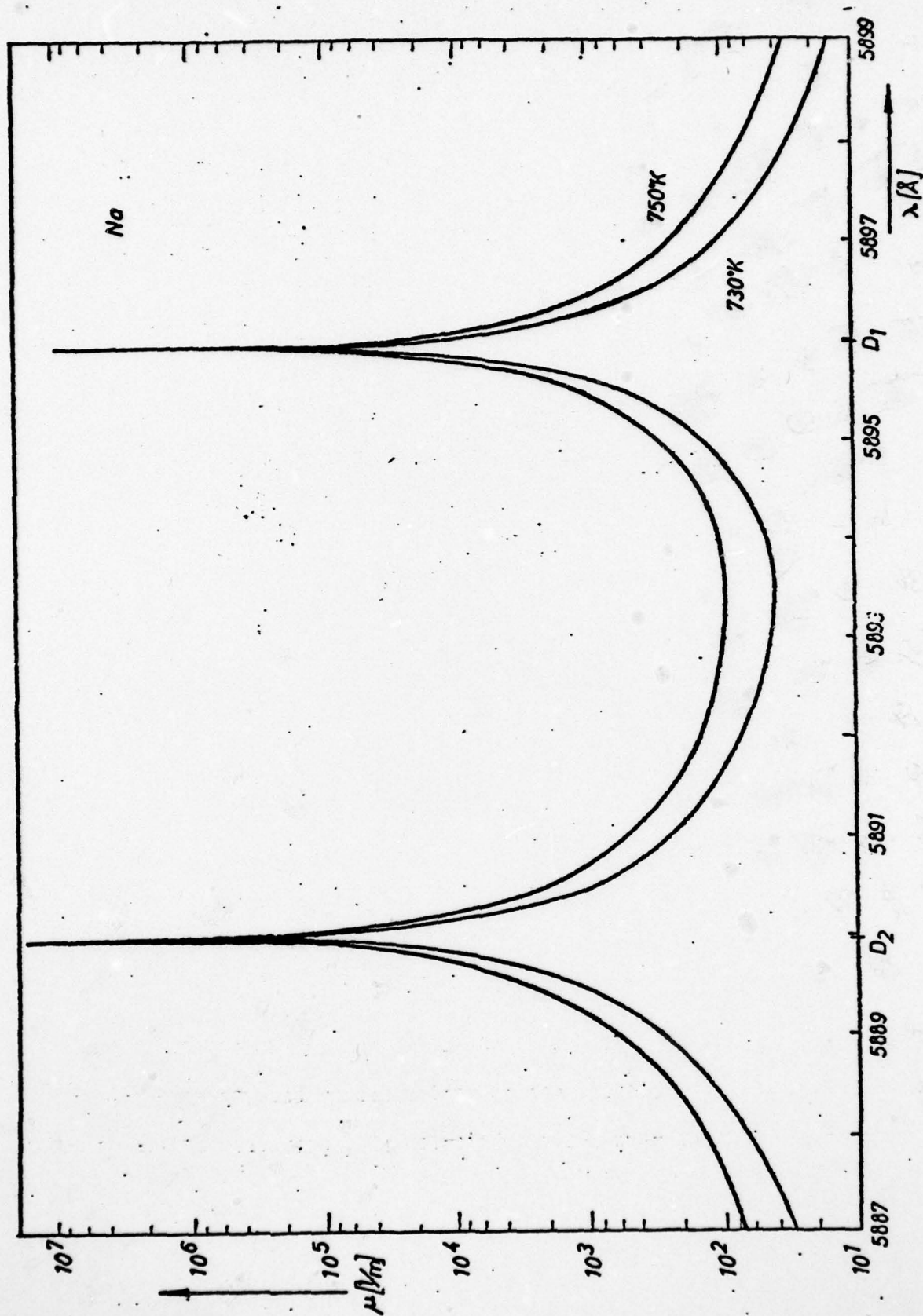


Fig. 9. Computed Absorption Coefficient of Sodium at D-Lines.

combined with a rapid decline in magnitude away from resonance compared to relatively low peak values but a slow decrease in resonant enhancement as one moves away from line center for the refractivity profiles $n_r(\lambda) - 1$.

3.4 Experimental Goal of this Study

The purpose and goal of the experimental part of this study is to check the analytically obtained resonant refractivity values. This is done in an apparatus under conditions similar to those in actual flow measurements in order to be able to transfer and apply easily the acquired data and information to the flow situation where sodium is used as a trace gas. In this context the experiment can be considered a first step to the final application of resonant refractivity in a wind-tunnel or similar device. It gives insight into the limiting parameters and the signal to noise ratio, and it helps to find and to solve problems in an early stage where the apparatus can be easily modified or changed.

In the following chapters the experimental set-up and technique will be described while emphasizing the questions of special interest like what is the maximum obtainable resonant enhancement and what are the stability and repeatability of the light source and the sensitivity of the measuring and recording devices over an extended period of time.

CHAPTER IV

EXPERIMENTAL APPARATUS4.1 Introduction

The experiment involves the determination of the resonant refractive index of sodium vapor close to the D-lines. A tunable dye laser is used as a light source to observe fringe shifts to corresponding changes in sodium density.

The development of this pulsed dye laser pumped by a nitrogen laser by T. W. Hänsch¹³ in 1972 made it possible to utilize the enhanced refractivity near resonance for improved flow visualization as proposed by Bershader¹¹ in 1970. This laser is ideally suited to utilize the enhanced refractivity near resonance since it combines excellent wavelength tunability and long-term stability with high output power necessary to overcome the strong absorption in the resonant regime. For the quantitative calibration measurement of the sodium atom dispersion curve, the dye laser is combined with an interferometer of the Mach-Zehnder type which determines the refractive index for a given wavelength and density change by the number of fringe shifts. Two so-called heat pipe ovens, one in each arm of the interferometer, are used to generate homogeneous sodium vapor and to contain the vapor under well defined and stable conditions in such a way that it is accessible for optical investigations.

This chapter will highlight some of the problems which had to be solved and will present and explain the various components of the total

system; their descriptions, properties and performances will be treated in detail. (For the alignment procedure of the dye laser the reader is referred to Appendix C.) A schematic and a photograph of the whole system is shown in Fig. 10 and Fig. 11, respectively. The outline of this chapter will follow the light beam from its origin in the dye-laser through the two heat pipe ovens in the M-Z interferometer to the recording and calibration devices.

4.2 The Dye Laser

4.2.1 General Description

The pulsed tunable dye laser described here is designed to be pumped transversely by a pulsed nitrogen laser at 3371 \AA with a pulse duration of roughly 10 nsec and a repetition rate of about 10 pps. The nitrogen laser in the present study is a commercially available unit (Molelectron UV300) with a peak power of 300 kW. Fig. 12 shows a photograph of the nitrogen pump laser together with the dye laser assembly in the foreground, both mounted on a heavy $1 \frac{1}{2}$ " thick aluminum plate. A schematic of the basic dye laser components and a photograph hereof are displayed in Figs. 13 and 14, respectively.

The horizontal UV beam coming from the nitrogen laser is of rectangular shape and approximately 25 mm wide and 5 mm high. It is focused by a 10 cm focal length aspheric quartz lens to a line at the inner wall of the dye cell roughly 8 mm long and 0.2 mm high. The dye cell itself was purchased commercially (Molelectron D1051) together with its magnetic stirrer and holder and can be translated in two

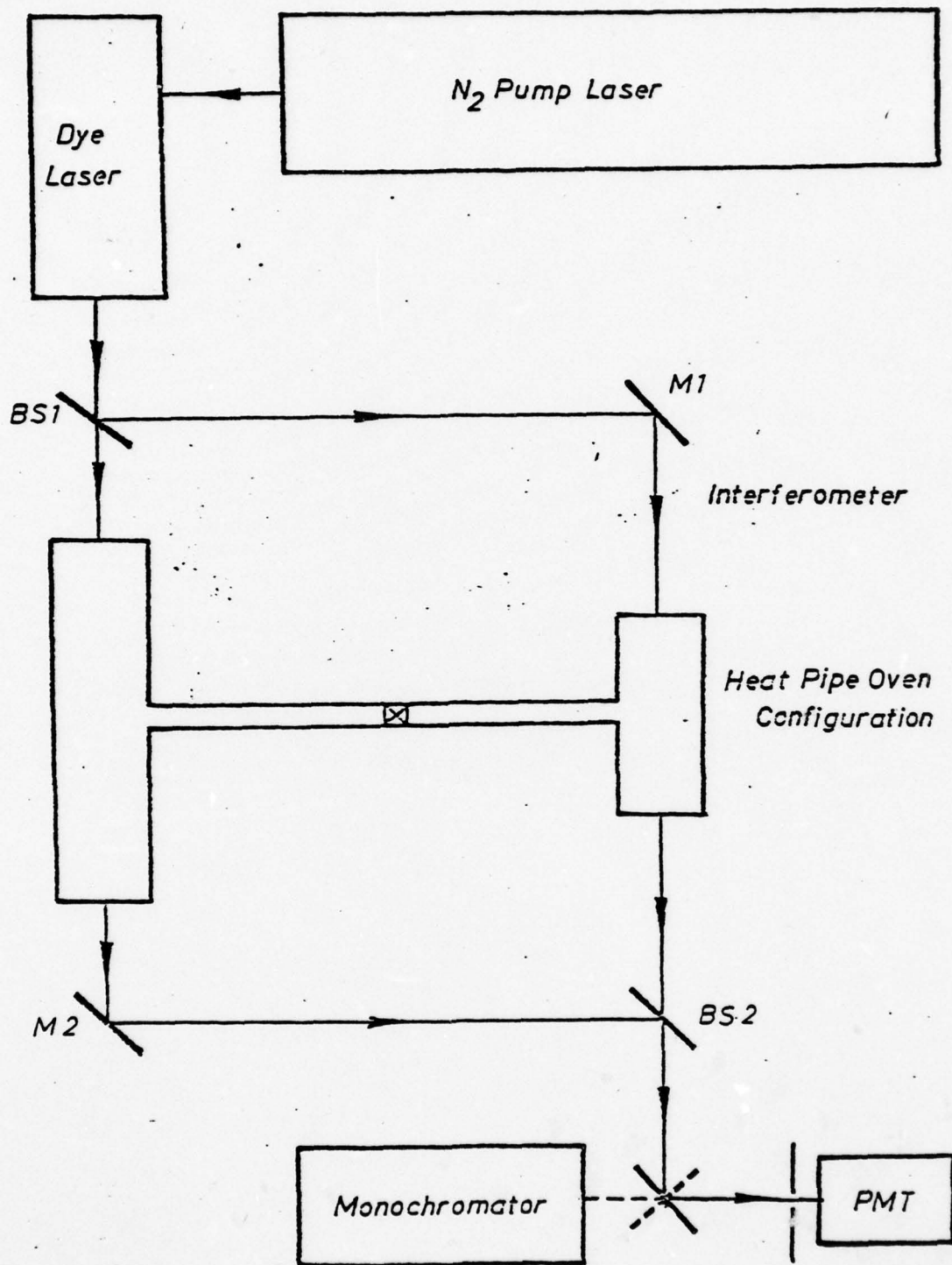


Fig. 10. Schematic of Experimental Set-up.

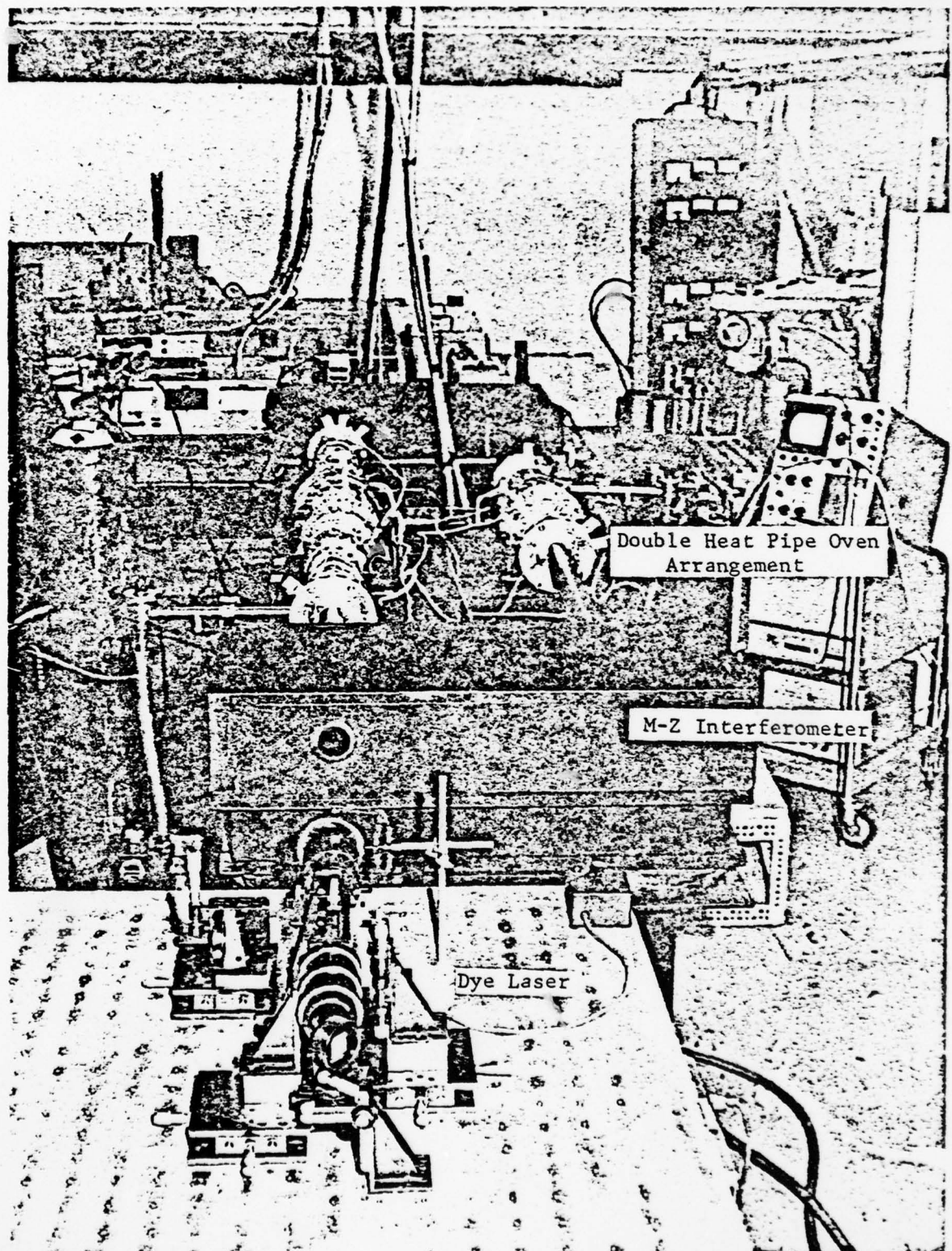


Fig. 11. Photograph of Resonant Refractivity Apparatus. The Dye Laser is Displayed in the Foreground with the Double Heat Pipe Oven Arrangement Sandwiched in the Two Paths of the M-Z Interferometer Between the Black Boxes Containing the Entrance and Exit Interferometer Plates.

THIS PAGE IS BEST QUALITY PRACTICABLE
FROM COPY FURNISHED TO DDC

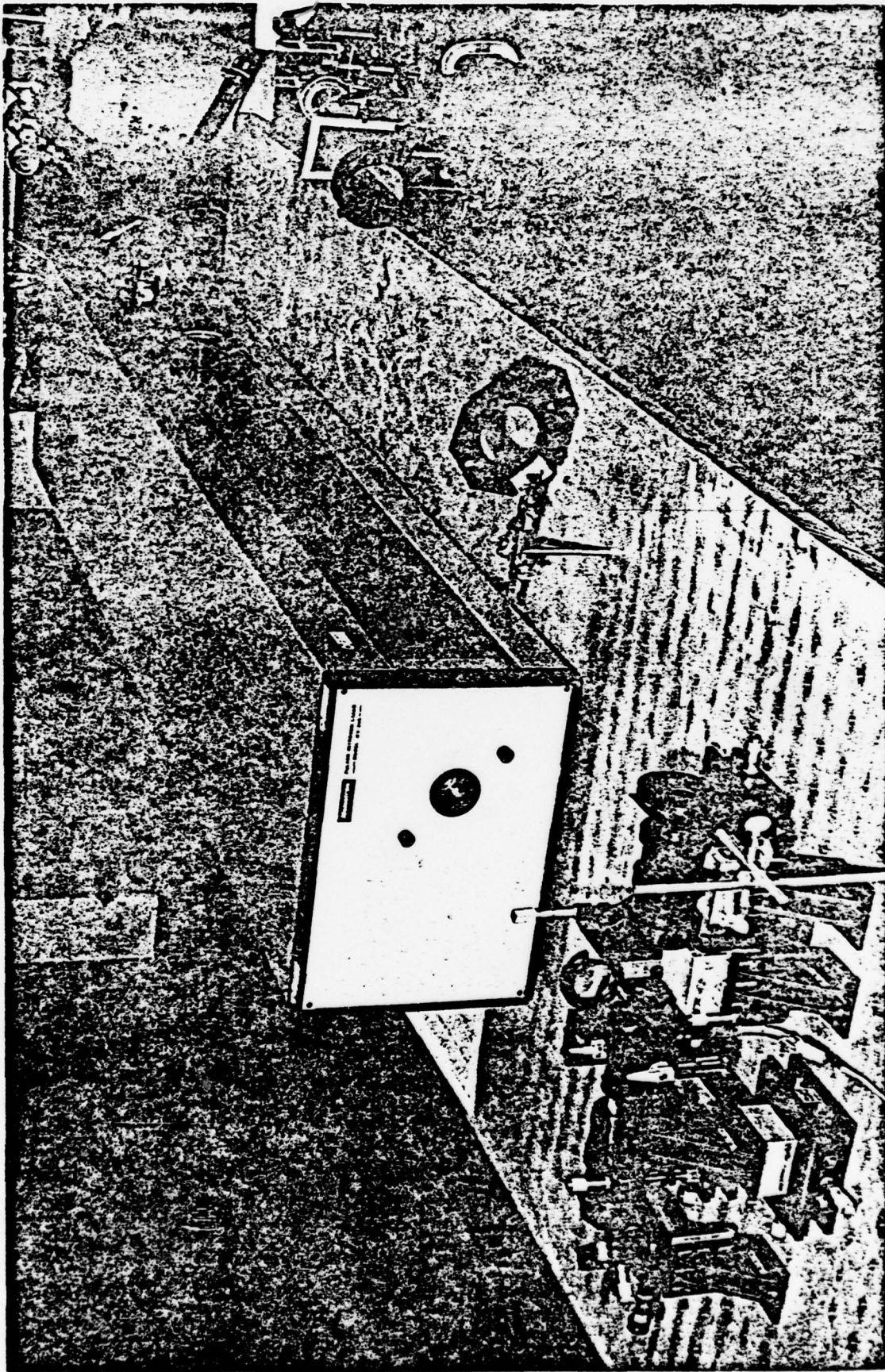


Fig. 12. Photograph of N₂-Pump Laser together with Dye-Laser Assembly in the Foreground.

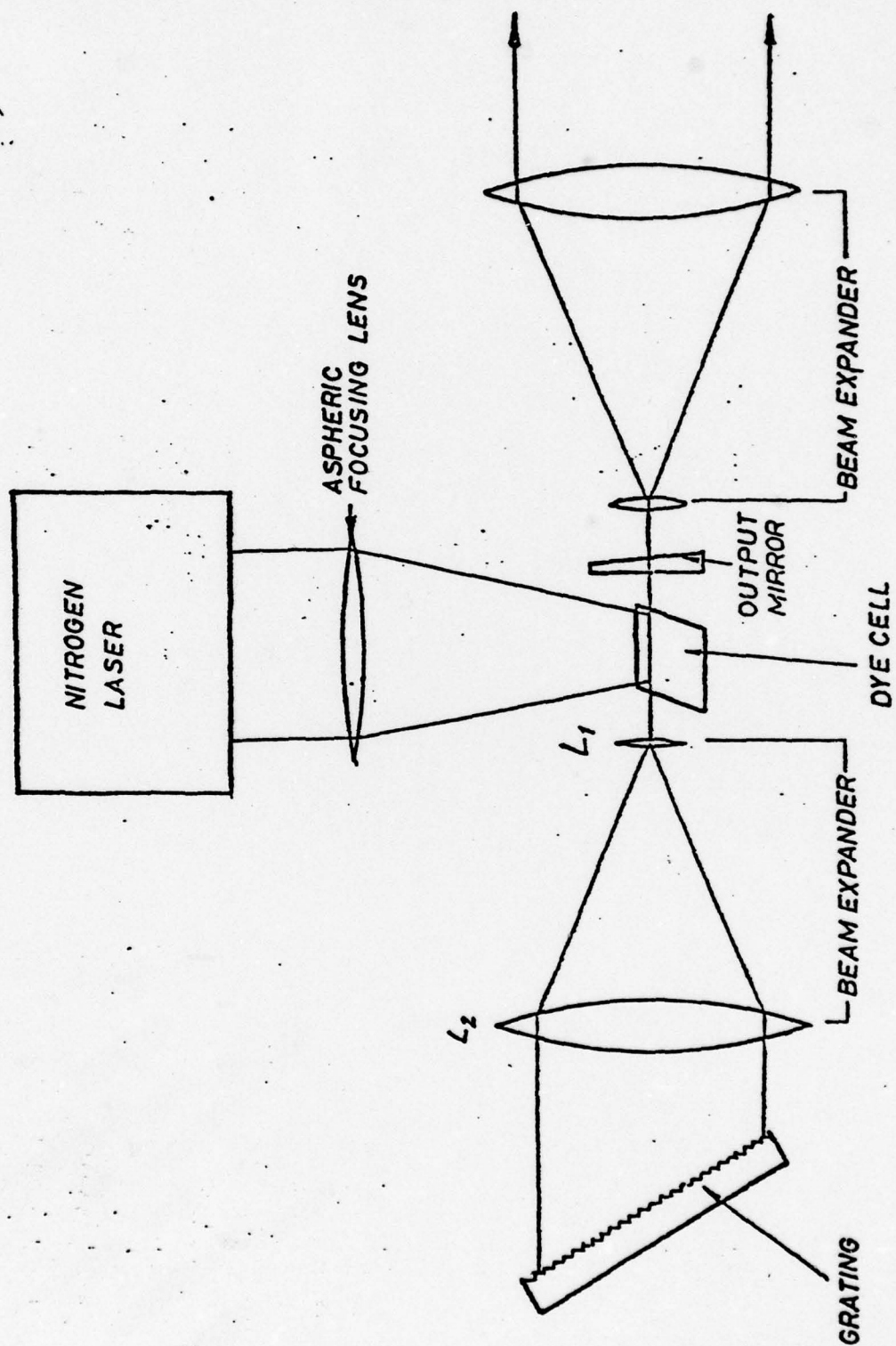


Fig. 13. Schematic of Dye Laser

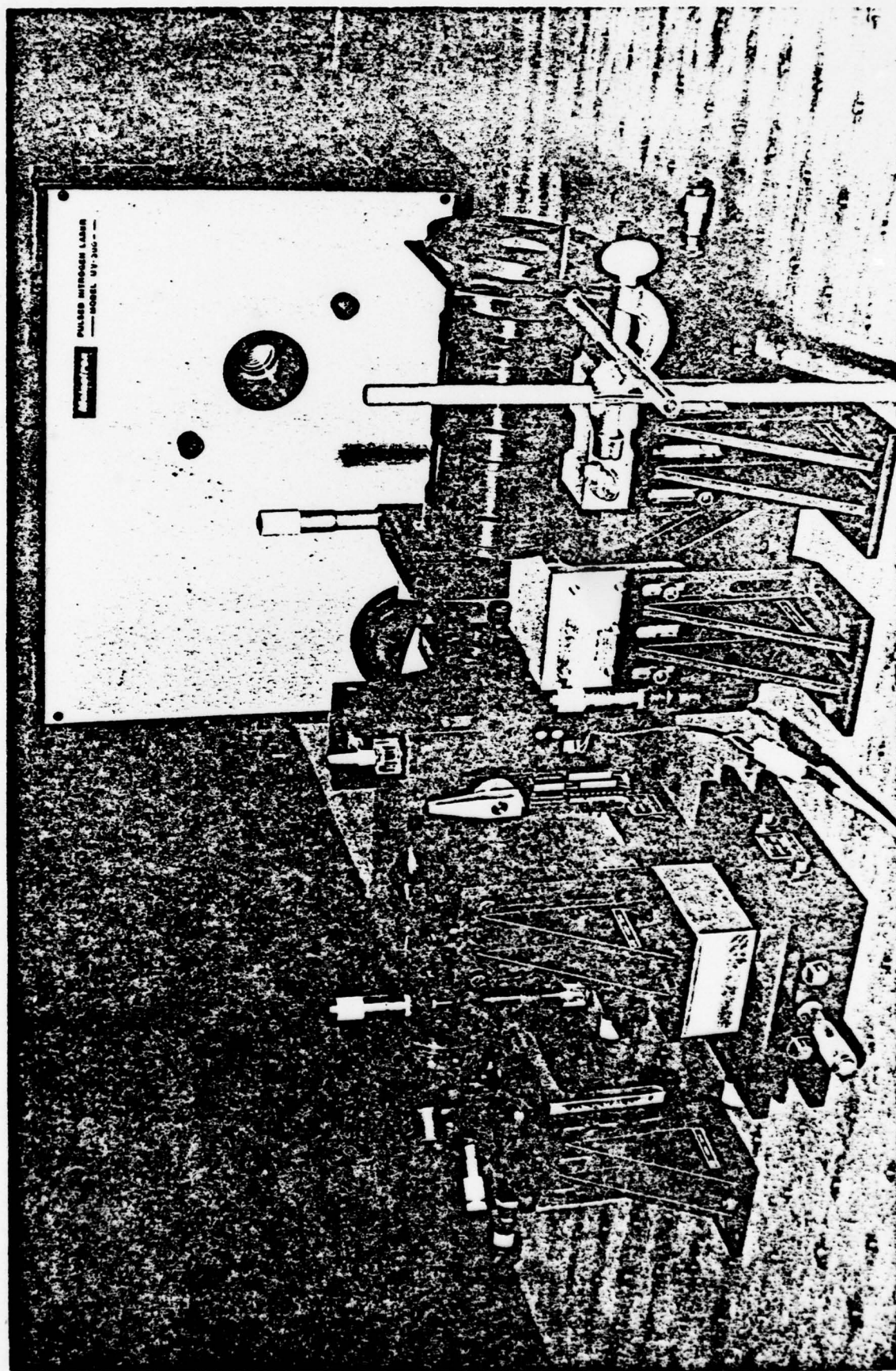


Fig. 14. Photograph of Dye-Laser Assembly

directions normal to the optical axis. The side windows are accurately parallel but slightly tilted to the optical axis to avoid unwanted back reflections. It contains 2 cc of magnetically stirred dye solution (Rhodamine 6G) whose concentration is adjusted to $5 \cdot 10^{-3}$ M/liter of ethanol so that the UV light can only penetrate 0.2 mm resulting in an approximately circular active cross section.

Due to the high gain of the nitrogen-pumped dye laser, the output mirror consists of uncoated quartz surfaces which serve as a broadband 4 percent reflector and are planar with a 30-minute wedge between them to avoid back reflections from the outer face. The wedge is oriented vertically so that the planes of the two faces intersect in a horizontal line below the mirror and is held in a beam-splitter mount which has orthogonal angular adjustments.

The spontaneous fluorescence light emitted from the excited Rhodamine 6G dye into the near-axial directions covers the wavelength range between 5680 \AA and 6050 \AA with a maximum in intensity at roughly 5790 \AA . The dye laser output wavelength is selected within this range by a high resolution first order grating (blaze angle 51° , 632 grooves per mm) held in Littrow mount by a precision mirror mount with 0.1 sec of arc mechanical resolution.

To expand the beam on the grating in order to illuminate more lines and to reduce beam divergence and thus increasing output power while minimizing output bandwidth, a beam-expanding telescope is added between the dye cell and the grating. The Galilean-type telescope consists of two lenses L_1 and L_2 of focal lengths $f_1 = -8 \text{ mm}$ and

$f_2 = 160$ mm. The two lenses are one-element systems both anti-reflection-coated and designed for minimum spherical aberration. The distance between dye-cell and lens L_1 is approximately 50 mm and lens L_1 is mounted slightly tilted off-axis to avoid back reflections. The beam expansion of 20 times results in a spot size on the grating of approximately 1 cm diameter. The position of the two telescope lenses is controlled separately by five micrometer screws. Lens L_1 can be moved by three precision translation stages in all lateral directions whereas lens L_2 can be translated only in the two horizontal directions.

All parts of the dye laser head are mounted rigidly together with the nitrogen pump laser on a 1 1/2" thick aluminum plate in such a way that the total length of the laser cavity (approximately 50 cm) allows only for a very few (four to eight) light passes during the 10 nsec excitation pulse. This ensures a high power output due to the high gain of the amplifying medium combined with a reasonably narrow band width. The aluminum plate rests on 16 motorcycle inner tubes to dampen any high frequency vibrations.

4.2.2 Performance Specifications

Experimental performance data are given for the dye laser tuned (if not otherwise noted) to 5890 \AA , using Rhodamine 6G dissolved in ethanol ($5 \cdot 10^{-3}$ M/liter ethanol) and excited by a 300 kW peak power nitrogen laser with 10 nsec pulse durations and at 10 pulses/sec.

A tabulation of these data is given in Table IV and a plot of the measured output power versus wavelength is shown in Figure 15.

A commercially available power meter (Molelectron J3-05) based on the pyroelectric principle is used to measure the peak power of the output pulses. The different output powers for different wavelengths are compared in Fig. 15 with the tuning curve published by the Molelectron Corp.⁷³ for the model DL200 and the specific dye. The measured values for a well adjusted laser are quite comparable with this curve.

In general, the bandwidth of the output beam is at a minimum at any wavelength after adjustments have been made for maximum power and optimum beam quality. The bandwidth increases with the gain of the dye so that it is at a maximum at the highest power wavelength for any dye and decreases as the output power decreases. A fixed, flat-plate Fabry Perot etalon is best for measuring bandwidth. It is mounted in the output beam between a lens of roughly 50 mm focal length in the diverging region and a white piece of paper. With the 3 mm fused silica etalon used (free-spectral range = $0.392 \text{ } \overset{\circ}{\text{A}}$) the resulting fringe pattern ("bulls-eye") which are displayed in Fig. 16 have a fringe separation of $0.24 \text{ } \overset{\circ}{\text{A}}$ at $5890 \text{ } \overset{\circ}{\text{A}}$. Thus the width of the fringes, as a fraction of the fringe spacing, gives a good approximation of the laser bandwidth.⁷⁴ This bandwidth is quite sufficient for the present study since the laser will be tuned to the wings of the sodium atom resonance line where a change in refractivity over a fraction of an Angstrom is negligible. However, should need arise for a smaller bandwidth, the

TABLE IV

Specifications of Dye-Laser

Dye Solution	Rhodamine 6G
Tuning Range	5680 - 6050 Å ⁰
Bandwidth (FWHM) at 5890 Å ⁰	0.24 Å ⁰
Wavelength Accuracy	< 0.1 Å ⁰
Wavelength Reproducibility	< 0.1 Å ⁰
Wavelength Stability	< 0.1 Å ⁰
Output Peak Power at 5890 Å ⁰	31 kW
Output Pulse Energy at 5890 Å ⁰	155 μJ
Repetition Rate	10 pps
Pulse Duration	5 ns

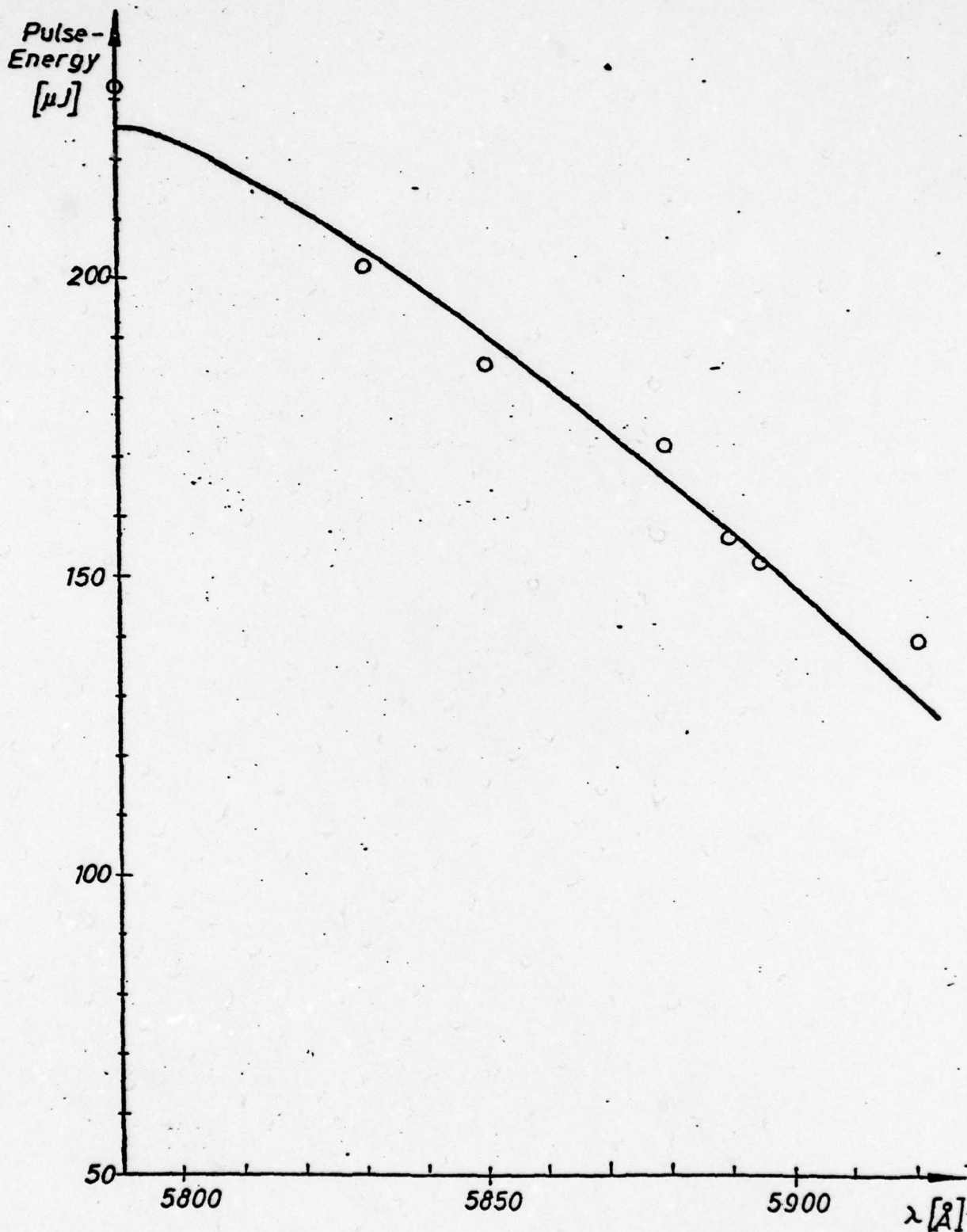


Fig. 15. Measured Pulse Energy of Dye Laser Using Rhodamine 6G versus Wavelength Compared with Tuning Curve of Molelectron DL200 Dye Laser.

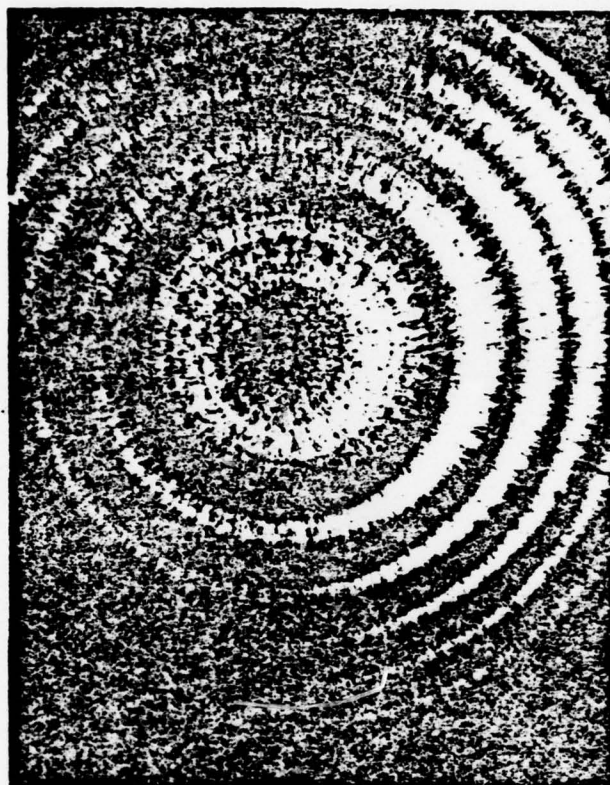


Fig. 16. Dye Laser Output at 5890 \AA Viewed through
3 mm Fabry-Perot Etalon

Free Spectral Range = 0.392 \AA

Laser Bandwidth = 0.24 \AA

insertion of an intra-cavity etalon reduces the bandwidth by at least two orders of magnitude. This improvement in bandwidth has to be bought with a significant drop in output power, up to one order of magnitude and with more complex handling and adjustment procedures.

Wavelength accuracy, wavelength reproducibility and wavelength stability are determined using a McPherson 1 m scanning Spectrometer (Model 2051) with a minimum instrumental linewidth of less than 0.1 \AA . For measurement of the wavelength accuracy and reproducibility, the laser is first tuned to a known spectral line of a neon or sodium vapor lamp whose light is superimposed in the spectrograph. The setting on the micrometer screw is noted and the laser tuned away from that wavelength. After a certain period of time, ranging from minutes to several hours and days the laser is tuned back to its initial setting and the wavelengths compared with the superimposed light of the spectral lamps. If no deviations can be detected with the spectrograph, any possibly existing wavelength shifts have to be smaller than the instrumental linewidth of the monochromator, which means smaller than 0.1 \AA . Such, in fact, was found to be the case here. Wavelength instabilities due to changes in ambient temperatures were not detected either and thus have to be smaller than 0.1 \AA . The temperatures of the aluminum plate and ambient air are monitored and at various time intervals checked against any possible drift of the tuned wavelength. It is found that, despite the fact that the ambient air temperature varied in a daily cycle by a few degrees, the temperature of the aluminum plate stayed almost constant. The maximum temperature change

combined with an overall very rigid mounting of the dye laser components and highly sensitive controls are probably the cause for the excellent precision and stability of the laser.

4.2.3 Wavelength Calibration of Dye Laser

Before being used as a lightsource for the study of the refractive behavior of sodium vapor and before any performance measurements can be taken, the dye laser has to be calibrated to its tuned wavelength. This calibration procedure is repeated everytime when the laser is realigned or its power optimized and it is routinely done every month to ensure proper operation. For the absolute and relative wavelength calibration in the region of interest two spectral lamps (Na and Ne) are needed which are placed in front of the McPherson spectroscope in such a way as not to obscure the dye laser beam which also is directed into the monochromator after being first diffused with a piece of ground glass, in order to insure that the monochromator grating is filled and the detector is not saturated. As a detector a photomultiplier tube (EMI 9658-B) served which is hooked up to a x-y plotter.

For the wavelength calibration in the immediate vicinity of the two sodium D-lines a sodium spectral lamp is sufficient. By tuning the dye laser first to one D-line and then to the other (see Fig. 17), absolute as well as relative calibration can be achieved. The corresponding change in micrometer settings when tuning from the D_1 line to the 5.97 \AA distant D_2 line is about 0.43 mm, yielding a resolution at

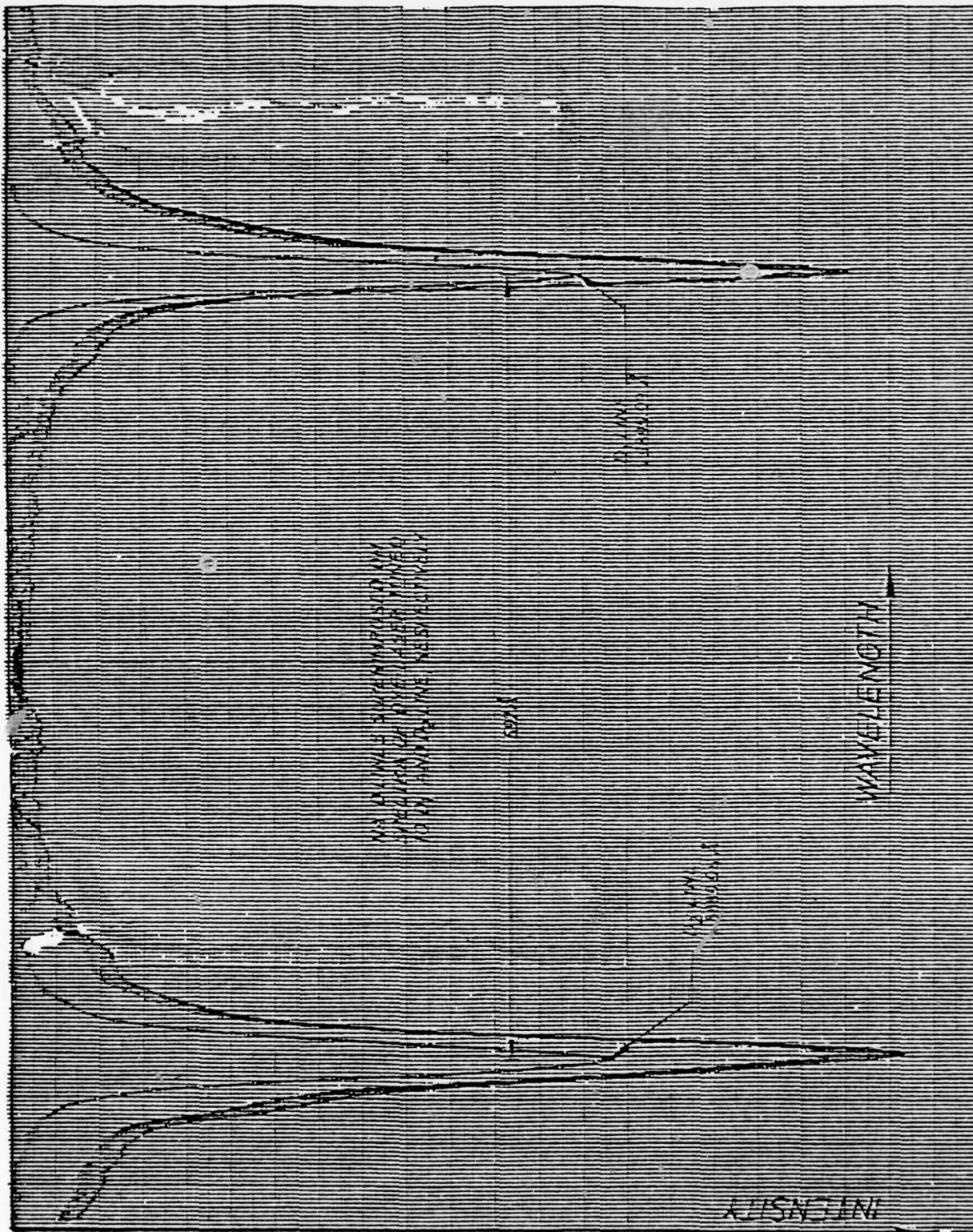


Fig. 17. Recorded Plot of Wavelength Calibration of Dye-Laser to Sodium D-Lines.

THIS PAGE IS BEST QUALITY PRACTICABLE
FROM COPY FURNISHED TO DDC

the D-lines of $13.9 \text{ }^{\circ}\text{A/mm}$. Of course, this value will change when the geometrics of the laser cavity due to alignments or component replacements are varied, and it should only serve as an illustration not as an absolute value. Furthermore, it is assumed that the micrometer settings are directly proportional to the wavelength. This is only a good approximation of the grating equation for small rotations. For larger values the full equation

$$n\lambda = 2d \sin i \quad (4.1)$$

has to be taken into account, where n is the order of diffraction, d the groove spacing, and i the angle of incidence measured from the normal. For construction of a calibration curve for an extended wavelength range, the laser is tuned to the spectral line of the Ne-lamp at $5852.5 \text{ }^{\circ}\text{A}$ and the corresponding micrometer settings for the interval between $5852.5 \text{ }^{\circ}\text{A}$ and the sodium D_2 -line are computed according to Eq. 4.1 and its boundary values. The calibration curve obtained in such a manner is found to be in good agreement with the readings of the wavelength indicator of the scanning McPherson monochromator when positioned to the dye laser wavelength.

4.3 The Mach-Zehnder Interferometer

The dye laser beam, originally having a diameter of approximately 1 mm, is expanded 20 times by a telescope outside the laser. That beam expander is identical to the one in the cavity, and is directed into the M-Z interferometer as shown in Fig. 11. The dye

laser is displayed in the foreground with the double heat-pipe oven arrangement sandwiched in the two paths of the M-Z interferometer between the black boxes containing the entrance and exit interferometer plates, respectively. These windows and beamsplitters are interferometer quality quartz flats of 2" diameter and are held in high precision mirror mounts which provide rotational motions about the vertical and horizontal axis with a resolution of less than 0.1 arc sec. A micrometer translation stage provides the necessary lateral mobility for mirror M2 (see Figure 10). The dimensions of the interferometer are rather large to accommodate the long heat pipe oven in one of its arms. The interferometer plates are mounted on a metal frame approximately 4 meters by 1 meter. The frame itself consists of 2" by 4" hollow rectangular beams welded together and rests on 16 motorcycle inner tubes which are used as shock absorbers. As can be seen on Fig. 15, the light beam in the interferometer is completely enclosed by black cardboard tubes and boxes to keep ambient air currents caused by the hot outer surface of the heat pipe ovens from disturbing the fringe shift measurements. This simple arrangement works quite satisfactorily and annihilates any wobbling of the fringes. However, due to the large size of the interferometer a fringe drift is observed which is probably caused by different temperature expansions in the beams of the interferometer. Fortunately this drift, normally of the order of 2 to 3 fringes per day, is negligibly small for the present experiments. Good quality fringes with the

heat pipe ovens in place are readily obtained with a mercury light-source and can be easily focused anywhere in the interferometer.

4.4 The Heat Pipe Oven

4.4.1 General Description

The two paths of the interferometer contain two sections of a double heat pipe oven arrangement as shown in Fig. 18. Both heat pipe ovens are identical except for a substantial difference of length (1 m) to cancel out refractive end effects in both light paths.

The development of the heat pipe oven originates from the design of the heat pipe, a device to transport heat in a very effective manner, introduced by G. M. Grover and his co-workers⁷⁵ in 1963. The operation of the heat pipe combines vapor heat transfer and capillary action in a way that very uniform conditions of the vapor are achieved. Vapor heat transfer is responsible for transporting the heat energy from the evaporator section at the hot end of the pipe to the condenser section at the cool end. The vapor stays at the same temperature during the entire heat transfer process until it condensates at the cooled zone since evaporation and condensation takes place at essentially the same temperature. Once condensated in the cool end of the heat pipe the now liquid working fluid gets pulled back to the hot region by the capillary action of a wick that connects the condenser with the evaporator making use of the surface tension of the condensate.

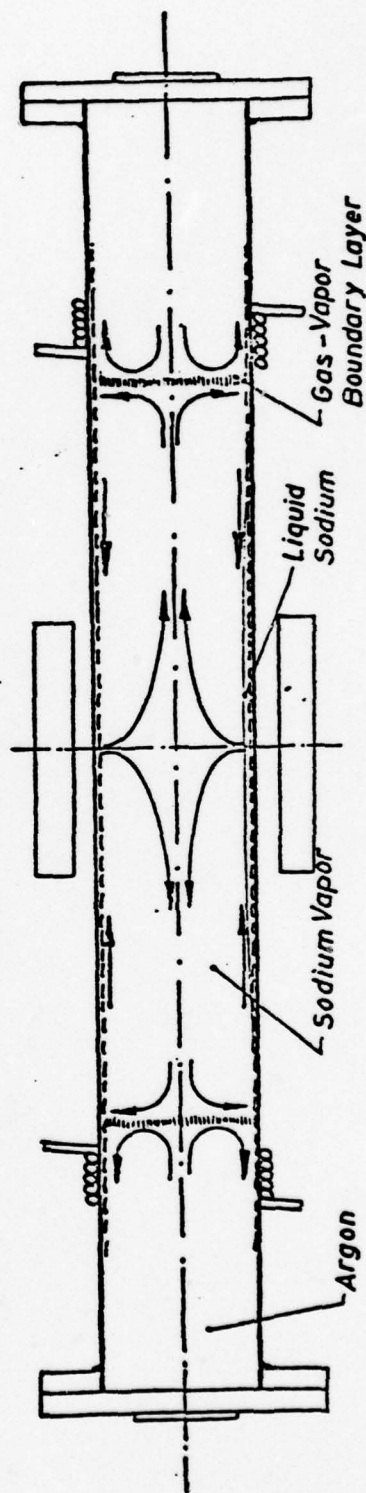
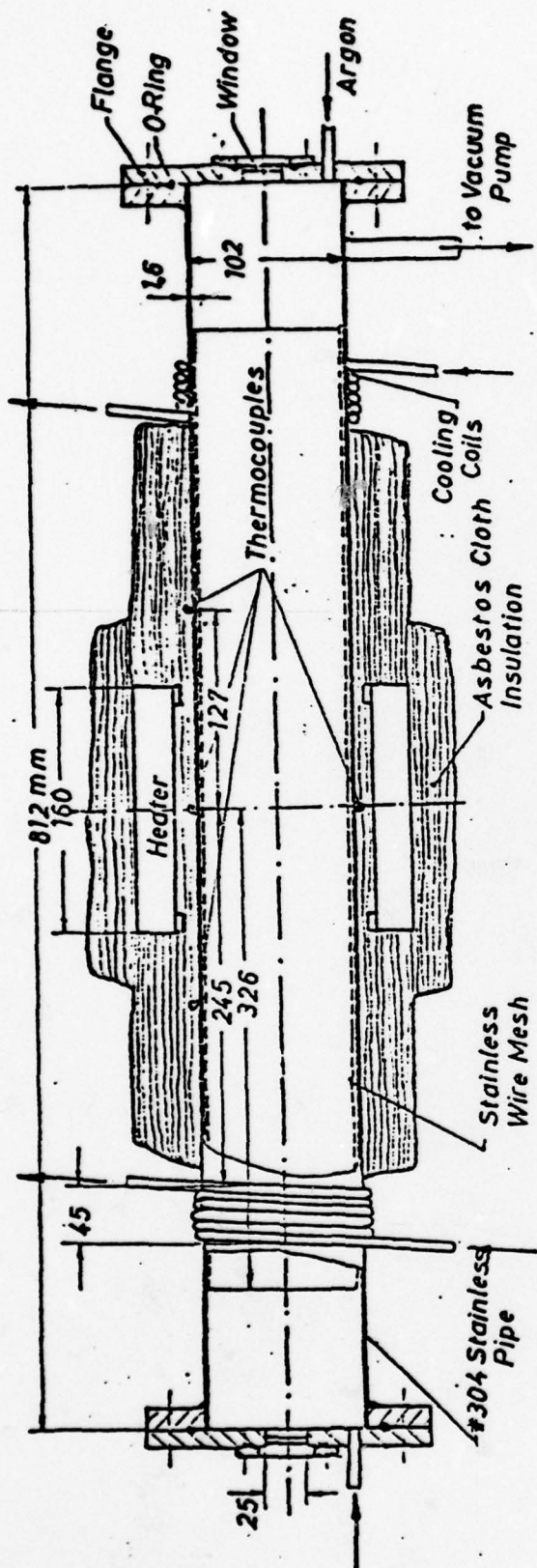


Fig. 18. Drawing of Small Heat Pipe Oven Together with its Principle of Operation.

C. R. Vidal and J. Cooper⁷⁶ in 1969 developed the heat pipe oven out of the heat pipe by uniting two heat pipes at their evaporation zones and confining the vapor by inert gas boundaries, thus creating a device which is ideally suited for spectroscopic or similar investigations. The design of the smaller one of the two heat pipe ovens used for the present study is shown in detail with its principle of operation in Fig. 18. It consists of 4" diameter stainless steel tubes with a wall thickness of 1/16". The wick is made of 4-5 layers of a 80-mesh stainless steel screen attached to the inside wall by spring-loaded stainless steel clamps and extends out to the cooled regions. Two (large oven: four) half-circle clam-shell radiation heaters of the type Lindberg 506-KSP-5" which consume 1050 W each, serve as heating elements for the small oven. Six windings of 1/4" copper tubings fastened to the pipes near their ends by epoxy blended with aluminum powder for better heat conductivity serve as cooling coils when flushed with water. Several layers of heavy asbestos cloth are wrapped around the hot parts of the heat pipe ovens and covered with aluminum foil for effective heat insulation.

The first step in oven operation is to load them with solid sodium. Approximately 150 gr (300 gr for the large tube) are needed to run the devices in a heat pipe mode, i.e., in a mode where the pressure inside the tube is determined by the vapor pressure of sodium according to its vapor pressure curve. The pipes are then filled with an inert gas, in the present case with argon, at a suitable pressure. Turning on the heaters will melt the sodium down and

wet the wick when its temperature exceeds 371°K . If there is enough liquid in the wick remaining to saturate the vapor, the sodium pressure will be given by the vapor pressure curve. When the sodium pressure reaches or exceeds the argon pressure the vapor diffuses to the cool end zones where it condenses again and is pulled back to the heated region by the capillary action of the stainless steel mesh. When an equilibrium is finally reached, the center portion of the oven is filled with sodium vapor at a pressure determined by the controlled temperature of the heating elements while the end zones contain only the buffer gas at a pressure equal to the vapor pressure. This is an important feature of the heat pipe oven since it makes it possible to measure the pressure of the sodium vapor directly and the cool inert gas buffers remove the window problem completely which, especially for highly reactive gases like sodium at high temperatures, has been a serious problem for spectroscopic investigations. Therefore, for the interferometric measurements high quality quartz windows can be used which show much better optical properties in respect to flatness and parallelism than e.g. sapphire flats.

The continuous evaporation and condensation of the vapor helps purify the sodium after some operation time and it keeps the buffer gas completely separated from the vapor except for a condensation interface whose thickness depends on the operating pressure. At this interface the temperature drops rapidly to the temperature of the cooled argon whereas the center portion of the heat pipe oven like the heat pipe operates under extremely uniform conditions.

4.4.2 Performance Characteristics

Sodium is a highly reactive material and forms sodium hydroxide on its surface immediately upon exposure with air. Extreme caution is therefore required when handling sodium to avoid excessive contamination. The loading of the solid sodium blocks into the heat pipe oven is done through a window opening while argon is flowing from the other end into the tube, thus reducing the contact of sodium with air and the later outgasing from the sodium. Nevertheless, after new sodium has been placed in the pipe it takes several days to weeks of continuously evacuating the systems with two pumps of the type Welch Duo-Seal Model 1405 to remove any constituents which contaminated the sodium during storage and during the short transfer from its container into the heat pipe. Heating the sodium up to just above the melting point while evacuating at the same time accelerates the outgasing process. The leakage and outgasing rate of the two separate heat pipe oven systems (heat pipe oven plus connecting vacuum lines plus vacuum gauges) is believed to be sufficiently small enough when it does not exceed $6 \cdot 10^{-3}$ mm Hg per hour and the evacuating process is stopped when this value is reached. To keep the leakage rate of the systems at this low level, all interconnecting vacuum lines consist of soft soldered copper tubing. Together with the O-rings and rubber connection pieces they are checked and cleaned on a routine basis and replaced if necessary. Each heat pipe oven has its separate pressure measurement system. It consists of a McLeod gauge, which is used for

high precision measurements and calibration of a Wallace and Tiernan absolute pressure gauge and of a thermocouple vacuum gauge (CVC type GTC-004). The latter is mainly used to check the system for leakage or outgasing, whereas the Wallace and Tiernan gauge is needed to measure pressures between 5 and 25 Torr. The accuracy of pressure measurement in the pressure regime from 0 to 5 Torr (McLeod gauge) and in the regime between 5 and 25 Torr (Wallace and Tiernan) is better than 1 percent.

A need for a highly reliable and accurate temperature control of the heaters became evident during preliminary experiments with non-resonant interference fringe shift studies in the regime between 750⁰K and 850⁰K, where a few degrees temperature change corresponds to an appreciable change in vapor pressure, and corresponding fringe shift. The installation of a heater control unit with feedback on-off switches makes it now possible to preset and control separately any desired temperature in the heat pipe ovens to a fraction of a degree Celsius. The thermocouple temperature measurements needed for the heater control unit and to provide redundancy for the pressure measurements by relying on the vapor pressure-temperature relation turned out to be less straight forward than expected. The use of chromel-alumel thermocouples generated difficulties because the alumel wire did not survive the high temperature environment (which evidently included oxidation) when in contact with the sauerisen cement, used for bonding. The replacement of the chromel-alumel thermocouples by platinel thermocouples (Engelhard Industries, Platinel #1503 vs Platinel #1813)

which are attached to the outer walls at various locations along the heat pipe ovens solved this problem. In both tubes the measured temperatures of the thermocouples which are located in the center at the bottom of the ovens are found to be within 5°K of the temperature determined by the vapor pressure of the sodium.

4.5 The Fringe Shift Recording Device

The light from the dye laser, after being divided in the interferometer into two beams, each of which passes through a heat pipe oven, and after being reunited at the exit beamsplitter, will form the familiar interference fringes when the interferometer is properly adjusted. A lens of 35 mm focal length serves as field lens to display the image of the location of the apparent intersection of the interfering beams on a screen. In order to make the geometrical dimensions as small as possible, this intersection point is chosen to be in between the mirror M2 and the exit beamsplitter BS2. A plate with a 0.5 mm pinhole which is mounted in front of a cooled photomultiplier tube of the type RCS C31000F serves as a screen. This tube combines high gain ($> 0.4 \cdot 10^6$) with a fast response time (≤ 2.5 nsec) and a relatively low dark current. This dark current which is strongly temperature dependent is reduced by placing the PMT in a refrigerated temperature-controlled chamber (Product for Research Model TE-104TS). Cooling the tube down to -30°C will decrease the dark current by a factor of 10, which means the signal to noise ratio of the PMT is increased by the same factor. This arrangement is

necessary to measure fringe shifts when the laser is tuned close to the sodium D-lines where strong absorption of the light beam takes place. The output of the PMT is then recorded with a x-y plotter (Hewlett Packard x-y recorder 7004B), monitoring the intensity changes in a typical periodic fashion as the fringes march across the pinhole. This method allows fringes to be counted over an extended period of time without any difficulties and with an accuracy of up to 1/10 of a fringe provided the fringe visibility is sufficient.

CHAPTER V

The Experimental Techniques

5.1 Preliminary Experiments

In the preceeding chapter the performance characteristics of the individual components of the resonant refractivity apparatus were described. Before the actual calibration experiments can take place, the behavior of these components as a system have to be investigated and optimized.

5.1.1 Operational Pressure Limits

The heat pipe ovens are first tested together with the interferometer using a mercury vapor lamp for non-resonant fringe shift studies. This preliminary experience led to the previously described installation of the heater control unit (Section 4.4.2), the enclosure of the light beam in the interferometer (Section 4.3), and the design of the fringe shift recording apparatus (Section 4.5).

Furthermore, these early studies helped determine the vapor pressure range for sodium in the heat pipe ovens for the actual resonant refractivity experiments. When the ovens are operating at pressures between 5 and 15 Torr, according to vapor temperatures of 790°K and 850°K , respectively, unsteady oscillations in the vapor occured. This phenomenon has evidently not been explained today, certainly

not in papers on heat pipe ovens. Fortunately, these oscillations disappear when the vapor pressure is lowered to less than 5 Torr. At these pressures the amount of the sodium dimer Na_2 is so small, that its influence on the refraction and absorption of the sodium monomer can be neglected. (See Appendix B for more details on this subject.) With five Torr being the upper pressure limit, the lower limit is more or less determined by the leakage/outgassing rates of the systems. A rough sample calculation will illustrate this point. Assuming a leakage rate of 10^{-2} Torr/hr (Sec. 4.4) and a duration of the experiment of the 1-2 hours shows that the vapor pressure has to be larger than 1 Torr in order to keep the error caused by the leakage/outgassing process as small as 1 percent. According to these criteria a pressure range is chosen for the resonant refractivity experiments which lies between 1.5 Torr and 3 Torr or, when expressed in temperatures, between 730°K and 760°K ; the latter, in turn, are equivalent to number densities of sodium atoms ranging from $2.0 \times 10^{22} \text{ m}^{-3}$ to $3.6 \times 10^{22} \text{ m}^{-3}$.

5.1.2 Fringe Contrast with the Dye Laser

After the initial test runs with a non-resonant light source, the dye laser is tuned to the high frequency (blue) wing of the sodium D_2 -line and directed through the interferometer and the heat pipe ovens. Both have been filled initially with argon at the same pressure (~ 1 Torr) and the sodium has been heated up so that its vapor pressure has reached approximately 2 Torr. With the dye laser tuned sufficiently far away from the resonant line (about 20 \AA), the

fringes are clearly visible and any change of the conditions in one of the heat pipe ovens results in a corresponding fringe shift. However, when the dye laser is tuned close to the D_2 -line, the fringes diminish slowly and at one point disappear completely. The reasons found for this phenomenon are two-fold, both have to do with substantial differences in length of the sodium columns in the two arms of the interferometer and with the resonant behavior of the sodium vapor itself. The first reason is quite obvious and is due to the mismatch in intensity of the interfering sodium lightbeams according to Beer's Law, (Eq. 2.12) the intensity absorbed by the sodium vapor is proportional to its column length and absorption coefficient at that specific wavelength. Since close to line center this absorption coefficient is relatively large (e.g., for conditions of the present study the absorption coefficient μ_r for sodium vapor 20 \AA away from the D_2 -line ($\lambda = 5870 \text{ \AA}$) are of the order of $1 - 2\text{m}^{-1}$). Substantially different long sodium columns result in a large difference in intensity of the two light beams coming out of the heat pipe ovens. The ratio of these intensities -- taking the above coefficients and assuming a 1 m difference in length between the two sodium columns -- amounts to 15 to 30 percent.

Secondly, one major criterion to obtain interference fringes states that the optical path difference between the two interfering must not exceed the coherence length ℓ_c of the light source. The coherence length can be physically interpreted as the length of an uninterrupted wave train and is related to the spectral width or band-

width $\Delta\lambda$ of the light source by $l_c = \lambda^2 / \Delta\lambda$. The spectral width of the dye laser at 5890 Å has been measured to be $\Delta\lambda = 0.24$ Å (Table IV), thus the coherence length can be determined as $l_c = 1.5$ cm. One would not expect such a short coherence length from a laser but this is typical for pulsed dye lasers without special narrow-band selectors.

It is quite obvious that in the resonant regime the refractive index becomes so large that the difference in optical path, which is defined as the product of the geometrical length l and the refractive index n in the medium, for a substantial difference in length of sodium column becomes of the order of the coherence length of the light source. That feature, together with the mismatch in intensities of the two beams is responsible for the disappearance of the fringes when the laser is slowly tuned closer to resonance.

The problem is solved by adjusting separately the initial argon pressures in both heat pipes in such a way that when the desired sodium vapor pressure is reached, a higher initial pressure of the buffer gas in the longer heat pipe oven shortens the effective length of the sodium vapor column, with the result that the two sodium columns have roughly the same length.

5.2 The Resonant Refractivity Experiment

After it has been ascertained that the dye laser is properly aligned and calibrated and that the leakage/outgassing rates in the two heat pipes do not exceed the prescribed values, the ovens are filled with argon at pressures P_{Ar} which are determined using the following formula

$$P_{Ar} = (T_1/T_2)_{Ar} \cdot P_{Na} (1 - \ell_{Na} \cdot A/V) \quad (5.1)$$

where T_1 and T_2 are the initial and final temperatures of the buffer gas (it was found that since T_2 is only slightly higher than the ambient temperature T_1 the ratio is very close to unity and can be neglected), P_{Na} and ℓ_{Na} specify the desired final pressure and length of the sodium column, respectively, and have to be chosen to be equal for both heat pipe ovens; while A and V describe the cross area and total system volume of the respective heat pipe oven. This equation is a result of basic volume considerations assuming the perfect gas law for both gases and an infinitely thin interface between the sodium and the buffer gas. It ensures that during the fringe shift measurements the two sodium columns are roughly matched in terms of pressure and length.

The heater control units are now switched on to their preset temperatures. It takes 12 to 15 hours until the ovens separately reach their final stable heat pipe mode which is characterized by constant pressure readings over an extended period of time (1 hour or longer). From this time on the temperatures and pressures in both heat pipe ovens are constantly monitored and their values recorded in 10 minute intervals. The dye laser, tuned to a wavelength close to the D_2 -line, is turned on and its output after passing through the interferometer recorded through the pinhole with a PMT as described in Section 4.5. Only when it is ensured that the system is absolutely stable, meaning that no fringe shifts, drifts or wobbling of the fringes occur, is the experiment initiated, by raising or lowering the temperature settings at the heater control unit for the small heat pipe oven. This causes

the vapor pressure in the small oven to change according to the vapor pressure-temperature relation and the length of the sodium column to adapt to the new equilibrium conditions, whereas the conditions in the long oven stay constant over the whole duration of the experiment. The amount of temperature change is limited to a few degrees (10^0 - 15^0 K) by the range of fringe visibility and sensitivity of the recording apparatus. Too large a temperature difference causes the conditions to change too rapidly, so that it is impossible to resolve the fringeshifts in the presence of the individual pulses of the dye laser. A typical output plot of consecutive traces of recorded fringe shifts is shown in Fig. 19, where a shift of 95 fringes is caused by a raise in temperature from 739.3^0 K to 750.9^0 K (pressure raise from 1.82 Torr to 2.36 Torr) with the laser tuned to 5870.7 \AA . During the experiments, which last normally 1 hour or longer, the sensitivity together with the damping of the individual laser pulses and the speed of the tracking is adjusted accordingly at the x-y plotter. The recording of the fringe shifts is stopped when no fringe movements can be observed and the pressure has stabilized. When the final conditions are reached, the laser is tuned to a different wavelength and the experiment is repeated, this time with an opposite temperature change, thus moving always around the according to Eq. 5.1 predetermined optimal condition, characterized by the same vapor density and same length of sodium column in both heat pipe ovens. At the end of each experimental session, consisting of 3 to 4 resonant refractivity measurements at different wavelengths, the heaters are switched off and the

heat pipes evacuated, to be ready again for the next set of measurements.

5.3 Resonant Absorption Measurements

Before and after every fringe shift measurement, when the conditions in the heat pipe ovens are constant, the collimated light beam of a 500 W quartz lamp is directed into the heat pipes by means of a mirror which is swivel-mounted in front of the dye laser. The absorptions of this white light by the two sodium columns, approximately 50 cm long, is measured separately with the McPherson scanning monochromator whose output is recorded with a PMT on the x-y plotter. Typical absorption spectra for different conditions start at the D_2 -line and extend over 40 \AA to the low wavelength (blue) side of the line. It is possible with the experimental configuration described, to measure the absorption to within 9 \AA of line center, beyond which no light can be detected. On the other hand, the absorption due to the presence of molecular sodium whose number densities for the conditions of the present study range from 2 to 3 percent of the number densities of atomic sodium plays a rather unimportant role out to 30 \AA from line center. This verifies the assumptions about the influence of the sodium dimer mentioned in Section 5.1.1. It is of evident importance to establish more information on the absorption of sodium atoms. Studies of this sort are in progress and are conducted by Irv Benard, a member of the Aerophysics group at Stanford University.

CHAPTER VI

EXPERIMENTAL RESULTS AND DISCUSSION6.1 Range of Measurements

The experimental results were determined from 15 sets of fringe shift measurements at different wavelengths in the temperature range of sodium vapor between 730°K and 750°K, corresponding to pressures and number densities between 1.50 Torr and 2.30 Torr, or $2.0 \times 10^{22} \text{ m}^{-3}$ and $3.0 \times 10^{22} \text{ m}^{-3}$, respectively. The dye laser was tuned in a wavelength range starting at 5862.8 Å and approaching the D₂-line at about 1.3 Å intervals from the high frequency side. The closest proximity to line center at which fringe measurements could be made was at 5881.3 Å or 8.6 Å away from the resonance wavelength. In the present configuration, the loss of contrast due to large differential absorption together with large difference in optical path length, as well as the increased absorptivity close to line center, all combined to preclude fringe shift measurements closer to the resonance frequency. A revised arrangement -- both heat pipe ovens having the same length -- would permit measurements nearer to resonance. This modification was not feasible in the present program but it is being made in connection with future work.

6.2 Data Reduction

The fringe shift equation relating a change in optical path length in the test section to a corresponding shift of fringes S can

be written in the following form

$$S = \frac{1}{\lambda_0} \int_0^L [n_1(z) - n_2(z)] dz \quad (6.1)$$

or with Eq. 2.2

$$S = \frac{K(\lambda_0)}{\lambda_0} \int_0^L [\rho_1(z) - \rho_2(z)] dz \quad (6.2)$$

where L denotes the length of the heat pipe oven and z the direction the light is traversing the test section. The subscripts "1" and "2" refer to the conditions before and after the temperature has changed.

In these expressions the influence of the buffer gas is neglected since its refractive index is, even in the non-resonant case, two orders of magnitude smaller than that of sodium vapor. (See Table I for a comparison of the static polarizabilities of the alkali-metal atoms and the inert buffer gases.) Under the assumptions of an infinitely thin interface between argon and sodium vapor and of constant temperature and density along the z -axis in the vapor, the integral in Eq. 6.2 can be evaluated and the Dale-Gladstone constant $K(\lambda_0)$ can be expressed as

$$K(\lambda_0) = \frac{S \cdot \lambda_0}{\rho_1 \ell_1 - \rho_2 \ell_2} \quad (6.3)$$

where ℓ_1 and ℓ_2 describe the initial and final lengths of the sodium column, respectively. These lengths can be determined for any known set of conditions by solving Eq. 5.1 for ℓ_{Na} :

$$\ell_{Na} = \frac{V}{A} \left[1 - \frac{P_{Ar in}}{P_{Na}} \left(\frac{T_2}{T_1} \right)_{Ar} \right] \quad (6.4)$$

Note again, that this expression also is obtained by assuming a sharp and plane argon-sodium boundary. However, as Vidal and Cooper⁷⁵ pointed out, this transition region is neither infinitely thin nor is it a plane. Especially at low pressures (lower than 10 Torr) this interface can be rather thick and will, in particular in the case of a large heat pipe oven, be more extensive at the center than at the walls. Since this special aspect of the heat pipe oven has not been investigated in detail (early attempts to measure the center temperature profile by thermocouple traverse met with difficulties), it was necessary to use Eqs. 6.3 and 6.4 to determine the Dale-Gladstone value from a given set of conditions. However, it should be kept in mind that these expressions serve only as first approximations to the effective length of the vapor zone which can be defined as $\int_0^L \rho(z) dz$, and that the evaluations for the Dale-Gladstone values according to these equations are likely to yield smaller values than analytically predicted. In Table V these two values are listed and compared to each other for each of the 15 wavelengths. In the following section it will be shown that the factor of about 2 which exists between these experimental and theoretical values cannot be explained by inaccuracies in the measurements or any systematic error, and that it is rather a fixed error due to overestimating the effective length of the sodium column by assuming a rectangular density profile along the axis of the heat pipe oven. Furthermore, it will be explained why a triangular shaped density distribution seems to be more appropriate for the present case.

The Dale-Gladstone constants obtained using this assumption, $(K_{\text{exp}})_{\text{triang}}$, are represented by the last column of Table V.

6.3 Estimation of Experimental Uncertainty

The procedure for calculating the uncertainty in the results consists of two steps. In the first step the uncertainty (error) in each variable is estimated. The second step calculates the uncertainty in the result due to the uncertainty in each of the variables. If there are intermediate results, step 2 has to be repeated to obtain the final results.

To determine from the recorded number of fringe shifts the Dale-Gladstone values according to Eqs. 6.3 and 6.4, one measures the initial pressure of argon, P_{Ar} , and the respective vapor pressures of sodium, P_1 and P_2 . From the latter information, the temperatures of the sodium vapor, $T_{1\text{Na}}$ and $T_{2\text{Na}}$, are evaluated using Eq. B.3. The partial pressures of the sodium monomer P_{Na_1} are then computed according to Eq. 3.30 and combined with the temperatures to yield the mass densities assuming the perfect gas law applies. The error limits (uncertainty intervals) for the measured data are estimated to be:

$$T_{1\text{Ar}} = \pm 1^\circ\text{K}; \quad T_{2\text{Ar}} = \pm 10^\circ\text{K}; \quad P_{\text{Ar}}, P_1, P_2 = \pm 0.02 \text{ Torr};$$

$$S = \begin{cases} \pm 2\% & (\text{away from resonance}) \\ \pm 10\% & (\text{close to resonance}) \end{cases}$$

The other parameters of Eqs. 6.3 and 6.4, such as the operating wavelength or the total volume of the system, have relative uncertainties which are much smaller than the ones listed above and can be neglected.

TABLE V

Comparison of Experimentally Determined Dale-Gladstone Constants of Sodium Vapor with Theoretical Values Assuming Different Density Profiles along the Axis of the Heat Pipe Oven

Wavelength Angstroms	$(K_{\text{exp}})_{\text{rect.}}$ m^3/kg	K_{theory} m^3/kg	$\frac{K_{\text{theory}}}{(K_{\text{exp}})_{\text{rect.}}}$	$(K_{\text{exp}})_{\text{triang}}$ m^3/kg
5862.8	0.209	0.408	1.95	0.418
5864.1	0.195	0.427	2.19	0.390
5865.4	0.208	0.449	2.16	0.416
5866.8	0.221	0.474	2.15	0.442
5868.1	0.230	0.501	2.18	0.460
5869.4	0.245	0.531	2.17	0.490
5870.7	0.263	0.564	2.15	0.526
5872.1	0.305	0.606	1.99	0.610
5873.4	0.323	0.650	2.01	0.646
5876.0	0.395	0.761	1.93	0.790
5877.4	0.439	0.839	1.91	0.878
5878.1	0.453	0.884	1.95	0.906
5878.7	0.496	0.927	1.87	0.992
5880.0	0.450	1.037	2.30	0.900
5881.4	0.541	1.177	2.17	1.082

Stone, et al.,⁸⁷ claim accuracies of ± 0.37 percent for their vapor pressure relation. A similar average deviation from measured values is reported by Nesmeyanov⁶⁶ for his equation of the monomer pressure of sodium vapor.

The effect of the uncertainty in each variable on the uncertainty of the result is found according to standard uncertainty analysis using the equation⁷⁷

$$\frac{W_{R_i}}{R} = \frac{\partial(\ln R)}{\partial(\ln V_i)} \cdot \frac{W_i}{V_i} \quad (6.5)$$

where the result is denoted by R , the variable by V_i , the uncertainty interval of the variable as W_i , and the uncertainty interval in the result due to W_i alone as W_{R_i} . If there is more than one variable affecting the result, say n independent variables, then it is a valid approximation⁷⁶ to add the square of the quantities given by Eq. 6.5 and to take the square root of the entire sum:

$$\frac{W_R}{R} = \left\{ \left[\frac{\partial(\ln R)}{\partial(\ln V_1)} \left(\frac{W_1}{V_1} \right) \right]^2 + \left[\frac{\partial(\ln R)}{\partial(\ln V_2)} \left(\frac{W_2}{V_2} \right) \right]^2 + \dots \left[\frac{\partial(\ln R)}{\partial(\ln V_n)} \left(\frac{W_n}{V_n} \right) \right]^2 \right\}^{1/2} \quad (6.6)$$

By application of the above expressions to the Eqs. B.3, 3.30, 6.3, 6.4, and the perfect gas law it is now possible to calculate the uncertainties

in the results. For the intermediate results these are as follows:

$$\left(\frac{\Delta T}{T}\right)_{\text{Na}} = 2.0\%; \quad \frac{\Delta \rho}{\rho} = 2.2\%; \quad \left(\frac{\Delta \ell}{\ell}\right)_{\text{Na}} = 3.6\%$$

The final uncertainties for the Dale-Gladstone values are determined by combining the above uncertainties according to Eq. 6.6, and are

$$\Delta S/S = 6.3\% \text{ (away from resonance)}$$

$$\Delta S/S = 12.5\% \text{ (close to resonance)}$$

These figures compare well with the deviations from the average ratio of the theoretical and experimental Dale-Gladstone values. The uncertainties for wavelengths close to resonance are more or less determined by the large error limits in counting fringe shifts. This is due to the diminishing contrast or poor visibility of the fringes when approaching line-center in the present configuration. As mentioned before, it is believed that these large, but uniform discrepancies between theory and experiment are caused by misjudging the temperature/density profile along the axis of the heat pipe oven (z-axis). In the derivation of Eqs. 6.4 and 6.3 this profile was assumed to be rectangular which apparently results in roughly too long an effective length of sodium vapor by about a factor of two. If one approximates the density profile by a triangle, the effective sodium column would be half as long as in the previous assumption (see Table V, last column). This assumption, requires two diffusion layers between the vapor and the confining inert buffer gas which have to be 20 to 25 cm thick. In these interfaces the argon mixes with the sodium and the temperature changes from 320°K to

around 740°K, which is even quite remarkable for a transition region of that size. By comparison, in their paper,⁷⁵ Vidal and Cooper describe a 10 to 12cm thick boundary layer in a heat pipe oven operating with lithium and using helium as the confining gas at a pressure of 10.9 Torr. It seems, that for pressures significantly lower than 10 Torr transition region thicknesses 20 to 25 cm long are entirely possible and can be assumed for the present configuration. In that case the analytically obtained Dale-Gladstone values reflect the true data.

6.4 Results and Discussion

6.4.1 Experimental Results

As reasoned in the preceeding section, it is permissible to use the theoretical Dale-Gladstone constants to show the real resonant refractive behavior of sodium; and to scale the experimental values determined according to Eqs. 6.3 and 6.4 by the average ratio $[K_{\text{theory}}/K_{\text{exp}}]_{\text{av}} = 2.07$ to match the theory. This has been done in Fig. 20. Note that the plot is semi-log, but the numbers represent actual values. The negative signs simply mean that on the high frequency side the anomalous dispersion curve, $n-1$, becomes negative -- a feature which is not important in this analysis. The right hand ordinate shows the ratio of the resonant values to the non-resonant value of sodium ($[K_0]_{\text{Na}} = 4.05 \times 10^{-3} \text{ m}^3/\text{kg}$). It indicates that the maximum obtainable enhancement at 5881.4 Å is roughly 300 times when compared to the zero-frequency value of Na. Even more important is the comparison with the non-resonant value of air ($[K_0]_{\text{Air}} = 2.3 \times 10^{-4} \text{ m}^3/\text{kg}$). As indicated in

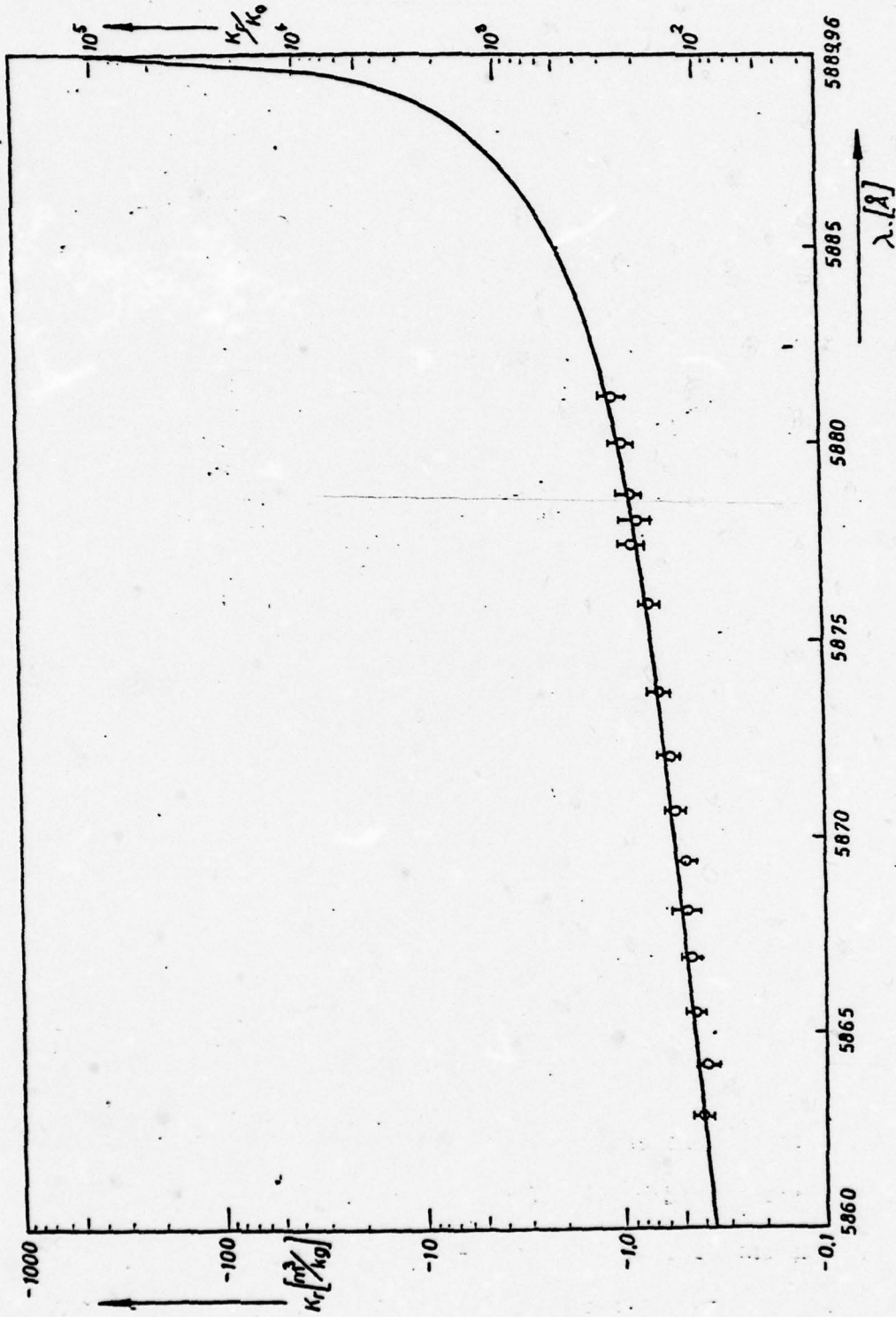


Fig. 20. Comparison between Experimental and Theoretical Values (dark line). The Negative Ordinate Numbers Relate to the High-Frequency Line Wing where $n < 1$.

Table VI these enhancement factors reach values up to 4500 at $\lambda = 5880 \text{ \AA}$! To illustrate the impact of the enhanced sensitivity for flow applications, an expression will be derived next which relates in a very concise form various experimental parameters to the maximum number of obtainable fringe shifts for a given disturbance.

6.4.2 Comparison of Resonant versus Non-Resonant Sensitivities for Flow Visualization Methods

From the experimental results discussed in the previous sections it can be seen that the operating wavelength range lies in the wings of the resonant line, for which the theory (Eq. 3.21) shows that the enhanced refractivity $(n_r - 1)$ varies inversely with frequency difference $(\omega_r - \omega)$ and can be well approximated by

$$n_r(\omega) - 1 \simeq \frac{1}{4} C \frac{c}{\omega_r} N_{Na} \frac{1}{\omega_r - \omega} \quad (6.7)$$

while the absorption coefficient $\mu_r(\omega)$ varies inversely with $(\omega_r - \omega)^2$ (Eq. 3.22) and can be written as

$$\mu_r(\omega) \simeq \frac{1}{4} C \gamma_L N_{Na} \frac{1}{(\omega_r - \omega)^2} \quad (6.8)$$

with

$$C = \frac{e^2 \cdot f_{Lu}}{c \cdot m \cdot \epsilon_0} = 6.95 \times 10^{-6} \text{ m}^2 \text{ s}^{-1}$$

These approximations make it possible to express the refractive index by the absorption coefficient or vice versa. By combining the above expressions with the two other governing equations of the experiment, namely the fringe shift equation in its simplest form

TABLE VI

RESONANT VS. NONRESONANT REFRACTIVITY

Values of Ratios of Gladstone-Dale Constant, Sodium and Air

NONRESONANT VALUES:

$$K_{o\text{Air}} = 2.3 \times 10^{-4} \text{ m}^3/\text{kg}$$

$$K_{o\text{Na}} = 4.05 \times 10^{-3} \text{ m}^3/\text{kg}$$

RESONANT VALUES:

λ [Å]	5870	5875	5880
$K_{r\text{Na}}$ [m ³ /kg]	0.546	0.698	1.0360
$K_{r\text{Na}}/K_{o\text{Na}}$	134.8	172.4	256
$K_{r\text{Na}}/K_{o\text{Air}}$	2374	3034	4504

NOTE: The Gladstone-Dale constant is the specific refractivity defined by $K = \frac{n-1}{\rho}$

$$S \cdot \lambda_0 = \Delta n \cdot L, \quad (6.9)$$

and Beer's Law (Eq. 2.12) one arrives at the following formula for the maximum obtainable interference fringe shifts S_{\max} in terms of fractional change in vapor density:

$$S_{\max} = \frac{1}{4\pi} \sqrt{C} \sqrt{\frac{L \cdot \ln(I_0/I_L)}{\gamma_L}} \cdot \left(\frac{\Delta \rho}{\rho} \right)_{\text{Na}} \quad (6.10)$$

where $\ln(I_0/I_L)$ describes the sensitivity of the recording apparatus in accordance with Beer's Law, $I_L/I_0 = e^{-\mu L}$, and

L = effective length of the absorbing medium

This relation is valid for both, selfbroadening as well as heterogeneous broadening in a buffer gas. In order to differentiate between these two cases one has to replace the lorentzian linewidth γ_L by the appropriate expression obtained from Eq. 3.28 to get

$$S_{\max} = \frac{1}{4\pi} \sqrt{C} \sqrt{\frac{L \cdot \ln(I_0/I_L)}{(C_r)_{\text{Na-Na}}}} \cdot \left(\frac{\Delta \rho}{\rho} \right)_{\text{Na}} \quad (6.10a)$$

for selfbroadening and

$$S_{\max} = \frac{1}{4\pi} \sqrt{C} \sqrt{\frac{L \cdot \ln(I_0/I_L) \cdot X}{(C_r)_{\text{Na-Ar}}}} \cdot \left(\frac{\Delta \rho}{\rho} \right)_{\text{Na}} \quad (6.10b)$$

for heterogenous broadening,

where $X = N_a/N_b$ describes the mole fraction or seeding ratio of sodium atoms in the buffer gas (see also Sec. 3.3.2), and $(C_r)_{\text{Na-Na}}$ and $(C_r)_{\text{Na-Ar}}$ denote, respectively, the collision parameters for self-

broadening and for heterogeneous broadening with argon (Table III). Fortunately, the latter is roughly 25 times smaller than the self-broadening parameter and therefore compensates partly for the seeding ratio X which is of the order of 10^{-3} for typical flow situations.

The above expressions represent limiting cases where the maximum number of obtainable fringe shifts S_{\max} for a given relative density change is found to be proportional to the square root of L . It means that if one changes the absorbing length L under these limiting conditions for a fixed sensitivity of the apparatus I_L/I_0 , one has to change the frequency accordingly to keep the product $\mu(\omega)L$ constant and to obtain the same number of fringe shifts S_{\max} . In this context, the above expressions for S_{\max} should be conceived as a guideline for the experimentalist, which does not violate the basic length and density relationships. They are not intended to give exact results since the effect of the other doublet partner of the sodium D-lines is not included. For the "near region" between 10 and 20 Å⁰ away from the D_2 -line the contribution of the D_1 -line amounts to about 30 percent of the overall refractivity and 5 percent to the total absorption coefficient.

A similar expression as Eq. 6.10b can be derived for schlieren photography. The governing equation of a schlieren system for a small angular deflection ϵ by a density gradient, say dp/dx , can be written as

$$\epsilon = L \cdot \frac{dn}{dx} \quad (6.11)$$

By comparing the above expression with the governing equation for fringe

shift measurements (Eq. 6.9) one will arrive at the following equation which expresses the maximum resonant angular deflection ϵ_{\max} in terms of the density gradient $d\rho/dx$:

$$\epsilon_{\max} = \frac{1}{4\pi} \sqrt{C} \cdot \lambda_0 \sqrt{\frac{2n(I_0/I_L) \cdot L \cdot X}{(C_r)_{\text{Na-Ar}}}} \cdot \frac{1}{\rho_{\text{Air}}} \left(\frac{d\rho}{dx} \right)_{\text{Air}} \quad (6.12)$$

In order to estimate the enhancement in sensitivity for resonant fringe shift measurements or resonant schlieren photography in fluid flow application as compared to the non-resonant techniques in air, one can introduce a refractivity enhancement factor (REF). This parameter is defined as the ratio of the maximum obtainable number of resonant fringe shifts S_{\max} or the maximum resonant angular deflection ϵ_{\max} for a given disturbance (Eqs. 6.10b and 6.12) to the corresponding non-resonant values S_{nr} and ϵ_{nr} in air (Eqs. 6.9 and 6.11):

$$\text{REF} \equiv \frac{S_{\max}}{S_{\text{nr}}} = \frac{\epsilon_{\max}}{\epsilon_{\text{nr}}} = \frac{1}{4\pi} \frac{\lambda_0}{K_{0,\text{Air}} \rho_{\text{Air}}} \sqrt{C} \sqrt{\frac{2n(I_0/I_L) \cdot X}{L \cdot (C_r)_{\text{Na-Ar}}}} \quad (6.13)$$

Substituting the appropriate values for the parameters C (Eq. 6.8), λ_0 , $K_{0,\text{Air}}$, and $(C_r)_{\text{Na-Ar}}$ (Table III), the refractivity enhancement factor becomes

$$\text{REF} = 7.96 \cdot \frac{1}{\rho_{\text{Air}}} \sqrt{\frac{2n(I_0/I_L) \cdot X}{L}} \quad (6.13b)$$

and depends now only on the density of air and on experimental parameters like the seeding ratio X , the recording sensitivity ratio I_0/I_L , and

the path length L . The latter is very often predetermined by the size of existing windtunnels and test sections and is normally of the order of a few centimeters up to one meter. In the present configuration the recording sensitivity I_0/I_L which determines the closest proximity to line center at which fringe shift measurements can be made, was found to be 10^3 . This ratio is likely to be improvable, e.g., by matching of the two heat pipe ovens and by using a narrow band selector like a Fabry Perot etalon in the dye laser cavity. These modifications should boost the above ratio I_0/I_L by at least two orders of magnitude to 10^5 . However, due to the very weak dependence of REF on this ratio ($REF \sim \sqrt{\ln I_0/I_L}$) even an improvement in recording sensitivity of that size can hardly increase the resonant enhancement.

It is believed that the seeding ratio X of sodium in a windtunnel flow may not exceed 10^{-3} due to the high reactivity of sodium.

Under these conditions and under atmospheric density the resonance enhancement does not exceed a factor of two or three. However, for densities less than atmospheric the resonant refractivity becomes more favorable and significant enhancements in sensitivity can be achieved, since they are according to Eq. 6.13b inversely proportional to the mass density of air. To illustrate this point the following numerical examples are presented. The first deals with fringe shift measurements in a supersonic flow whereas the second sample calculation describes the difference between resonant and non-resonant flow measurements by means of schlieren photography of audible sound waves at 10 percent atmospheric density.

(i) Fringe Shift Measurements in a Supersonic Flow

Suppose it were desired to study phenomena like boundary layers, vortices of expansion fans in a supersonic air flow at $M = 2.0$. At this Mach number the density ratio ρ/ρ_0 is equal to 0.23 where ρ_0 is the stagnation density taken as atmospheric for the present. For small changes in density ($\Delta\rho = d\rho$), $d\rho$ can be written in terms of changes in Mach number dM as

$$d\rho = \rho_0 \left(1 + \frac{\gamma-1}{2} M^2\right)^{-\gamma/(\gamma-1)} M \cdot dM \quad (6.14)$$

and for the flow conditions assumed here, this expression can be evaluated as

$$\frac{d\rho}{\rho} = 1.11 \times dM \quad (6.15)$$

The resonant fringe shift equation (Eq. 6.10b) can then be written using the following values: $L = 0.10$ m, $I_0/I_L = 10^3$ and $X = 10^{-3}$ as

$$S_{\max} = 92 \times dM \quad (6.16)$$

If 0.1 fringe shift is assumed to be the detection limit, then the smallest change in Mach number dM , detectable would be

$$dM_r = 1.09 \times 10^{-3} \quad (6.17)$$

By comparison, the conventional set-up with the same geometrical dimension and the same flow conditions is only able to resolve changes in the Mach Number dM as small as

$$dM_{nr} = 1.78 \times 10^{-2} \quad (6.18)$$

which is about 20 times larger than the minimum detectable Mach number change with a resonant light source.

Hence, it will be possible to resolve, with the resonant fringe shift measurement technique, many more details of the supersonic flow than was previously possible.

(ii) Schlieren Photography of Audible Sound Waves

Assuming that the sound wave of interest in the present sample calculation generalized at 10 percent atmospheric density is around 10kHz and that the schlieren system when suitably adjusted is capable of detecting 10^{-6} radians, the weakest-amplitude sound wave detectable by a resonant and non-resonant light source can be computed.

The sound overpressure P of a sound wave may be assumed to have a sinusoidal distribution in x ,

$$P = P_0 \sin kx \quad (6.19)$$

where k is the wave number, $2\pi/\lambda$. The density gradient may now be written

$$d\rho/dx = (d\rho/dP)_{ad} (dP/dx) = \frac{k}{a^2} P_0 \cos kx \quad (6.20)$$

where the subscript "ad" stands for adiabatic, that derivative thus being equal to the reciprocal of a^2 , the sound speed squared. The gradient's maximum value will be

$$(d\rho/dx)_{\max} = \frac{k P_0}{a^2} = \frac{2\pi P_0 \cdot v}{a^3} \quad (6.21)$$

combining the above relation with Eqs. 6.11 and 6.12, substituting for

the following values: $L = 0.10$ m, $I_0/I_L = 10^3$, $x = 10^{-3}$,
 $\rho_{\text{Air}} = 0.1 \cdot \rho_0 = 0.1293$ kg m $^{-3}$ and solving for P_0 , the following expressions
 are obtained for the non-resonant and resonant case, respectively:

$$P_{0_{nr}} = 4.35 \times 10^4 \frac{\epsilon \cdot a^3}{2\pi v} \quad (6.22a)$$

$$P_{0_r} = 2.7 \times 10^3 \frac{\epsilon \cdot a^3}{2\pi \cdot v} \quad (6.23a)$$

Choosing $a = 340$ m/sec the above equations can be evaluated as

$$P_{0_{nr}} = 27.2 \text{ Nm}^{-2} \quad (6.22b)$$

and

$$P_{0_r} = 1.69 \text{ Nm}^{-2} \quad (6.23b)$$

In terms of the usual decibel notation for sound pressure levels

$$(\text{Sound pressure level})_{\text{non-resonant}} = 20 \log \frac{P_{0_{nr}}}{2 \times 10^{-5}} = 122.7 \text{ dB} \quad (6.22c)$$

where 2×10^{-5} N/m 2 is the standard reference value. This is a very loud sound, comparable to the noise made by a jet engine at fairly close distance. On the contrary, the minimum sound pressure level detectable with a resonant schlieren system can be evaluated as

$$(\text{sound pressure level})_{\text{resonant}} = 98 \text{ dB} \quad (6.23c)$$

which constitutes a significant improvement to a conventional schlieren system and corresponds to the noise made by a motorcycle with a poor muffler at about 25 ft distance.

CHAPTER VII

SUMMARY AND OUTLOOK

In this experimental study the resonant enhancement of refractivity has been confirmed and measured in the near region of the sodium D-lines. The refractive index was determined interferometrically in the wavelength range 5862.8 \AA to 5881.3 \AA by use of a tunable dye laser serving as a light source for a Mach-Zehnder instrument. The experimental results were found to be in good agreement with analytically predicted values within the experimental uncertainties. Absorption considerations have limited the closest proximity to line center to which the operating wavelength can be tuned and have determined the ultimate maximum enhancement factor obtainable in pure sodium to be 4500 compared to the non-resonant specific refractivity of air. It has been shown that use of the resonant refractive index of sodium vapor can be a very powerful technique to increase the sensitivities of flow visualization methods.

The experimental work has been supplemented by the application of optical dispersion and absorption theory. Special attention has been paid to the shape of the resonance lines under conditions of doppler and lorentzian broadening mechanisms. The line broadening parameters of the alkali metal resonances in the case of selfbroadening and in the presence of an inert buffer gas have been investigated. In this context, it has been found that the relatively smaller collision line-

width for heterogeneous broadening makes it possible to approach nearer to the resonance line and to utilize a larger specific index of refraction than in the case of selfbroadening. This feature will lower the required seeding ratio still more when sodium atoms are injected in small quantities into the flow. Sample calculations for these conditions have shown that resonant refractivity techniques will prove useful for flow visualization methods, such as interferometry of schlieren, over the full range of pressures and temperatures with the low pressure regime being a particularly favorable one.

Appreciable development work remains to make this technique suitable for wind-tunnel applications. First, the enhanced refractivity associated with heterogeneous broadening should be experimentally verified. Secondly, schlieren photographs of a disturbance using a non-resonant and resonant light source will give direct indication of the increased sensitivity of the resonant method. Last, but not least, existing techniques of sodium vapor injection into a carrier gas flow have to be assessed, probably modified, and a working model for windtunnel application has to be built. At that stage, resonant refractivity techniques will be used to study and to reveal fluid flow phenomena which were precluded from previous flow visualization methods.

APPENDIX A

COMPUTER PROGRAM AND TABLE OF THE $W(Z)$ -FUNCTION

We present here a computer program for the evaluation of the $W(z)$ -function of Eq. 3.15 that was first written by P. Langhoff in FORTRAN for the CDC 6600 computer. It is based on the generating procedure developed by D. G. Hummer⁷¹ and was then modified by the present author for use with the IBM 370 computer and to include the approximations for large x (Eqs. 3.21 and 3.22). Table VII gives the real and imaginary part of the $W(z)$ -function, $z = x + ia$, with the dimensionless frequency x (Eq. 3.12) varying between 0 and 30 in increments of 1 and for 20 values of the Voigt parameter a (Eq. 3.12) between 0.05 and 1.00. Figure 21 can be used to convert these Voigt parameters into temperatures T , pressures P and number densities N of sodium vapor for the case of selfbroadening.


```

DIMENSION A(20),X(51),CE(20,51)
COMPLEX CE
DO 20 IA=1,20
  A(IA)=0.05*IA
  AA=A(IA)
  X(1)=0.
  DO 10 II=2,51
    X(II)=X(II-1)+1.
10 CONTINUE
  DO 15 IX=1,51
    CALL WW(X(IX),AA,WR,WI)
    CE(IA,IX)=CMPLX(WR,WI)
15 CONTINUE
20 CONTINUE
  N1=1
  N2=5
25 PRINT 50,(A(IB),IB=N1,N2)
50 FORMAT (1H1////,21X,4(3HA=,F5.2,16X),3HA=,F5.2/)
  PRINT 51
51 FORMAT (9X,1HX,5(5X,8HRE(W(Z)),3X,8HIM(W(Z))) /)
  DO 21 J=1,51
    PRINT 52,(X(J),CE(IC,J),IC=N1,N2)
52 FORMAT (6X,F5.1,1X,5(E12.4,E11.4,1X))
21 CONTINUE
  N1=N1+5
  N2=N2+5
  IF (N2.LT.22) GOTO 25
  STOP
END

```

```

SUBROUTINE WAPROX (XX,AA,WR,WI)
C  COMPUTES W(Z) FOR  $A=XX+I*AA$  WHERE EITHER  $XX.GT.3.9$  OR  $AA.GT.3.$ 
C  LINE 40 GIVES ACCURACY TO  $.LT. 2.E-6$  (ABSOLUTE)
C  LINE 50 GIVES ACCURACY TO  $.LT. 1.E-6$  (ABSOLUTE)
C  REF IS ABRAMOWITZ AND STEGUN
COMPLEX Z,Z2,ZI,WZ
COMPLEX CMPLX
WI=0.
WR=0.
IF (XX.LE.3.9 .AND. AA.LE.3.) GO TO 70
Z= CMPLX(XX,AA)
Z2=Z*Z
ZI= CMPLX(-AA,XX)
IF (XX.GT.6. .OR. AA.GT.6.) GO TO 50
40 WZ=ZI*(0.4613135/(Z2-0.1901635)+0.09999216/(Z2-1.7844927)
1 +0.002883894/(Z2-5.5253437))
GO TO 60
50 WZ=ZI*(0.5124246/(Z2-0.2752551)+0.05176536/(Z2-2.724745))
60 WR=REAL(WZ)
WI=AIMAG(WZ)
70 RETURN
END

```

C SUBROUTINE WW (XX, AA, WR, WI)
 C SUBROUTINE WW COMPUTES $W(Z) = W(XX + I*AA) = WR + I*WI$.
 C THE UNNORMALIZED VOIGT FUNCTION.

```

COMMON /SAXZ/ CX2, SX2
REAL IMX, IMA
DIMENSION C(31)
COMPLEX Z, CN, BN
COMPLEX CMPLX
COMPLEX CCOS
COMPLEX CEXP
DATA ICVK/0/
IF(ICVK.EQ.0) GO TO 20000
20001 CONTINUE
A=ABS(AA)
X=ABS(XX)
IF(A.EQ.0.) GO TO 40
IF (A.LT.1.E-12.OR. A.GT.1.E7) PRINT 11000, XX, AA
11000 FORMAT(' WARNING, IN WW XX, AA=', 2E15.6)
IF (X.EQ.0.) GO TO 11001
IF (X.LT.1.E-7.OR. X.GT.1.E7) PRINT 11000, XX, AA
11001 CONTINUE
A1=3.*A
A2=A*A
A15=1.5*A
AX2=2.*A*X
CX2=COS(AX2)
SX2=SIN(AX2)
IF (X.GT.30.) GOTO 42
IF (X.GT.3.9.OR. A.GT.3.) GO TO 41
IF(A.LT.0.1) GO TO 10
CONST=9.42477796026938
REA=-CONST*A
IMX=CONST*X
BN= CMPLX(REA, IMX)
Z=CEXP(BN)
WR=0.
WI=0.
GO TO 15
10 CONST=9.42477796026938
REX=CONST*X
IMA=CONST*A
CN= CMPLX(REX, IMA)
Z=CCOS(CN)
DIFF=A2-X*X
EX2=EXP(DIFF)
WR=EX2*CX2
WI=-EX2*SX2
15 CONTINUE
BR=REAL(Z)
BRR=1.-BR
BR=2.*BR
B1=BRR*A15
B2=-AIMAG(Z)
S=-8.-1.5*X
T=S*S+2.25*A2
  
```



```

DO 30 N=1,31
T=T+S+.25
S=S+.5
B1=A1-B1
B2=-B2
BRB=BRB+BR
BR=-BR
IF (T.GT.2.5E-12) GO TO 20
WR=WR-C(N)*A*29.60881320326
WI=WI-C(N)*S*19.739208802179
GO TO 30
20 WR=WR+C(N)*(B1+B2*S)/T
WI=WI+C(N)*(A15*B2-S*BRB)/T
30 CONTINUE
IF (IX.LT.0.) WI=-WI
35 RETURN
40 CONTINUE
SX2=0.
IF (X.GT.3.9) GO TO 41
WR=EXP(-X*X)
EX2=WR
BR=COS(9.42477796076938*X)
WI=-EX2*SX2
BRB=1.-BR
BR=2.-BR
S=-8.-1.5*X
T=S*S
DO 31 N=1,31
T=T+S+.25
S=S+.5
CX2=1.
BRB=BRB+BR
BR=-BR
IF (T.GT.2.5E-12) GO TO 21
WI=WI-C(N)*S*BRB/T
GO TO 31
21 WI=WI-C(N)*S*BRB/T
31 CONTINUE
IF (XI.LT.0.) WI=-WI
RETURN
41 CONTINUE
CALL WAPROX(X,A,WR,WI)
IF (XX.LT.0.) WI=-WI
RETURN
42 CONTINUE

```

C
C
C
C

APPROXIMATIONS OF $w(z)$ FOR LARGE x

```

WI=1./ (SQRT(3.1416)*IX)
WR=AA/ (SQRT(3.1416)*(IX**2))
RETURN
20000 CONTINUE
ICVK=1
TP=1./ (2.*3.1415926535898)
K=-16
DO 50 N=1,31
K=K+1
50 C(N)=EXP(-FLOAT(K*K)/9.)*TP
GO TO 20001
END

```

TABLE VII. Real and Imaginary Parts of the $W(t)$ Function

t	$\lambda = 0.05$		$\lambda = 0.10$		$\lambda = 0.15$		$\lambda = 0.20$		$\lambda = 0.25$	
	$Re(W(t))$	$Im(W(t))$	$Re(W(t))$	$Im(W(t))$	$Re(W(t))$	$Im(W(t))$	$Re(W(t))$	$Im(W(t))$	$Re(W(t))$	$Im(W(t))$
0.0	0.9458-00	0.1016E-06	0.8963E+00	0.6248E-07	0.8511E+00	0.1075E-07	0.8090E+00	0.3653E-07	0.7703E+00	0.2977E-07
1.0	0.3712E+00	0.5217E+00	0.3721E+00	0.5388E+00	0.3730E+00	0.5577E+00	0.3732E+00	0.4790E+00	0.3717E+00	0.4522E+00
2.0	0.2957E-01	0.3316E+00	0.4020E-01	0.3316E+00	0.5018E-01	0.3076E+00	0.5953E-01	0.3213E+00	0.6826E-01	0.3157E+00
3.0	0.4044E-02	0.2010E+00	0.7943E-02	0.2007E+00	0.1181E-01	0.2003E+00	0.1563E-01	0.1907E+00	0.1939E-01	0.1902E+00
4.0	0.1962E-02	0.1459E+00	0.3921E-02	0.1450E+00	0.5076E-02	0.1457E+00	0.7823E-02	0.1455E+00	0.9751E-02	0.1453E+00
5.0	0.1204E-02	0.1152E+00	0.2407E-02	0.1151E+00	0.3608E-02	0.1151E+00	0.4807E-02	0.1150E+00	0.6002E-02	0.1149E+00
6.0	0.8107E-03	0.9539E-01	0.1637E-02	0.9533E-01	0.2455E-02	0.9533E-01	0.3271E-02	0.9520E-01	0.4086E-02	0.9522E-01
7.0	0.5942E-03	0.8140E-01	0.1188E-02	0.8142E-01	0.1782E-02	0.8142E-01	0.2375E-02	0.8138E-01	0.2967E-02	0.8134E-01
8.0	0.4515E-03	0.7109E-01	0.9029E-03	0.7108E-01	0.1354E-02	0.7106E-01	0.1805E-02	0.7104E-01	0.2255E-02	0.7102E-01
9.0	0.3549E-03	0.6308E-01	0.7098E-03	0.6307E-01	0.1064E-02	0.6306E-01	0.1419E-02	0.6305E-01	0.1145E-02	0.6303E-01
10.0	0.2848E-03	0.5670E-01	0.5728E-03	0.5670E-01	0.8591E-03	0.5669E-01	0.1145E-02	0.5668E-01	0.1431E-02	0.5667E-01
11.0	0.2361E-03	0.5150E-01	0.4721E-03	0.5150E-01	0.7081E-03	0.5149E-01	0.9440E-03	0.5149E-01	0.9094E-03	0.5148E-01
12.0	0.1980E-03	0.4710E-01	0.3959E-03	0.4710E-01	0.5938E-03	0.4717E-01	0.7017E-03	0.4717E-01	0.6418E-03	0.4716E-01
13.0	0.1684E-03	0.4353E-01	0.3368E-03	0.4353E-01	0.5052E-03	0.4352E-01	0.6735E-03	0.4352E-01	0.5406E-03	0.4351E-01
14.0	0.1450E-03	0.4040E-01	0.2901E-03	0.4040E-01	0.4351E-03	0.4040E-01	0.6406E-03	0.4040E-01	0.4720E-03	0.4040E-01
15.0	0.1262E-03	0.3770E-01	0.2524E-03	0.3770E-01	0.3786E-03	0.3769E-01	0.6048E-03	0.3769E-01	0.4177E-03	0.3769E-01
16.0	0.1108E-03	0.3533E-01	0.2217E-03	0.3533E-01	0.3325E-03	0.3533E-01	0.5648E-03	0.3533E-01	0.3720E-03	0.3533E-01
17.0	0.9812E-04	0.3325E-01	0.1962E-03	0.3324E-01	0.2933E-03	0.3324E-01	0.5248E-03	0.3324E-01	0.3344E-03	0.3324E-01
18.0	0.8747E-04	0.3139E-01	0.1749E-03	0.3139E-01	0.2624E-03	0.3139E-01	0.4908E-03	0.3139E-01	0.3032E-03	0.3139E-01
19.0	0.7847E-04	0.2974E-01	0.1569E-03	0.2973E-01	0.2354E-03	0.2973E-01	0.4598E-03	0.2973E-01	0.2732E-03	0.2973E-01
20.0	0.7079E-04	0.2824E-01	0.1416E-03	0.2824E-01	0.2124E-03	0.2824E-01	0.4311E-03	0.2824E-01	0.2567E-03	0.2824E-01
21.0	0.6419E-04	0.2690E-01	0.1284E-03	0.2690E-01	0.1925E-03	0.2690E-01	0.4062E-03	0.2690E-01	0.2420E-03	0.2690E-01
22.0	0.5847E-04	0.2567E-01	0.1169E-03	0.2567E-01	0.1754E-03	0.2567E-01	0.3838E-03	0.2567E-01	0.2281E-03	0.2567E-01
23.0	0.5348E-04	0.2455E-01	0.1070E-03	0.2455E-01	0.1604E-03	0.2455E-01	0.3644E-03	0.2455E-01	0.2149E-03	0.2455E-01
24.0	0.4910E-04	0.2353E-01	0.9820E-04	0.2353E-01	0.1473E-03	0.2353E-01	0.3484E-03	0.2353E-01	0.2045E-03	0.2353E-01
25.0	0.4524E-04	0.2259E-01	0.9049E-04	0.2259E-01	0.1357E-03	0.2259E-01	0.3358E-03	0.2259E-01	0.1962E-03	0.2259E-01
26.0	0.4182E-04	0.2172E-01	0.8364E-04	0.2172E-01	0.1255E-03	0.2172E-01	0.3258E-03	0.2172E-01	0.1891E-03	0.2172E-01
27.0	0.3879E-04	0.2091E-01	0.7755E-04	0.2091E-01	0.1163E-03	0.2091E-01	0.3182E-03	0.2091E-01	0.1832E-03	0.2091E-01
28.0	0.3605E-04	0.2016E-01	0.7210E-04	0.2016E-01	0.1081E-03	0.2016E-01	0.3122E-03	0.2016E-01	0.1782E-03	0.2016E-01
29.0	0.3360E-04	0.1947E-01	0.6720E-04	0.1947E-01	0.1008E-03	0.1947E-01	0.3072E-03	0.1947E-01	0.1740E-03	0.1947E-01
30.0	0.3146E-04	0.1882E-01	0.6279E-04	0.1882E-01	0.9419E-04	0.1882E-01	0.3032E-03	0.1882E-01	0.1702E-03	0.1882E-01
31.0	0.2958E-04	0.1820E-01	0.5871E-04	0.1820E-01	0.8806E-04	0.1820E-01	0.3002E-03	0.1820E-01	0.1668E-03	0.1820E-01
32.0	0.2795E-04	0.1763E-01	0.5510E-04	0.1763E-01	0.8264E-04	0.1763E-01	0.3002E-03	0.1763E-01	0.1638E-03	0.1763E-01
33.0	0.2590E-04	0.1710E-01	0.5181E-04	0.1710E-01	0.7771E-04	0.1710E-01	0.3032E-03	0.1710E-01	0.1612E-03	0.1710E-01
34.0	0.2440E-04	0.1659E-01	0.4881E-04	0.1659E-01	0.7321E-04	0.1659E-01	0.3072E-03	0.1659E-01	0.1592E-03	0.1659E-01
35.0	0.2203E-04	0.1612E-01	0.4606E-04	0.1612E-01	0.6908E-04	0.1612E-01	0.3122E-03	0.1612E-01	0.1572E-03	0.1612E-01
36.0	0.2177E-04	0.1567E-01	0.4353E-04	0.1567E-01	0.6530E-04	0.1567E-01	0.3172E-03	0.1567E-01	0.1552E-03	0.1567E-01
37.0	0.2061E-04	0.1525E-01	0.4121E-04	0.1525E-01	0.6192E-04	0.1525E-01	0.3222E-03	0.1525E-01	0.1532E-03	0.1525E-01
38.0	0.1954E-04	0.1485E-01	0.3907E-04	0.1485E-01	0.5841E-04	0.1485E-01	0.3272E-03	0.1485E-01	0.1512E-03	0.1485E-01
39.0	0.1855E-04	0.1447E-01	0.3709E-04	0.1447E-01	0.5548E-04	0.1447E-01	0.3322E-03	0.1447E-01	0.1492E-03	0.1447E-01
40.0	0.1763E-04	0.1410E-01	0.3526E-04	0.1410E-01	0.5289E-04	0.1410E-01	0.3372E-03	0.1410E-01	0.1472E-03	0.1410E-01
41.0	0.1678E-04	0.1376E-01	0.3356E-04	0.1376E-01	0.5034E-04	0.1376E-01	0.3422E-03	0.1376E-01	0.1452E-03	0.1376E-01
42.0	0.1599E-04	0.1343E-01	0.3190E-04	0.1343E-01	0.4798E-04	0.1343E-01	0.3472E-03	0.1343E-01	0.1432E-03	0.1343E-01
43.0	0.1526E-04	0.1312E-01	0.3051E-04	0.1312E-01	0.4577E-04	0.1312E-01	0.3522E-03	0.1312E-01	0.1412E-03	0.1312E-01
44.0	0.1457E-04	0.1282E-01	0.2914E-04	0.1282E-01	0.4371E-04	0.1282E-01	0.3572E-03	0.1282E-01	0.1392E-03	0.1282E-01
45.0	0.1393E-04	0.1254E-01	0.2786E-04	0.1254E-01	0.4179E-04	0.1254E-01	0.3622E-03	0.1254E-01	0.1372E-03	0.1254E-01
46.0	0.1333E-04	0.1226E-01	0.2666E-04	0.1226E-01	0.3999E-04	0.1226E-01	0.3672E-03	0.1226E-01	0.1352E-03	0.1226E-01
47.0	0.1277E-04	0.1200E-01	0.2554E-04	0.1200E-01	0.3831E-04	0.1200E-01	0.3722E-03	0.1200E-01	0.1332E-03	0.1200E-01
48.0	0.1224E-04	0.1175E-01	0.2449E-04	0.1175E-01	0.3673E-04	0.1175E-01	0.3772E-03	0.1175E-01	0.1312E-03	0.1175E-01
49.0	0.1175E-04	0.1151E-01	0.2350E-04	0.1151E-01	0.3525E-04	0.1151E-01	0.3822E-03	0.1151E-01	0.1292E-03	0.1151E-01
50.0	0.1128E-04	0.1128E-01	0.2257E-04	0.1128E-01	0.3385E-04	0.1128E-01	0.3872E-03	0.1128E-01	0.1272E-03	0.1128E-01

TABLE VII (continued)

	A = 0.30			A = 0.40			A = 0.45			A = 0.50		
X	BE(W(2))	IN(W(2))	RE(W(2))	BE(W(2))	IN(W(2))	RE(W(2))	BE(W(2))	IN(W(2))	RE(W(2))	BE(W(2))	IN(W(2))	RE(W(2))
0.0	0.73465-00	0.2317E-07	0.7015E-00	0.3097E-08	0.6708E-00	0.4856E-07	0.6423E-00	0.3282E-07	0.6157E-00	0.4249E-07	0.3591E-00	0.3429E-00
1.0	0.3694E-00	0.4272E-00	0.3652E-00	0.4039E-00	0.3630E-00	0.3822E-00	0.3591E-00	0.3619E-00	0.3549E-00	0.3429E-00	0.3349E-00	0.3282E-00
2.0	0.7640E-01	0.3098E-00	0.8395E-01	0.3038E-00	0.9094E-01	0.2972E-00	0.9741E-01	0.2912E-00	0.1034E-00	0.2848E-00	0.1034E-00	0.2848E-00
3.0	0.2309E-01	0.1980E-00	0.2673E-01	0.1969E-00	0.3028E-01	0.1957E-00	0.3375E-01	0.1944E-00	0.1711E-01	0.1930E-03	0.1711E-01	0.1930E-03
4.0	0.1169E-01	0.1450E-00	0.1360E-01	0.1446E-00	0.1542E-01	0.1422E-00	0.1727E-01	0.1438E-00	0.1922E-01	0.1433E-00	0.1922E-01	0.1433E-00
5.0	0.7194E-02	0.1140E-00	0.8380E-02	0.1146E-00	0.9560E-02	0.1142E-00	0.1071E-01	0.1142E-00	0.1190E-01	0.1140E-00	0.1190E-01	0.1140E-00
6.0	0.4899E-02	0.914E-01	0.5710E-02	0.9505E-01	0.6518E-02	0.9494E-01	0.7323E-02	0.9482E-01	0.8125E-02	0.9469E-01	0.8125E-02	0.9469E-01
7.0	0.3555E-02	0.8129E-01	0.4149E-02	0.8213E-01	0.4738E-02	0.8117E-01	0.5325E-02	0.8109E-01	0.5913E-02	0.8101E-01	0.5913E-02	0.8101E-01
8.0	0.2705E-02	0.7098E-01	0.3154E-02	0.7095E-01	0.3603E-02	0.7090E-01	0.4050E-02	0.7092E-01	0.4497E-02	0.7080E-01	0.4497E-02	0.7080E-01
9.0	0.2127E-02	0.6301E-01	0.2481E-02	0.6298E-01	0.2034E-02	0.6295E-01	0.3186E-02	0.6292E-01	0.3538E-02	0.6288E-01	0.3538E-02	0.6288E-01
10.0	0.1717E-02	0.5665E-01	0.2003E-02	0.5663E-01	0.2288E-02	0.5661E-01	0.2573E-02	0.5659E-01	0.2857E-02	0.5656E-01	0.2857E-02	0.5656E-01
11.0	0.1415E-02	0.5147E-01	0.1651E-02	0.5145E-01	0.1886E-02	0.5144E-01	0.2121E-02	0.5142E-01	0.2356E-02	0.5140E-01	0.2356E-02	0.5140E-01
12.0	0.1187E-02	0.4715E-01	0.1385E-02	0.4714E-01	0.1502E-02	0.4713E-01	0.1779E-02	0.4711E-01	0.1976E-02	0.4710E-01	0.1976E-02	0.4710E-01
13.0	0.1010E-02	0.4351E-01	0.1178E-02	0.4350E-01	0.1346E-02	0.4349E-01	0.1518E-02	0.4348E-01	0.1682E-02	0.4346E-01	0.1682E-02	0.4346E-01
14.0	0.8698E-03	0.4038E-01	0.1015E-02	0.4038E-01	0.1159E-02	0.4037E-01	0.1304E-02	0.4036E-01	0.1449E-02	0.4035E-01	0.1449E-02	0.4035E-01
15.0	0.7570E-03	0.3768E-01	0.8831E-03	0.3768E-01	0.1009E-02	0.3767E-01	0.1135E-02	0.3766E-01	0.1261E-02	0.3765E-01	0.1261E-02	0.3765E-01
16.0	0.6649E-03	0.3532E-01	0.7755E-03	0.3531E-01	0.8842E-03	0.3531E-01	0.9968E-03	0.3530E-01	0.1107E-02	0.3530E-01	0.1107E-02	0.3530E-01
17.0	0.5885E-03	0.3323E-01	0.6866E-03	0.3323E-01	0.7845E-03	0.3323E-01	0.8825E-03	0.3323E-01	0.9804E-03	0.3322E-01	0.9804E-03	0.3322E-01
18.0	0.5247E-03	0.3138E-01	0.6121E-03	0.3138E-01	0.6994E-03	0.3138E-01	0.7866E-03	0.3137E-01	0.8740E-03	0.3137E-01	0.8740E-03	0.3137E-01
19.0	0.4707E-03	0.2973E-01	0.5491E-03	0.2973E-01	0.6255E-03	0.2972E-01	0.7058E-03	0.2972E-01	0.7841E-03	0.2971E-01	0.7841E-03	0.2971E-01
20.0	0.4246E-03	0.2824E-01	0.4954E-03	0.2824E-01	0.5661E-03	0.2823E-01	0.6368E-03	0.2823E-01	0.7075E-03	0.2822E-01	0.7075E-03	0.2822E-01
21.0	0.3850E-03	0.2689E-01	0.4492E-03	0.2689E-01	0.5131E-03	0.2689E-01	0.5774E-03	0.2688E-01	0.6415E-03	0.2688E-01	0.6415E-03	0.2688E-01
22.0	0.3507E-03	0.2567E-01	0.4092E-03	0.2567E-01	0.4676E-03	0.2566E-01	0.5260E-03	0.2566E-01	0.5844E-03	0.2566E-01	0.5844E-03	0.2566E-01
23.0	0.3208E-03	0.2455E-01	0.3743E-03	0.2455E-01	0.4277E-03	0.2455E-01	0.4811E-03	0.2454E-01	0.5385E-03	0.2454E-01	0.5385E-03	0.2454E-01
24.0	0.2946E-03	0.2352E-01	0.3436E-03	0.2352E-01	0.3927E-03	0.2352E-01	0.4418E-03	0.2352E-01	0.4908E-03	0.2352E-01	0.4908E-03	0.2352E-01
25.0	0.2714E-03	0.2258E-01	0.3166E-03	0.2258E-01	0.3619E-03	0.2258E-01	0.4071E-03	0.2258E-01	0.4523E-03	0.2258E-01	0.4523E-03	0.2258E-01
26.0	0.2509E-03	0.2171E-01	0.2927E-03	0.2171E-01	0.3452E-03	0.2171E-01	0.3763E-03	0.2171E-01	0.4181E-03	0.2171E-01	0.4181E-03	0.2171E-01
27.0	0.2326E-03	0.2091E-01	0.2714E-03	0.2091E-01	0.3101E-03	0.2091E-01	0.3469E-03	0.2090E-01	0.3876E-03	0.2090E-01	0.3876E-03	0.2090E-01
28.0	0.2163E-03	0.2016E-01	0.2523E-03	0.2016E-01	0.2881E-03	0.2016E-01	0.3244E-03	0.2016E-01	0.3604E-03	0.2016E-01	0.3604E-03	0.2016E-01
29.0	0.2016E-03	0.1945E-01	0.2352E-03	0.1945E-01	0.2688E-03	0.1946E-01	0.3024E-03	0.1946E-01	0.3359E-03	0.1946E-01	0.3359E-03	0.1946E-01
30.0	0.1884E-03	0.1881E-01	0.2197E-03	0.1881E-01	0.2511E-03	0.1881E-01	0.2825E-03	0.1881E-01	0.3139E-03	0.1881E-01	0.3139E-03	0.1881E-01
31.0	0.1761E-03	0.1820E-01	0.2055E-03	0.1820E-01	0.2340E-03	0.1820E-01	0.2642E-03	0.1820E-01	0.2935E-03	0.1820E-01	0.2935E-03	0.1820E-01
32.0	0.1653E-03	0.1763E-01	0.1928E-03	0.1763E-01	0.2204E-03	0.1763E-01	0.2479E-03	0.1763E-01	0.2755E-03	0.1763E-01	0.2755E-03	0.1763E-01
33.0	0.1554E-03	0.1710E-01	0.1813E-03	0.1710E-01	0.2072E-03	0.1710E-01	0.2331E-03	0.1710E-01	0.2590E-03	0.1710E-01	0.2590E-03	0.1710E-01
34.0	0.1464E-03	0.1659E-01	0.1708E-03	0.1659E-01	0.1952E-03	0.1659E-01	0.2196E-03	0.1659E-01	0.2440E-03	0.1659E-01	0.2440E-03	0.1659E-01
35.0	0.1382E-03	0.1612E-01	0.1612E-03	0.1612E-01	0.1842E-03	0.1612E-01	0.2071E-03	0.1612E-01	0.2303E-03	0.1612E-01	0.2303E-03	0.1612E-01
36.0	0.1306E-03	0.1567E-01	0.1524E-03	0.1567E-01	0.1741E-03	0.1567E-01	0.1959E-03	0.1567E-01	0.2177E-03	0.1567E-01	0.2177E-03	0.1567E-01
37.0	0.1236E-03	0.1525E-01	0.1442E-03	0.1525E-01	0.1646E-03	0.1525E-01	0.1855E-03	0.1525E-01	0.2061E-03	0.1525E-01	0.2061E-03	0.1525E-01
38.0	0.1172E-03	0.1485E-01	0.1367E-03	0.1485E-01	0.1563E-03	0.1485E-01	0.1758E-03	0.1485E-01	0.1954E-03	0.1485E-01	0.1954E-03	0.1485E-01
39.0	0.1113E-03	0.1447E-01	0.1298E-03	0.1447E-01	0.1494E-03	0.1447E-01	0.1699E-03	0.1447E-01	0.1853E-03	0.1447E-01	0.1853E-03	0.1447E-01
40.0	0.1058E-03	0.1410E-01	0.1234E-03	0.1410E-01	0.1430E-03	0.1410E-01	0.1657E-03	0.1410E-01	0.1783E-03	0.1410E-01	0.1783E-03	0.1410E-01
41.0	0.1007E-03	0.1376E-01	0.1175E-03	0.1376E-01	0.1373E-03	0.1376E-01	0.1613E-03	0.1376E-01	0.1708E-03	0.1376E-01	0.1708E-03	0.1376E-01
42.0	0.9595E-04	0.1343E-01	0.1119E-03	0.1343E-01	0.1279E-03	0.1343E-01	0.1569E-03	0.1343E-01	0.1699E-03	0.1343E-01	0.1699E-03	0.1343E-01
43.0	0.9154E-04	0.1312E-01	0.1068E-03	0.1312E-01	0.1221E-03	0.1312E-01	0.1533E-03	0.1312E-01	0.1652E-03	0.1312E-01	0.1652E-03	0.1312E-01
44.0	0.8743E-04	0.1282E-01	0.1020E-03	0.1282E-01	0.1166E-03	0.1282E-01	0.1511E-03	0.1282E-01	0.1637E-03	0.1282E-01	0.1637E-03	0.1282E-01
45.0	0.8358E-04	0.1254E-01	0.9751E-04	0.1254E-01	0.1114E-03	0.1254E-01	0.1494E-03	0.1254E-01	0.1632E-03	0.1254E-01	0.1632E-03	0.1254E-01
46.0	0.7999E-04	0.1226E-01	0.9332E-04	0.1226E-01	0.1067E-03	0.1226E-01	0.1472E-03	0.1226E-01	0.1628E-03	0.1226E-01	0.1628E-03	0.1226E-01
47.0	0.7662E-04	0.1200E-01	0.8939E-04	0.1200E-01	0.1022E-03	0.1200E-01	0.1458E-03	0.1200E-01	0.1624E-03	0.1200E-01	0.1624E-03	0.1200E-01
48.0	0.7346E-04	0.1175E-01	0.8571E-04	0.1175E-01	0.9795E-04	0.1175E-01	0.1444E-03	0.1175E-01	0.1620E-03	0.1175E-01	0.1620E-03	0.1175E-01
49.0	0.7049E-04	0.1151E-01	0.8224E-04	0.1151E-01	0.9399E-04	0.1151E-01	0.1430E-03	0.1151E-01	0.1616E-03	0.1151E-01	0.1616E-03	0.1151E-01
50.0	0.6770E-04	0.1128E-01	0.7899E-04	0.1128E-01	0.9027E-04	0.1128E-01	0.1416E-03	0.1128E-01	0.1612E-03	0.1128E-01	0.1612E-03	0.1128E-01

THIS PAGE IS BEST QUALITY PRACTICABLE
FROM COPY FURNISHED TO DDC

TABLE VII (continued)

[illegible]

THIS PAGE IS BEST QUALITY FRAGMENT

TABLE VII (continued)

X	A = 0.85				A = 0.90				A = 0.95				A = 1.00			
	RE(W(2))	IM(W(2))	RE(W(2))	IM(W(2))	RE(W(2))	IM(W(2))	RE(W(2))	IM(W(2))	RE(W(2))	IM(W(2))	RE(W(2))	IM(W(2))	RE(W(2))	IM(W(2))	RE(W(2))	IM(W(2))
0.0	0.4691E+00	-0.1033E-06	0.4723E+00	-0.6014E-07	0.4565E+00	-0.9506E-07	0.4416E+00	-0.4667E-07	0.4276E+00	-0.9675E-07	0.4047E+00	-0.2082E+00	0.3847E+00	-0.2082E+00	0.3647E+00	-0.2082E+00
1.0	0.3254E+00	0.2520E+00	0.3203E+00	0.2400E+00	0.3151E+00	0.2280E+00	0.3099E+00	0.2182E+00	0.3047E+00	0.2082E+00	0.2995E+00	0.2082E+00	0.2943E+00	0.2082E+00	0.2891E+00	0.2082E+00
2.0	0.1283E+00	0.2448E+00	0.1328E+00	0.2402E+00	0.1356E+00	0.2341E+00	0.1381E+00	0.2281E+00	0.1402E+00	0.2222E+00	0.1422E+00	0.2161E+00	0.1442E+00	0.2101E+00	0.1461E+00	0.2041E+00
3.0	0.5531E-01	0.1824E+00	0.5797E-01	0.1803E+00	0.6053E-01	0.1782E+00	0.6298E-01	0.1761E+00	0.6522E-01	0.1739E+00	0.6767E-01	0.1718E+00	0.7002E-01	0.1697E+00	0.7237E-01	0.1676E+00
4.0	0.2983E-01	0.1392E+00	0.3149E-01	0.1385E+00	0.3312E-01	0.1376E+00	0.3472E-01	0.1368E+00	0.3628E-01	0.1358E+00	0.3783E-01	0.1348E+00	0.3938E-01	0.1338E+00	0.4093E-01	0.1328E+00
5.0	0.1870E-01	0.1120E+00	0.1900E-01	0.1116E+00	0.2008E-01	0.1112E+00	0.2088E-01	0.1108E+00	0.2158E-01	0.1104E+00	0.2238E-01	0.1100E+00	0.2318E-01	0.1096E+00	0.2398E-01	0.1092E+00
6.0	0.1205E-01	0.9338E-01	0.1262E-01	0.9338E-01	0.1338E-01	0.9338E-01	0.1408E-01	0.9338E-01	0.1478E-01	0.9338E-01	0.1548E-01	0.9338E-01	0.1618E-01	0.9338E-01	0.1688E-01	0.9338E-01
7.0	0.9377E-02	0.8034E-01	0.9945E-02	0.8034E-01	0.1051E-01	0.8005E-01	0.1107E-01	0.7990E-01	0.1163E-01	0.7973E-01	0.1219E-01	0.7956E-01	0.1275E-01	0.7939E-01	0.1331E-01	0.7922E-01
8.0	0.7193E-02	0.7036E-01	0.7585E-02	0.7036E-01	0.8020E-02	0.7016E-01	0.8453E-02	0.7008E-01	0.8884E-02	0.6995E-01	0.9368E-02	0.6982E-01	0.9841E-02	0.6966E-01	0.1031E-01	0.6951E-01
9.0	0.5632E-02	0.6257E-01	0.5978E-02	0.6251E-01	0.6322E-02	0.6244E-01	0.6666E-02	0.6236E-01	0.7008E-02	0.6229E-01	0.7383E-02	0.6222E-01	0.7758E-02	0.6215E-01	0.8133E-02	0.6208E-01
10.0	0.4553E-02	0.5634E-01	0.4833E-02	0.5629E-01	0.5113E-02	0.5624E-01	0.5392E-02	0.5619E-01	0.5670E-02	0.5613E-01	0.5948E-02	0.5608E-01	0.6223E-02	0.5603E-01	0.6503E-02	0.5598E-01
11.0	0.3757E-02	0.5123E-01	0.3989E-02	0.5113E-01	0.4220E-02	0.5115E-01	0.4451E-02	0.5112E-01	0.4682E-02	0.5107E-01	0.4913E-02	0.5098E-01	0.5144E-02	0.5093E-01	0.5374E-02	0.5088E-01
12.0	0.3153E-02	0.4637E-01	0.3388E-02	0.4634E-01	0.3543E-02	0.4631E-01	0.3708E-02	0.4628E-01	0.3873E-02	0.4625E-01	0.4038E-02	0.4622E-01	0.4203E-02	0.4619E-01	0.4368E-02	0.4616E-01
13.0	0.2684E-02	0.4336E-01	0.2851E-02	0.4334E-01	0.3017E-02	0.4332E-01	0.3183E-02	0.4329E-01	0.3348E-02	0.4326E-01	0.3513E-02	0.4323E-01	0.3678E-02	0.4320E-01	0.3843E-02	0.4317E-01
14.0	0.2313E-02	0.4037E-01	0.2456E-02	0.4035E-01	0.2600E-02	0.4032E-01	0.2743E-02	0.4029E-01	0.2886E-02	0.4026E-01	0.3029E-02	0.4023E-01	0.3172E-02	0.4020E-01	0.3315E-02	0.4017E-01
15.0	0.2014E-02	0.3759E-01	0.2139E-02	0.3757E-01	0.2264E-02	0.3756E-01	0.2388E-02	0.3754E-01	0.2513E-02	0.3751E-01	0.2638E-02	0.3748E-01	0.2763E-02	0.3745E-01	0.2888E-02	0.3742E-01
16.0	0.1769E-02	0.3524E-01	0.1879E-02	0.3521E-01	0.1989E-02	0.3522E-01	0.2099E-02	0.3521E-01	0.2208E-02	0.3519E-01	0.2318E-02	0.3518E-01	0.2428E-02	0.3517E-01	0.2538E-02	0.3516E-01
17.0	0.1566E-02	0.3317E-01	0.1664E-02	0.3316E-01	0.1761E-02	0.3315E-01	0.1858E-02	0.3314E-01	0.1956E-02	0.3313E-01	0.2054E-02	0.3312E-01	0.2152E-02	0.3311E-01	0.2250E-02	0.3310E-01
18.0	0.1397E-02	0.3132E-01	0.1484E-02	0.3132E-01	0.1571E-02	0.3131E-01	0.1657E-02	0.3130E-01	0.1744E-02	0.3129E-01	0.1832E-02	0.3128E-01	0.1920E-02	0.3127E-01	0.2008E-02	0.3126E-01
19.0	0.1253E-02	0.2968E-01	0.1311E-02	0.2968E-01	0.1409E-02	0.2967E-01	0.1487E-02	0.2966E-01	0.1565E-02	0.2965E-01	0.1643E-02	0.2964E-01	0.1721E-02	0.2963E-01	0.1799E-02	0.2962E-01
20.0	0.1112E-02	0.2820E-01	0.1201E-02	0.2819E-01	0.1272E-02	0.2819E-01	0.1342E-02	0.2818E-01	0.1412E-02	0.2817E-01	0.1482E-02	0.2816E-01	0.1552E-02	0.2815E-01	0.1622E-02	0.2814E-01
21.0	0.1052E-02	0.2686E-01	0.1089E-02	0.2685E-01	0.1151E-02	0.2685E-01	0.1217E-02	0.2684E-01	0.1281E-02	0.2683E-01	0.1345E-02	0.2682E-01	0.1409E-02	0.2681E-01	0.1473E-02	0.2680E-01
22.0	0.9428E-03	0.2564E-01	0.9924E-03	0.2563E-01	0.1051E-02	0.2563E-01	0.1109E-02	0.2562E-01	0.1167E-02	0.2561E-01	0.1225E-02	0.2560E-01	0.1283E-02	0.2559E-01	0.1341E-02	0.2558E-01
23.0	0.8563E-03	0.2452E-01	0.9079E-03	0.2452E-01	0.9611E-03	0.2452E-01	0.1014E-02	0.2451E-01	0.1068E-02	0.2450E-01	0.1122E-02	0.2449E-01	0.1176E-02	0.2448E-01	0.1230E-02	0.2447E-01
24.0	0.7848E-03	0.2350E-01	0.8337E-03	0.2350E-01	0.8826E-03	0.2350E-01	0.9315E-03	0.2349E-01	0.9803E-03	0.2348E-01	0.1029E-02	0.2347E-01	0.1078E-02	0.2346E-01	0.1127E-02	0.2345E-01
25.0	0.7232E-03	0.2256E-01	0.7601E-03	0.2256E-01	0.8133E-03	0.2256E-01	0.8584E-03	0.2255E-01	0.9034E-03	0.2254E-01	0.9485E-03	0.2253E-01	0.9936E-03	0.2252E-01	0.1037E-02	0.2251E-01
26.0	0.6645E-03	0.2170E-01	0.7102E-03	0.2169E-01	0.7519E-03	0.2169E-01	0.7938E-03	0.2168E-01	0.8357E-03	0.2167E-01	0.8776E-03	0.2166E-01	0.9195E-03	0.2165E-01	0.9614E-03	0.2164E-01
27.0	0.6199E-03	0.2089E-01	0.6585E-03	0.2089E-01	0.6972E-03	0.2089E-01	0.7358E-03	0.2088E-01	0.7745E-03	0.2087E-01	0.8132E-03	0.2086E-01	0.8519E-03	0.2085E-01	0.8906E-03	0.2084E-01
28.0	0.5783E-03	0.2015E-01	0.6123E-03	0.2014E-01	0.6462E-03	0.2014E-01	0.6842E-03	0.2013E-01	0.7201E-03	0.2012E-01	0.7581E-03	0.2011E-01	0.7961E-03	0.2010E-01	0.8341E-03	0.2009E-01
29.0	0.5372E-03	0.1945E-01	0.5708E-03	0.1945E-01	0.6042E-03	0.1945E-01	0.6378E-03	0.1944E-01	0.6713E-03	0.1943E-01	0.7048E-03	0.1942E-01	0.7383E-03	0.1941E-01	0.7718E-03	0.1940E-01
30.0	0.5020E-03	0.1880E-01	0.5333E-03	0.1880E-01	0.5648E-03	0.1880E-01	0.5959E-03	0.1880E-01	0.6272E-03	0.1880E-01	0.6587E-03	0.1879E-01	0.6900E-03	0.1878E-01	0.7213E-03	0.1877E-01
31.0	0.4672E-03	0.1820E-01	0.4990E-03	0.1820E-01	0.5280E-03	0.1820E-01	0.5577E-03	0.1820E-01	0.5871E-03	0.1820E-01	0.6164E-03	0.1819E-01	0.6451E-03	0.1818E-01	0.6738E-03	0.1817E-01
32.0	0.4408E-03	0.1761E-01	0.4683E-03	0.1761E-01	0.4959E-03	0.1761E-01	0.5231E-03	0.1761E-01	0.5492E-03	0.1761E-01	0.5755E-03	0.1760E-01	0.6018E-03	0.1759E-01	0.6281E-03	0.1758E-01
33.0	0.4185E-03	0.1710E-01	0.4408E-03	0.1710E-01	0.4663E-03	0.1710E-01	0.4922E-03	0.1710E-01	0.5181E-03	0.1710E-01	0.5444E-03	0.1709E-01	0.5707E-03	0.1708E-01	0.5970E-03	0.1707E-01
34.0	0.3994E-03	0.1659E-01	0.4188E-03	0.1659E-01	0.4432E-03	0.1659E-01	0.4636E-03	0.1659E-01	0.4841E-03	0.1659E-01	0.5046E-03	0.1658E-01	0.5251E-03	0.1657E-01	0.5456E-03	0.1656E-01
35.0	0.3844E-03	0.1612E-01	0.3915E-03	0.1612E-01	0.4145E-03	0.1612E-01	0.4358E-03	0.1612E-01	0.4571E-03	0.1612E-01	0.4784E-03	0.1611E-01	0.4997E-03	0.1610E-01	0.5210E-03	0.1609E-01
36.0	0.3683E-03	0.1567E-01	0.3700E-03	0.1567E-01	0.3910E-03	0.1567E-01	0.4136E-03	0.1567E-01	0.4351E-03	0.1567E-01	0.4566E-03	0.1566E-01	0.4781E-03	0.1565E-01	0.4996E-03	0.1564E-01
37.0	0.3577E-03	0.1525E-01	0.3501E-03	0.1525E-01	0.3709E-03	0.1525E-01	0.3915E-03	0.1525E-01	0.4121E-03	0.1525E-01	0.4327E-03	0.1524E-01	0.4533E-03	0.1523E-01	0.4739E-03	0.1522E-01
38.0	0.3426E-03	0.1485E-01	0.3321E-03	0.1485E-01	0.3516E-03	0.1485E-01	0.3712E-03	0.1485E-01	0.3907E-03	0.1485E-01	0.4102E-03	0.1484E-01	0.4297E-03	0.1483E-01	0.4492E-03	0.1482E-01
39.0	0.3267E-03	0.1447E-01	0.3138E-03	0.1447E-01	0.3338E-03	0.1447E-01	0.3528E-03	0.1447E-01	0.3719E-03	0.1447E-01	0.3910E-03	0.1446E-01	0.4101E-03	0.1445E-01	0.4292E-03	0.1444E-01
40.0	0.2821E-03	0.1410E-01	0.2997E-03	0.1410E-01	0.3174E-03	0.1410E-01	0.3350E-03	0.1410E-01	0.3526E-03	0.1410E-01	0.3702E-03	0.1409E-01	0.3878E-03	0.1408E-01	0.4054E-03	0.1407E-01
41.0	0.2685E-03	0.1376E-01	0.2853E-03	0.1376E-01	0.3021E-03	0.1376E-01	0.3188E-03	0.1376E-01	0.3355E-03	0.1376E-01	0.3522E-03	0.1375E-01	0.3689E-03	0.1374E-01	0.3856E-03	0.1373E-01
42.0	0.2559E-03	0.1341E-01	0.2719E-03	0.1341E-01	0.2879E-03	0.1341E-01	0.3038E-03	0.1341E-01	0.3198E-03	0.1341E-01	0.3358E-03	0.1340E-01	0.3518E-03	0.1339E-01	0.3678E-03	0.1338E-01
43.0	0.2441E-03	0.1312E-01	0.2594E-03	0.1312E-01	0.2746E-03	0.1312E-01	0.2899E-03	0.1312E-01	0.3051E-03	0.1312E-01	0.3204E-03	0.1311E-01	0.3359E-03	0.1310E-01	0.3514E-03	0.1309E-01
44.0	0.2311E-03	0.1282E-01	0.2477E-03	0.1282E-01	0.2623E-03	0.1282E-01	0.2768E-03	0.1282E-01	0.2914E-03	0.1282E-01	0.3059E-03	0.1281E-01	0.3204E-03	0.1280E-01	0.3349E-03	0.1279E-01
45.0	0.2229E-03	0.1254E-01	0.2368E-03	0.1254E-01	0.2508E-03	0.1254E-01	0.2647E-03	0.1254E-01	0.2787E-03	0.1254E-01	0.2926E-03	0.1253E-01	0.3065E-03	0.1252E-01	0.3204E-03	0.1251E-01
46.0	0.2133E-03	0.1226E-01	0.2266E-03	0.1226E-01	0.2400E-03	0.1226E-01	0.2533E-03	0.1226E-01	0.2666E-03	0.1226E-01	0.2799E-03	0.1225E-01	0.2932E-03	0.1224E-01	0.3065E-03	

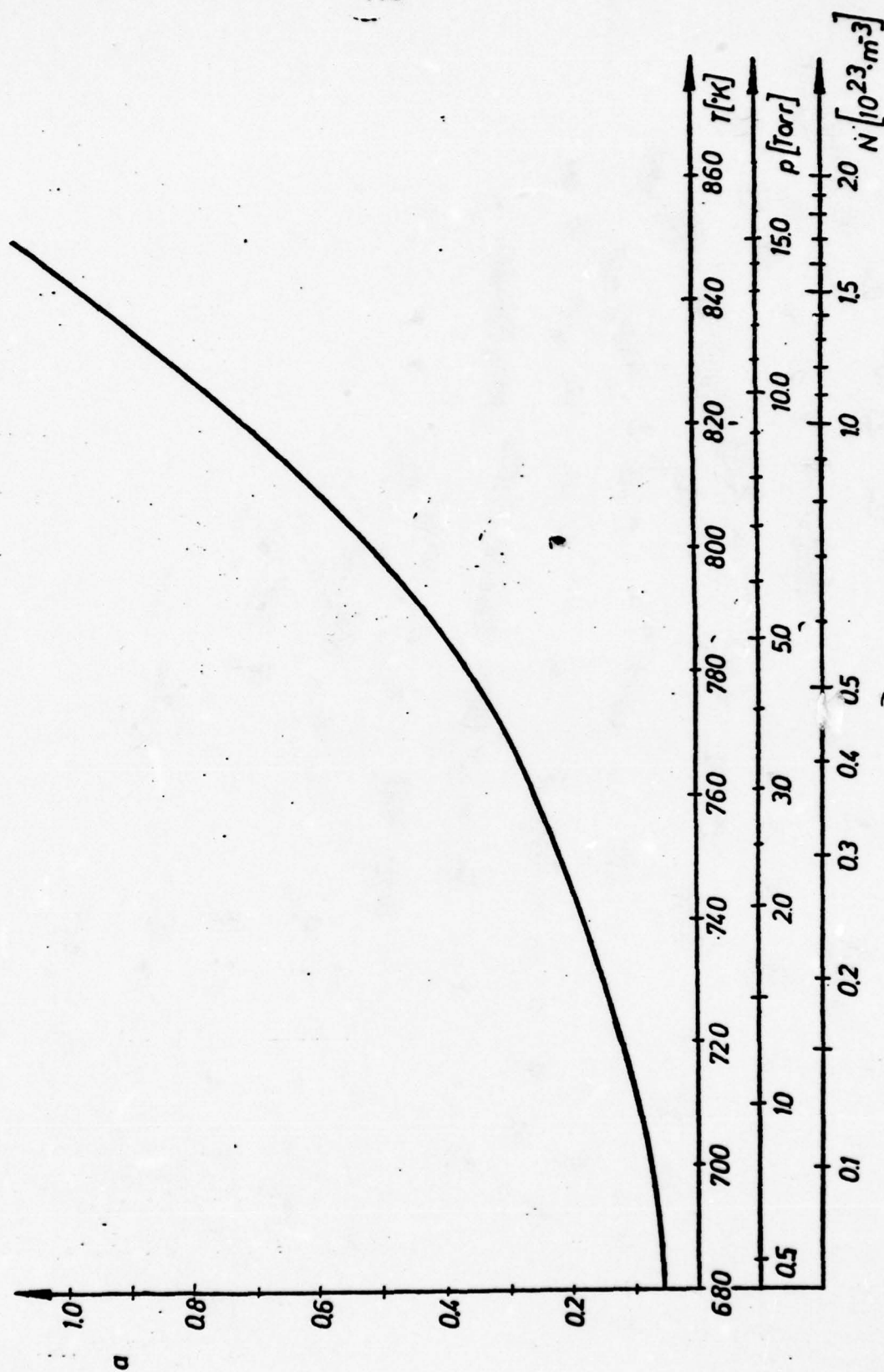


Fig. 21. Voigt Parameter a versus Temperature, Pressure, and Number Density of Sodium Vapor for Homogeneous Broadening.

APPENDIX B

PROPERTIES OF SODIUMB.1 General Description

Sodium, at standard temperature and pressure, is a soft, silvery white metal having a low melting point, a relatively high boiling point, high thermal conductivity, and low density. In its metallic state, it can be easily cut with a knife. The surface usually appears greyish due to the formation of a film of sodium hydroxide upon exposure to air. Liquid sodium has a low viscosity and the ability to wet iron and steel surfaces.

The outstanding chemical property of sodium is its high reactivity. It reacts with water with explosive violence and will generally ignite spontaneously in air at temperatures about 115°C. Extreme caution is therefore required when handling sodium (see Reference 78 for handling techniques).

B.2 Physical Data and Formulas

The presented values and formulas for sodium constitute a summary and comparison of the latest available data found in the literature. In the following table (Table VIII) these data are listed together with their references in a very concise manner. For thermodynamic and other properties of saturated and superheated sodium not listed here, see References [78-82]. For the refractive index and the absorption coefficient for sodium vapor under various conditions see Section 3.3.4.

TABLE VIII. Physical Properties of Sodium

	Value/Formula	Reference
Atomic weight	22.991	83
Melting Point	$370.98 \pm 0.02^{\circ}\text{K}$	83
Boiling point	1154°K	84,87
<u>Equilibrium Mixture</u>		
Heat of fusion	27.06 cal/g	79
Heat of vaporization	951 cal/g	79
Vapor pressure	$\log P_v[\text{atm}] = 6.6811 - 5544.97/T - 0.61344 \log T$	84

B.2.1 Vapor Pressure

Ditchburn and Gimour⁸⁴ developed an equation for the total vapor pressure by correlating the experimental results of a number of investigators:

$$\log P[\text{atm}] = -5567/T - 0.5 \log T + 6.354 \quad (\text{B.1})$$

This equation gives the normal boiling point of 1154°K . An equation in two parameters was obtained from their own experimental work by Makansi, Muendel, and Selke.^{85,86}

$$\log P[\text{atm}] = -5220/T + 4.521 \quad (\text{B.2})$$

This equation gives a normal boiling point of 1154.5°K . Stone, et al.,⁸⁶ measured the saturation vapor pressure of sodium with a static capsule

technique. The best square fit of the data resulted in the Kirchhoff-type equation

$$\log P[\text{atm}] = 6.68111 - 5544.97/T - 0.61344 \log T \quad (\text{B.3})$$

This equation gives a normal boiling point of 1154.6°K.

The vapor pressure data given by Sittig⁷⁹ yield a normal boiling point of 1156°K. The temperature pressure data presented in this report are obtained by the use of Eq.(B.3) above, which gives a normal boiling point temperature of 1154.6°K. The average deviation of all the experimental data from corresponding values computed from Eq. (B.3) is reported to be -0.37%. The results of the other investigators listed above show good agreement with the normal boiling point temperature as well as with values at other pressures. The Liquid-Metals Handbook⁷⁸ and the 1976 JANAF Table⁸³ list 1154°K and 1156°K, respectively, as the boiling point for sodium at one atmosphere.

Sodium vapor is composed of the monomer, dimer, and possibly the tetramer, the fraction of each species depending both upon temperature and pressure. If only monomer and dimer species are considered the equations for an equilibrium mixture can be written as

$$\text{Na}_1 \rightleftharpoons 0.5 \text{Na}_2 \quad (\text{B.4})$$

$$P = P_1 + P_2 \quad (\text{B.5})$$

$$K_2[\text{atm}^{-1}] = P_2/(P_1)^2 \quad (\text{B.6})$$

where the total pressure P is equal to the sum of the partial pressures P_1 and P_2 of the monomer and dimer. K_2 is the equilibrium constant and can be expressed according to Stull and Sinke⁸⁸ as

$$\log K_2 = -4.2229 + 4027.6868/T \quad (\text{B.7})$$

The mole fraction of the monomer, X_1 , can be calculated from Eqs. (B.4) and (B.5) as:

$$P_1 = \frac{P_1}{P} = \frac{(1 + 4K_2P)^{1/2} - 1}{2K_2P} \quad (\text{B.8})$$

The in such a way obtained vapor pressure values for the monomer show good agreement in the region between 700°K and the boiling point with corresponding values computed from Eq. 3.30 given by Nesmeyanov.⁶⁶ However, a later publication of sodium vapor pressure data derived by Fairbank⁸⁹ from density measurements show about 10 percent higher pressures for the sodium monomer in the region of interest. Unfortunately, the most recent report on sodium vapor pressure⁹⁰ is unavailable at this date so that this disagreement remains somewhat unresolved. Nevertheless, it is believed that the correct total and monomer vapor pressure curves can be approximated to a high degree of accuracy by the above given equations and they are plotted versus temperature in Fig. 22.

B.3 The Spectrum of Atomic Sodium

The electronic structure of atomic sodium, having eleven electrons, consists of full K and L electron shells, which form a neon-like core, and one single valence electron outside this core. This valence electron

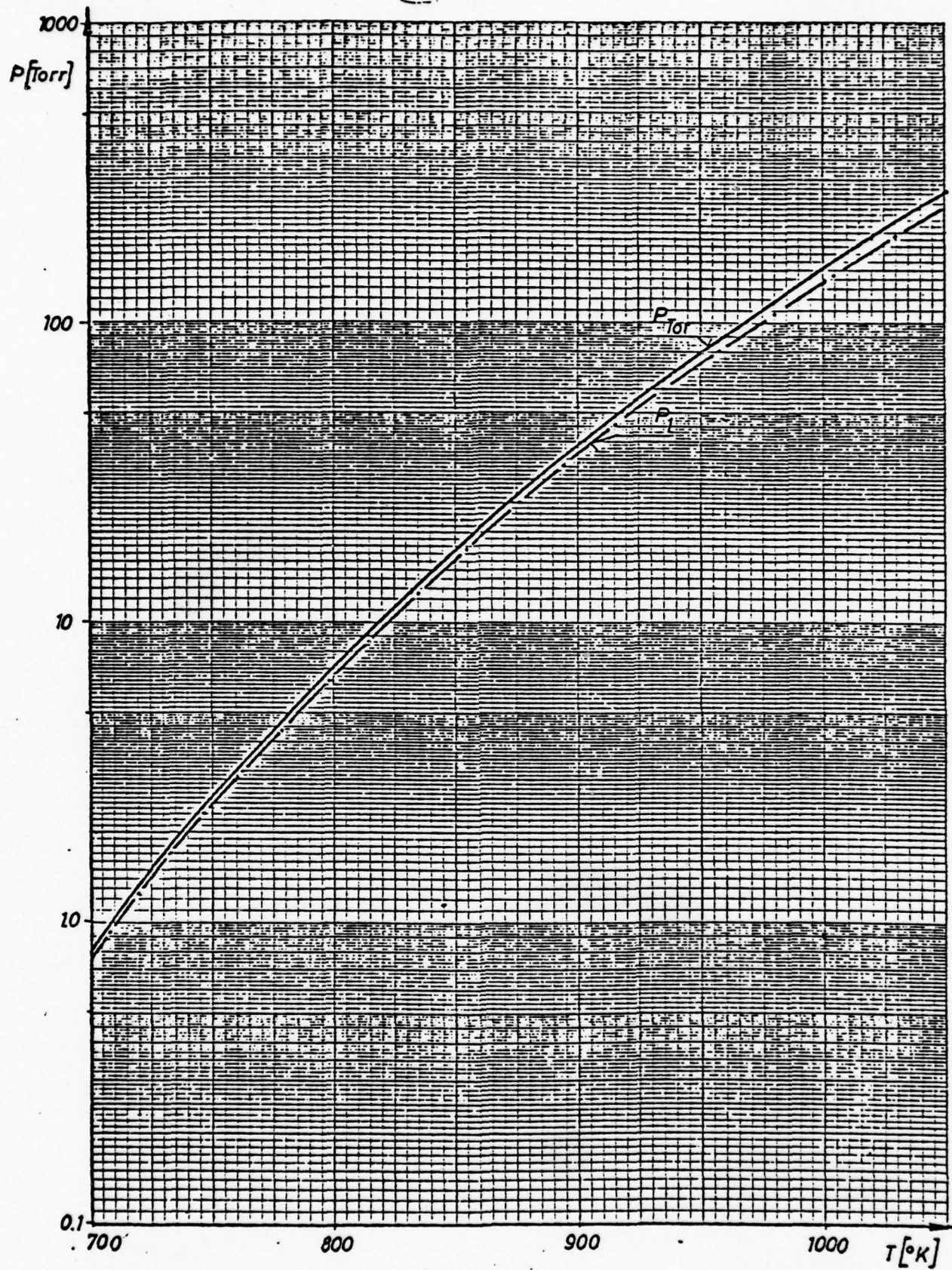


Fig. 22. Total and Monatomic Vapor Pressure of Sodium versus Temperature

spends most of its time outside the core and can therefore be considered as moving in an effective Coulomb field of approximately one nuclear charge. Its ionization potential amounts to about 5 eV and its degree of ionization, that is the fraction of the originally neutral sodium atoms that have become ionized is of the order of 10^{-14} for the conditions of the present study.

Since this electron in sodium is the only one which is optically active, its spectrum is very much like hydrogen, and the energy levels start with the first unoccupied levels, $n = 3$. The strongly allowed transitions between these levels and the ground level account for the D-lines. The splitting between the upper doublet states having the same n and ℓ values ($n = 3$; $\ell = 1$) is due to the opposite spin direction of the valence electron whose angular momentum adds or subtracts to the total angular momentum $j = \pm 1/2$. On each of the fine structure levels there is also hyperfine splitting which arises from magnetic dipole and electric quadrupole interactions of the active electron with the nucleus. The hyperfine structure of the sodium D-lines do not need to be taken into account in the present study since the relatively broad band dye laser integrates over the hyperfine lines. Fig. 23 displays the energy levels of atomic sodium including electron spin as shown by Mitchell and Zemansky.⁴⁵

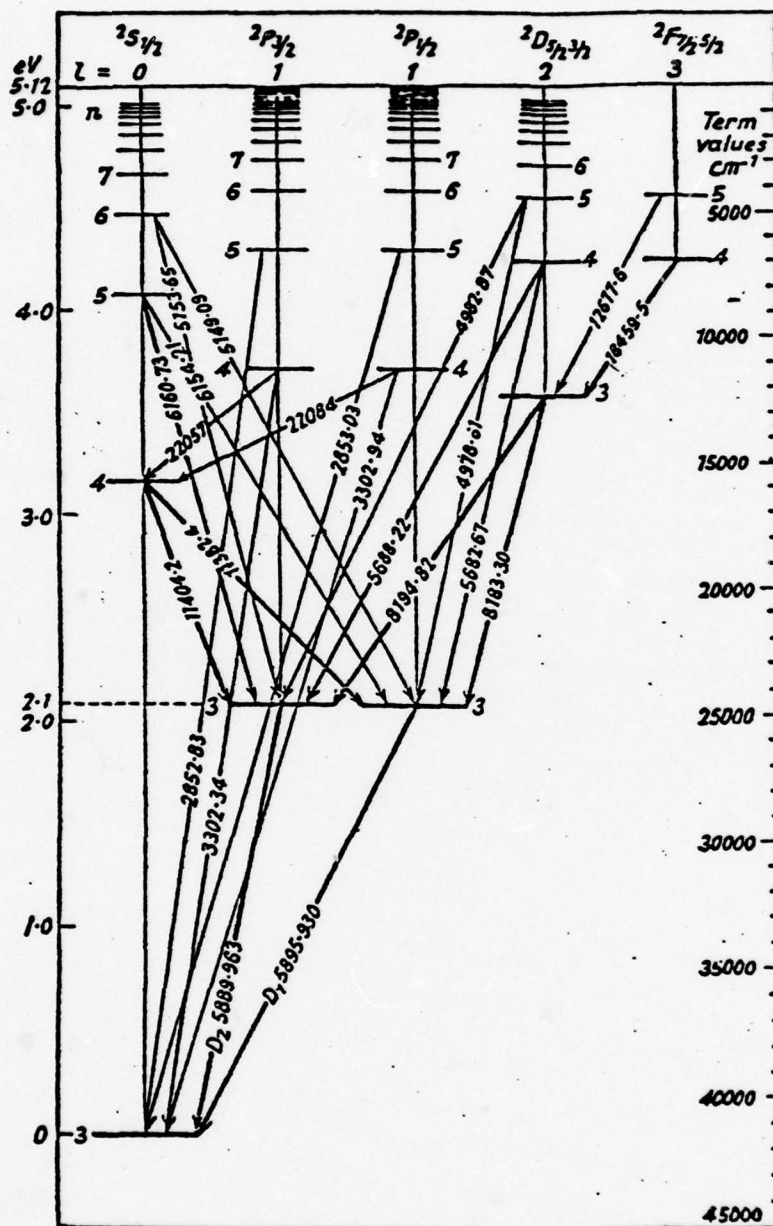


Fig. 23. Energy Level Diagram of Atomic Sodium

APPENDIX C

Alignment Procedure of Dye Laser and Optimizing Beam Power

Lack of money made it necessary to construct the dye laser in the laboratory. This required one to build in contrast to buying a commercial unit various mountings and holders for the components as well as aligning the whole assembly along a previously fixed optical axis. Since the alignment and adjustment-procedure is not readily available and had to be developed for this study, it is worth mentioning.

The following equipment is needed for the alignment and optimization of the dye laser.

- (a) He-Ne laser with spot size approximately 0.5 mm and divergence 0.5 mrad. A common laboratory model should suffice.
- (b) Several index cards or pieces of white cardboard.
- (c) Joule meter to measure the output power (Molelectron Pyroelectric Joulemeter J3)

The following procedure describes the steps to be taken if laser alignment is ever lost through misadjustment or component replacement or when the laser is newly assembled. The description is intended to be as complete as possible. However, with experience an operator may be able to skip some of the steps listed

- 1) Remove both lenses of telescope and take out dye cuvette.
- 2) Place the He-Ne in front of the dye laser and align its beam along the optical axis of the system. This position is very important since the dye laser output will be on the same axis.

- 3) Punch a clean 1-2 mm hole in the center of the white card and fasten it on the front of the He-Ne laser so the beam passes clearly through the hole. This card is used to observe back reflections from the dye laser.
- 4) Translate output mirror in such a way that the beam hits it in the center.
- 5) Observe the back reflection from the front mirror on the white card as shown below:

- | | | |
|---|---|----------------------------------|
| 1 | . | secondary reflection (very weak) |
| 2 | ● | inside surface reflection |
| 3 | ● | outside surface reflection |

If this pattern is rotated so that the weakest spot (1) is not at the top, remove the front mirror holder and rotate the mirror in its holder so that the pattern is as shown above.

- 6) Tilt output mirror in such a way that the inside surface reflection (spot 2) is reflected back into He-Ne laser.

The following steps describe the alignment of the dye cell to the pump laser; they can be left out if dye cell is already in place. In that case proceed from step 11.

- 7) Place dye cell holder in cavity so that the He-Ne beam is centered in 5 mm holder aperture or just between the stirrer head and the inner wall of dye
- 8) Turn pump laser on.
- 9) Adjust the vertical position of the aspherical lens until the pump beam is centered on focusing lens housing. A white card held between the two lasers will aid in locating the UV beam.
(Note: The height of the UV beam should coincide with height of the He-Ne beam to obtain maximum output efficiency.)
- 10) Adjust the distance between the focusing lens and the dye cell until the pump beam is focused into a narrow line at the inner cell wall. This can be done by inserting a strip of polaroid film instead of the dye cuvette in the holder. The UV beam will burn stripes into the paper from which the width of the focused beam can be determined.
(Don't spend too much time trying to optimize the pump stripe, because this will be done later much more efficiently when maximizing the output power. The initial adjustments should only be sufficient to bring the laser to lase.)
- 11) Install grating and rotate to 90° incidence and adjust tilt adjustments to put reflection back into He-Ne laser.
- 12) Rotate grating to high positive order (4th) and adjust twist of grating to put reflection back in He-Ne. (Do not touch tilt controls.)

- 13) Rotate grating to high negative order and check if reflection is still back in He-Ne. If not, then the vertical axis of rotation must be adjusted and steps 11 through 13 repeated.
 - 14) Return grating to the positive order at which it should operate.
 - 15) Install large lens of telescope in place and adjust its transverse position to center reflected spot on He-Ne.
 - 16) Install small lens of telescope and adjust its transverse position to let He-Ne beam pass through in both directions.
 - 17) Adjust focusing of telescope to produce reflected beam of same size as original He-Ne beam.
 - 18) Switch on stirring motor and turn pump laser on.
 - 19) By inserting a white cardboard between the two lenses of telescope two super-radiant spots will be seen with a slight vertical separation.
- Both spots should have equal intensity. If this is not the case, slightly tilting of the smaller lens to avoid backreflection from its front surface will help.
- 20) Adjust the angle and height of the pump stripe and the transverse position of the dye cell to bring the lower superradiant beam through the telescope to hit the center of the grating.
 - 21) Now look for the back reflected light from the grating. It should form a stripe of light near the small lens of the telescope. (A white cardboard with a small hole will help locating the stripe.)

- 22) Rotate the grating about the vertical axis to bring part of this stripe back through the small lens. (Do not touch the other axis of rotation.)
- 23) The dye laser should now be lasing off of the grating on the same optical axis as He-Ne. Check by inserting card in front of the grating -- laser should go out.
- 24) Adjust focus of telescope to produce best dye laser mode.
- 25) Place a power meter in the output beam.
- 26) Adjust height and angle of pump stripe as well as focusing of pump beam to produce most power in the best mode.

The dye laser can be considered properly aligned if output powers similar to the tuning curve (Fig. 13) can be achieved. If the output is too low make the following adjustments in order of decreasing importance:

- (a) Dye cell translation
- (b) Dye cell rotation
- (c) Focus of UV beam
- (d) Front mirror tilt.

If after these adjustments the output still does not conform to the tuning curve, make sure the stirring magnet in cuvette is operating properly and/or change to a fresh dye.

REFERENCES

1. Merzkirch, W., Flow Visualization (Academic, N.Y., 1974).
2. Steel, W. H., Interferometry (Cambridge University Press, Cambridge, 1967).
3. Fowles, G. R., Introduction to Modern Optics (Holt, Rinehart and Winston, N.Y., 1975).
4. Beams, J. W., "Shadow and Schlieren Methods", pp. 26-46 in Ladenburg, R. W. et al., ed., Physical Measurements in Gas Dynamics and Combustion (Princeton University Press, Princeton, 1954).
5. Ladenburg, R., Bershader, D., "Interferometry ", pp. 47-78 in the volume cited in reference 4 above.
6. Zehnder, L., Z. Instrumentenkunde 11, 275 (1891); Mach L., ibid. 12, 89 (1892).
7. Dosanjh, D. S., Editor, Modern Optical Methods in Gas Dynamic Research (Plenum, N.Y., 1971).
8. Durrani, T. S., Greated, C. A., Laser Systems in Flow Measurement (Plenum, N.Y., 1976).
9. Emerick, R., Experimental Methods in Fluid Physics (Academic, N.Y., 1978).
10. Leonard, D. A., Keck, J. C., ARS J., 1112 (July 1962).
11. Bershader, D., "Some Aspects of the Refractive Behavior of Gases," pp. 65-83 in the volume cited in reference 7 above.
12. Bershader, D., Prakash, S. G., Huhn, G., "Improved Flow Visualization by Use of Resonant Refractivity", pp. 595-610 in Zinn, B. T.,

- ed., Experimental Diagnostics in Gas Phase Combustion Systems, Volume 53, Progress in Astronautics and Aeronautics, (Princeton University Press, Princeton, N.J., 1977).
13. Haensch, T. W., Appl. Opt. 11, 895 (1972).
 14. Haensch, T. W., "Applications of Dye Lasers", in Dye Lasers, F. Schaefer (ed.), (Springer Verlag, N.Y., 1973).
 15. Wu, F. Y., Ezekiel, S., 1977 IEEE/OSA Conference on Laser Engineering and Appl., June 1-3, 1977, Paper #716.
 16. Schuda, F., Merscher, M., and Stroud, C. R., Jr., Appl. Phys. Lett. 22, 360 (1973).
 17. Wang, C. P., Report SAMSO-TR-75-150 (1975).
 18. Miles, R. B., Udd, E., and Zimmermann, M., "Quantitative Flow Visualization in Sodium Vapor Seeded Hypersonic Helium", Dept. of Aerospace and Mechanical Engineering, Princeton University, 1977.
 19. Wood, R. W., Physical Optics, 3rd ed., Chapter XV, pp. 497-500 (The Macmillan Co., N.Y., 1934).
 20. Mach, E., The Principles of Physical Optics: A Historical and Philosophical Treatment (Dover Publications, New York, 1934).
 21. Christiansen, C., Pogg. and Weid. Ann. 141, 479 (1870).
 22. Kundt, A., Pogg. and Weid. Ann. 14, 259 (1871); Pogg. and Weid. Ann. 144, 132 (1872).
 23. Wood, R. W., Phil. Mag. 3, 128 (1902); 6, 96 (1903); 8, 293 (1904).

24. Cauchy, A. L., Bull. Sc. Math. 14, 9 (1830); Compt. Rend. 2 (1836); Compt. Rend. 51 (1861).
25. Maxwell, C., Math. Tripos. Exam., Cambridge Calendar (1869).
26. Sellmeier, W., Pogg. Ann. 143, 271 (1871); 145, 399, 520 (1872); 147, 386, 525 (1872).
27. v. Helmholtz, H., Pogg. Ann. 154, 582 (1875).
28. Wood, R. W., Phil. Mag. 46, 380 (1898); 1, 664 (1909).
29. Lorentz, H. A., The Theory of Electrons, Leipzig (1900).
30. Ditchburn, R. W., Light, Vol. 2 (Blackie & Son Limited, London, 1963).
31. Klein, M. V., Optics (John Wiley & Sons, Inc., New York, 1970).
32. Naturw. 11, 596 (1923); Tolman, R. C., Phys. Rev. 23, 609 (1924).
33. Nussenzweig, H. M., Causality and Dispersion Relations (Academic, New York, 1972).
34. Kramers, H. A., Nature 113, 673 (1924); 114, 310 (1924).
35. Kramers, H. A. and Heisenberg, W., Zeits. f. Physik 31, 681 (1925).
36. Davydov, A. S., Quantum Mechanics (Pergamon Press, Oxford, 1965).
37. Planck, M., Ann. Physik 4, 533 (1901).
38. Wood, R. W., Proc. Am. Acad., x1, 396; Phil. Mag., May (1912).
39. Bohr, N., Phil. Mag., 26, 1, 476, 857 (1913), Phil. Mag. 30, 394 (1915).
40. Einstein, A., Zeits. f. Physik 18, 121 (1917).
41. Ladenburg, R., Zeits. f. Physik 48, 15 (1928).
42. Ladenburg, R. and Minkowski, R., Zeits. f. Physik 6, 153 (1927);
Ladenburg, R., and Wolfsohn, G., Zeits. f. Physik 63, 616 (1930).

43. Lengyel, B. A., Am. J. Phys. 34, 903 (1966).
44. Vincenti, W. and Kruger, C., Physical Gas Dynamics (Wiley, 1965).
45. Mitchell, A. C. G. and Zemansky, M. W., Resonance Radiation and Excited Atoms (Cambridge University Press, Cambridge, 1961), Chapt. III.
46. Breene, R. G., Jr., The Shift and Shape of Spectral Lines (Pergamon, New York, 1962).
47. Armstrong, B. H. and Nicholls, R. W., Emission, Absorption and Transfer of Radiation in Heated Atmospheres (Pergamon, New York, 1972), pp. 228-234.
48. Lorentz, H. A., Proc. Amst. Acad. 18, 134 (1915).
49. Abramowitz, M. and Stegun, I. A., Handbook of Mathematical Functions (Dover Publications, Inc., New York, 1970), Chapt. 7.
50. Kielkopf, J. F., J. Opt. Soc. Am. 63, 987 (1973).
51. Langhoff, P. W. and Karplus, M., J. Opt. Soc. Am. 59, 863 (1969).
52. Langhoff, P. W., J. Chem. Phys. 57, 2604 (1972).
53. Dalgarno, A. and Davison, W. D., Mol. Phys. 13, 479 (1967).
54. Niemax, P. and Pichler, G., J. Phys. B8, 179 (1975).
55. Kielkopf, J., J. Phys. B10, 2631 (1977).
56. Values obtained from the tabulations of Moore, G. E., Atomic Energy Levels NBS Circular 467, U.S. GPO, Washington, D.C., 1949, Vols. I, II, and III, multiplying the entries given there in cm^{-1} by the speed of light in vacuo ($c = 2.99793 \times 10^8 \text{ m/s}$).
57. Static or zero-frequency polarizability values taken from the tabulations of ref. 51. See also, Teachout, R. R., and Pack, R. T., Atomic Data 3, 195 (1971).

58. Oscillator strengths for Li and Rb taken from Dalgarno, A. and Davison, W. D., Mol. Phys. 13, 479 (1967) employing the 2:1 rule; for Na and K from Wiese, W. L., Smith, M. W., and Miles, B. M., Atomic Transition Probabilities NSDRDS 22, Vol. II (1969); for Cs from Niemax, K., and Pichler, G., J. Phys. B8, 179 (1975).
59. Natural Full-halfwidths (Einstein A coefficients) taken from the compilations of Wiese, W. L., Smith, M. W., and Miles, B. M., cited in reference 58 above.
60. Atomic mass values cited by Hodgman, C. D., Editor, Handbook of Chemistry and Physics (Chemical Rubber Printing Co., Ohio, (1952), p. 303.
61. Gallagher, A., Phys. Rev. A12, 133 (1975); Smith, G., Collins, B. S., J. Phys. B9, L117 (1976).
62. McCartan, D. G., and Farr, J. M., J. Phys. B9, 985 (1976).
63. Hindmarsh, W. R., and Farr, J. M., Collision Broadening of Spectral Lines by Neutral Atoms (Oxford, UP, 1972).
64. Ottinger, Ch., Scheps, R., York, G. W., and Gallagher, A., Phys. Rev. A11, 1815 (1975).
65. Smith, G., J. Phys. B9, 985 (1975).
66. Nesmeyanov, A. N., Vapour Pressure of the Elements (Academic, New York, 1963).
67. Posener, D. W., Aust. J. Phys. 12, 184 (1959).
68. Penner, S. S., Quantitative Molecular Spectroscopy and Gas Emissivities (Addison-Wesley, Reading, Mass., 1959).
69. Whiting, E. E., JQSRT 8 1379 (1968).

70. Armstrong, B. H., JQSRT 7, 61 (1967).
71. Hummer, D. G., Mem. R. Astr. Soc. 70, 1 (1965).
72. Hui, A. K., Armstrong, B. H., and Wray, A. A., JQSRT 19, 509 (1978).
73. Molelectron Corporation, "Molelectron Dye List for Use in DL-Series" (Sunnyvale, Ca., Aug. 1975).
74. Born, M. and Wolf, E., Principles of Optics, 4th edition (Pergamon Press, Oxford, 1970).
75. Grover, G. M., Cotter, T. P., and Erickson, G. F., J. Appl. Phys. 35, 1990 (1964).
76. Vidal, C. R., Cooper, J., J. Appl. Phys. 40, 3370 (1969).
77. Kline, S. J. and McClintock, F. A., Mech. Eng. 75 (1953).
78. Lee, R. E., "Safety and Fire Protection, Non-Radiative Sodium", Liquid-Metals Handbook, Sodium-NaK Supplement, U. S. Government Printing Office (July 1955).
79. Sittig, M., Sodium, Its Manufacture, Properties, and Uses, (Reinhold Publishing Co., N. Y. 1956).
80. Dunning, E. L., ANL-6246, Argonne National Laboratory (October 1960).
81. Lee, C. S., Lee, D. I., and Bonilla, C. F., Nucl. Eng. Des. 10, 83 (1969).
82. Golden, G. H., Tokar, J. V., ANL-7323, Argonne National Laboratory (1967).
83. JANAF-Interim Thermochemical Tables. Vol. 3, Sodium Data (1976).

84. Ditchburn, R. W. and Gilmour, J. C., Rev. Mod. Phys. 13, 310 (1941).
85. Makansi, M. M., Muendel, C. H., and Selke, W. A., J. Phys. Chem. 59, 40 (1955).
86. Makansi, M. M., Selke, W. A., and Bonilla, C. F., J. Chem. Eng. Data 5(4), 441 (1960).
87. Stone, J. P., et al., NRL-6241, Naval Research Laboratory (Sept. 1965).
88. Stull, D. R., and Sinke, G. C., Thermodynamic Properties of the Elements, Amer. Chem. Soc. (1965).
89. Fairbank, W. M., Jr., M. L. Report 2301, Microwave Laboratory, W. W. Hansen Laboratories of Physics, Stanford University (May 1974).
90. Bhise, V. S., Bonilla, C. F., Proc. Int. Conf. Lic. Met. Technol. Energy Prod. 77, 2657 (1977).

Appendix IV

EXPERIMENTAL STUDIES OF
SODIUM RESONANT ABSORPTION

A THESIS
SUBMITTED TO THE DEPARTMENT OF AERONAUTICS
AND ASTRONAUTICS AND THE COMMITTEE ON GRADUATE STUDIES
OF STANFORD UNIVERSITY
IN PARTIAL FULFILLMENT OF THE REQUIREMENTS
FOR THE DEGREE OF
ENGINEER

By
Irvin Joseph Benard
June 1979

TABLE OF CONTENTS

	<u>Page</u>
Acknowledgments	iii
List of Tables	vi
List of Figures	vii
Chapter 1.0 INTRODUCTION	
1.1 Introductory Comments	1
1.2 Study Objectives	6
1.3 Historical Background	8
1.4 Experimental Measurements	12
Chapter 2.0 THEORY OF RESONANT ABSORPTION IN SODIUM VAPOR	
2.1 General Relationships	14
2.2 Classical Absorption Theory	18
2.3 Oscillator Strength	21
2.4 Absorption Considering Quantum Mechanical Concepts	23
2.5 Line Broadening Mechanisms	26
2.6 Predicted Far Wing Absorption	34
Chapter 3.0 EXPERIMENTAL EQUIPMENT AND TECHNIQUE	
3.1 Experimental Design	36
3.2 Experimental Apparatus	39
3.3 Calibrations	47
3.4 Experimental Methods and Techniques	50
3.5 Results of Measurements	52
3.6 Experimental Error	57

TABLE OF CONTENTS (Continued)

	<u>Page</u>
Chapter 4.0 ASSESSMENT OF EXPERIMENTAL RESULTS	
4.1 Far-Wing Resonant Behavior	62
4.2 Sources for Deviation from Theory	68
4.3 Suggestions for Follow-On Studies	74
Chapter 5.0 CONCLUSIONS AND RECOMMENDATIONS	77
Appendix A KRAMERS-KRÖNIG RELATIONSHIP	80
Appendix B TRANSIENT RESPONSE OF THE PHOTOMULTIPLIER RECORDER	92
Appendix C DIFFUSION OF SODIUM INTO A BUFFER GAS	98
Appendix D THE ABSORPTION SPECTRUM OF ATOMIC SODIUM	101
References	103

LIST OF TABLES

		<u>Page</u>
1.	Chronology of Sodium Resonant Absorption Experiments	9
2.	Comparison of Classical and Quantum Mechanical Absorption Parameters	24
3.	Sodium Resonant Absorption Measurements	56
4.	Absorption Coefficient Measurement Errors	58
5.	Frequency Measurement Errors	61
6.	Data Error Diagnostics	69

LIST OF FIGURES

	<u>Page</u>
1. Comparison of Doppler and Lorentzian Lineshapes with Equal Intensities and Linewidths	30
2. Schematic of Experimental Arrangement	40
3. Absorption Measurements	53
4. Comparison of Measured Absorption with Theory	63
5. Effect of Molecular Sodium	65
6. Sodium Resonant Absorption Experiments	67
A-1 Relation Between Causality and Dispersion	91
A-2 Effect of Damping on Dispersion	91
B-1 Photomultiplier Recorder Transient Response	95
B-2 Photomultiplier Recorder Time Constant	96
B-3 Photomultiplier Recorder Signal-to-Noise Ratio	97
D-1 Energy Level Diagram for Atomic Sodium	102

1.0 INTRODUCTION

1.1 Introductory Comments

Flow visualization techniques used in investigations of complex flows of gases continue to be a powerful tool in both fluid dynamics, including especially aerodynamics and combustion. The ability to view the flow field of interest in its entirety provides the experimenter with an understanding of pertinent features and the places where the flow is particularly complex, needing further study. Flow visualization also aids in the interpretation of other types of measurements and in many cases can provide quantitative data.

The theoretical aerodynamicist also benefits from flow visualization techniques in the modeling of complex flow fields as it is often necessary to know the physical extent of the various flow regimes in order to satisfactorily bound the mathematical treatment. For example, flow over a surface which creates separated regions can be treated without considering the details of the separated region if the physical extent of the separation is known a priori. Flow visualization can also provide the theorist with an overall check on his model by locating flow features such as shock waves for comparison with theoretical positions.

Flow visualization techniques such as schlieren, shadowgraph and interferometry have been used and continue to be useful in aerodynamic research. These techniques utilize density gradients in the flow field to deflect light passed through the flow region of interest. Because the index of refraction for air (and other gases of aerodynamic

interest) is very nearly unity, only flows with relatively large density gradients have been studied with these methods. This usually restricts the use of schlieren and shadowgraph techniques to supersonic flows. If, however, the index of refraction could be enhanced, flows with smaller density gradients could be viewed with any of the traditional visualization techniques.^{1,2,3}

Such enhancement is possible near the electronic resonant frequency of certain atoms. At wavelengths one-half of the line width from the center of the resonance, the index of refraction reaches a maximum (or minimum) with the difference from unity being several orders of magnitude larger than the non-resonant difference from unity. For air, this resonant behavior occurs in the far ultra-violet portion of the spectrum and would present difficulties in terms of observing the flow field. However, sodium has resonances in the yellow portion of the visual spectrum which would avoid the need to work in the ultra-violet. A flow seeded with sodium vapor would exhibit enhanced refractivity and significantly lower density gradients could be observed.

To utilize this enhanced refractivity, the light source used to illuminate the flow field would need to be very narrow band with the center of the band located near the resonant frequency. Because the index of refraction diminishes very rapidly away from the peak value (located one-half line width from resonance), the spectral width of the source must be on the order of a fraction of an Angstrom. A dye-laser can fulfill this requirement since it can be tuned to a frequency near the sodium resonance and has a spectral width of a few tenths of an Angstrom.

Another characteristic of resonant behavior is very strong absorption. To make use of the enhanced refractivity, it is necessary to "tune" the light source very near the center of resonance where very strong absorption is encountered. Therefore, as resonance is approached to increase the refractivity, the absorption increases with an attendant decrease in transmitted light available for observation. The selection of the optimum frequency which maximizes the sensitivity while maintaining a usable transmitted beam must trade the refractivity and absorptivity of the seed species (sodium). The high absorption in the spectral region of enhanced refractivity is a further justification for using a dye-laser as a light source. High intensity emission from a dye-laser is ideally suited for use near resonance where absorption will limit the useful transmitted beam.

The role of absorption in the use of resonant refractivity for flow visualization enhancement is more than one of a limiting process. Both refraction and absorption display frequency dependence. Kramers and Krönig have shown that the index of refraction and the extinction coefficient (which is related to the absorption coefficient) are connected to each other through integrals over the frequency spectrum (see Appendix A). In particular, the index of refraction at a given frequency is proportional to the integral of extinction coefficient with the integration extending over all frequencies. Similarly, the extinction coefficient is proportional to the integral of the index of refraction over all frequencies. This allows the point of view of treating the absorption as a "cause" with index of refraction as the "effect". That is, having established the frequency dependence of

absorption, there can be only one dependence of refractive index with frequency and that dependence is specified by the Kramers-Krönig relation.

Thus it is seen that resonant absorption is a central feature in the use of resonant enhancement of visualization techniques. The documentation of the absorptive properties of sodium near resonance will not only provide data for determination of the intensity of the transmitted beam in visualization experiments but will also serve as an independent check on the refractive behavior through the Kramers-Krönig relation. Although the resonant absorption of sodium has been studied in the past (see section 1.3), the chemical activity of sodium vapor has produced experimental problems resulting in data uncertainties. Reaction of sodium vapor with the windows of absorption cells which contain the vapor results in lowered light transmission that has the same effect as increased absorption.⁴ Therefore, an experimental approach which avoids chemical attack of optical components by the sodium vapor through the use of an inert buffer gas (used here) should provide a potentially more accurate measurement of absorption. Since the experimental equipment used in confining the sodium vapor is identical with that used for measuring the refractive index,⁵ a comparison of measured absorption with theory should provide independent information on phenomena which, due to the experimental arrangement, might have influence on the departure of refractivity from theory. Apart from all these features, an absorption study provides desirable redundancy relative to the refractive study, thereby helping to confirm the precision of the results.

For these reasons, an experimental study of the resonant absorption of sodium vapor was undertaken.

1.2 Study Objectives

The investigation of the resonant absorption of sodium vapor is a part of a more extensive study to use resonant refractivity to increase the sensitivity of flow visualization techniques. The initial experimental verification of the resonant refractive behavior of sodium vapor was carried out by Blendstrup.⁵ Because of the importance of absorption in a practical application using resonant refractivity, an experimental verification of sodium resonant absorption was considered necessary. Although the theory of resonant absorption based on classical principles is well established (see chapter 2) and deviations from this theory have been investigated to some extent, certain aspects* of the experiments to verify the refractive behavior suggest that absorption should also be experimentally verified.

As a result, the specific objectives of the study of the resonant absorption of sodium vapor can be enumerated:

- 1) Experimental verification of the absorption behavior in the far wing (blue wing of the D_2 -line, $\lambda_r = 5890 \overset{0}{\text{\AA}}$).
The measured absorption as a function of frequency together with the Kramers-Krönig relation will provide an independent experimental check of the refractivity behavior.

* Difficulties were encountered in establishing the length of the sodium vapor column and comparisons with refractive theory suggested that the interface between the sodium and the buffer gas may not be thin.

- 2) Experimental verification of the absorption coefficient in the near resonant frequency range of interest for enhancement of refractivity. These data will provide basic information for the determination of the output beam intensity in practical applications of enhanced refractivity.
- 3) Identification of deviations from theory and the possible sources thereof. Of particular concern are possible problems peculiar to the experimental set-up which might have an effect on the results of the refractive experiment. Heat pipe ovens (described in chapter 3) which were used to generate and confine the sodium vapor may have internal phenomena which influence the observed optical properties.

1.3 Historical Background

Sodium, which has long been recognized as an element in many compounds, was first isolated as the metal in 1807. It is the most abundant of the alkali metals and comprises about 2.6% of the earth's crust. The presence of sodium in stellar atmospheres is evident from the prominence of the D-lines. Although its presence in emission spectra of many substances is common due to contamination resulting from its abundance in the earth's crust, the optical properties of sodium vapor have not been subjected to extensive experimentation.

Its strong ground state transitions in the visible spectrum at 5890 and 5896 Å (see Appendix D for energy levels of atomic transitions) have lead to the use of sodium as a convenient species to study self-broadening and the interaction potential between rare gases and alkali metal gases. As a consequence, much of the literature treats the absorption characteristics of sodium with a noble gas such as argon. Although these data may seem to be of little importance regarding the resonant absorptive behavior of sodium vapor, the experimental arrangement used in this study (and in the refractive experiment) employed argon as a buffer gas to prevent contamination of optical components. In the event that the boundary layer between the heated sodium and the cool argon is more diffuse than expected from past experiments, the broadening due to an inert buffer gas may be of importance in interpreting results from the heat pipe oven.⁶

Table 1 presents a chronology of resonant absorption experiments with sodium. The early work of Wood⁷ is included because of historical interest and as an example of the state of the art of quantitative

TABLE 1. CHRONOLOGY OF SODIUM RESONANT ABSORPTION EXPERIMENTS

Author, Ref.	Date	Data	Frequency	Experimental Method	Remarks
Wood, R. W. ⁷	1904	--	--	--	Historical interest only
Watanabe, K. ⁸	1941	$\Delta\nu_{1/2}$	D ₁ and D ₂	Photometry of calibrated spectrographic plates	Na ₂ bands interfere with measurements at pressures > 20 mm.
Mitchell, A. C. G. ⁹ and Zemansky, M. W.	1961	f, τ , $\Delta\nu_D$	D ₁ and D ₂	Various (see ref. p 145)	Excellent survey of work performed between 1926 and 1932
Deleage, J. P. et al. ¹⁰	1973	γ/N with He	D ₁ and D ₂	Fabry-Perot spectrometer, PMT detection	Pressures < 100 Torr
Niemax, K. and Pichler, G. ⁴	1975	γ/N , line shape in wings	D ₁ and D ₂ $\Delta\lambda$ 0.1 to 5 Å	High resolution scanning monochromator, PMT detection	Asymmetry observed in wings
McCartan, D. G. and Farr, J. M. ¹¹	1976	γ , K/N^2 line shape in wings with noble gases	D ₁ and D ₂ $\Delta\nu = 0.3$ to 200 cm ⁻¹	High resolution scanning spectrograph, PMT detection	Asymmetry due to argon observed
Movre, M. and Pichler, G. ¹²	1977	Self-broadening asymmetries	D ₁ and D ₂	Analytical treatment of previous data ⁴	Location of beginning of asymmetries
This work	1979	μ	D ₂ , $\Delta\lambda = 10$ to 45 Å	Scanning monochromator, PMT detection	Far wing data only

spectroscopy in the early 1900's. Watanabe⁸ in 1941 investigated the resonant broadening of sodium. Using photometric techniques and spectrographic plates, Watanabe measured the width of the D₁- and D₂-lines and found the ratio of the widths to be 1.16.* Chapter III of Mitchell and Zemansky's book⁹ gives a modern treatment of absorption and experiments documenting the resonant behavior of sodium from 1926 through 1932 which are summarized at the end of the chapter. Deleage et al¹⁰ measured the broadening of sodium D-lines by helium at low pressure. Although these data are not directly applicable to this investigation, the line width deduced by extrapolating to zero helium pressure is in close agreement with other experiments. Niemax and Pichler⁴ were the first experimenters to detail the absorption in the wings of the sodium D-lines. Asymmetries were noted in the red wing of the D₂-line but the blue wing out to 5 Å⁰ from the line center shows the expected inverse square dependence on wavelength. The data of Niemax and Pichler will provide the most useful comparison with the results of experiments reported here. McCarten and Farr¹¹ have measured the collision broadening of sodium with noble gases. The absorption profiles of sodium with argon measured in the wings will provide information regarding the possibility of argon distorting the wing shape observed in the heat pipe oven. Additional information regarding self-broadening of sodium and asymmetries in the wings is provided by Movre and Pichler¹².

* A value of 1.12 is reported in the paper although the average value from experiments 4 through 13, recommended as most reliable, is 1.16. Later experiments by Niemax and Pichler⁴ confirm the value of 1.16 within 2%.

A collection of the physical properties of sodium is given in Appendix B of reference 5. Included are thermodynamic properties, vapor pressure, equilibrium constant for the Na-Na_2 reaction and the atomic structure leading to its spectral behavior.

1.4 Experimental Measurements

The measurement of the absorption coefficient of a gas is simply the measurement of the attenuation a beam of light experiences when passing through a known length of the gas. In principle, this is a straightforward experiment to conduct; but, as will be discussed in the chapter 3, attention to the experimental details is essential to obtaining accurate data. The absorption coefficient is, in general, a function of the frequency of the incident light, very strongly so near resonance. Frequency (or wavelength) dependence was observed by dispersing the attenuated beam from a white light source with a scanning monochromator. The signal was detected with a photomultiplier tube (PMT).

Since one of the experimental objectives was to verify the sodium absorptive behavior in the experimental equipment used in the refractive experiment⁵, the heat pipe ovens were also used in the absorptive experiment reported here. The shorter of the two heat pipe ovens was illuminated with a collimated beam of light which entered the interferometer on the same axis as the dye laser. Blocking the optical path through the longer heat pipe oven, allowed the light to pass through only the shorter oven. The output beam was focused on the monochromator slit and the PMT output was recorded on an x-y plotter.

The unattenuated beam intensity was recorded (over the wavelength range of interest) with the heat pipe oven at room temperature. The heat pipe ovens were then brought to thermal equilibrium (over the period of several hours) and the attenuated beam intensity was recorded.

Refractive experiments were carried out with the interferometer which required changing the temperature and pressure of the heat pipe ovens. Following each refractive experiment, the absorption was measured after the oven reached equilibrium as detected by monitoring internal pressures. When the ovens had cooled down to room temperature following a series of experiments, the unattenuated beam intensity was again recorded to check the pre-test value. As a result of these experimental procedures, the absorptive behavior of sodium could be studied at the same conditions used in the refractive experiment and, therefore, extend over the same range of pressures and temperatures. Consequently, any phenomena peculiar to the experimental apparatus would be detectable by the absorption experiment.

2.0 THEORY OF RESONANT ABSORPTION IN SODIUM VAPOR

2.1 General Relationships

The absorption of radiation by a gas, although first observed by Fraunhofer in 1817 as dark lines in solar spectra, was not identified as absorption until 1863 by Bunsen and Kirchhoff (see historical introduction in ref. 13). These discoveries that each gaseous element displays its own characteristic absorption spectrum lead the way to a more detailed understanding of the atomic processes which are responsible for the spectra. The role of absorption in furthering the atomic physics has always been prominent and in the experiment reported here, provides additional information concerning the behavior of the sodium vapor.

Certain aspects of the absorption process can be quantified without a detailed understanding of the atomic mechanisms that cause absorption other than the experimentally observable fact that absorption depends on frequency of the incident radiation. For example, consider a collimated beam of light of intensity I_0 and frequency ν , incident on a volume of homogeneous gas. Also, assume that the gas is capable of absorbing radiation but that its temperature is low enough so that emission does not occur. Then the amount of the incident beam absorbed (δI_ν) in a differential distance (δz) along the path of the beam is proportional to the incident intensity (I_{ν_0}) times differential distance (δz).¹⁴ If a constant of proportionality (μ_ν) is specified, absorption is given by:

$$\delta I_\nu = -\mu_\nu I_{\nu 0} \delta z \quad (1)^*$$

The constant of proportionality μ_ν is the linear or volume absorption coefficient at the frequency ν defined by

$$\mu_\nu = \lim_{\delta z \rightarrow 0} \left\{ \frac{\delta I_\nu}{I_{\nu 0} \delta z} \right\} \quad (2)$$

In the limit as $\delta z \rightarrow 0$, equation (1) becomes a differential equation which when integrated becomes

$$I_\nu = I_{\nu 0} e^{-\mu_\nu z} \quad (3)$$

Equation (3) was first derived by Bouguer and later independently by Lambert.¹⁵ The coefficient μ_ν can be interpreted as an inverse length

$$\ell_\nu = \frac{1}{\mu_\nu} \quad (4)$$

so that equation (3) becomes

$$I_\nu = I_{\nu 0} e^{-\frac{z}{\ell_\nu}} \quad (5)$$

The length ℓ_ν is usually thought of as the mean free path for absorption and an equation of form identical to (3) can be derived by considering absorption as a loss of photons from the beam by collision with the gas atoms. However, this non-classical approach requires the introduction of a cross-section for the photon-atom "collision." The collision frequency ν_c is the product of the

* The subscripting with ν acknowledges that the incident radiation as well as the constant of proportionality are frequency dependent. The details of this frequency dependence will be explored later. At this point the frequency dependence is simply a statement of the experimentally observable fact that absorption depends on frequency.

cross-section $\sigma_{c\nu}$, the photon velocity v and the number density of the gas atoms N :

$$\nu_c = \sigma_{c\nu} v N \quad (7)$$

The mean free path is simply the photon velocity divided by the collision frequency so that

$$\ell_\nu = \frac{v}{\nu_c} = \frac{1}{\sigma_{c\nu} N} \quad (8)$$

Comparing equations (8) and (4) reveal that

$$\mu_\nu = \sigma_{c\nu} N \quad (9)$$

and an alternate form of equation (3) is

$$I_\nu = I_{\nu_0} e^{-\sigma_{c\nu} N z} \quad (10)$$

Equation (10) is generally referred to as Beer's law although it was originally formulated in terms of gas partial pressures rather than atom number density N . The two forms are, of course, equivalent since pressure is directly proportional to number density. The motivation for reformulating equation (3) as (10) is that for some gases, $\sigma_{c\nu}$ is essentially independent of N . In the form of equation (10) it is seen that absorption depends on the number of absorbers (atoms) N , a relation which might be expected intuitively. As to whether or not $\sigma_{c\nu}$ depends on N is not intuitive and will be discussed later. Sodium vapor near its resonance, in particular, will not have $\sigma_{c\nu}$ independent of N .

The absorption of light by a gas as described by either equation (3) or (10) forms the basis for this experimental study. By simply measuring the ratio I_ν/I_{ν_0} as a function of frequency ν and suitably

determining the length of the optical path z through the gas, one can determine the absorption coefficient μ , as a function of frequency.

The remainder of chapter 2 will be devoted to showing how the absorption coefficient depends on the incident light frequency and the fundamental atomic properties. The role of line broadening mechanisms will be introduced and the generalized absorption behavior will be simplified to the form used in the far wing for this study. Using the far wing approximation, the absorption will be predicted for comparison to measurements.

2.2 Classical Absorption Theory

In the classical treatment of the interaction between an electromagnetic field and a dielectric medium, Lorentz¹⁶ considered the medium composed of damped harmonic oscillators. The response of the damped harmonic oscillators can be related to the complex index of refraction given by the following expression (see Appendix A for the derivation):

$$\hat{n}^2 - 1 = \frac{Ne^2}{\epsilon_0 m} \frac{1}{\omega_r^2 - \omega^2 + i\gamma_r \omega} \quad (11)$$

The complex index of refraction is defined as

$$\hat{n} = n - i\kappa \quad (12)$$

where n is the real index of refraction which is equal to the ratio c/v

κ is the extinction coefficient and represents the damping. Expanding the expression for $\hat{n}^2 - 1$ (noting that $n \gg 1$ and the extinction coefficient is typically 2 orders of magnitude less than n so that $\kappa^2 \approx 0$) gives the following relation

$$\frac{\hat{n}^2 - 1}{2} \approx (n^2 - 1) - i\kappa \quad (13)$$

Separating the real and imaginary parts of the RHS of equation (11), equating to the RHS of equation (13) and then equating the coefficients of the imaginary parts yields

$$\kappa = \frac{Ne^2}{2\epsilon_0 m} \frac{\gamma_r \omega}{(\omega_r^2 - \omega^2)^2 + \gamma_r^2 \omega^2}$$

$$= \frac{Ne^2}{2\epsilon_0 m \gamma_r \omega} \frac{1}{1 + \left[(\omega_r^2 - \omega^2) / \gamma_r \omega \right]^2} \quad (14)$$

However, for frequencies ω near the resonant frequency ω_r (i.e., $\omega \cong \omega_r$)

$$\omega_r^2 - \omega^2 \cong 2\omega(\omega_r - \omega) \quad (15)$$

substituting equation (15) into (14)

$$\kappa = \frac{Ne^2}{2\epsilon_0 m \gamma_r \omega_r} \frac{1}{1 + \left[2(\omega_r - \omega) / \gamma_r \right]^2} \quad (16)$$

Examining equation (16) reveals that κ is proportional to the number density of the absorbing atoms suggesting that a preferred parameter for the absorption would be κ/N . It is also seen that the frequency dependence of κ for a given resonant frequency ω_r consists of the factor $(\omega_r - \omega)/\gamma_r$ where, to a good approximation,

$$\gamma_r = \frac{e^2 \omega_r^2}{6\pi\epsilon_0 mc^3} \quad (17)$$

When $(\omega_r - \omega) = \frac{1}{2} \gamma_r$, it can be seen from equation (16) that κ is 1/2 of its maximum value. Therefore, γ_r is the full width of the line at half maximum, commonly referred to as the half-width. The frequency dependence is non-dimensionalized by the line half-width γ_r so that the extinction coefficient depends on the frequency separation from the resonant frequency $(\omega_r - \omega)$ in terms of the line width (γ_r). It follows that $(\omega_r - \omega)/\gamma_r$ is a natural variable to describe resonant

absorptive behavior.

At many line widths from the resonance, the squared term in the denominator of equation (16) dominates and

$$\begin{aligned}\kappa &\cong \frac{Ne^2}{2\epsilon_0 m \gamma_r \omega_r} \frac{1}{\left[2(\omega_r - \omega)/\gamma_r\right]^2} \\ &\cong \frac{Ne^2 \gamma_r}{8\epsilon_0 m \omega_r} \frac{1}{(\omega_r - \omega)^2}\end{aligned}\tag{18}$$

Therefore, in the wings of the line the extinction coefficient varies directly with the half-width γ_r suggesting still another parameter for absorption, $\kappa/N\gamma_r$. Recalling the definition of γ_r (equation 17), this does not appear to provide a preferred parameter for absorption because γ_r simply depends on atomic constants and ω_r . However, the introduction of line broadening mechanisms and the properties on which they depend will reveal why the far wing absorption behavior is related to line width. The role of line broadening will be introduced later. Before leaving the classical concept of absorption, it is noted that if the parameter $\kappa/N\gamma_r$ is chosen to describe the wing behavior, then the frequency dependence is simply $1/(\omega_r - \omega)^2$, the inverse of the square of the frequency separation from the resonance.

2.3 Oscillator Strength

The concept of oscillator strength was introduced to reconcile the difference between the measured and the theoretical absorption. The factor associated with the ability of an atom to absorb (or emit) a spectral line is the f -value. It can be interpreted⁹ as the ratio of the "dispersion electrons" to the total number of atoms and is found to be a constant (between 0 and 1) for a particular spectral line (transition). The f -value is proportional to the Einstein A coefficient and for a resonance line, it is inversely proportional to the lifetime of the resonance.

The f -value can be determined by integrating the absorption coefficient over the width of the spectral line.

$$f = \frac{mc}{\pi e^2 N} \int_0^\infty \mu_\nu d\nu \quad (19)$$

Taking the point of view that the f -value is the number of dispersion electrons, the number density N in equation (18) for the extinction coefficient should be replaced by Nf_r

$$\kappa \cong \frac{Ne^2 f_r \gamma_r}{8 \epsilon_0 m \omega_r} \frac{1}{(\omega_r - \omega)^2} \quad (20)$$

Equation (20) represents the extent of absorptive behavior that can be explained with classical theory and was developed well before the Einstein theory. The fact that a correction factor was needed points to a potential shortcoming of classical theory. Quantum theory goes beyond the classical approach and explains the departures from classical behavior. In the case of this study of resonant absorption

in sodium vapor at relatively low temperatures, classical theory will be adequate; but, it will be necessary to briefly examine quantum theory to establish why this is true.

2.4 Absorption Considering Quantum Mechanical Concepts

The introduction of quantum mechanical concepts will be essential to an accurate description of resonant absorption because the damping constant γ_r (or natural line width) in the classical theory grossly underestimates the line width for sodium vapor conditions of interest here. In addition, quantum mechanical concepts provide a more concise understanding of other parameters affecting resonant absorption but, as will be seen, they do not provide any fundamentally new inputs to the absorption model for sodium vapor required in this study.

Blendstrup⁵ has shown that the classical model can be modified to include quantum mechanical concepts by replacing classical parameters with those from quantum mechanics. Table 2 compares the two models. Applying these modifications to equation (16) gives a quantum mechanical representation of an absorptive transition between a lower state and some upper state:

$$\kappa = \frac{e^2 f_{lu}}{2 \epsilon_0 m \gamma_{lu} \omega_{lu}} \left\{ N_l \left[\frac{1}{1 + \left[2(\omega - \omega_{lu})/\gamma_{lu} \right]^2} \right] - \frac{g_l}{g_u} N_u \left[\frac{1}{1 + \left[2(\omega - \omega_{lu})/\gamma_{ul} \right]^2} \right] \right\} \quad (21)$$

Comparing equations (21) and (16) shows the similarity in form for either the upward or downward transition but clearly the second term for the downward transition (emission) is not considered in formulation of the classical model. The importance of the second term relative to the first becomes apparent by examining N_l and N_u . For a gas in

Table 2. Comparison of Classical and Quantum Mechanical Absorption Parameters

Parameter	Classical Lorentz Model	Quantum Mechanical Model
Oscillator resonant frequency	ω_r	$\omega_{qu} = (E_u - E_l)/\hbar$
Damping constant	$\gamma_r = \frac{e^2 \omega_r^2}{6\pi\epsilon_0 mc^3}$	$\gamma_{qu} = \frac{1}{\tau_{qu}} \sim A_{qu}$ actual line width
Oscillator number density	$N = p_i/kT$ (p_i = gas partial pressure)	N_l, N_u where $\frac{N_u}{N_l} = e^{-\omega_{qu} \cdot \hbar/kT}$ population density of state
Oscillator strength	f_r an empirical constant	f_{qu} (for absorption transition) transition probability

Note: $\hbar = \frac{h}{2\pi}$

thermal equilibrium, the ratio of population densities is given by

$$\frac{N_u}{N_l} = e^{-\omega_{ul} \cdot \hbar/kT} \quad (22)$$

At optical frequencies such as the sodium D-lines, the temperature equivalent of $\omega_{ul} \hbar/k$ is $24,400^\circ\text{K}$ which is very much larger than the sodium vapor experimental temperature investigated here (750°K , maximum). At the experimental temperature, the ratio N_u/N_l would be approximately 7×10^{-15} and the second term of equation (21) can be ignored. This reduces equation (21) to the form identical to equation (16) except that γ_{lu} has replaced γ_r and $N_l f_{lu}$ has replaced N^* . The far wing approximation then becomes

$$\kappa \cong \frac{N e^2 \gamma_{lu}}{8 \epsilon_0 m \omega_{lu}} \frac{1}{(\omega_{lu} - \omega)^2} \quad (23)$$

To complete the theoretical treatment of sodium resonant absorption it will be necessary to examine line broadening mechanisms and establish the line width γ_{lu} to use in the above equation. This will be the subject of the next section.

* Actually, as a consequence of equation (22), a very good approximation for N_l is N ; i.e., $N_l \cong N$.

2.5 Line Broadening Mechanisms

In the classical treatment, the excited electron oscillates in a damped motion as it relaxes to the unexcited state. The time constant for this motion τ is the inverse of the classical damping constant γ_r . For oscillation frequencies in the visible spectrum, the value of τ (the transition lifetime) is of the order 10^{-8} seconds.¹⁶ Because the frequency is very high, the number of oscillatory cycles during the lifetime of the excited state is of the order 10^7 . It follows that the reduction in amplitude during one cycle, although very small, results in radiation that is not monochromatic. The line width of radiation from a collection of unperturbed classical oscillators would be very small but experimental evidence shows that actual line widths are orders of magnitude larger than the natural width γ_r . Clearly, other more dominant processes are involved.

Broadening of an absorption line can be due to any of the following effects:

- 1) Natural broadening due to the natural lifetimes of the excited state.
- 2) Doppler broadening due to thermal motions of the radiating atoms.
- 3) Pressure broadening due to the interaction of the radiating atom with the surrounding particles. Pressure broadening can be further classified in terms of the interacting particle:
 - a) Stark broadening due to interaction with charged particles (electrons or ions),

- b) Resonant broadening due to interaction with neutral atoms of the same kind and
- c) van der Waals broadening due to interaction with other atoms.

The experimental investigation here utilized sodium vapor at temperatures sufficiently low so that ionization would be negligible and consequently Stark broadening could not be expected.

Pressure Broadening

Pressure broadening due to collisions with foreign gases and due to collisions with other atoms of the same kind (self-broadening) are now recognized as equivalent processes based on recent studies. Broadening due to collisions with other gases is proportional to the number density of the foreign gas.¹¹ In the case of self-broadening, the broadening is proportional to the number density of the absorber.⁴ Broadening due to collisions (with atoms of either the same kind or foreign atoms) is, therefore, proportional to the number density of the perturber. For this study, self-broadening is expected and Niemax and Pichler⁴ have measured sodium D-line self-broadening to show that

$$\gamma_c = \frac{2\pi}{3} C_3 N$$

or

$$\gamma_c = C_r N \quad (24)*$$

* The units for γ_c are rad/sec and γ_c is the full width at 1/2 maximum. The subscript c is to be interpreted as representing collision broadening.

Lorentz¹⁷ recognized that natural broadening and collision broadening could be combined (because of the similarity of the damping processes) into a single damping term of the form

$$\begin{aligned}\gamma_L &= \gamma_r + \gamma_c \\ &= \gamma_r + C_r N\end{aligned}\tag{25}$$

Doppler Broadening

When the absorbing atoms of a gas are moving in the direction of the propagation of the incident radiation (at frequency ν_r), they will absorb a frequency

$$\nu = \nu_r (1 - v_z/c)\tag{26}$$

The fraction of atoms within a speed range dv_z is¹⁸

$$\frac{dN}{N} = \sqrt{\frac{M}{2\pi kT}} e^{-(M/2kT)v_z^2} dv_z\tag{27}$$

where M = mass of the absorbing atom, kg
 k = Boltzman's constant, joules/⁰K
 T = temperature, ⁰K

Equation (27) also represents the fraction of the total incident intensity absorbed at frequency ν . The intensity over the entire absorption line is

$$I_\nu = \sqrt{\frac{Mc^2}{2\pi kT \nu_r^2}} e^{-(Mc^2/2kT \nu_r^2)(\nu - \nu_r)^2}\tag{28}$$

The Doppler half-width of the line is

$$\Delta\nu_D = \frac{2\nu_r}{c} \sqrt{\ln 2} \sqrt{\frac{2kT}{M}}\tag{29}$$

Substituting equation (29) into (28) gives

$$I_{\nu} = \frac{2\sqrt{\ln 2}}{\sqrt{\pi}} \frac{1}{\nu_r} e^{-4 \ln 2 \left(\frac{\nu - \nu_r}{\Delta \nu_D}\right)^2} \quad (30)$$

A comparison of the shape of a Doppler broadened line with a Lorentzian line is shown in Figure 1 and was obtained by generating line shapes from equation (30) (Doppler) and equation (16) (Lorentzian). At frequencies less than half the line width from the line center, little difference between the two line shapes is seen. However, at frequencies greater than half the line width from the line center, the Doppler line intensity decays rapidly to zero while the Lorentzian line intensity decays considerably slower. As a consequence, the absorption in the far wings of the sodium D-lines should display Lorentzian behavior with an inverse square dependence on the separation from the line center as specified by the approximation of equation (20).

Relative Sizes of Broadening

To put the three line widths (natural, collision and Doppler) in perspective, nominal values of each will be calculated for the conditions of this experiment. The natural width γ_r is given by equation (17).

$$\gamma_r = \frac{e^2 \omega_r^2}{6 \pi \epsilon_0 m c^3}$$

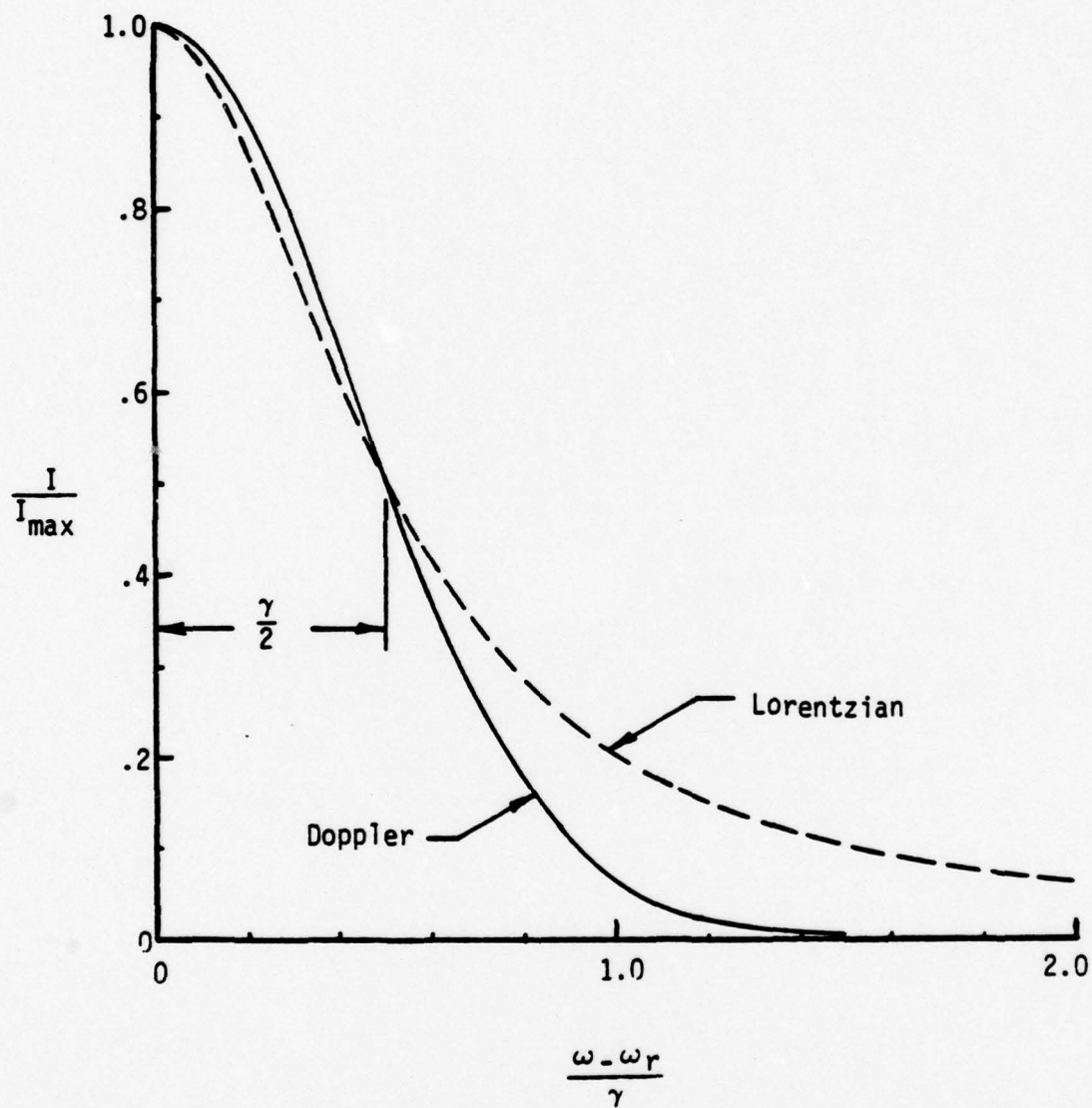


Figure 1. Comparison of Doppler and Lorentzian Lineshapes with Equal Intensities and Linewidths

where $e = 1.602 \times 10^{-19}$ coulombs

$$\omega_r = 2\pi \frac{c}{\lambda_r} = 2\pi \frac{2.9979 \times 10^{10} \text{ cm/sec.}}{5890 \times 10^{-8} \text{ cm}}$$

$$= 3.198 \times 10^{15} \text{ rad/sec.}$$

$$\epsilon_0 = 8.85 \times 10^{-12} \text{ farads/m}$$

$$m = 9.109 \times 10^{-31} \text{ kg}$$

$$c = 2.9979 \times 10^8 \text{ m/sec.}$$

$$\gamma_r = \frac{(1.602 \times 10^{-19} \times 3.198 \times 10^{15})^2}{6\pi \times 8.85 \times 10^{-12} \times 9.109 \times 10^{-31} (2.9979 \times 10^8)^3}$$

$$= 6.4 \times 10^7 \text{ rad/sec}$$

$$\gamma_r = 0.00012 \text{ A}^0$$

The collision width is given by equation (24)

$$\gamma_c = C_r N$$

where $C_r = \frac{2\pi}{3} C_3$ from reference 4

$$= \frac{2\pi}{3} \times 5.2 \times 10^{-8} \text{ (rad/sec) cm}^3$$

$$= 1.09 \times 10^{-7}$$

$$= 1.09 \times 10^{-13} \text{ (rad/sec) m}^3$$

$$N = 2.5 \times 10^{22} \text{ 1/m}^3$$

$$\gamma_c = 1.09 \times 10^{-13} \times 2.5 \times 10^{22}$$

$$= 2.73 \times 10^9 \text{ rad/sec}$$

$$\gamma_c = 0.005 \text{ A}^0$$

Here it is seen that $\gamma_c \gg \gamma_r$ so that a good approximation of the Lorentzian line width is

$$\gamma_L \cong C_r N \quad (31)$$

The Doppler line width is given by equation (24)

$$\gamma_D = \frac{2\sqrt{\ln 2} \omega_r}{c} \sqrt{\frac{2kT}{M}}$$

where $\omega_r = 3.198 \times 10^{15}$ rad/sec

$c = 2.9979 \times 10^8$ m/sec

$k = 1.3805 \times 10^{-23}$ J/ $^{\circ}$ K $T = 763^{\circ}$ K

$$M = \frac{m}{Z} = \frac{22.99}{6.0225 \times 10^{23}}$$

$$= 3.82 \times 10^{-23} \text{ gm}$$

$$= 3.82 \times 10^{-26} \text{ kg}$$

$$\gamma_D = 2\sqrt{\ln 2} \frac{3.198 \times 10^{15}}{2.9979 \times 10^8} \sqrt{\frac{2 \times 1.3805 \times 10^{-23} \times 763}{3.82 \times 10^{-26}}}$$

$$= 1.32 \times 10^{10} \text{ rad/sec}$$

$$\gamma_D = 0.024 \text{ }^{\circ}\text{A}$$

Comparing γ_D to γ_L (which is $\cong \gamma_c$), it is found that the Doppler width is approximately 5 times larger than the Lorentzian width. Even though γ_D is larger than γ_L , the shape of the two line forms will ensure that the Doppler effect can be ignored in the far wings.

Finally, it is of interest to examine the separation from resonance in terms of line widths. Experimental data were collected in the blue

wing between 10 and 45 Å⁰ from the D₂-line. As discussed above, the Lorentzian line width will control the far wing behavior and the range of the experiment will extend from 2000 to 9000 Lorentzian line widths from resonance.

2.6 Predicted Far Wing Absorption

The far wing approximation for the extinction coefficient given in equation (20) will be used to predict the absorption measured in this study. The natural line width γ_r will be replaced with the Lorentzian width γ_L which was shown to be closely approximated by $\gamma_c = C_r N$. In the discussion following equation (18), an absorption parameter $\kappa/N\gamma$ was suggested without proof. It can now be seen that with the above assumptions

$$\frac{\kappa}{N\gamma} \sim \frac{\kappa}{N^2}$$

and equation (20) becomes

$$\frac{\kappa}{N^2} \cong \frac{e^2 f_r C_r}{8 \epsilon_0 m \omega_r} \frac{1}{(\omega_r - \omega)^2} \quad (32)$$

where κ/N^2 is seen to depend on the frequency separation from resonance and a collection of physical constants. This expression will be converted to the absorption coefficient μ which is related to the extinction coefficient by

$$\mu = \frac{2\omega}{c} \kappa \quad (33)$$

which gives

$$\frac{\mu}{N^2} \cong \frac{e^2 f_r C_r}{4 \epsilon_0 m c} \frac{1}{(\omega_r - \omega)^2} \quad (34)$$

where

e	$=$	1.602×10^{-19}	coulombs
f_r	$=$	0.655	(reference 3)
C_r	$=$	$1.09 \times 10^{-13} \frac{\text{rad}}{\text{sec}}$	$\cdot \text{m}^3$ (see Section 2.5)

$$= 1.73 \times 10^{-14} \frac{\text{cycles}}{\text{sec}} - m^3$$

$$\epsilon_0 = 8.85 \times 10^{-12} \text{ farads/m}$$

$$m = 9.109 \times 10^{-31} \text{ kg}$$

$$c = 2.9979 \times 10^8 \text{ m/sec}$$

We evaluate the constant as follows:

$$\begin{aligned} \frac{e^2 f_r C_r}{4 \epsilon_0 m c} &= \frac{(1.602 \times 10^{-19})^2 0.655 \times 1.73 \times 10^{-14}}{4 \times 8.85 \times 10^{-12} \times 9.109 \times 10^{-31} \times 2.9979 \times 10^8} \\ &= 3.01 \times 10^{-20} \frac{m^5}{\text{sec}^2} \end{aligned}$$

$$\boxed{\frac{\mu}{N^2} = \frac{3.01 \times 10^{-20}}{(\omega_r - \omega)^2}} \quad (35)$$

Another form of equation (34) is

$$\mu = \frac{e^2 f_r}{4 \epsilon_0 m c C_r} \frac{\gamma_L^2}{(\omega_r - \omega)^2} \quad (36)$$

Thus, there results

$$\begin{aligned} \frac{e^2 f_r}{4 \epsilon_0 m c C_r} &= \frac{(1.602 \times 10^{-19})^2 .655}{4 \times 8.85 \times 10^{-12} \times 9.109 \times 10^{-31} \times 2.9979 \times 10^8 \times 1.73 \times 10^{-14}} \\ &= 1.01 \times 10^8 \text{ m}^{-1} \end{aligned}$$

$$\boxed{\mu = \frac{1.01 \times 10^8}{X^2} \text{ in the units of } m^{-1}} \quad (37)$$

where $X \equiv \frac{\omega_r - \omega}{\gamma_L}$

3.0 EXPERIMENTAL EQUIPMENT AND TECHNIQUE

3.1 Experimental Design

The measurement of the absorption of light by a gas, as described in Section 2.1, is simply the measurement of the attenuation a beam of light experiences when passing through a length of the gas. Equation (3) can be rewritten in the form used to analyze the experimental data.

$$\mu_{\nu} = \frac{\ln (I_{\nu 0} / I_{\nu})}{z} \quad (38)$$

Where $I_{\nu 0}$ = light intensity at frequency ν after passing through all optical components of the experiment without sodium vapor present.

I_{ν} = light intensity at frequency ν after passing through all optical components of the experiment with the sodium vapor "inserted" in the optical path.

z = the length of sodium vapor column along the optical path.

Determining the absorption coefficient μ_{ν} as a function of frequency ν is simply a matter of measuring the attenuated beam intensity I_{ν} and the unattenuated beam intensity $I_{\nu 0}$ at discrete frequencies. This is accomplished by scanning the desired portion of the spectrum near the D_2 -line with the monochromator. Determining the length of sodium vapor column might appear to be a simple matter but, as will be pointed out in the discussion of the heat pipe oven, this experimental variable could not be determined by direct measurement.

One additional measurement is required to correlate μ_{ν} with the theory and that is the number density N of the sodium atoms. No

attempt was made to measure N because sodium vapor pressure relations are well documented.⁵ Vapor pressure was measured and number density was calculated from the equation of state.

The design of the experiment to measure absorption must consider a number of other aspects:

- 1) The intensity of the light source must be high enough to produce a measurable amount of transmitted light at the sodium vapor densities used in the refractive experiment over the frequency range of interest. This is an important requirement since it was desirable to measure the absorption at exactly the same sodium vapor conditions used in the refractive experiment.
- 2) The absorption measurements must not interfere with the optical adjustment of the laser or interferometer.
- 3) The stability of the light source and the recording equipment and the sodium vapor must be consistent with minimum drifts over the period of data collection which was as long as 24 hours.
- 4) In situ calibration of the overall recording system is desired.
- 5) The technique for generating the sodium vapor must eliminate (or minimize) absorbing or scattering phenomena in the beam. An item of major concern is condensation of sodium on optical windows in the sodium container.
- 6) The spectral resolution of the dispersing device (monochromator) must be sufficient to separate features of the spectrum.

The achievement of these experimental objectives will be discussed in the following section along with the component descriptions. In cases where the objectives are not met, an insight into possible experimental errors will be treated.

3.2 Experimental Apparatus

The apparatus used in the refractive experiment (described in reference 5) along with the additional equipment used for the absorption measurements is shown in Figure 2. The addition of the collimated light source and the monochromator are the items used specifically for the absorption portion of the experiment. As shown in Figure 2, the light source and the monochromator are added to the optical arrangement by inserting mirrors at locations M_3 and M_4 to deflect the beam into the interferometer and out to the monochromator. This is accomplished without disturbing any of the optical adjustments of the interferometer or dye laser used in the refractive experiment. The light beam through the interferometer was blocked to excluded the longer heat pipe oven and only the shorter oven was used for absorption measurements. Use of the shorter heat pipe oven was necessary to obtain a measureable light output over the frequency range of interest with available the light source.* The specific details of each of the components of the absorption experiment will now be described.

Light Source

Light from a 500 watt, quartz enclosed, incandescent filament lamp was collimated and directed into the interferometer by mirror M_3 shown in Figure 2. The beam was aligned with the optical axis of the short oven and arranged to fill the aperature of the end windows. The

* The dye laser was found to be unsuitable for use in the absorptive experiments due to the short pulse duration (5 nanoseconds) which leads to recorder response problems and due to pulse-to-pulse variations in intensity.

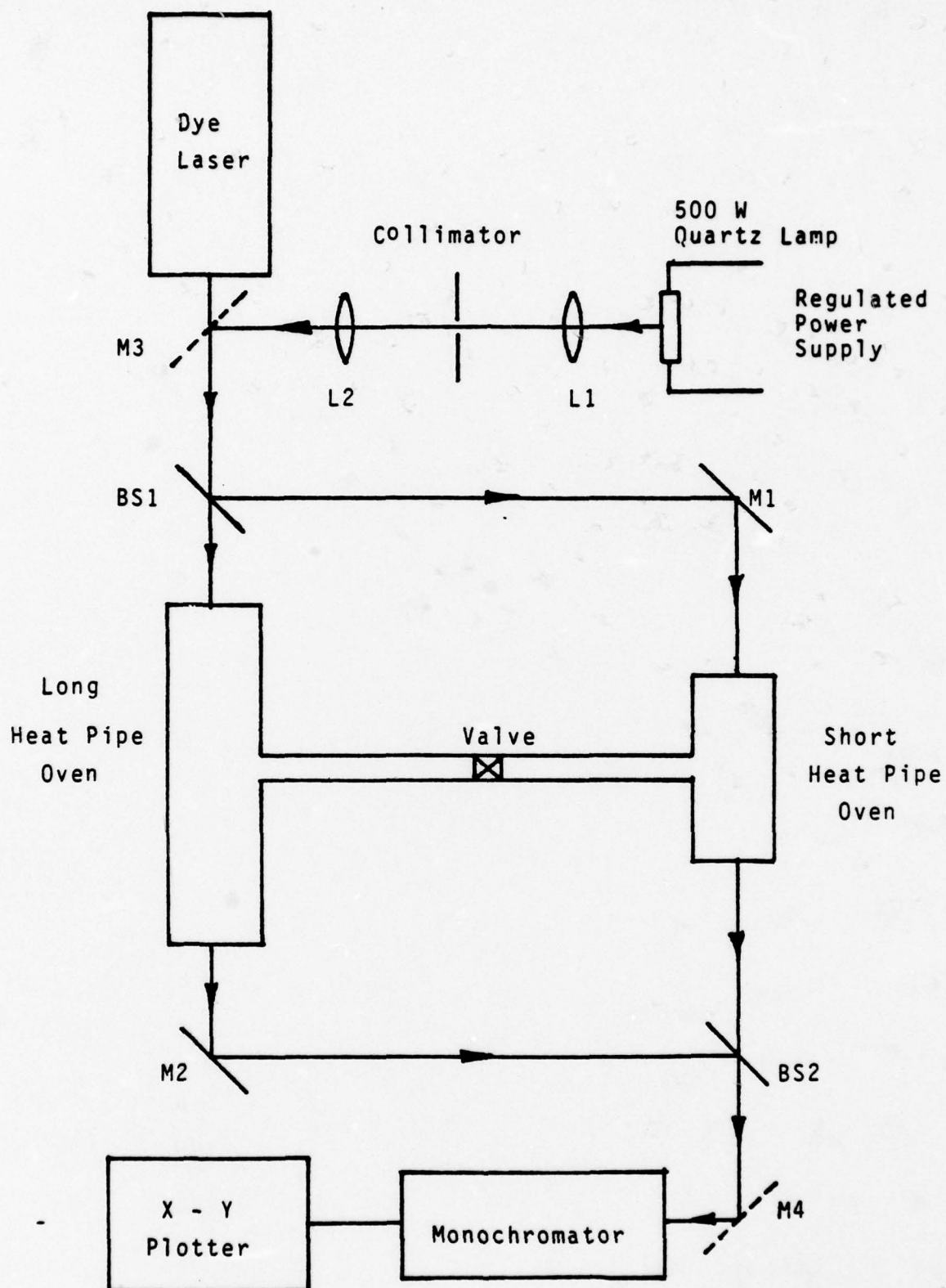


Figure 2. Schematic of Experimental Equipment

output beam was deflected to the monochromator by mirror M_4 and focused on the input slit.

Power to the lamp was provided with a voltage regulated power supply to avoid fluctuations in intensity due to variations in line voltage. Because incandescent filaments show a large sensitivity of light intensity to voltage and due to the extended period between initial and final unattenuated intensity measurements (up to 24 hours), a regulated power supply was considered necessary.

The intensity of the lamp was sufficient to obtain measureable output to within 12 \AA^0 of line center at a sodium vapor pressure of 2.0 torr and 5 \AA^0 at 1.3 torr with the short heat pipe oven. This was sufficient intensity to cover the wavelength range of the refractive experiment which extended to within 9 \AA^0 of the line center. The spectral output of the lamp was documented from 5890 \AA^0 (line center) to 5845 \AA^0 . No variation in intensity was detected throughout the above range of wavelengths and I_{ν_0} was assumed to be a constant value independent of frequency ν .

Heat Pipe Oven

The heat pipe as first conceived by Grover et al¹⁹ as a device with unusually high thermal conductivity was modified by Vidal and Cooper⁶ to operate as an oven for the generation and containment of metal vapors. The heat pipe oven consists of a tube with an external heater covering a portion of the tube at mid-length. Solid sodium added to the tube is melted by the heater and flows into the layers of metal screen which covers the internal perimeter of the tube. Sufficient

sodium is provided so that the entire screen matrix is fully wetted by the liquid sodium and the liquid sodium remains in thermal equilibrium with the saturated vapor. In regions just inboard from the tube ends, external cooling is provided by several rows of water cooled tubing. Within the cooled region, sodium vapor condenses and collects in the screen where it is transported back to the heated region by capillary action. An inert buffer gas, argon in this experiment, is added to the tube prior to sodium melt-down and is swept to the cool end regions by convective currents within the sodium vapor as it moves to the end zones where condensation occurs. Because sodium is carried back toward the tube center by capillary action and argon is not, the argon remains in the end regions and protects optical windows located there. However, diffusion of the argon into the sodium does effect the concentration boundary layer between the sodium and the argon. The velocity at which argon diffuses into the sodium is opposed by the mass velocity of sodium vapor moving to replace vapor which has condensed in the cooled regions. Since the rate of condensation is proportional to the heat loss (or heat input), the mass velocity of the sodium toward the cooled regions must be proportional to the heat input. At low powers it could be expected to find a thicker concentration boundary layer between the two gases than at high powers. Vidal and Cooper⁶ experimentally explored the thermal boundary layers in the end regions and found the axial distance for which the temperature drops 100°C from the steady temperature in the central region is approximately 2.5 cm. Although this is a reasonably small boundary in the short heat pipe oven with

a nominal length of 1 m, the extent of the concentration boundary has not been established and will be a point of concern in interpretation of the experimental results (Chapter 4.0).

Vidal and Cooper⁶ have shown that increasing the power to the heat pipe oven (at constant pressure) tends to move the condensation zone closer to the tube ends but does not alter the thermal profile within the condensation region. This presumably occurs because the condensation zone moves along the axial thermal gradient, which must exist in the wall, until the temperature difference between the condensate and the local wall temperature is sufficient to dissipate the input power to the cooling water. Because the thermal profiles are identical, variations in input power can be used to create changes in the length of the constant temperature internal region that can be used to determine the absolute length of the vapor column. This experiment, because of the need to generate different conditions in each heat pipe oven for interferometric reasons, could not employ this technique to measure vapor column length. Furthermore, the mechanical arrangement of the apparatus did not allow the argon pressure to be controlled externally. The method used to determine vapor column length will be discussed in Section 3.4.

The use of heat pipe ovens for the generation and confinement of sodium vapors is tied to two features:

- 1) homogeneous spatial temperature and hence density distribution which is constant over long periods of time and
- 2) the isolation of optical windows from the sodium vapor by an inert buffer gas.

These features of the heat pipe oven were instrumental in their successful use in this experiment. The details of their operation and temperature control is described in reference 5.

Monochromator

A McPherson model 2051, 1 meter scanning monochromator was used to measure the spectral output in the absorption experiment. The monochromator uses a diffraction grating with 1200 lines/mm giving a dispersion of 8.33 \AA/mm at the focal plane (output slit). The input and output slits are adjustable from 5 to 2000 microns. Slit widths of 50 microns were used for these experiments giving an effective slit width (at the focal plane) of 0.42 \AA . In terms of scanning the far wing of the D_2 -line from 5890 to 5845 \AA , this will provide considerably greater resolution than required. However, the rotational lines of Na_2 in this wavelength range are closely spaced with separations as small as 0.69 \AA . A slit width of 50 microns is clearly insufficient for resolving the rotational lines of Na_2 . At a minimum slit width of 5 microns (0.042 \AA at the focal plane), the specification resolution limit of the monochromator of 0.1 \AA could be obtained. This would, however, require a ten-fold increase in light source intensity to obtain a measureable light signal at 10 \AA from line center. Since the main objective of this experiment was to document absorption in the wavelength range explored during the refractive experiments, a slit width of 50 micron was chosen. As a result, in the spectral regions where Na_2 absorption becomes discernable, errors in atomic sodium absorption will occur due to the inability to resolve the Na_2 rotational spectrum.

Wavelength scanning is accomplished with a precision drive mechanism which rotates the grating to produce a linear time rate of change in wavelength. This mechanism has wavelength reproducibility of 0.1 \AA and has a wavelength counter (in \AA) which is accurate to 0.5 \AA . The wavelength counter was used as the primary wavelength standard. A check on wavelength positioning of the drive was possible by comparing the location of Na_2 rotational spectrum features during successive scans.

A photomultiplier tube (PMT) at the output slit was used to detect the dispersed light signal. An uncooled EMI 9658-B PMT was used with a Fluke 421B high voltage power supply providing the necessary voltage for the dynodes. The voltage to the PMT was adjusted to maximize the gain but was limited to values below where nonlinearities were observed (see Calibrations, Section 3.3).

Recorder

The output of the PMT was recorded on a Hewlett-Packard Model 7004B, x-y plotter. This plotter has a specified accuracy of $\pm 0.2\%$ of full scale with a linearity of $\pm 0.1\%$. Frequency response of the servo drive mechanism depends on the amplitude of the signal being recorded. The time spent scanning the 45 \AA from 5890 \AA to 5845 \AA was approximately 380 seconds and no problem could be expected in following the slowly varying intensity due to atomic sodium absorption. Because of the close spacing of the rotational lines of Na_2 , the time to scan a line was approximately 5 seconds. At deflections experienced for the Na_2 lines of approximately 0.5 inch, the specified maximum frequency for

linear plotting is 10 cps. Consequently, the plotter is easily capable of following the spectral induced transients expected.

3.3 Calibrations

Several calibrations of the recording devices were carried out to establish the best operational range of certain instrumental variables and to establish end-to-end sensitivities of the apparatus. These calibrations are described here.

PMT Linearity

The gain of a PMT is sensitive to the supply voltage and as voltage is increased to near maximum values to increase the output, non-linearities can arise from large currents through the PMT²⁰. To establish a usable gain within the linear range of operation, the output from the light source was recorded with various neutral density filters inserted into the beam. By comparing the change in recorded signal with the transmission factor of the neutral density filter, deviations from linearity could be measured. The supply voltage to the PMT was increased until unacceptable non-linearities were observed. At 900 VDC, the non-linearities varied between 1.0 and 1.5 percent of full output. Since this was considered an acceptable error, 900 VDC to the PMT was used for the absorption measurements.

Spectral Response of PMT/Light Source

The sensitivity of the photocathode of a PMT depends on the wavelength of the incident radiation²⁰ and although this could be expected to be a minor change over a wavelength range of 45 Å⁰, documentation of this change eliminates an experimental error. Furthermore, the spectral characteristics of the light source was not known. To establish the combined spectral characteristics of the photocathode and the light

source as well as the heat pipe oven windows, mirrors and the lens used to focus the output on the monochromator slit, the spectrum from 5890 to 5845 $\overset{0}{\text{\AA}}$ was scanned. The optical path was identical to that used during absorption measurements except that no sodium vapor was present (oven was not heated). It was found that the deviation from a constant output over the wavelength range was less than 0.5% of full-scale intensity as determined by the median of the peak-to-peak noise. The peak-to-peak noise level was 2.1% of full-scale intensity so that the deviation from constant intensity over the wavelength range was within the noise band. Therefore, the formalism of treating the unattenuated intensity as frequency dependent (I_{ν_0} in equation 38) is not required and the unattenuated intensity can be treated as a constant I_0 .

Wavelength Calibration of x-y Plotter

The scanning monochromator uses a precision drive mechanism to affect a sweep of wavelength. This drive has been found to be very accurate supporting the claim to 0.1 $\overset{0}{\text{\AA}}$ reproducibility. Wavelength, therefore, becomes a linear function of time. The x-axis of the plotter is driven at a constant speed which inverts the x-axis back to wavelength. Although the sweep rate of the plotter x-axis was quite repeatable, the rate was sufficiently different from the front panel value to merit a calibration of wavelength on the x-axis. The monochromator scan was started and as the wavelength counter registered 5890 $\overset{0}{\text{\AA}}$, the sweep of the x-axis was initiated. As the wavelength counter registered specific wavelength values, the x-location of the

pen was marked. The change in wavelength per x-axis distance was found to vary by only 0.3% as checked at several wavelength readings over the 45 Å range of the scan. This would account for a maximum error of 0.1 Å in reading wavelength from the plotter output. As this value is considerably smaller than the accuracy with which the wavelength counter can be read, determination of wavelength should be considered accurate to ± 0.5 Å⁰.

Time Constant of Recorder

As described in Appendix B, noise generated by thermal emission in a PMT can be damped by including capacitance connected across the input terminals of the x-y recorder. A capacitance of 0.68 mfd was selected which produces a time constant τ of 0.72 seconds (see Figure B-2) and a signal-to-noise ratio S/N of approximately 40 (see Figure B-3). The time to scan the 45 Å wavelength range was 380 seconds so no distortion could be expected on this time scale. The time to scan a rotational line of Na₂ was approximately 5 seconds which is considerably larger than the time constant of 0.72 seconds. Therefore, no distortion of the rotational spectra can be expected as a result of adding damping to increase the overall recorder signal-to-noise ratio. The resolution of the Na₂ rotational lines is, consequently, a matter of monochromator resolution as determined by the slit width used to obtain a measureable signal over the wavelength range.

* The wavelength counter registers wavelength in 1 Å increments. The instant when the numeral is exactly centered in the window can be determined quite accurately but the true wavelength value can be different by ± 0.5 Å as stated in the specifications.

3.4 Experimental Methods and Techniques

With the heat pipe ovens cold, the light source was aligned with the optical axis of the short heat pipe oven by adjusting mirror M_3 in Figure 2. The mirror was adjusted to completely fill the output window of the heat pipe oven. Since the diameter of the collimated beam was somewhat larger than aperture of the interferometer, the alignment of light beam was not critical. Having established optical alignment, a monochromator scan of the wavelength range was made to document the value I_0 . The evacuated heat pipe oven was then filled with argon to an initial pressure $P_{Ar, in}$ and temperature T_1 . The valves to the heat pipe oven were then closed sealing the argon into a volume V composed of the free volume of the heat pipe oven plus tubing up to the valves. Heating to vaporize the sodium was started and continued for 6 to 8 hours until equilibrium was established in the ovens as detected by a constant internal pressure P_{Na} . Prior to the start of a refractive experiment, a spectral scan for the short heat pipe oven was made to measure I_v . The length of the sodium column within the oven was calculated assuming a thin interface between the sodium vapor and the argon⁵:

$$l_{Na} = \frac{V}{A} \left[1 - \frac{P_{Ar, in}}{P_{Na}} \left(\frac{T_2}{T_1} \right)_{Ar} \right] \quad (39)$$

where l_{Na} = length of sodium column

V = free volume of heat pipe oven and associated tubing to shut-off valves

A = cross-sectional area of heat pipe oven

$P_{Ar_{in}}$ = initial argon pressure (no sodium)

P_{Na} = pressure with sodium present

T_1 = initial argon temperature (no sodium)

T_2 = argon temperature with sodium present.

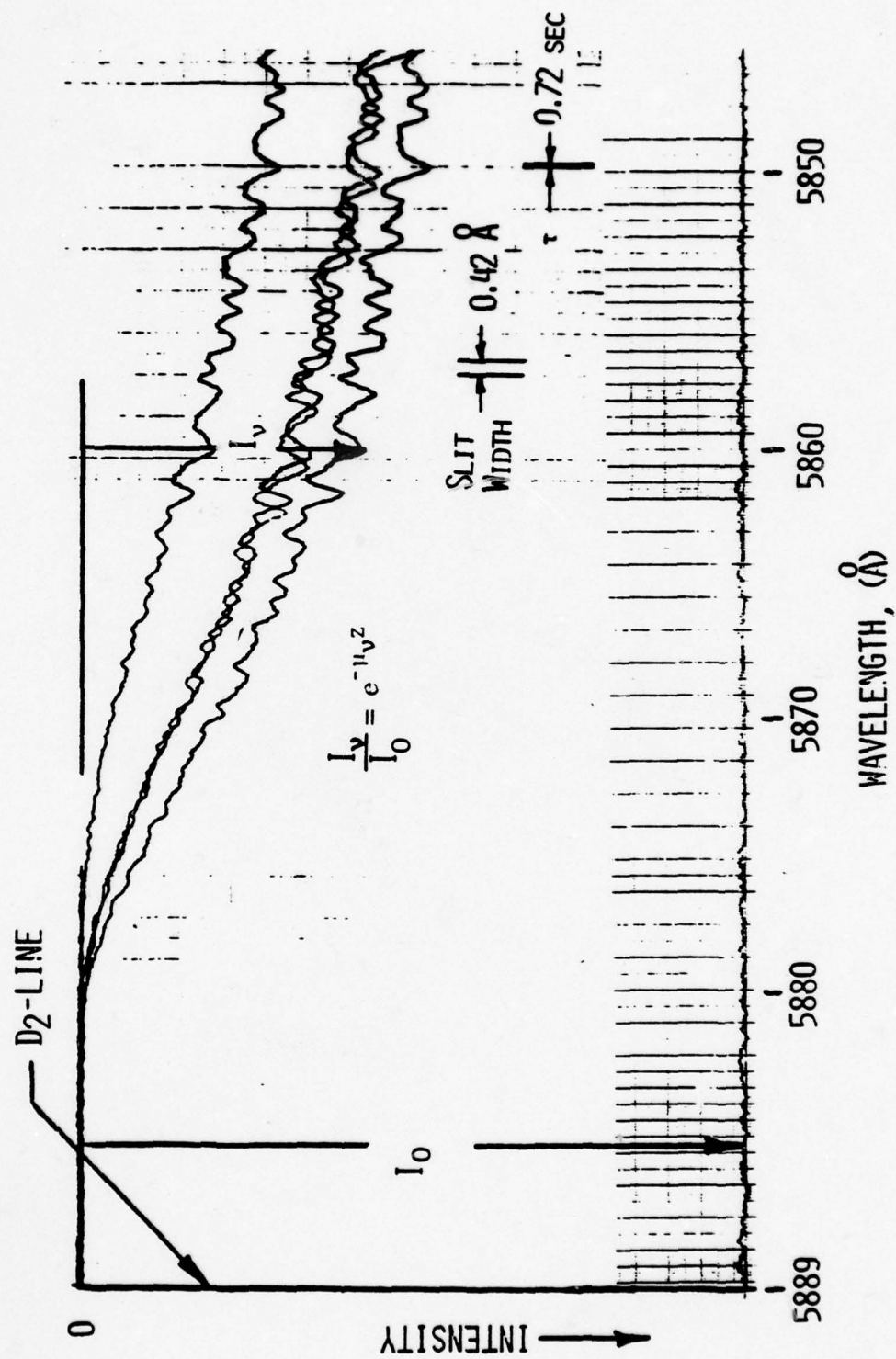
The refractive experiment was conducted by removing mirror M_3 and relocating M_4 to direct the output to the fringe counting PMT. One of the heat pipe oven temperatures was changed and the transient to return to equilibrium was monitored with the interferometer. After achieving equilibrium in the heat pipe oven, mirror M_3 and M_4 were relocated, the spectrum was again scanned with the monochromator and the new sodium column length was calculated from equation (39). This process was repeated several times in the period of a day with a final spectral scan at the end of the sequence. The heat pipe ovens were then allowed to cool down and a final check on I_0 was made by a spectral scan.

3.5 Results of Measurements

Figure 3 shows a typical series of spectral scans as recorded on the x-y plotter. The scan starts at the D_2 -line center at 5889 \AA and proceeds to lower wavelengths. Output intensity is measured downward on Figure 3 and the unattenuated intensity I_0 is shown at the bottom of the figure. Between the line center (5889 \AA) and 5880 \AA all of the incident light is absorbed and no measureable output is observed. At wavelengths less than 5880 \AA measureable output is shown by the four irregular lines which represent different heat pipe oven pressures. From the line center out to 5870 \AA the traces are smooth due to the heavy absorption of atomic sodium. Beyond 5870 \AA (to lower wavelength) the absorption of atomic sodium has decreased sufficiently so that the presence of molecular sodium (Na_2) can be observed. The individual peaks on the traces are due to the rotational lines of Na_2 and their regularity is evident by comparing the wave forms of the top and bottom traces. The two center traces appear shifted in wavelength due to minor errors in starting the wavelength scan.

The intensity at any frequency ν is indicated by the arrow labeled I_ν and was measured at the maximum value (valleys between Na_2 rotational lines) as being the best approximation of atomic sodium absorption. However, as discussed in section 3.2, the compromise on slit width to give measureable output near the line center does not give good resolution of Na_2 rotational lines. A qualitative impression of the resolution capability is obtained by comparing the slit width at the focal plane of the monochromator shown on Figure 3 with the spacing of the rotational features. If the rotational lines

Figure 3. Absorption Measurements



are not completely resolved, then the minimum value between the two lines is dependent on the absorption of the two rotational lines as well as the atomic sodium absorption at that wavelength. A good example of this occurs directly above the lines labeled "slit width" on Figure 3 where it is obvious that the valley between the two peaks is not following the general trend set by the adjacent valleys. The spacing of the two peaks was $0.69 \overset{0}{\text{\AA}}$ and it can be seen that an effective slit width of $0.42 \overset{0}{\text{\AA}}$ can establish the center wavelength of the two close lines. The wide slit, however, spreads the intensity over a larger increment of wavelength than the true line width. To numerically illustrate the effect of Na_2 absorption on atomic absorption, the peaks (rather than the valleys) of the rotational structure were measured. This would approximately represent the maximum error that could be expected due to Na_2 but it must be pointed out that if the monochromator has not sufficiently resolved the rotational lines, the peak values will be in error also. A more complete discussion of the effects of spectral resolution will be given when discussing experimental error in section 3.6.

The time constant of the recording apparatus can have a similar distorting effect on spectral lines if the time to scan the line is nearly the same size as the recorder time constant τ (see Appendix B). The time constant for these measurements was 0.72 sec and this is also shown on Figure 3. Obviously, τ is small compared to the spacing of the rotational features and the recorder time constant would not affect the data.

Data collected at various heat pipe oven pressures was used with equation (38) to determine the absorption coefficient μ_p . These data are presented in Table 3. Also shown is the non-dimensional separation in frequency from the line center (X) as defined by equation (37). As suggested above, data were measured using the "peaks" rather than the "valleys" to estimate the effect of Na_2 absorption and these data are also presented in Table 3.

TABLE 3. SODIUM RESONANT ABSORPTION MEASUREMENTS

<u>P</u> (torr)	<u>N</u> (Na atoms/M ³)	<u>λ_{Na}</u> (M)	<u>I_O</u> (cm)	<u>λ</u> (Å)	<u>I_v</u> (cm)	<u>μ_v</u> (M ⁻¹)	<u>X</u>
2.00	2.507 x 10 ²²	0.478	19.3	5890	0	-	0
				5880	0	-	2.0 x 10 ³
				5875	0.20	9.6	3.0
				5870	0.75	6.79	4.0
				5865	1.55	5.28	5.0
				5860	3.10	3.83	6.0
				5855	3.75	3.43	7.0
				5850	4.45	3.07	8.0
1.89	2.373 x 10 ²²	0.454	19.3	5890	0	-	0
				5880	0	-	2.1 x 10 ³
				5875	0.62	7.6	3.1
				5870	2.2	4.8	4.2
				5865	4.5	3.2	5.3
				5860	7.0	2.2	6.3
				5855	7.9	2.0	7.4
				5850	9.3	1.6	8.5
1.59	2.029 x 10 ²²	0.385	19.3	5890	0	-	0
				5880	0.6	9.0	2.4 x 10 ³
				5875	3.7	4.3	3.7
				5870	6.4	2.9	4.9
				5865	9.2	1.9	6.1
				5860	11.4	1.37	7.4
				5855	11.9	1.26	8.6
				5850	12.9	1.05	9.9
1.89	2.373 x 10 ²²	0.454	19.3	5845	10.55	1.33	9.5
				5890	0	-	0
				5880	0.6	9.0	2.4 x 10 ³
				5875	3.7	4.3	3.7
				5870	6.4	2.9	4.9
1.89	2.373 x 10 ²²	0.454	19.3	5865	4.1	3.4	5.3 x 10 ³
				5860	6.1	2.5	6.3
				5855	8.2	1.89	7.4
				5850	8.0	1.94	8.5
				5845	8.5	1.8	9.5

NOTE: Values of I_v were read at peaks of Na₂ rotational lines.

Therefore, $\mu_v \approx \mu_{Na} + \mu_{Na_2}$

3.6 Experimental Error

Equation (38) gives μ_ν as a function of I_0 , I_ν and z . Using equation (38) to write the total differential of μ_ν gives

$$d\mu_\nu = \frac{1}{z} \left[\frac{dI_0}{I_0} - \frac{dI_\nu}{I_\nu} - \ln(I_0/I_\nu) \frac{dz}{z} \right] \quad (40)$$

Dividing equation (40) by equation (38) gives the relative error in μ_ν

$$\frac{d\mu_\nu}{\mu_\nu} = \frac{1}{\ln(I_0/I_\nu)} \frac{dI_0}{I_0} - \frac{1}{\ln(I_0/I_\nu)} \frac{dI_\nu}{I_\nu} - \frac{dz}{z} \quad (41)$$

If the errors in I_0 , I_ν and z are not correlated, the propagation of error in μ_ν is

$$\left(\frac{d\mu_\nu}{\mu_\nu} \right)^2 = \left[\frac{1}{\ln(I_0/I_\nu)} \right]^2 \left(\frac{dI_0}{I_0} \right)^2 + \left[\frac{1}{\ln(I_0/I_\nu)} \right]^2 \left(\frac{dI_\nu}{I_\nu} \right)^2 + \left(\frac{dz}{z} \right)^2 \quad (42)$$

By establishing the individual errors in each measured value (I_0 , I_ν and z), the resulting error in μ_ν is found. Examining equation (42) reveals that the relative error in μ_ν depends on the value of I_0/I_ν . Near the line center where complete absorption occurs, $I_\nu \rightarrow 0$ and $I_0/I_\nu \rightarrow \infty$. It follows that the error in μ_ν may be quite sensitive to the proximity of the region of complete absorption. To put this in perspective, the error in μ_ν will be evaluated near complete absorption ($X \cong 3000$) and also well away from complete absorption ($X \cong 10,000$).

The individual contributions to errors in each of the measured variables leading to the calculation of absorption coefficient μ_ν are summarized in Table 4. The total relative error in each variable

TABLE 4. ABSORPTION COEFFICIENT MEASUREMENT ERRORS

Measured Variable	Source of Error	Error	Relative Error	Total Variable Relative Error
I_o , Unattenuated Intensity	X-Y Plotter Reading Error	± 0.5 mm	$\frac{\Delta I_o}{I_o} = \frac{.05}{19.3} = 0.0026$	$\frac{dI_o}{I_o} = 0.102$
	Non-linearity of PMT/Recorder	$\pm 1.5\%$ of Full scale	$\frac{\Delta I_o}{I_o} = 0.015$	
	Difference between initial and final I_o	1.95 cm	$\frac{\Delta I_o}{I_o} = \frac{1.95}{19.3} = 0.101$	
	$\left(\frac{dI_o}{I_o}\right)^2 = (.0026)^2 + (.015)^2 + (.101)^2$			
I_v , Attenuated Intensity	X-Y Plotter Reading Error	± 0.5 mm	$\frac{\Delta I_v}{I_v} = \frac{.05}{.20} = 0.25$ # X = 3000	$\frac{dI_v}{I_v} = 1.47$ $\frac{dI_v}{I_v} = 0.022$
			$\frac{\Delta I_v}{I_v} = \frac{.05}{13.0} = 0.0039$ # X = 10,000	
	Non-linearity of PMT/Recorder	$\pm 1.5\%$ of Full scale = .029 cm	$\frac{\Delta I_v}{I_v} = \frac{0.29}{0.20} = 1.45$ # X = 3000	
			$\frac{\Delta I_v}{I_v} = \frac{0.29}{13.0} = 0.022$ # X = 10,000	
	$\left(\frac{dI_v}{I_v}\right)^2 = (.25)^2 + (1.45)^2$ # X = 3000			
	$= (.0039)^2 + (.022)^2$ # X = 10,000			
z, Sodium Vapor Column Length	End interface thickness (Ref 6)	2 x 2.5 cm	$\frac{\Delta z}{z} = \frac{.05}{.385} = 0.13$	$\frac{dz}{z} = 0.13$
ν_v , Absorption Coefficient	For X = 3000 $I_o/I_v \approx 19.3/.02 = 965$ $\left(\frac{d\nu_v}{\nu_v}\right)^2 = \left[\frac{1}{\ln 965}\right]^2 (.102)^2 + \left[\frac{1}{\ln 965}\right]^2 (1.47)^2 + (.13)^2$			$\frac{d\nu_v}{\nu_v} = 0.063$
	For X = 10,000 $I_o/I_v \approx 19.3/13.0 = 1.485$ $\left(\frac{d\nu_v}{\nu_v}\right)^2 = \left[\frac{1}{\ln 1.485}\right]^2 (.102)^2 + \left[\frac{1}{\ln 1.485}\right]^2 (.022)^2 + (.13)^2$			$\frac{d\nu_v}{\nu_v} = 0.087$

is taken as the RSS (root of the sum of squares) value and its computation is also included in Table 4. As discussed above, the errors are estimated near complete absorption and well away from complete absorption. The estimated error in μ_v at $X = 3000$ is 6.3% and at $X = 10,000$ is 8.7%. The fact that the error is somewhat smaller close to complete absorption is due to the value of μ_v being larger. The absorption coefficient experiences approximately an order of magnitude decrease as X increases from 3000 to 10,000.

The experimental determination of wavelength (or frequency) depends on the drive mechanism which rotates the diffraction grating in the monochromator. As discussed in section 3.3, after calibrating the x-axis of the recorder the remaining significant error is the inaccuracy of the wavelength counter of the monochromator.

Wavelength or frequency is usually made dimensionless by dividing the separation of line center by the Lorentzian line width. This dimensionless frequency X is defined in equation (37) as

$$X = \frac{\omega_r - \omega}{\gamma_L}$$

where $\gamma_L \cong C_r N$ (from equation 31)

C_r = line width constant of proportionality

N = number density

which gives the following relation for X

$$X = \frac{\omega_r - \omega}{C_r N} \quad (43)$$

Following the method used to determine the propagation of error in μ_v , equation (43) can be used to derive an expression for the error in X

$$\left(\frac{dX}{X}\right)^2 = \left(\frac{d\omega}{\omega_r - \omega}\right)^2 + \left(\frac{dC_r}{C_r}\right)^2 + \left(\frac{dN}{N}\right)^2 \quad (44)$$

The relative errors of each of these variables are presented in Table 5. The resulting relative error in X is 10.1% for X = 3000 and 9.7% for X = 10,000.

In the calculation of the error in number density N, it was assumed that the only error is the error in measuring vapor temperature. This, of course, presumes that number density is known precisely as a function of temperature. As pointed out in Appendix B of reference 5, the error in vapor pressure for a given temperature is reported to be 0.37%. Since this error is small compared to the experimental uncertainty of measuring vapor temperature, it was not included. In any event, the influence of number density error is relatively small on the error in X (see Table 5).

TABLE 5. FREQUENCY MEASUREMENT ERRORS

Measured Variable	Source of Error	Error	Relative Error	Total Variable Relative Error
ω , Incident Light Frequency	Wavelength drive of Monochromator (McPherson Spec)	$\Delta\lambda = \pm 0.5 \text{ \AA}$	$\frac{d\omega}{\omega_r - \omega} = \frac{0.26 \times 10^{12}}{8.1 \times 10^{12}}$ $= 0.032$ $\text{@ } X = 3000$	$\frac{d\omega}{\omega_r - \omega} = 0.032$ $\text{@ } X = 3000$
			$\frac{d\omega}{\omega_r - \omega} = \frac{0.26 \times 10^{12}}{21.9 \times 10^{12}}$ $= 0.012$ $\text{@ } X = 10,000$	$\frac{d\omega}{\omega_r - \omega} = 0.012$ $\text{@ } X = 10,000$
C_r , Line Width Constant	Reported error (Ref. 4)	$\Delta C_r = \pm .5$	$\frac{dC_r}{C_r} = \frac{0.5}{5.2}$ $= 0.096$	$\frac{dC_r}{C_r} = 0.096$
N , Atom Number Density	Error in measuring sodium vapor temperature (Ref. 5)	$\Delta T = \pm 5^\circ K$	$\frac{\Delta T}{T} = \frac{\Delta N}{N}$ $\frac{dN}{N} = \frac{5}{750}$ $= 0.0067$	$\frac{dN}{N} = 0.0067$
X , Dimensionless Frequency	For $X = 3000$ $\left(\frac{dX}{X}\right)^2 = (.032)^2 + (.096)^2 + (.0067)^2$ For $X = 10,000$ $\left(\frac{dX}{X}\right)^2 = (.012)^2 + (.096)^2 + (.0067)^2$			For $X = 3000$ $\frac{dX}{X} = 0.101$ For $X = 10,000$ $\frac{dX}{X} = 0.097$

4.0 ASSESSMENT OF EXPERIMENTAL RESULTS

4.1 Far-Wing Resonant Behavior

As suggested in section 2.6 and in particular equation (37), the frequency separation from the line center is conveniently made non-dimensional by the Lorentzian line width γ_L . Since γ_L is proportional to atom number density (or pressure), this normalization of frequency should collapse the self-broadening and absorption coefficient μ_ν should be independent of pressure when plotted as a function of $X = (\omega_r - \omega)/\gamma_L$. The experimental data tabulated in Table 3 has been plotted as a function of X in Figure 4. In this figure, the D_2 -line center is to the right side on the X -axis. The range of X -values for the refractive experiment is shown. The test data are compared with the theoretical absorption coefficient obtained from equation (37). The bars at $X = 3000$ and $10,000$ represent the estimated error in μ_ν .

An initial impression from Figure 4 is that the measured values of μ_ν agree quite well with theory. However, closer scrutiny will reveal some systematic deviations from expected trends. Closer to the line center (smaller X) the slope of the experimental data is similar to the expected theoretical value of -2. Further away from line center, the slope tends to decrease to a value of 1.05 at $X = 10,000$. This tendency appears in data collected over the range of sodium vapor pressures used in the refractive experiment.

The data for each of the three pressures shown on Figure 4 is systematically displaced vertically giving the highest value of μ_ν for the highest pressure and the lowest for the lowest pressure. Theory

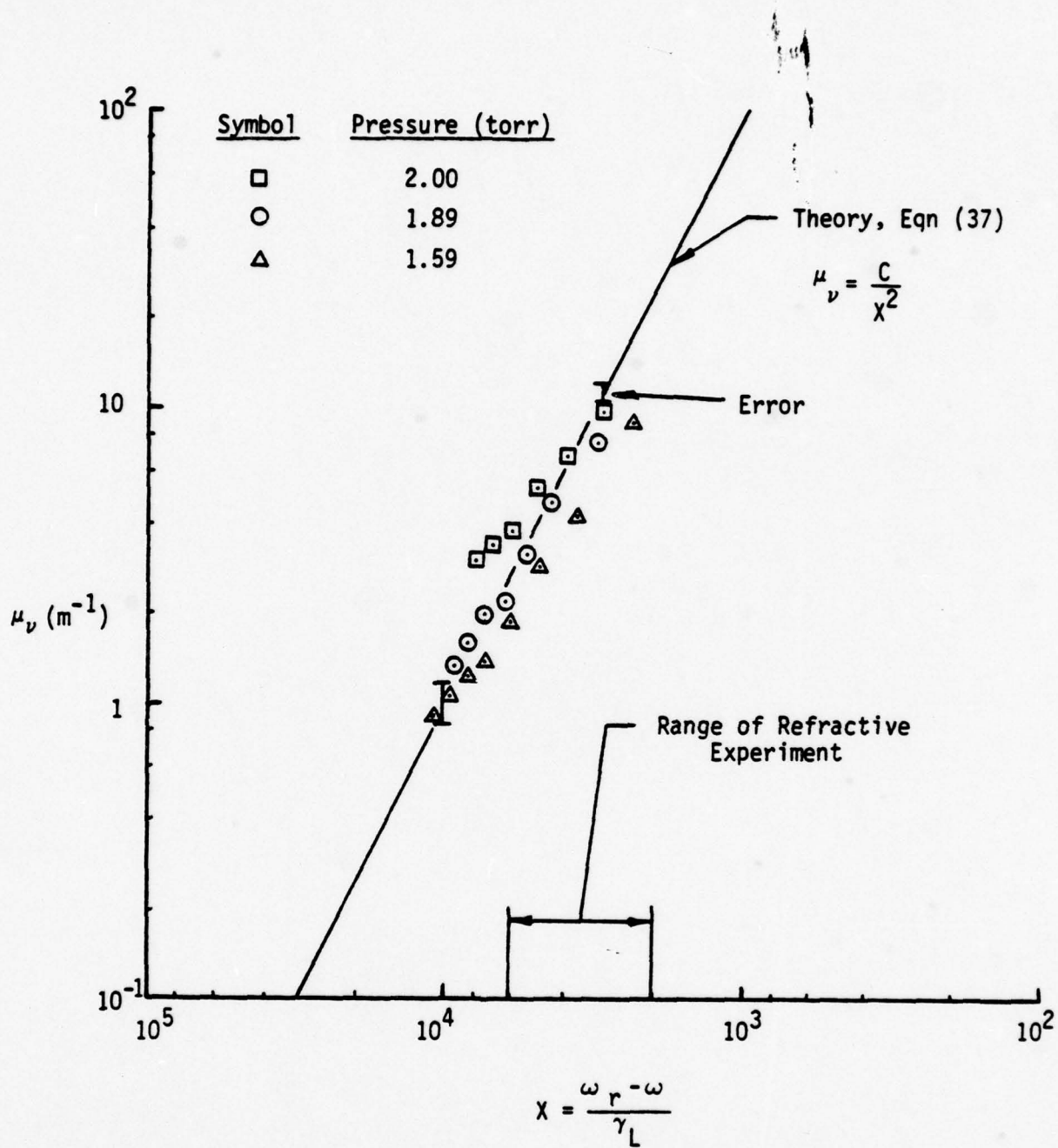


Figure 4. Comparison of Measured Absorption with Theory

suggest that all pressure effects should be normalized by the definition of X so that pressure should enter only through γ_L . The variations in μ_p are considerably greater than expected errors. At $X = 8000$, the total range of measured μ_p is 119% of the theoretical value while the expected error is approximately 8.7%.

The observed deviation from theory could be due to the presence of unresolved rotational lines of molecular sodium Na_2 . Referring to Figure 3, the presence of Na_2 is noted at wavelengths farther away from the line center. If the peaks of the rotational lines are read as the value for I_p (rather than the valleys between the peaks), a higher value of μ_p would be obtained and would represent an approximation of the sum of Na and Na_2 absorption. These data are compared with the data obtained by the normal analysis technique (reading values of I_p between peaks) on Figure 5. For X -values less than 5000, strong Na absorption obscures the rotational structure of Na_2 and no difference in μ_p could be detected. At $X > 5000$, the value of μ_p including Na_2 is larger than for Na as expected. The difference is roughly the size of the estimated experimental error and not large enough to explain the large variations from theory for X in the range of 10,000. The slope is 0.75 for X -values between 6000 and 10,000 and the deviation from the inverse square dependence is probably due to the unresolved Na_2 rotational lines.

A comparison is made of the data collected in this experiment with data reported by Niemax and Pichler⁴ using the alternate form of the far-wing approximation given in equation (35). Here the line broadening effects are collected in the square of atom number density

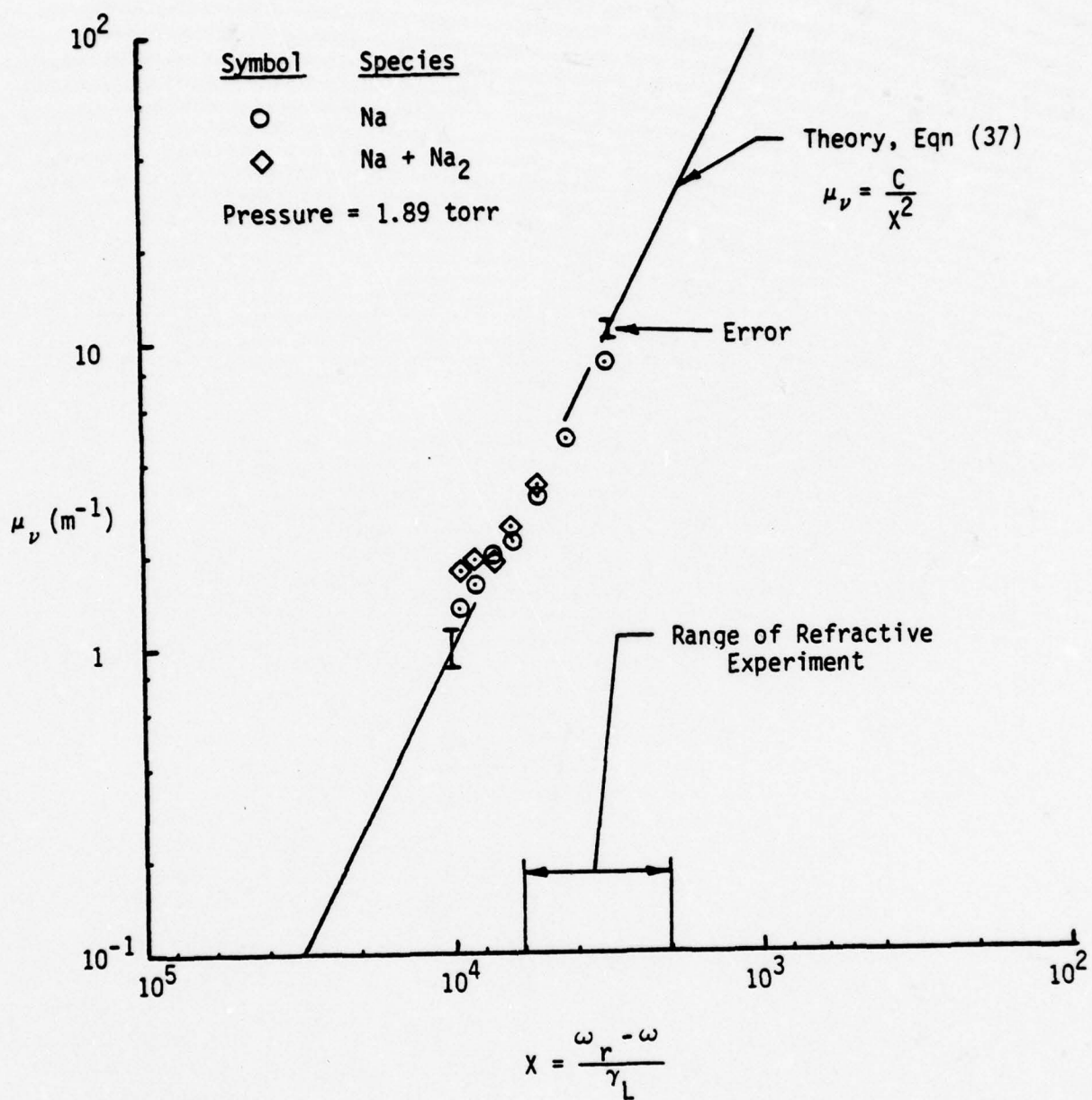


Figure 5. Effect of Molecular Sodium

N and μ_p/N^2 is a function of the frequency (or wavelength) separation from the line center. Data from reference 4 are reproduced in Figure 6 where μ_p/N^2 is plotted as a function of wavelength separation from the D_2 -line center. On this plot, the line center is to the left on the $\Delta\lambda$ scale. The data of Niemax and Pichler covered the wavelength range from 0.2 to 5 Å from line center. The data of this work are superimposed on the lower right portion of the figure. As before, the initial impression is that the data agree quite well with the previous experiment. The inverse square dependence on $\Delta\lambda$ is used to extrapolate Niemax and Pichler's data to the range of $\Delta\lambda$ of this work. Although the data scatters about the extrapolated line, trends identical to those observed above are still apparent. There is a systematic variation with pressure and a deviation from the inverse square dependence at wavelengths farther away from the line center.

Niemax and Pichler observed an asymmetry in the red wing of the D_2 -line as shown on Figure 6. These asymmetries in alkali resonance lines arise from the mutual repulsion between atoms of the same species. Although a red wing asymmetry is observed in the D_2 -line of sodium, the line is Lorentzian in the blue wing out to 5 Å from the line center. The possibility of asymmetries in the wavelength range of this work remains as a possibility and might explain the departure from the inverse square dependence. The systematic dependence on pressure does not seem to be explainable based on interaction potentials.

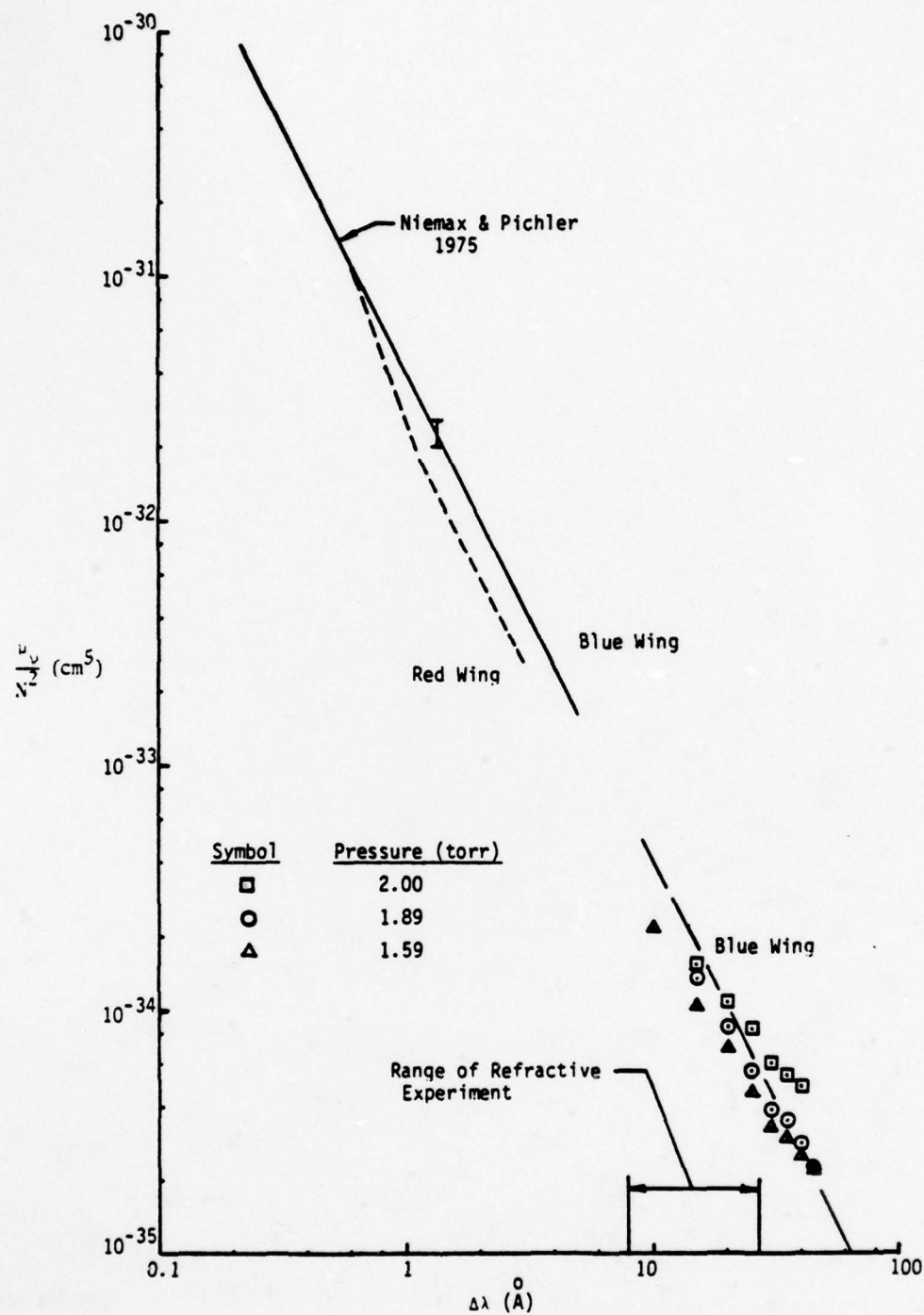


Figure 6. Sodium Resonant Absorption Experiments

4.2 Sources for Deviation from Theory

From the examination of the data in the previous section, three distinct data anomalies appear:

- 1) There is a deviation from the expected inverse square dependence on frequency separation from the line center,
- 2) There is a systematic dependence on sodium vapor pressure and
- 3) There is a large variation in the absolute values of μ_ν , particularly at large values of X .

There are a number of possible physical explanations of these anomalies. The possible sources for error are listed in Table 6 along with an evaluation of the probability that they could contribute to each of the above data anomalies. The likely contributors to data anomalies are outlined in Table 6. Two of the listed sources of error, items 2 and 3, can be eliminated as they could not produce wavelength anomalies or that the possible errors they introduce are too small to explain observed deviations. Item 6, sodium coating of the windows, can be eliminated because the time to scan the 45 \AA of the spectrum was approximately 6 minutes out of many hours for a sequence of absorption and refractive experiments. If sodium deposition on the windows resulted in an increased absorption at shorter wavelengths (recalling the spectral scan started at line center and proceeded to lower λ), then the deposition over a period of hours would have obscured the windows. Furthermore, the effects due to pressure that were observed would remain unexplainable as the sequence of pressures tested does not correlate with the order of the experiments.

TABLE 6. DATA ERROR DIAGNOSTICS

Possible Sources for Error	Data Anomalies		
	Deviation From $1/X^2$ Dependence	Dependence on Na Pressure	Large Variation in μ
1. Calculation of z from internal pressure	No - effects all λ equally	Possible, though not too likely - not documented	Unlikely - a 119% change in z not possible in equipment
2. I_0 not verified between each absorption experiment	No - effects all λ equally	No - effects all pressures equally	No - observed changes in I_0 too small
3. Recorder non-linearity	No - errors too small	No - unrelated dependence	No - error too small
4. Argon diffusion into sodium column resulting in broadening and asymmetries	Possible - asymmetries observed with argon, ref. 11	Possible through collision broadening with argon, ref. 11	Possible - deviation from $1/X^2$ results in factor >2.0 in extinction coefficient, ref. 11
5. N calculated from oven pressure assuming saturated vapor	No - effects all λ equally	Possible - although effect is probably small, see section 3.6	No - variation large at large X only
6. Sodium coating of windows - may be progressive in nature	No - effects all λ equally (time for μ experiment too short)	No - sequence of pressures not related to sequence of tests	No - sequence of pressures not related to sequence of tests
7. Na_2 rotational lines not resolved	Very likely although may not be only effect	No - not a pressure dependence	No - difference too small - see Figure 5
8. Scattering due sodium droplets in optical path	No - scattering not λ dependent ($\Delta\lambda = 45\text{\AA}$)	Possible - higher pressures may aid droplet growth	Unlikely - largest variation at large X - not λ dependent

Similar logic can partially eliminate items 1, 5, 7 and 8 as sources for two of the three anomalies but they remain as possible sources for one of the anomalies. The calculations of sodium column length from equation (39) presumes a thin boundary between the sodium and argon. The thickness of this layer, if comparable to the 2.5 cm observed in reference 6, is not large enough to account for the observed pressure effects as discussed in the section 3.6. However, if the column length changes due to the different power dissipation at the different pressures as suggested in reference 6, equation (39) may not be sufficient to predict length due to changes in interface layer thickness. Because reference 6 has measured interface layer thickness of approximately 2.5 cm, this is viewed as a relatively weak possibility as an explanation of the pressure dependence.

Similarly, calculating number density (and then γ_L) from pressure assuming a saturated vapor (item 5) could result in an apparent pressure dependence if the vapor was not saturated. However in section 3.6, the error attributed to difference between measured temperatures and saturated vapor temperature for a measured pressure produces a very small error in μ_v . Item 5 remains as a contributing source of error but is not viewed as a dominant mechanism for producing the observed pressure dependence.

Light scattering from liquid sodium droplets forming in the optical path due to condensation might show a pressure dependence due to pressure effecting droplet growth rates. Internal periodic optical unsteadiness was observed in early absorption experiments at higher pressures as reported in reference 5. A partial obscuring of the

optical path could be observed which appeared similar to a translucent curtain being lowered through the sodium vapor. This was hypothesized to be condensation initiated near the upper portion of the heat pipe oven which proceeded downward by gravitational effects forming larger and larger droplets as they coalesced. When the phenomenon had passed, the output light intensity returned to the initial value and after a short period of time the process started again. The period of occurrence was approximately 15 seconds. Because the variations in transmitted light were unacceptably large, the heat pipe oven pressures were reduced and the unsteady phenomenon disappeared. As to whether the reduction of pressure eliminated condensations in the central portion of the tube or merely eliminated the unsteadiness of the process cannot be ascertained. Consequently, the possibility of mid-tube condensation causing scattering must remain as a possible explanation for the observed pressure dependence.

Deviations from the inverse square dependence are very likely due to unresolved Na_2 rotational lines (item 7) but as suggested in the discussion of Figure 5, the effect may not account for all the observed deviation.

Another possible source of error is the diffusion of argon into the sodium vapor with resulting collision broadening (item 4). McCarten and Farr¹¹ measured the collision broadening of sodium in the presence of argon and observed asymmetries in the red wing of the D_1 -line. The broadening is directly proportional to argon number density (or pressure) and would explain the systematic variation with pressure observed in this work through the calculation of Lorentzian

line width. The asymmetry in the red wing of the D_1 -line is similar to the characteristics of the departure from the inverse square dependence observed in this experiment. Unfortunately, McCarten and Farr did not explore the asymmetries in the blue wing of the D_2 -line. These asymmetries can result in departures from the inverse square law that affect the extinction coefficient by a factor greater than 2.0 and could, therefore, also explain the large variations in μ_ν seen in this experiment. The perturbation of wing shape by argon is typically:

- 1) Inverse square dependence near line center
- 2) Deviation to slopes less than 2.0 (McCarten and Farr show a slope of approximately 1.5)
- 3) Return to inverse square dependence far away from the line center but at a higher extinction coefficient than expected based on near wing extrapolation.

The slope in the region of transition from Lorentzian behavior is approximately 1.5. This is close to the value of 1.62 observed here and is tempting as a justification for the case that argon diffusion into the sodium explains the current experiment. However, in the excellent survey article by Margenau and Watson¹⁷, a slope of 1.5 is noted for the red wing of the D-lines while the blue wing maintains a slope of 2.0 (see p. 45).

An even more attractive reason for suspecting collision broadening due to argon diffusion into the sodium is due to the argument that this phenomenon could, by itself, explain all the data anomalies. This becomes a more likely reason when one returns to other possible causes

and finds them only marginally capable of explaining the magnitude of observed effects or of speculative nature as to their existence in this experiment. It would appear that the circumstantial evident is sufficiently well based to recommend exploration of this possible cause for future work.

4.3 Suggestions for Follow-On Studies

Based on section 4.2, an investigation of the possibility of the argon buffer gas diffusing into the sodium and producing additional collision broadening is recommended. The phenomenon could be attacked from several points of view:

- 1) The simplest experimental approach would be to replace argon with neon as the buffer gas. As shown in Appendix C, the broadening due to the buffer gas should decrease by 37%. However, the diffusion coefficient increases by 72% and the net effect would probably be an increased pressure dependence of the sodium absorption coefficient. Another approach would be to replace the argon with xenon which decreases the diffusion coefficient and has essentially no effect on the collision broadening coefficient. Xenon, however, displays large asymmetries in the wings of the D-lines (see Ref. 11) where neon does not. Repeating the absorption measurements of this experiment but replacing the buffer gas argon with neon or xenon should have a measurable effect on the observed pressure dependence as well as the departure from the inverse square dependence.
- 2) Extraction of gas samples at various distances from the center of the heat pipe oven to the end regions would give direct evidence of buffer gas diffusion into the sodium vapor column. While the sodium could be expected to condense in the sampling process, the presence of any buffer gas could be detected. The problem of extracting gas samples from the heat pipe oven

without disturbing the axial concentration profiles is not trivial. With careful attention to mechanical details, such an experiment could yield definitive data on the causes of the observed pressure dependence of sodium absorption.

- 3) A documentation of the thermal profile in the sodium/argon interface region would establish if there are any systematic changes in column length with pressure that are not predicted by equation (39). Although thermocouple measurements through movable seals in the heat pipe oven end caps failed in this experiment, Vidal and Cooper⁶ measured internal temperature distributions.
- 4) A rearrangement of the heat pipe ovens to allow external control of the pressure so that different power levels could be tested would provide changes in sodium vapor column length (see Ref. 6) that could be used to obtain the absolute value of length.

The problem of unresolved rotational lines is an experimental problem which can be treated by two techniques:

- 1) The obvious solution to obtaining higher resolution is increasing the light source intensity which allows smaller slit widths and greater resolving power.
- 2) The slit width could be adjusted to maximize the resolution in each portion of the spectrum while providing usable output intensity. By overlapping each portion of the spectrum, a continuous absorption spectrum could be obtained.

The use of the Kramers-Krönig relation to relate the absorption spectrum to the index of refraction requires an integration over all frequencies. This would require additional measurements through the line center into the red wing of the D_2 -line. Such experimental measurements would face problems already encountered regarding resolution and light source intensity but these are not insurmountable problems. Another approach to exploring the effect of the observed absorption on the refractive properties, although approximate, would be to assume $1/\lambda^2$ dependence for the portion of the line where μ_r was not measured. Then the Kramers-Krönig relation would give the index of refraction as a function of frequency and the difference from theory would approximate the errors introduced by this experiment.

5.0 CONCLUSIONS AND RECOMMENDATIONS

Absorption measurements in the blue wing of the sodium D_2 -line have shown reasonable agreement with other experiments and with theory. In the wavelength range of the refractive experiments (9 to $27 \overset{0}{\text{\AA}}$ from line center), the measured absorption coefficient varies approximately as the inverse square of the frequency separation from line center. There is, however, a residual pressure dependency not predicted by theory which results in higher absorption coefficients at higher pressure. This deviation from theory appears to be due to the diffusion of the argon buffer gas from the end regions of the heat pipe oven into the sodium vapor. The resulting collision broadening, which is expected to be pressure sensitive, produces a line which is broader than predicted using self-broadening data for sodium. Although this effect has not been verified experimentally, replacement of the argon with either neon or xenon will produce measureable changes to the amount of diffusion as well as the amount of broadening.

The measurement of the absorption beyond the range of the refractive experiment (i.e., from 27 to $45 \overset{0}{\text{\AA}}$ from line center) was limited due to unresolved rotational lines of molecular sodium. This results in a change in slope from the theoretical value of -2 to -0.75 . Although this departure from theory is significant and results in apparent asymmetries in the shape of the wing, there are other asymmetries which could not be due to Na_2 absorption and appear to be pressure dependent. These asymmetries could also be due to diffusion of argon into the sodium producing asymmetries similar to those observed by other

experimenters in other portions of the D-line spectrum. Because the perturbing effects of neon and xenon are quite different from each other, use of these buffer gases would provide insight into the causes of the observed asymmetries. In addition, improved experimental methods and increased light source intensity to increase spectral resolution could be used to resolve the Na_2 rotational lines, thereby eliminating this effect in the far wing. Better resolution would allow more data to be collected to study the asymmetries in greater detail.

The possibility of the buffer gas diffusing into the sodium column raises questions about the internal operational details of the heat pipe oven and suggests future spectroscopic work with this device should explore this detail. Gas samples carefully extracted from various locations within the sodium column should contain amounts of the buffer gas if diffusion is occurring. Gas sampling along with measurement of the sodium/buffer gas temperature profile at the interface would resolve the experimental anomalies.

In conclusion, the documentation of sodium absorption in the far wing has not revealed any phenomena which would substantially interfere with the application of resonant refractivity to flow visualization techniques. The effects on broadening which might be expected from working gases for wind tunnel applications have been treated in the literature. The apparent broadening effects seen in this experiment do not constitute a new phenomenon with regard to the application of resonant refractivity but do suggest that heat pipe ovens operated in the pressure range of 2 torr may function differently than originally

envisioned. More experimentation will resolve these aspects. The absorption data collected here will be a basis for determining optical intensity with various visualization techniques which may find future application.

APPENDIX A

Kramers-Krönig Relationship

The propagation of light through a medium depends upon the nature of the medium; in particular, the atomic species of the medium. From a macroscopic point of view, certain properties such as refractivity and absorptivity must depend upon the nature of the medium. Intuition (and physical evidence) certainly leads one to expect that these macroscopic properties depend on the kind of atom in the medium. This reasoning may be extended further to suggest that there are certain properties of atoms (of a species) that result in the macroscopic properties of refractivity and absorptivity. If this is so, then it is not unreasonable to expect that refractivity and absorptivity are in some vague way related. This should not suggest that all macroscopic properties of a particular species are in some way related because many macroscopic properties, in addition, depend upon the number density of atoms and the thermal activity (temperature).

A more detailed examination of the optical properties of a medium reveal that they are not simply a single value but, in fact, depend upon the frequency of the incident light. The emission (and absorption) spectra of atomic species are characterized by discrete lines occurring at frequencies that are invariant for that particular species. The lines show strongly peak changes in emitted (or absorbed) light at these discrete frequencies and since the frequencies are unique for each atomic species, the frequency dependency of a property, such as absorptivity, must depend on atomic properties. Refractivity also exhibits frequency dependence and this behavior is most pronounced

near the same frequencies at which emission (or absorption) is strongly peaked (a phenomenon which was experimentally verified by Blendstrup⁵). This leads one to anticipate that refractivity and absorptivity and the way each behave with regard to frequency are related. The details of the relationship between refractivity and absorptivity are attributed to H. Kramers and R. Krönig^{21,22} but due to the mathematical and physical complexities of the concepts required for a rigorous proof, references to related works in mathematics and theoretical physics are extensive (see, for example, references following Chapter 1 of Nussenzweig²³ or the references in the paper by Toll²⁴).

An assumption that is usually made in connection with a proof of dispersion relations (i.e., the frequency dependency of certain optical properties) is that of causality. The causality condition simply states: The effect cannot precede the cause. Although this is an intuitively appealing assumption, the mathematical proof of causal relationships are extensive.²³ However, the applicability of causality as a condition for certain physical phenomenon can be questioned and Toll²⁴ treats the exact validity of causality and its accurate definition as an unsettled problem. Toll²⁴ offers a logical explanation of dispersion relations in terms of causality and this will be reviewed here.

Consider an incident wave train arriving at the surface of a slab of a dielectric medium as shown in Figure A-1a. This wave train is formed by the superposition of many Fourier components at many frequencies which extend in time from $t = -\infty$ to $t = +\infty$. One such component is shown in Figure A-1b. For the input signal to be zero for $t < 0$,

destructive interferences occur between all these components at times less than zero.

If it were possible to independently specify the frequency dependence of the refractive index and the absorption coefficient, then it would be possible to have a medium which could absorb only a single frequency and not affect any other component. Suppose that the medium absorbs only the frequency of component B shown in Figure A-1b. The output would then be the input wave minus component B and is shown in Figure A-1c. Here it is seen that output would contain the complement of component B at $t < 0$. That is, there would be an output (at $t < 0$) before the arrival of the input wave A. This is clearly a contradiction of causality which implies that the absorption of component B must be accompanied by phase shifts of other frequency components such that the input remains zero at $t < 0$. It follows that the absorption at a particular frequency must be related to the phase shifts at all other frequencies and this relation is specified by the dispersion relation.

The intent of this appendix is to outline the derivation of the Kramers-Krönig relation. The propagation of an electromagnetic wave through a dielectric medium will be reviewed briefly to introduce the concept and implications of a complex index of refraction. The condition of causality will be discussed in connection with the derivation of the Kramers-Krönig relation. Finally, the significance of the relation in terms of line broadening mechanisms and the resulting dispersion behavior are explored.

Propagation of an Electromagnetic Wave in a Dielectric Medium

The Maxwell equations for propagation of electromagnetic radiation in a dielectric medium in which the free electron density is zero reduce to:

$$\nabla^2 \vec{E} - \mu \epsilon \frac{\partial^2 \vec{E}}{\partial t^2} - \mu \sigma \frac{\partial \vec{E}}{\partial t} = 0 \quad (\text{A-1})$$

If the radiation waves are assumed to be harmonic with frequency ω , the electric field can be represented by:

$$\vec{E} = \vec{E}_s e^{-i\omega t} \quad (\text{A-2})$$

Differentiation and some algebraic manipulation will show that:

$$\frac{\partial \vec{E}}{\partial t} = \frac{i}{\omega} \frac{\partial^2 \vec{E}}{\partial t^2} \quad (\text{A-3})$$

Substituting (A-3) into (A-1) gives:

$$\nabla^2 \vec{E} - \mu \left(\epsilon + \frac{i\sigma}{\omega} \right) \frac{\partial^2 \vec{E}}{\partial t^2} = 0 \quad (\text{A-4})$$

Algebraic manipulation of the coefficient of the second term of (A-4) with the following relationships:

$$\mu_* = \frac{\mu}{\mu_0} \quad (\text{A-5a})$$

$$\epsilon_* = \frac{\epsilon}{\epsilon_0} \quad (\text{A-5b})$$

$$c = (\mu_0 \epsilon_0)^{-1/2} \quad (\text{A-5c})$$

yields:

$$\mu \left(\epsilon + \frac{i\sigma}{\omega} \right) = \frac{\mu_*}{c^2} \left(\epsilon_* + \frac{i\sigma}{\omega \epsilon_0} \right) \quad (\text{A-6})$$

Defining a complex index of refraction as:

$$\hat{n}^2 = \mu_* (\epsilon_* + \frac{i\sigma}{\omega\epsilon_0}) \quad (\text{A-7})$$

reduces the coefficient of equation (A-4) to \hat{n}^2/c^2 .

While (A-7) may appear to be a rather arbitrary definition, it should be recalled that the real refractive index is defined by:

$$n = \frac{c}{v} = \sqrt{\mu_* \epsilon_*} \quad (\text{A-8})$$

Returning to equation (A-6), it is noted that if a complex dielectric constant is defined as:

$$\hat{\epsilon} = \epsilon + i \frac{\sigma}{\omega} \quad (\text{A-9})$$

then:

$$\hat{n} = \sqrt{\mu_* \hat{\epsilon}_*} \quad (\text{A-10})$$

The physical significance of the complex index of refraction can be illustrated by examining the solution to (A-4) for a plane wave with harmonic properties specified in (A-2). The solution is (see reference 13, Chapter XIII).

$$\vec{E} = \vec{E}_0 e^{-i(\hat{k} \cdot \vec{r} - \omega t)} \quad (\text{A-11})$$

The complex wave number \hat{k} is replaced by:

$$\hat{k} = \hat{n} k_0 = \hat{n} \frac{\omega}{c} \quad (\text{A-12})$$

and the complex index of refraction by:

$$\hat{n} = n - i\kappa \quad (\text{A-13})$$

$$\begin{aligned} \vec{E} &= \vec{E}_0 e^{-i\{\vec{k}_0(n-i\kappa) \cdot \vec{r} - \omega t\}} \\ &= \vec{E}_0 e^{-\kappa \vec{k}_0 \cdot \vec{r}} e^{-i(n\vec{k}_0 \cdot \vec{r} - \omega t)} \end{aligned} \quad (\text{A-14})$$

Here it is seen that the imaginary part of \hat{n} is an extinction coefficient κ which produces an exponential attenuation of the wave as it propagates through the medium. The real part of \hat{n} is, of course, the real refractive index n defined by equation (A-8).

Dispersion in a Gas at Low Pressure

Up to this point, the propagation of an electromagnetic wave through a dielectric medium has considered only a monochromatic wave (at a fixed frequency, ω). Although the above equations can be applied at any frequency ω they have not addressed the fact that optical properties of dielectric media such as n and κ have dispersive characteristics (that is, n and κ depend upon frequency ω). The dispersive characteristics appear through a dependence of ϵ_* and σ on frequency which results from the interaction of the incident light wave with the electron cloud of the atoms. From the classical point of view, the atom is viewed as a massive nucleus with electrically bound electrons that behave as a damped harmonic oscillator. The classical atom responds to an incident electromagnetic wave by the electron cloud oscillating at the frequency of the incident wave but not in phase with it. The phase relationship between the incident radiation and the response is a manifestation of the damping which is also central to the mechanism of absorption.

The classical description of the atom will be used to derive the dispersion relations. The success of this simplistic approach is due to the fact that the classical and quantum descriptions of the atomic resonance are very similar (see Chapter 10, reference 25). Consider

the motion in the x-direction of a damped harmonic oscillator. The differential equation for the balance of forces is (see Chapter 2, reference 13 or Chapter 15, reference 25).

$$\ddot{x} - \gamma_r \dot{x} + \omega_r^2 x = \frac{e}{m} (E_{\text{eff}})_x \quad (\text{A-15})$$

where

$$\gamma_r = \frac{e^2 \omega_r^2}{6 \pi \epsilon_0 m c^3} \quad (\text{A-16})$$

ω_r = resonant frequency of the oscillator

$(\omega_r^2 = \frac{q}{m})$ where q is the stiffness of the electron
binding force: $q = F/x$

The effective electric field E_{eff} is:

$$(E_{\text{eff}})_x = E_x + \frac{P_x}{3\epsilon_0} \quad (\text{A-17})$$

which for a gas at low pressure, where the polarization force is small compared to E, reduces to:

$$(E_{\text{eff}})_x = E_x \quad (\text{A-18})$$

Substituting (A-18) into (A-15) and making use of the relation between the dipole moment P and the charge separation distance x :

$$P = Nex \quad (\text{A-19})$$

Equation (A-15) becomes:

$$\ddot{P} + \gamma_r \dot{P} + \omega_r^2 P = \frac{Ne^2}{m} E \quad (\text{A-20})$$

The solution is²⁵:

$$P = \frac{Ne^2 E}{m} \frac{1}{\omega_r^2 - \omega^2 + i \gamma_r \omega} \quad (\text{A-21})$$

The index of refraction is related to the polarization of the dielectric medium and electric field through:

$$\hat{n}^2 - 1 = \frac{P}{\epsilon_0 E} \quad (A-22)$$

using (A-21), the index of refraction becomes:

$$\hat{n}^2 - 1 = \frac{Ne^2}{\epsilon_0 m} \frac{1}{\omega_r^2 - \omega^2 + i\gamma_r \omega} \quad (A-23)$$

With equation (A-23) it is seen that the complex index of refraction depends on frequency ω ; that is, it displays dispersive properties. The frequency dependence is, more precisely, a dependence on the separation between the incident field frequency ω and the resonant frequency of the oscillator ω_r . Recalling equation (A-13), a frequency dependency of the real index of refraction n and the extinction coefficient κ is expected. The relation between the frequency dependence of n and the frequency dependence of κ was first derived by Kramers²¹ and Krönig²². The following will outline the derivation of this relation and shows some of the consequences of the interdependency of refraction and absorption.

The Kramers-Krönig Relation

The Kramers-Krönig relation gives analytic expressions which relate the real and imaginary parts of the complex index of refraction for a dispersive medium. Specifically, the real part of \hat{n} which is the real index of refraction n is given by an integral of the imaginary part κ over all frequencies. Similarly, the imaginary part κ is given by an integral of the real part n over all frequencies. Either of these

relations can be considered as the "cause" with the other as the "effect." That is, for a given absorption profile in frequencies extending through a resonance, there is only one function of refractive index possible for the same variation in frequencies.

"A function of an integrable square is zero for all negative values of its argument if and only if its Fourier transform is a causal transform."^{24,23} A necessary and sufficient condition for a causal transform of a complex function:

$$\phi(\omega) = \phi_r(\omega) + i \phi_i(\omega) \quad (\text{A-24})$$

is that the real and imaginary parts are Hilbert transforms of each other:

$$\phi_r(\omega) = \frac{P}{\pi} \int_{-\infty}^{\infty} \frac{\phi_i(\omega') d\omega'}{\omega' - \omega} \quad (\text{A-25a})$$

and

$$\phi_i(\omega) = \frac{P}{\pi} \int_{-\infty}^{\infty} \frac{\phi_r(\omega') d\omega'}{\omega' - \omega} \quad (\text{A-25b})$$

where P denotes the principal value of the contour integral and ω' denotes the integration variable.

These relations can be obtained more directly from contour integration of a complex function* in the complex plane around a closed loop which avoids the poles. It can be shown (reference 25, section 12.8.3) that the line integral around any closed loop of an analytic complex

* such as susceptibility which is related to the complex index of refraction by:

$$\chi(\omega) = \frac{1}{4\pi} [\hat{\epsilon}(\omega) - 1] = \frac{1}{4\pi} [\hat{n}^2(\omega) - 1]$$

function is zero if the loop does not enclose a pole; i.e., a resonance. Furthermore, if the integration about a circle centered on a pole is evaluated as the radius approaches zero, it is found that the value of the line integral is equal to $2 \pi i$ times the residues at the pole. If the line integral only extends over the half circle, then its value is πi times the residue at the pole.

Using these concepts, it can be shown that the contour integration of a complex function $u(\omega)$ from $-\infty$ to $+\infty$ but not including the vanishingly small region around ω_0 is given by:

$$P \int_{-\infty}^{\infty} u(\omega) d\omega = -\pi i v(\omega_0) \quad (A-26)$$

where the function $v(\omega_0)$ is the residue at the pole (Chapter 7, reference 26). If the complex function is the complex index of refraction \hat{n} expressed as:

$$u(\omega) = \frac{\hat{n}-1}{\omega-\omega_0} \quad (A-27)$$

and the residue at the pole is $\hat{n}-1$, equation (A-26) becomes:

$$\hat{n}-1 = \frac{1}{\pi i} P \int_{-\infty}^{\infty} \frac{\hat{n}(\omega')-1}{\omega'-\omega} d\omega' \quad (A-28)$$

Separation of the real and imaginary parts of (A-28) gives the real index of refraction n and the extinction coefficient κ :

$$n(\omega)-1 = \frac{1}{\pi} P \int_{-\infty}^{\infty} \frac{\kappa(\omega')}{(\omega'-\omega)} d\omega' \quad (A-29a)$$

$$\kappa = \frac{1}{\pi} P \int_{-\infty}^{\infty} \frac{n(\omega')-1}{(\omega'-\omega)} d\omega' \quad (A-29b)$$

where n is the real part and κ is the imaginary part of \hat{n} defined by (A-13). These integrals relate the frequency dependence of the index of refraction to the integral of the extinction coefficient over all frequencies and vice-versa and are known as the Kramers-Krönig relation.

The effects of this relation on the resonant behavior of the real index of refraction n is shown in Figure A-2. If the damping of the harmonic oscillator is taken to be zero, the index of refraction goes to infinity at resonance as shown by the solid line in Figure A-2. However, if damping (i.e., absorption) occurs, the index of refraction does not go to infinity at resonance, as shown by the dashed line of Figure A-2. As damping is increased (or as the absorption is spread over a larger range of frequencies near resonance) the maximum deviation of n from its value far away from resonance, n_0 , would tend to decrease. In conclusion, line broadening mechanisms will tend to diminish the peak resonant refractivity and are, therefore, an important consideration in any application which plans to use this resonant behavior.

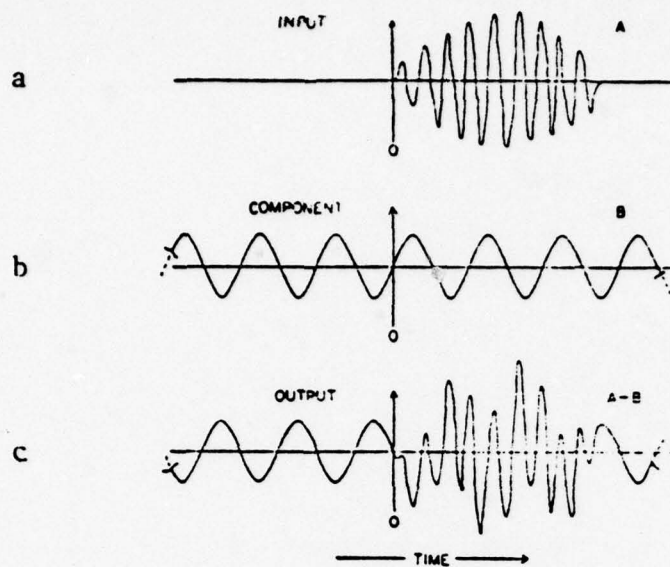


Figure A-1 Relation Between Causality and Dispersion

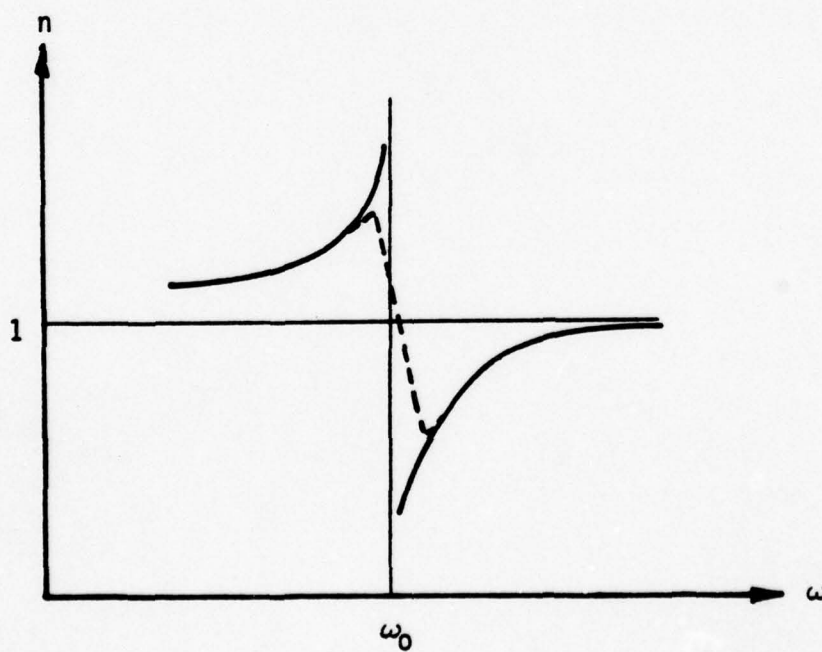


Figure A-2 Effect of Damping on Dispersion

APPENDIX B

Transient Response of the Photomultiplier Recorder

The McPherson scanning monochromator utilizes a photomultiplier tube (PMT) at the output slit to detect the dispersed light signal. The wavelength scanning of the spectrum is accomplished by precisely rotating a diffraction grating in such a manner that wavelength is a linear function of time (for a fixed drive speed). As a result, during the recording process of scanning the desired wavelength range, wavelength becomes a function of time.

An inherent feature of a PMT is the noise generated by thermal (random) emission of electrons from the light sensitive cathode. While the generation of noise from this source can be minimized by cooling the PMT, it is often unnecessary to do so because electrical (capacitive) damping can effectively reduce the detected noise. The presence of damping does, however, change the transient response of the recording system. Recalling that scanning the spectrum with the monochromator in effect transforms wavelength to time, the recorder transient response can influence the resolution of spectral details. As damping is increased to reduce the noise level, the time constant of the recorder increases and the rate at which a spectral line may be scanned must be decreased. In this experiment where the input signal to the monochromator is steady with time, the addition of damping does not present a difficult problem because the scanning rate can simply be adjusted to make the time to scan a spectral feature much greater than the recorder time constant. The upper limit on scanning time is

related to either the minimum spectral scan rate of the monochromator or the time for which the input optical signal can be assumed constant. Electrical drift of the high voltage power supply for the PMT and the recorder amplifiers should also be considered when the scanning time becomes large.

Considering these aspects of recording the output of a monochromator, it is necessary to establish the time constant of the recorder as a function of damping inserted between the PMT and the input amplifier of the recorder. The entrance slit of the monochromator was illuminated with a steady light source. The output of the PMT was recorded on a HP-7004B x-y plotter. Various capacitors were inserted directly across the input terminals of the x-y plotter. Since the transient response of the PMT and the amplifier of the x-y plotter is orders of magnitude shorter than the mechanical drive of the plotter with capacitive damping, the observed response will be due to the drive mechanism and the capacitive damping. Actually, the x-y plotter is capable of recording frequencies up to 10 cps so that capacitance inserted at the input results in an overdamped behavior for time constants of interest here ($\tau \cong 0.2$ to 1.6 sec.).

The steady light input to the entrance slit of the monochromator was interrupted by closing the entrance shutter of the monochromator thereby creating a step change in input signal. The decay to zero signal was monitored as illustrated in Figure B-1. The time from shutter closing to 63% of the change in signal is the desired time constant. The change in signal was found by establishing the zero signal recorded level. First, the zero signal noise level was

determined by drawing horizontal lines which bracket the peak-to-peak fluctuations in zero signal as shown in Figure B-1. The median value of these limit lines was then taken as the average zero input level. The magnitude of the step change in signal is the difference between the average zero level and the level before shutter closing denoted by S on Figure B-1. The peak-to-peak noise level shown as N in Figure B-1 was used with the signal change S to form a signal-to-noise ratio. This method, therefore, represents the signal-to-noise ratio where the noise is generated by the PMT, the plotter electronics and the plotter drive system. It represents the minimum signal-to-noise ratio of the recording system and obviously does not include short duration unsteadiness in the input signal.

By inserting various capacitors across the plotter input terminal, the time constant τ of the system was determined and is presented in Figure B-2. The resulting signal-to-noise ratio (S/N) is plotted in Figure B-3 as a function of the time constant τ . From Figure B-3 it is apparent that the PMT/recorder signal-to-noise ratio can be improved dramatically by damping but at the expense of reduced response.

The data collected here was used to assess the response of the recorder for the absorption measurements. Clearly, the time to scan a spectral line must be considerably greater than the time constant τ . When examining the shape of a particular spectral feature, the time spent scanning it must be greater than τ .

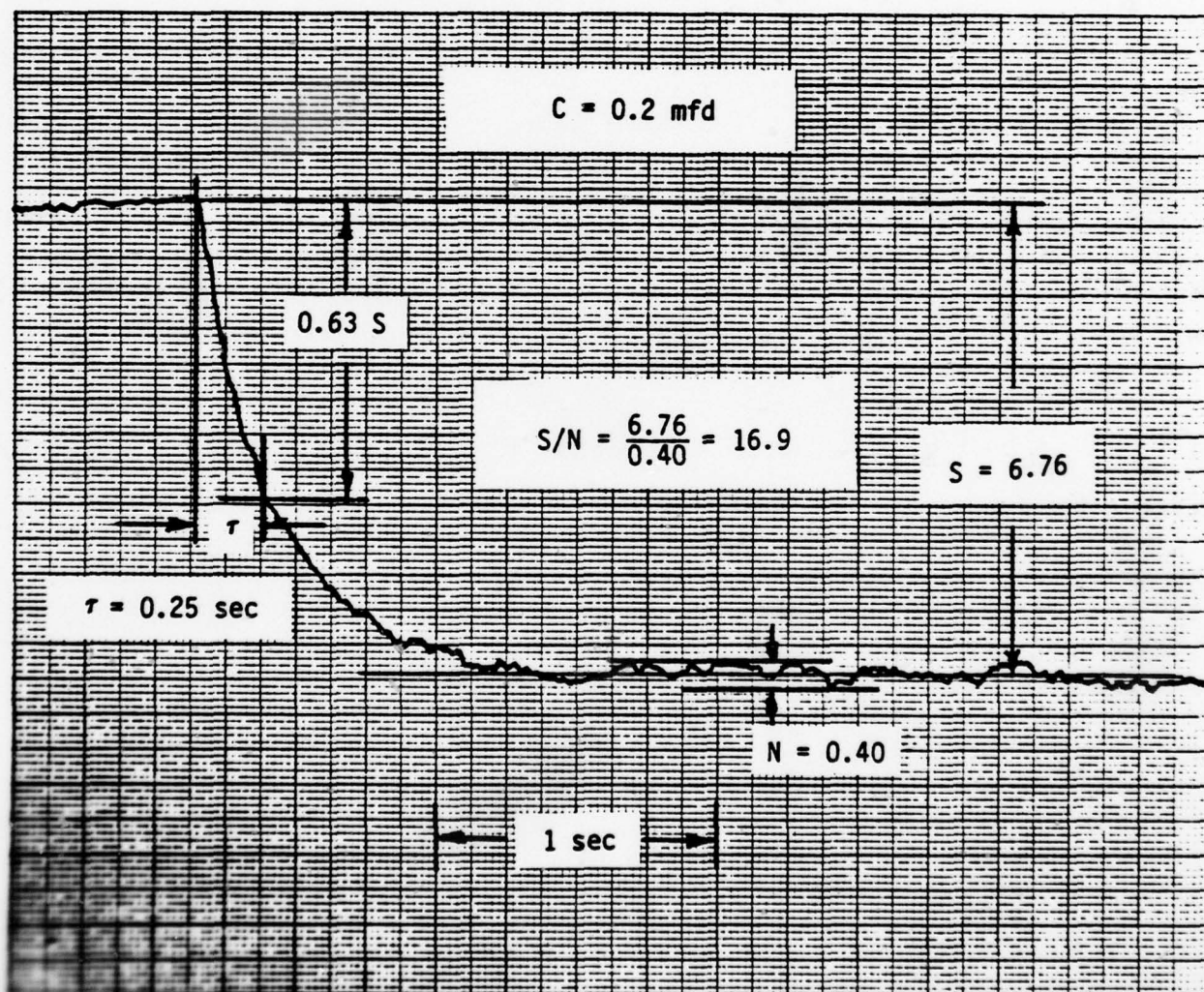


Figure 8-1. Photomultiplier Recorder Transient Response

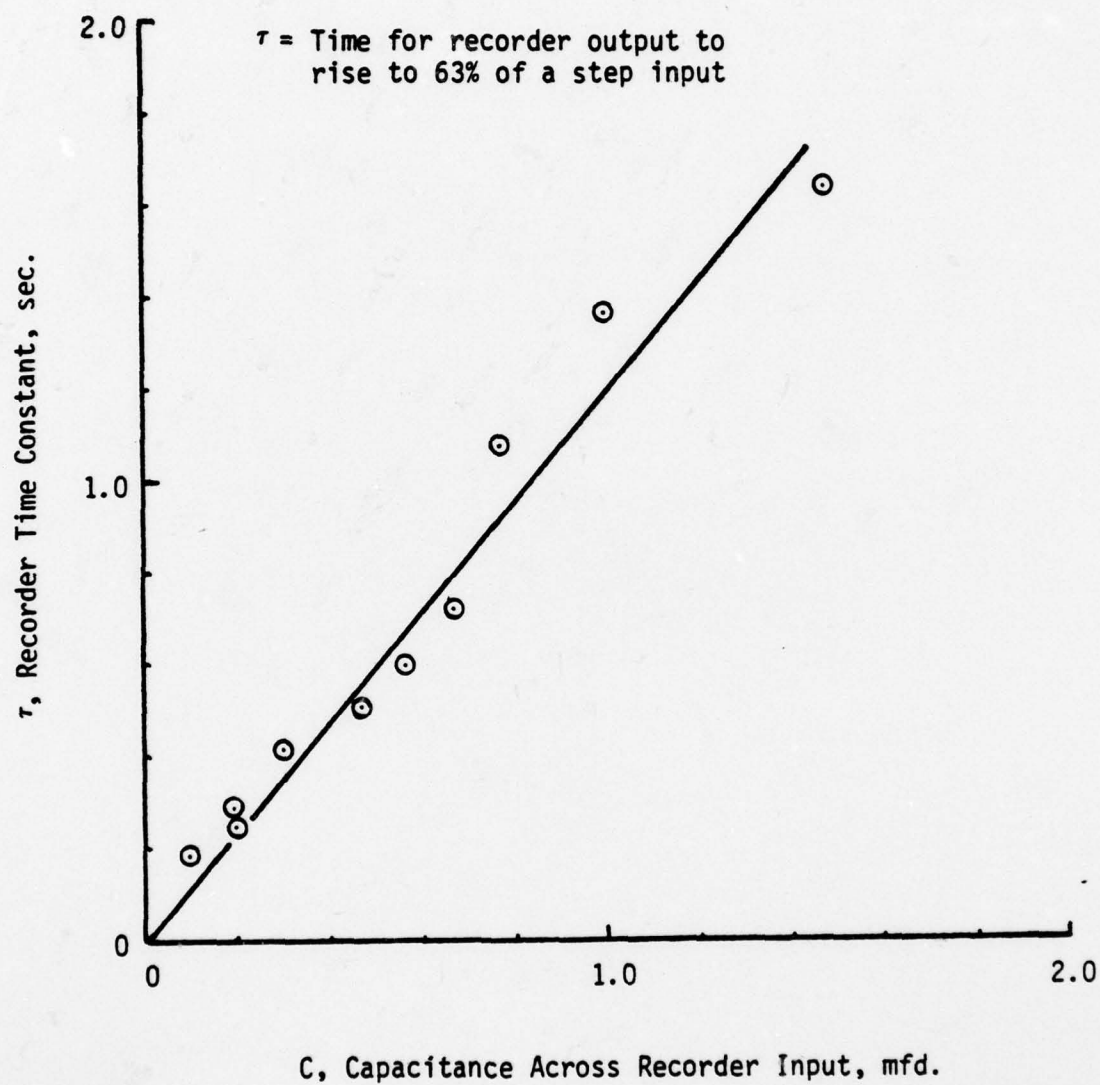


Figure B-2. Photomultiplier Recorder Time Constant

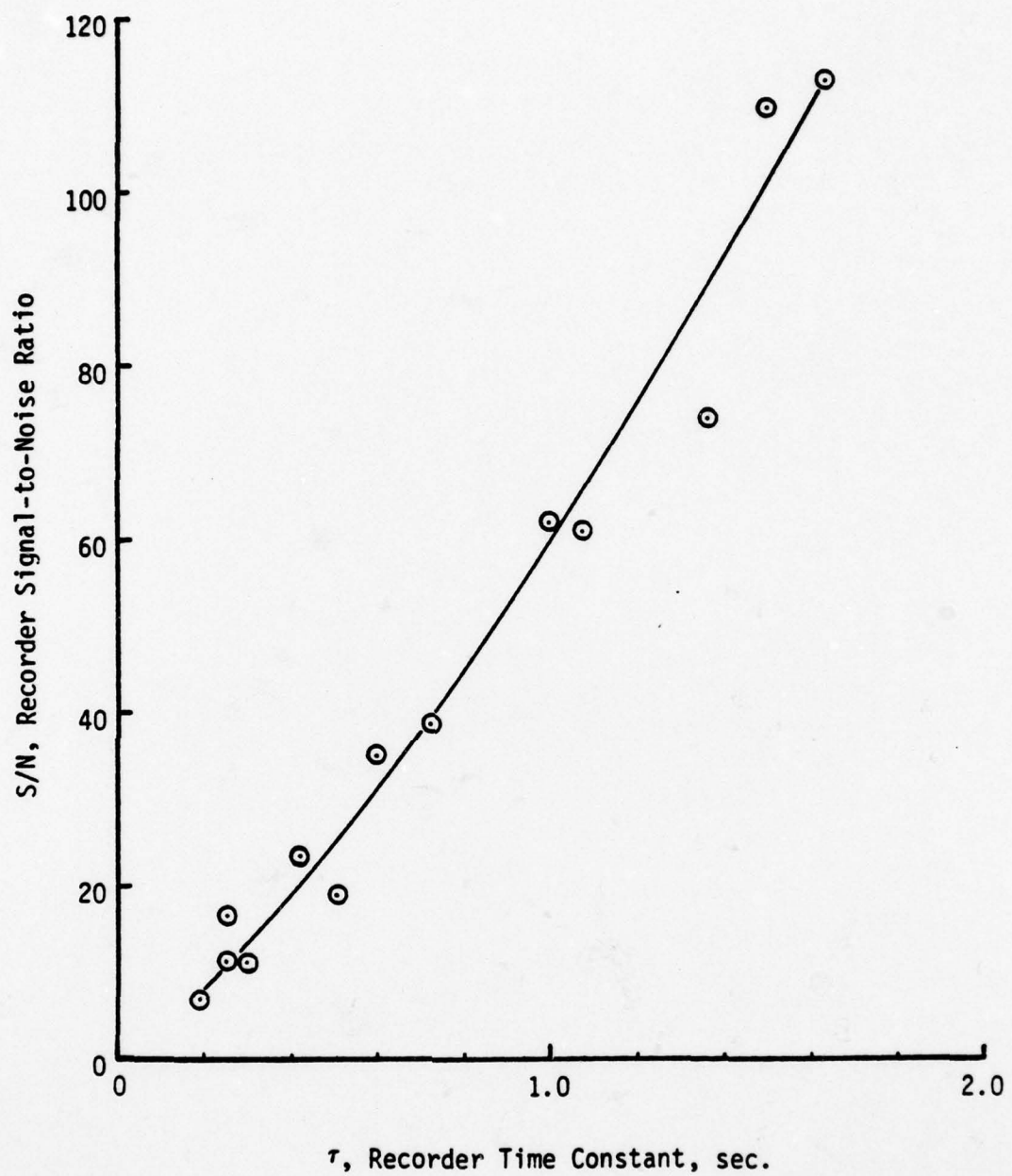


Figure B-3. Photomultiplier Recorder Signal-to-Noise Ratio

APPENDIX C

Diffusion of Sodium into a Buffer Gas

Jeans²⁷ gives the rate of diffusion of one gaseous species into another as:

$$\frac{dN_1}{dt} = D_{12} \frac{\partial^2 N_1}{\partial z^2} \quad (C-1)$$

where

$$D_{12} = \frac{2}{3\pi (N_1 + N_2) d_{12}^2} \sqrt{\frac{2kT}{\pi} \left(\frac{1}{M_1} + \frac{1}{M_2}\right)}$$

N = number density

$d_{12} = \frac{d_1 + d_2}{2}$, average atomic diameter

k = Boltzmann's constant

T = temperature

M = mass of the atom

z = length

t = time

It is seen that the diffusion coefficient D_{12} depends on the mean atomic diameter of the two species and their atomic masses. Since the atomic mass is proportional to atomic weight, D_{12} is proportional to the atomic weights and atomic diameters of the species.

$$D_{12} \sim \frac{\sqrt{\frac{1}{m_1} + \frac{1}{m_2}}}{(d_1 + d_2)^2} \quad (C-2)$$

The diffusion constant for sodium and various buffer gases can now be calculated. Physical properties of the species are:

<u>Species</u>	<u>m</u>	<u>d (cm)</u> ^{27,28}
Na	22.99	2.30×10^{-8}
Ar	39.95	3.66
Ne	20.18	2.60
Xe	131.30	4.02

Using the expression of (C-2), the ratio of the diffusion constants of sodium with the three noble gases can be determined and are tabulated along with the collision broadening constant from reference 11:

<u>Buffer Gas</u>	<u>D_{12}/D_{ref}</u>	<u>$\gamma_c/N_{\text{Buffer}}$ ($\frac{\text{cm}^{-1}}{\text{atoms/cc}}$)</u>
Ar	1.00	2.41×10^{-20}
Ne	1.72	1.53
Xe	0.77	2.46

It can be seen that collision broadening can be reduced by 37% if neon replaces argon as the buffer gas. However, the diffusion coefficient is 72% larger indicating a substantial increase in the amount of diffusion into the sodium. Another approach would be to reduce the amount of diffusion by using a higher molecular weight gas such as xenon. Here it is seen that a 23% reduction in diffusion coefficient is possible but there will be substantially no change in the collision broadening.

The net effect on the absorption coefficient depends on both the diffusion coefficient and collision broadening constant. Therefore, replacing argon with neon or xenon should have a measureable effect

on the pressure dependence of sodium absorption measured in the heat
pipe oven.

APPENDIX D

The Absorption Spectrum of Atomic Sodium

The absorption spectrum of atomic sodium (and other alkali metal vapors) is quite similar to the absorption spectrum of atomic hydrogen (the Lyman series) but displaced considerably toward longer wavelengths.²⁹ The spectrum consists of a series of lines with regularly decreasing separation with the first (the D-lines) in the series being the most intense. This series is called the principal series.

The energy levels associated with atomic sodium transitions are shown in Figure D-1. Splitting of the D-lines, which produces a wavelength separation of 6 \AA , is caused by electron spin.

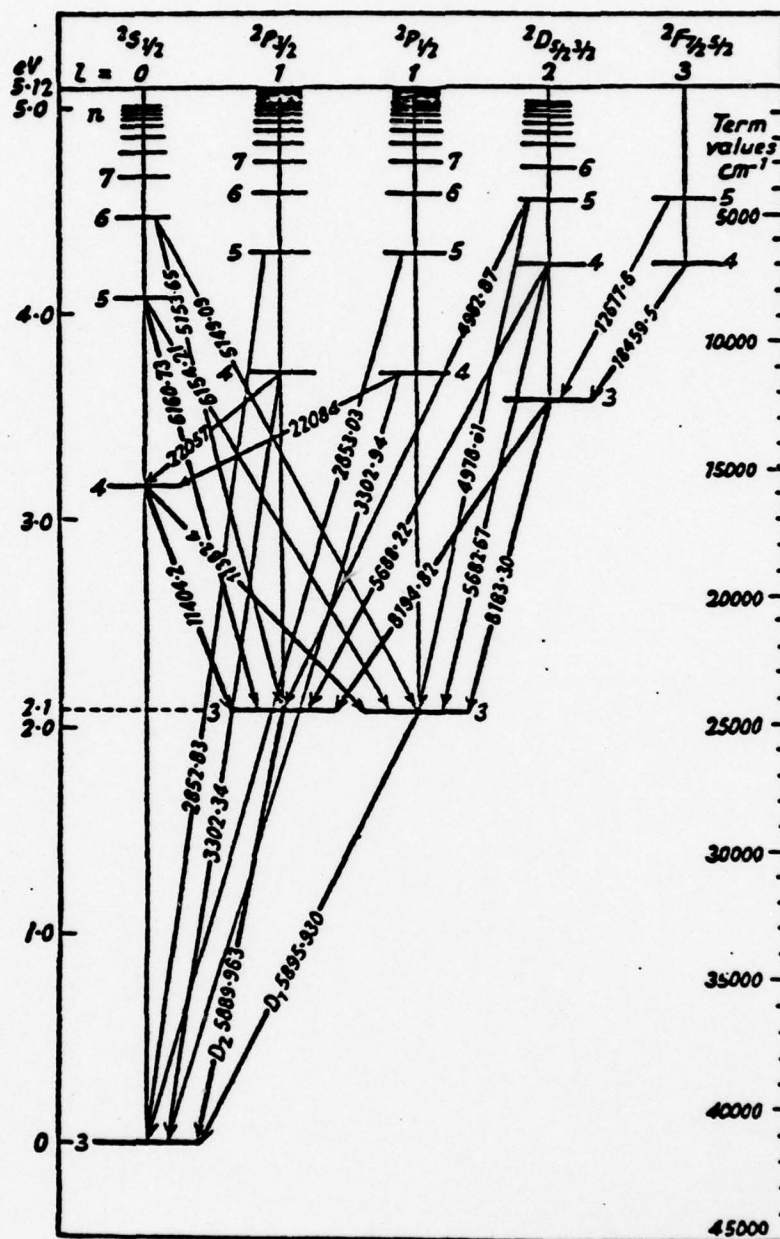


Figure D-1. Energy Level Diagram for Atomic Sodium
(From Reference 5)

REFERENCES

1. Bershader, D., "Some Aspects of the Refractive Behavior of Gases," pp. 65-83 in Dosanjh, D. C., Editor, Modern Optical Methods in Gas Dynamics Research, (Plenum, N. Y., 1971).
2. Bershader, D., Prakash, S. G., Huhn, G., "Improved Flow Visualization by Use of Resonant Refractivity," pp. 595-610 in Zinn, B. T., Editor, Experimental Diagnostics in Gas Phase Combustion Systems, Vol. 53, Progress in Astronautics and Aeronautics, (Princeton University Press, Princeton, N. J., 1977).
3. Blendstrup, G., Bershader, D., and Langhoff, P. W., "Resonant Refractivity Studies of Sodium Vapor for Enhanced Flow Visualization" AIAA J. 16, 10, p. 1106 (1978).
4. Niemax, K. and Pichler, G., J. Phys. B 8, 179 (1975).
5. Blendstrup, G. W., "Resonance Refractivity Studies of Sodium Vapor for Enhanced Flow Visualization," Stanford University, Ph. D. dissertation, 1978.
6. Vidal, C. R. and Copper, J., J. Appl. Phys. 40, 3370 (1969).
7. Wood, R. W., Phil. Mag. 8, 293 (1904).
8. Watanabe, K., Phys. Rev. 59, 151 (1941).
9. Mitchell, A. C. G. and Zemansky, M. W., Resonant Radiation and Excited Atoms (Cambridge University Press, Cambridge, 1961).
10. Deleage, J. P., Kunth, D., Testor, G., Rostos, F., and Roueff, E., J. Phys. B 6, 1892 (1973).
11. McCartan, D. G. and Farr, J. M., J. Phys. B 9, 985 (1976).
12. Movre, M. and Pichler, G., J. Phys. B 10, 2631 (1977).

13. Born, M. and Wolf, E., Principles of Optics, 3rd Edition (Pergamon Press, Oxford, 1965).
14. Armstrong, B. H. and Nicholls, R. W., Emission, Absorption and Transfer of Radiation in Heated Atmospheres (Pergamon Press, Braunschweig, 1972).
15. Hottel, H. C. and Sarofim, A. F., Radiative Transfer, Chap 6, (McGraw-Hill Book Co., New York, 1967).
16. Stone, J. M., Radiation and Optics, Chap 12, (McGraw-Hill Book Co., New York, 1963).
17. Margenau, H. and Watson, W., Revs. Modern Phys. 8, 22 (1936).
18. Vincent, W. and Kruger, C., Physical Gas Dynamics (Wiley, New York, 1965).
19. Grover, G. M., Cotter, T. P. and Erickson, G. F., J. Appl. Phys. 35, 1990 (1964).
20. EMI Gencom Inc., "An Introduction to the Photomultiplier" (Plainview, New York).
21. Kramers, H. A., Estratto dagli Atti del Congresso Internazionale de Fisici Como, 2, 545 (1927).
22. Krönig, R., J. Opt. Soc. Amer. Rev. Sci. Instrum., 12, 547 (1926).
23. Nussenzweig, H. M., Causality and Dispersion Relations (Academic Press, New York, 1972).
24. Toll, J. S., Phys. Rev. 104, 1760 (1956).
25. Lipson, S., and Lipson, H., Optical Physics, (Cambridge University Press, Cambridge, 1969).

26. Churchill, R., Complex Variables and Applications, 2nd Edition (McGraw-Hill, New York, 1960).
27. Jeans, J., An Introduction to the Kinetic Theory of Gases (Cambridge University Press, Cambridge, 1962).
28. Neast, R. C., ed., Handbook of Chemistry and Physics (The Chemical Rubber Co., Cleveland, 1965).
29. Herzberg, G., Atomic Spectra and Atomic Structure (Dover Publications, New York, 1945).

RECENT RESULTS OF RESONANT REFRACTIVITY STUDIES FOR IMPROVED FLOW VISUALIZATION

G. Blendstrup*, D. Bershader** and P. Langhoff†

*McKinsey & Co., **Dept. of Aeronautics & Astronautics, †Dept. of Chemistry

*Dusseldorf, Germany, **Stanford Univ., USA, †Indiana University, USA

Objective of this work is to achieve a two-order-of magnitude increase in the sensitivity of refractive-type optical flow diagnostic techniques, e.g., interferometry, schlieren methods and shadowgraphy. Useful applications would include visualization of audio-frequency sound waves at moderate levels, vortices and other disturbances in nearly-incompressible flow, turbulent structure in shear layers and other flows, and boundaries of rocket exhaust and plume flows where the refractivity variations are marginal. The method makes use of sodium vapor whose specific refractivity in the D-line region (589 nm) is several orders of magnitude higher than that of air or combustion gases. Injection of the vapor into a flow facility in highly diluted proportions (around $1:10^3 - 1:10^4$, depending on flow conditions) would achieve the desired result. A tunable dye laser is required as the light source to provide the wavelength control and resolution needed in the resonant region. By now the calibration measurements of resonant dispersion have been completed together with an analytic study of the effects of Doppler and collisional line broadening on the shape of the refractivity profile near resonance. The results confirm a successful trade-off between enhanced refraction and manageable absorption in the "near" region (several Å off resonance), a feature which makes the technique feasible.

INTRODUCTION

The sensitivity of nearly all refractive-type flow visualization studies to date has been limited by the value of the specific refractivity parameter (Dale-Gladstone constant) of diatomic gases. That quantity, K_0 , relates the refractive index n and mass density ρ in the well-known constitutive relation¹

$$n - 1 = K_0 \rho \quad I$$

For air K_0 is relatively constant over the visible portion of the spectrum, equal to $2.3 \times 10^{-4} \text{ m}^3/\text{kg}$. Physically, K_0 represents the volume density of dipole moment induced in the atomic or molecular gas by the electric field associated with the traversing light waves. This polarizability

is not highly dispersive, except near electronic ground-state transition frequencies, where its value increases by some orders of magnitude. Unfortunately, these resonances for air lie in the far vacuum ultra-violet. Indeed, such transitions in the visible spectrum are not easy to come by. The yellow-orange D₂-line of sodium vapor (wavelength $\lambda = 588.9963 \text{ nm}$) was chosen after consideration of the possibilities. It turns out that the non-resonant refractivity for sodium, $K_{0, \text{Na}}$ is $4.05 \text{ m}^3/\text{kg}$, 17.6 times that of air, so there is already an initial advantage. At about 8\AA off resonance this ratio increases to approximately 4,000. However, the latter figure is for so-called homogeneous line broadening as determined by Na-Na collisions. Line broadening for sodium highly diluted by a carrier gas X is of the heterogeneous type, controlled by Na-X collisions. For carrier gases of interest, the latter is another favorable factor: for example, the collision line width for sodium in argon is about 25 times smaller than for self-broadening in pure sodium vapor, which yields an additional factor of about 5 for the specific refractivity enhancement.

The calibration phase of the work consists of a combined experimental-analytical effort whose description forms the essence of the present paper. An experimental configuration was designed and constructed which measured the near-resonant dispersion of a sodium vapor column by interferometry. The analysis yielded a theoretical dispersion curve with which to compare the experiments. The theoretical basis starts with the Lorentzian analysis of electromagnetic wave dispersion by molecular dipoles, with the addition of Doppler and collisional line broadening features (Voigt profile). The formulation was done in terms of the Kramers-Kronig integral transforms relating refractive and absorptive dispersion, resulting in a computer output of both sets of profiles over the resonant region.

EXPERIMENT

The idea is illustrated in the schematic diagram of Figure 1. We see a

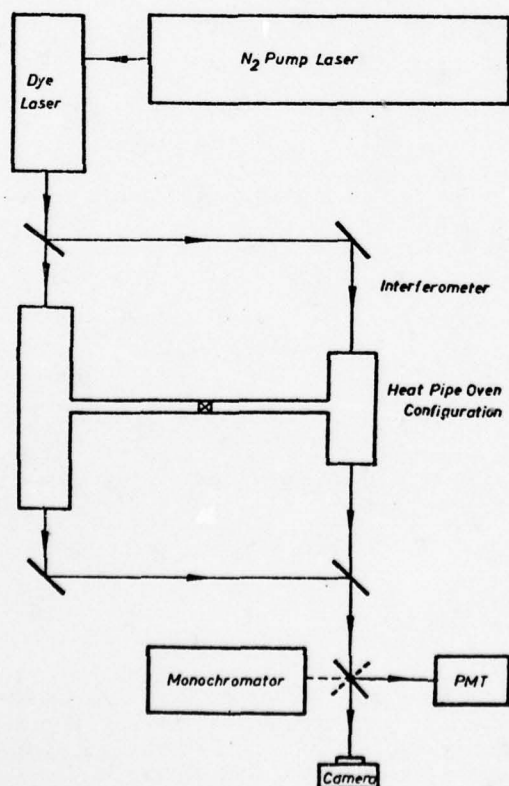


Figure 1. Overall schematic diagram for sodium resonant dispersion calibration.

double heat-pipe oven configuration occupying both arms of a Mach-Zehnder interferometer², with a dye laser as the light source and various output devices used in different parts of the experiment. A few words are warranted about some of the components.

The heat-pipe oven is a relatively new concept³ for containing a uniform, steady-state column of metal vapor in a defined volume, buffered by an inert gas. Briefly, the steady-state behavior includes vaporization of sodium in the central portion of the tube surrounded by a clam-shell heater, occupation by the vapor of the heated volume at a pressure determined by the metal's vapor pressure-temperature curve, condensation of the vapor at the boundary of the heated and cooled regions, and transport of the condensate back to the center of the tube by capillary action along a stainless steel mesh lining the inside walls of the oven. The use of a double oven of different column lengths allows cancellation of boundary and end effects on the optical path difference measured by interferometry. For reference, we note that the vapor pressure of sodium (torr) is related to temperature (°K) by

$$\ln P = 10.864 - 5619/T + (3.45 \times 10^{-6}) T - 1.041 \ln T$$

The tunable dye-laser light source designed and built by us for the purpose, is the component which makes resonant refractive work possible in the first place. It is shown schematically in Figure 2. The cavity is defined

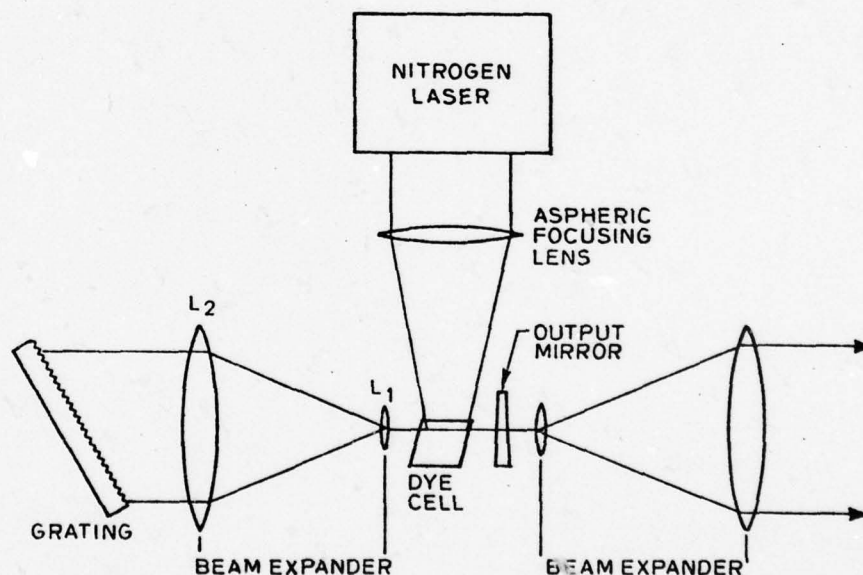


Figure 2. Schematic of Dye Laser Configuration

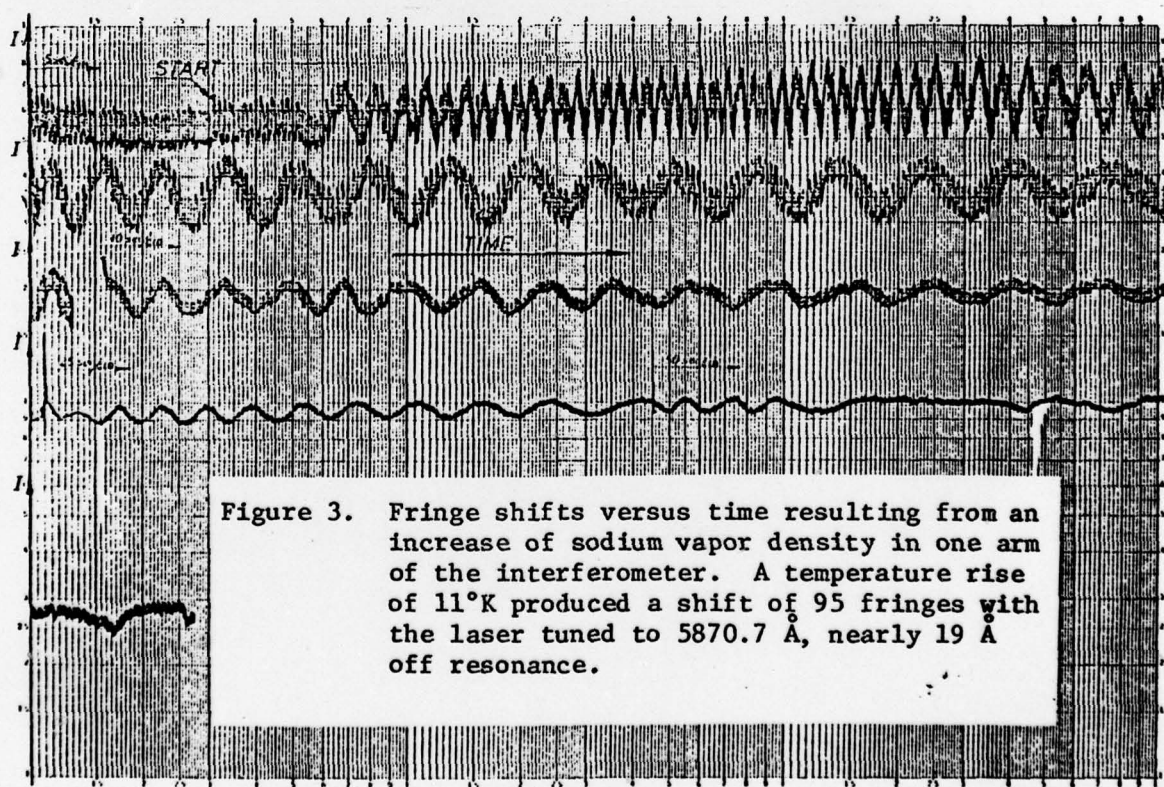
by a high-resolution blazed grating with micrometer angular control and an output window having a very small wedge angle. The dye cell (Molelectron Co. No. D1051) contains rhodamine 6G and is magnetically stirred. Activation is supplied by a pulsed nitrogen laser (Molelectron UV300) at 3371 Å, with a repetition rate of 10 pps and a pulse duration of about 10 nsec and a peak power of 300 kw. Fluorescence emitted by the dye solution lies between 5680 Å and 6050 Å with a maximum around 5790 Å, enabling convenient tuning to the D-line wavelength at 5890 Å with the rotatable grating. The laser cavity is about 50cm long; thus a 10 nsec pulse allows for only a few light passes, helping to ensure a suitably high power output combined with a reasonably narrow band width. Specifications of the dye laser are given in Table I. The listed bandwidth of 0.24 Å was satisfactory for present purposes.

TABLE I
Specifications of Dye-Laser

Dye Solution	Rhodamine 6G
Tuning Range	5860 - 6050 Å
Bandwidth (FWHM) at 5890 Å	0.24 Å
Wavelength Accuracy	< 0.1 Å
Wavelength Reproducibility	< 0.1 Å
Wavelength Stability	< 0.1 Å
Output Peak Power at 5890 Å	31 kW
Output Pulse Energy at 5890 Å	155 μJ
Repetition Rate	10 pps
Pulse Duration	5 ns

Sharpening the wavelength spread with a Fabry-Perot etalon would have resulted in a significant loss of output power, a feature we wished to avoid.

Wavelength accuracy, reproducibility and stability were determined with a McPherson 1-meter scanning monochromator (Model 2051) with a minimum instrumental line width of < 0.1 Å. It turned out that wavelength shifts due to temperature changes or other causes were smaller than this tolerance. Wavelength calibration was performed before each run, with the help of a sodium spectral lamp.⁴



The basic experiment consisted of measurement of shifts of the Mach-Zehnder fringes associated with a change in sodium vapor concentration; data was obtained at several wavelengths in the near-resonance region as described later in this paper. The shifting fringes traversed a 0.5 mm pinhole in front of a type RC5 C31000F photomultiplier tube cooled to -30°C to increase signal to noise ratio by a factor of 10. Output was recorded with an x-y plotter (Hewlett-Packard Type 7004B). Figure 3 shows the type of data obtained. Fringe shifts were considered to be precise to 0.1 fringes.

THEORETICAL CONSIDERATIONS

Both collision and doppler broadening produce marked changes in the dispersion profiles near resonance for the conditions of the present calibration experiment, or in a typical flow application. Collision broadening is essentially Lorentzian, i.e., the functional form is $\Delta\nu/(A+(\Delta\nu)^2)$, where $\Delta\nu$ is the frequency separation from resonance, with A a constant. Doppler broadening, on the other hand, is characterized by the exponential functional factor $e^{-B(\Delta\nu)^2}$, where B is also a constant; that factor stems from the random (Maxwellian) velocity distribution of the molecular dipoles. The combined collision-doppler phenomenon gives a convoluted Lorentzian-doppler shape termed a Voigt profile. The latter is represented by the following expressions for the refractive index $n(\nu)$ and absorption coefficient $\mu(\nu)$ as functions of the frequency ν :

$$n_r(\nu) - 1 = \frac{\sqrt{\ln 2}}{8\pi^2 \sqrt{\pi}} \frac{e^{2Nf_r}}{m\epsilon_0 \gamma_D \nu_r} \int_{-\infty}^{\infty} \frac{\epsilon - \nu}{(\epsilon - \nu)^2 + \gamma_L^2/4} e^{-4\ln 2 (\epsilon - \nu_r)^2 / \gamma_D^2} d\epsilon \quad \text{II}$$

$$\mu_r(\nu) = \frac{\sqrt{\ln 2}}{4\pi \sqrt{\pi}} \frac{e^{2Nf_r} \gamma_L}{m\epsilon_0 \gamma_D} \int_{-\infty}^{\infty} \frac{1}{(\epsilon - \nu)^2 + \gamma_L^2/4} e^{-4\ln 2 (\epsilon - \nu_r)^2 / \gamma_D^2} d\epsilon \quad \text{III}$$

where the usual symbols are used for well-known physical constants, and where f is the oscillator strength for the transition, N the atomic number density and γ_D and γ_L the characteristic doppler and Lorentzian spectral widths, respectively, given by

$$\gamma_D = \frac{4\pi\nu_r}{c} \sqrt{\frac{2kT\ln 2}{M}} \quad \text{IV}$$

and

$$\gamma_L = 2C_r N \quad \text{V}$$

with C_r a proportionality constant obtained from collision theory⁷. Note also that M represents the atomic mass and ν_r the resonant frequency. Table II gives some basic numerical data for the sodium D-lines. The calibration studies were performed on the high-frequency side of the D_2 -lines. When expressed in suitable nondimensional form, the integrals in equations II and III can be treated as the imaginary and real parts, respectively, of the function

$$W(z) = e^{-z^2} \text{erfc}(-iz), \quad z = u + ia \quad \text{VI}$$

TABLE II

Resonant Parameters for Sodium D-Lines. Subscript r Represents Resonant Frequency. C_r is the Parameter Which Determines Collision Broadening of the Lines.

	$\lambda_r [\text{\AA}]$	$\nu_r [10^{14} / \text{sec}]$	$f\#$	$C_r [10^{15} \text{ m}^3 / \text{sec}]$
D ₁	5895.930	5.083345	0.327	7.32
D ₂	5889.963	5.088500	0.655	8.59

where erfc represents the complementary error function and u is a non-dimensional doppler width given by $u = 2 \ln 2 (\nu - \nu_r) / \gamma_D$; while a , the so-called Voigt parameter, is essentially a Lorentzian-doppler width ratio: $a = \gamma_L \ln 2 / \gamma_D$. This formulation was used for the computer program. Results for the dispersion are shown as the solid line in Figure 4, based on results obtained in .01 Å intervals.

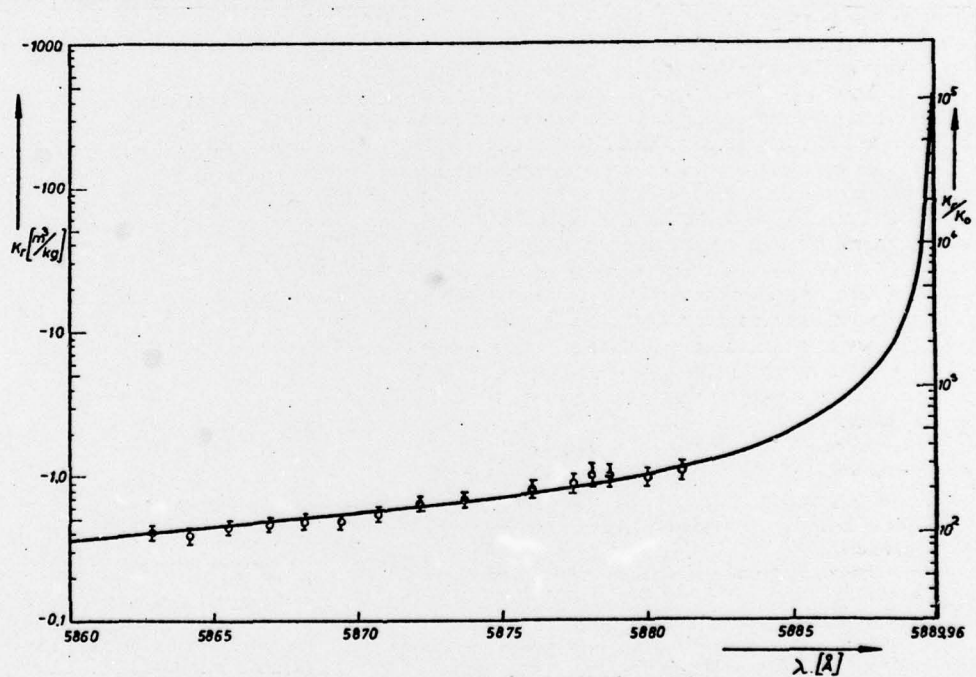


Figure 4. Wavelength dependence of refractivity parameter $K(=(n-1)/\rho)$ on high frequency side of sodium D₂ line. Solid curve is the theoretical prediction on which are superimposed measured points. Right-hand ordinate gives ratio to the non-refractive value for sodium. Ratio to nonrefractive value for air would be about 20 times larger.

FURTHER DISCUSSION

The refractivity peaks occur at the frequencies of half-maximum absorption which, in practice, are of order of 10^{-2} Å away from resonance. This spread stems from both collision and doppler broadening which, in turn, modify appreciably the predicted peak refractivity enhancement. For typical

conditions in the present experiment, namely an atomic density of around $10^{21}/\text{met}^3$ at a temperature in the range near 750°K , peak refractive amplification lies somewhat under 10^5 . In practice high absorption at or very near the refractivity maximum requires one to utilize the "near region" which is of the order of a few Å away from resonance. This trade-off between absorption and dispersion works because the spectral region of highly enhanced refractivity is considerably broader than the absorption region. As seen in Figure 4, the calibration experiments were performed at wavelengths where the refractive constant for the sodium vapor is around 10^2 times its nonresonant value. Experimental points superimposed on the theoretical curve show good agreement between the two, establishing good confidence in the predicted dispersion. Vertical uncertainty segments on the measured points stem largely from a corresponding uncertainty in the effective length of the sodium vapor column in the heat-pipe oven. Further work is required for more accurate determination of the position and shape of the diffusion boundary between the condensing sodium vapor and the argon buffer gas. Another limitation is the degradation of signal to noise ratio when the increased absorption near resonance lowers the transmitted wavelength intensity relative to the broad band noise background associated with the pulsed dye-laser arrangement. For example, at 7 Å away from resonance with $T = 465^\circ\text{C}$, the absorption coefficient $\mu = 7 (\text{met})^{-1}$, and fringe shift measurement becomes difficult.⁵ However, this problem becomes less severe with a more powerful light source, or in an aerodynamic application when sodium is diluted in a carrier gas, as described below.

In assessing the practical application of the resonant refractive method, one (1) needs to confirm the technology for injecting sodium vapor, say in atomic concentrations of 10^{-3} , with a laboratory flow, (2) apply the trade-off between enhanced refractivity and absorption to the flow parameters of the particular experiment and (3) decide on the objective, the latter determining which particular refractive diagnostic method will be used. Note that Fig. 4 also shows an ordinate which gives K in ratio to the nonresonant value for sodium K_0 , and we note further that $K_{0, \text{Na}} = 4.051 \times 10^{-3} \text{ met}^3/\text{kg}$ while a typical value for $K_{\text{air}} = 2.3 \times 10^{-4} \text{ met}^3/\text{kg}$. Thus, with sodium seeded into a flow of nitrogen, for example, the ordinate ratios are increased by about a factor of 18. The corresponding total refractivity enhancement reaches a value of 2.5×10^3 .

Another favorable factor relates to the change of Lorentzian line width for the case of heterogeneous broadening (sodium in a bath of buffer gas such as nitrogen or argon) as compared with self-broadening in pure sodium vapor, as was the case in these calibration experiments. A sensitivity analysis of the parameters indicates that the magnitude of the absorption in the wings of its profile is proportional to γ_L whereas the refractivity line shape is relatively insensitive to this same parameter. Thus a decrease of γ_L would permit closer approach to the resonance wavelength with corresponding considerable increase in refractive enhancement. Recent calculations indicate that the collision line width is much smaller in the heterogeneous case, and this result, in turn, indicates an additional factor of 5 in refractive amplification compared to the case of sodium self-broadening. A sample calculation for flow visualization of sound waves is performed in another paper.⁶

Injection of small amounts of sodium vapor from an oven into a flow has been a technique used by research chemists and others, but needs further development in aerodynamic applications. For quantitative interferometric studies, the absolute concentration of sodium vapor will have to be known, but that would not be the case for schlieren and shadow-type studies. All features considered, it looks quite feasible to improve sensitivities of these methods surely by one and possibly up to two orders of magnitude by suitable experimental design. The method also offers a quasi-localized diagnostic capability resulting from localized injection of the seed vapor. The results

of the present calibration study and related analysis warrant development of a pilot facility designed to utilize the resonant refractive technique.

REFERENCES

1. (a) M. Born and E. Wolf, Principles of Optics, 5th edition, p. 88, Pergamon Press, 1975.
(b) D. Bershader, "Some Aspects of the Refractive Behavior of Gases" in Modern Optical Methods in Gas Dynamic Research, D. Dosanjh (Ed.), pp. 65-83, Plenum Press (1971)
2. R. Ladenburg and D. Bershader, "Interferometry," in Physical Measurements in Gas Dynamics and Combustion, Princeton University Press, 1954.
3. C.R. Vidal and J.J. Cooper, J. Appl. Physics **40**, 3370 (1969).
4. G.H. Blendstrup, Resonance Refractivity Studies of Sodium Vapor for Enhanced Flow Visualization, Doctoral Thesis, Department of Aeronautics and Astronautics, Stanford University, December 1978.
5. G. Blendstrup, D. Bershader and P. Langhoff, A.I.A.A. Journ. **16**, pp. 1106-1108, October 1978.
6. D. Bershader, G. Prakash and G. Huhn, "Improved Flow Visualization by Use of Resonance Refractivity", Experimental Diagnostics in Gas Phase Combustion Systems, (B.T. Zinn, Ed.), pp. 595-609, American Inst. of Aeronautics and Astronautics, New York, 1977.
7. K. Niemax and G. Pichler, J. Physics, **B8**, Feb. 1975, p. 179.

ACKNOWLEDGEMENT

We acknowledge support for this work from the U.S. Air Force Office of Scientific Research, Department of Defense, Grant AFOSR 74-2670.